AIR PLASMA SPRAYING OF COPPER-BASED SOFC ANODES FOR DIRECT OXIDATION OF HYDROCARBON FUELS

by
Nir Light

B.Sc., Technion Israel Institute of Technology, 1994
M.Sc., Ben Gurion University of the Negev, 2002

A THESIS SUBMITTED IN PARTIAL FULFILLMENT OF THE REQUIREMENTS FOR THE DEGREE OF
DOCTOR OF PHILOSOPHY

in
The Faculty of Graduate Studies

(Mechanical Engineering)

THE UNIVERSITY OF BRITISH COLUMBIA
(Vancouver)

July 2012

Abstract

This thesis investigates the utilization of atmospheric plasma spraying (APS) utilizing a DC axial injection torch to produce porous composite SOFC anodes for direct oxidation of hydrocarbon fuels based on samaria doped ceria (SDC) or gadolinia doped ceria (GDC) and Cu or Cu-Co. Currently, these anodes are manufactured by multi-step wet ceramic processes, which makes them difficult to produce economically at moderate volumes. In contrast to wet ceramic processing, APS allows rapid, easy-to-automate processing and easy scale-up to mass production of SOFCs.

The main challenge in producing these anodes by APS is to co-deposit materials with a large difference between their melting temperatures in a coating having a porous structure, which is required in SOFC anodes for good mass transport and high performance. In addition, in the case of Cu-Co based anodes, surface alloying of the Cu and Co phases enriches the surface of this mixture with Cu. This mechanism was suggested to explain the excellent tolerance of Cu-Co anodes manufactured by wet ceramics process for carbon deposition [1]. However, it is not clear whether surface alloying occurs during APS due to the larger mixing scale and rapid solidification of the deposited materials.

A range of plasma process parameters has been examined in this work for the production of homogeneously mixed anode coatings from pre-mixed spray dried micron-sized agglomerated feedstock powders. Fine and coarse powders have been used to produce anode coatings, which were characterized for crystallography, composition, microstructure, porosity, and gas permeation. Anode electrochemical performances

were also characterized by impedance spectroscopy, and the extent of carbon deposition was determined by weight gain of the anode during exposure to methane.

By adequate control and refinement of processing parameters and starting powders, it is possible to achieve coatings with properties not typical to the plasma spray process. This work overcame processing challenges stemming from a material set having large a difference between the melting temperatures of each material, demonstrating the feasibility of obtaining fairly homogenous Cu-SDC and Cu-Co-SDC/GDC anodes with performances comparable to those of Cu-based anodes fabricated by wet ceramic processing.

Preface

A version of chapter 2 and 3 has been published. Nir Benoved, O. Kesler,' Air plasma spray processing and electrochemical characterization of Cu–SDC coatings for use in solid oxide fuel cell anodes', Journal of Power Sources 193 (2009) 454–461. I conducted all the testing and wrote the first draft of the manuscript.

Chapter 4 and 5 is based on work conducted at UBC and NRC-IFCI. I conducted all experiments and first draft of writing except symmetrical cathode cell tests and equivalent circuit fitting, which was conducted by Dr. Elisa Lay at the Fuel Cell Materials and Manufacturing Laboratory at the University of Toronto.

Table of Contents

List of Tables

List of Figures

Acknowledgements

I gratefully acknowledge the dedicated guidance of my supervisor Dr. Olivera Kesler and her endless support and help in any aspect of my work. Thank you Olivera for so much time, patience, and discussions generosity dedicated to my research work. Thank you very much for my committee members, Drs. Walter Merida and Dr. Martin Davy for their input during the years.

I gratefully acknowledge the help of past and present colleagues within our group especially Dr. David Waldbillig, Dr. Javier Gazzarri, Dr. Elisa Lay, Lars Rose, Craig Metcalfe, Dr. Michael Poon, and Brad White.

I am gratefully acknowledging the generous support of Northwest Mettech Corp. and the Natural Sciences and Engineering Research Council of Canada for funding and of the National Research Council Institute for Fuel Cell Innovation (NRC-IFCI) for access to their facilities. This research was supported in part through funding to the NSERC Solid Oxide Fuel Cells Canada Strategic Research Network from the Natural Science and Engineering Research Council (NSERC) and other sponsors listed at www.sofccanada.com.

I gratefully acknowledge the assistance of Dr. David Waldbillig for the production of suspension sprayed electrolytes for the full cells, and the generous help of Dr. Cyrille Deces-Petit from NRC-IFCI for the testing of symmetrical cells and the design and maintenance of testing equipment. I also would like to thank NRC-IFCI staff for their help through this project. Special thanks to Mark Robertson and Sing Yick.

Special thanks are owed to my parents, whose have supported me throughout my years of education, both morally and financially.

Very special thanks for my loving wife and life partner Sandra and my daughter Melodie for your endless love encouragement and support. Without you this work would have never been possible.

Dedication

To my loving wife, Sandra, and my wonderful daughter, Melodie

1. Introduction

1.1 Solid oxide fuel cells (SOFCs)

Fuel cells convert the chemical energy of a fuel, such as hydrogen, into electrical energy very efficiently on many size scales, without combustion and with little or no emission of pollutants. Solid oxide fuel cells (SOFCs) are highly efficient, entirely solid-state fuel cells that operate at high temperatures. They can be used for large-scale central power generation, for distributed generation, or for auxiliary power in transportation. When hydrogen is used to power solid oxide fuel cells, water is the only local emission produced, and the fuel cells experience relatively low degradation rates and fast electrochemical kinetics. However, hydrogen must be generated, compressed, and transported, thus creating high energy requirements and correspondingly higher costs compared to more readily available fuels. Using carbon-containing fuels, such as coal gas, methanol, ethanol, natural gas, gasoline, diesel, carbon monoxide, or renewable bio-fuels to power SOFCs may allow faster commercialization and more widespread use. Widespread power generation from carbon containing fuels using fuel cells rather than combustion engines will result in substantial reductions in greenhouse gas and acid gas emissions due to the absence of nitrogen oxides and the higher efficiency of electrochemical energy conversion.

Commonly, SOFCs require a high operating temperature (for example: 800-1000°C) to ensure sufficiently high ionic conductivity and fast electrode kinetics. However, there are technological and cost issues associated with high temperature operation. These issues drive current attempts to reduce the operation temperatures of SOFCs to a lower temperature range (for example: 600-750°C), and thus to reduce

costs and increase reliability, which will allow SOFCs to become more commercially feasible [2].

1.2 Principle of operation of an SOFC

The operation principle of an SOFC utilizing methane is illustrated in Figure 1.1. An SOFC is composed of three layers: a cathode, an electrolyte, and an anode. The cathode and the anode are exposed to air and fuel, respectively. At the cathode, oxide ions are formed by disassociation of oxygen gas and reduction by the electrons flowing to the cathode from an external circuit. The oxide ions migrate through the ceramic based electrolyte, which is an oxide ion conductor and electronic insulator. This migration occurs due to the electrochemical potential difference across the cell that results from the different oxygen concentrations at the cathode-electrolyte and anode-electrolyte interfaces. At the anode, oxide ions react with the fuel, for instance hydrogen or methane, giving up electrons to the external circuit and forming water and also CO_2 if the fuel contains carbon. The released electrons flow through the external circuit back to the cathode, thus producing electric current.

Figure 1.1: Operation principle of an SOFC

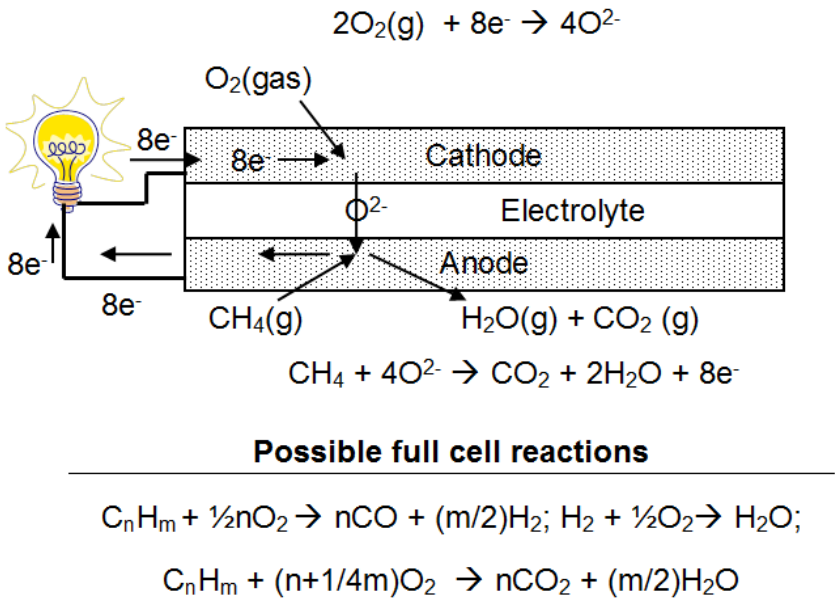

1.3 SOFC components

1.3.1 SOFC anodes

SOFC anodes must combine sufficient catalytic activity for fuel oxidation with sufficient electrical conductivity to convey the released electrons to the external circuit. To obtain these requirements, SOFC anodes are processed commonly of a composite of nickel and yttria-stabilized zirconia (YSZ) [3]. Nickel is utilized as an electronic conductor and a catalyst necessary to obtain rapid kinetics of fuel oxidation with the oxide ions coming through the solid electrolyte. YSZ is utilized as an ionic conductor and as a microstructural stabilizer to allow operation at high temperatures. A composite consisting of a metallic phase and a ceramic phase, such as Ni-YSZ, is known as a cermet. Utilization of an ionically conducting material such as YSZ allows the anode to

spread the oxide ions across a broader volume of the anode, beyond the planar anode/electrolyte interface, and thereby increase anode performance.

There are several attributes required of SOFC anodes. These attributes include a reasonably good matching of thermal expansion coefficient and chemical compatibility with the electrolyte, sufficient electronic and ionic conductivity, sufficient porosity to allow fuel gas diffusion to the reaction sites, chemical stability within fuel-rich and steam-rich environments, and mechanical strength.

The electrochemical reactions in the anode occur at the triple phase boundaries (TPBs), which are the linear boundaries where the gas phase meets both ionic and electronic conducting phases. TPB length has an important effect on cell performance. Greater TPB length means that more reaction sites are present, thereby potentially reducing activation losses and increasing cell performance. One of the strategies applied to increase TPB length at the anode is the utilization of fine particles, which result in a greater reaction surface area. Therefore, SOFC anodes are typically produced by utilization of nano-size particles. An additional strategy is to utilize a mixed ionic-electronic conductor, for example, doped ceria, which becomes a mixed conductor in the reducing fuel environment.

Figure 1.2 shows (a) a TPB region of purely electronically (Ni) and ionically (YSZ) conducting materials and (b) reaction surface area of a mixed ionic-electronic conductor. In the case of a mixed ionic-electronic conductor the TPB area is extended. Ceria is added to the anode as an additive to increase its performance, or it is utilized to entirely replace the ionically conductive phase, typically YSZ. Figure 1.2b shows an anode containing ceria only utilizing methane. Such an anode has been demonstrated

as a functional electrochemically active layer for utilization of hydrocarbon fuel [4]. Alternatively, ceria-containing anodes can also contain other materials such as Ni, Cu, Co, or YSZ

Figure 1.2: TPB regions of (a) purely electronically (Ni) and ionically (YSZ) conducting materials and (b) a mixed ionic-electronic conductor

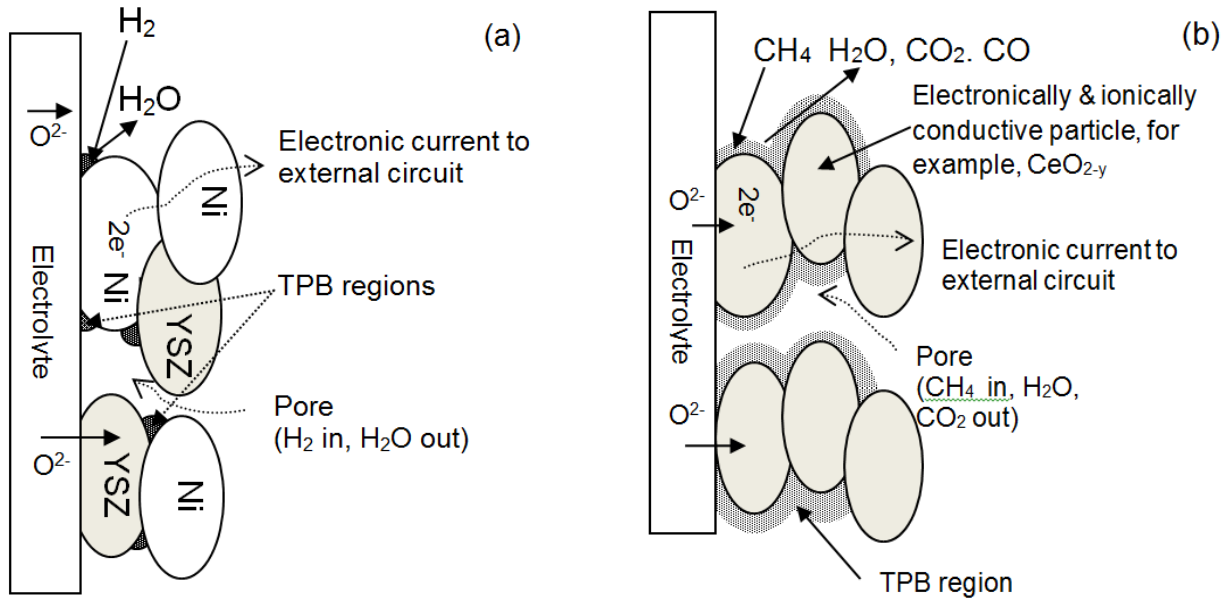

At the anode, electrons are conducted to the external circuit through the electronically conductive phase within the anode cermet. To minimize ohmic losses at the anode, the relative volume of the electronically conductive phase should be above the percolation threshold of approximately 30% [5].

Open porosity volume fraction has an important role in anode performance, as the gaseous reaction species diffuse through the porous anode microstructure to the reaction sites. Anodes are commonly fabricated with an open porosity of 30% to 40% to allow adequate gas diffusion.

1.3.2 SOFC electrolytes

The electrolyte in SOFCs must be stable in both reducting and oxidizing environments, and must have sufficiently high ionic conductivity and very low electronic conductivity at the cell operation temperature. Electronic conductivity facilitates undesirable electronic current in the electrolyte and reduces cell performance. In addition, the electrolyte must be chemically compatible with both the anode and cathode materials, to avoid inter-reactions resulting in the formation of non-conductive phases. Furthermore, thermal expansion coefficients of electrolyte materials must be close to that of the other cell layers, i.e., anode, cathode, and substrate, to decrease stresses due to thermal expansion mismatch.

The electrical conductivity of most common electrolyte materials, which are ionically conductive ceramics, is much lower than that of metals. For example, the electrical conductivity of 8 mol% yttria stabilized zirconia (YSZ, $(ZrO_2)_{0.92}(Y_2O_3)_{0.08}$), which is commonly used as the electrolyte in SOFCs, is 1.74 $x10^{-2}$ S cm^{-1} at 700°C [6]. In comparison, the electrical conductivity of nickel at 700°C is 3.12$X10^4$ S cm^{-1} [7]. The low ionic conductivity of the electrolyte is the major contributor to the ohmic losses in SOFCs. Therefore, the SOFC electrolyte must be thin (on the order of a few microns to 30µm) to reduce ohmic losses. In addition, the electrolyte must be gas tight to avoid mixing between the fuel and the oxidant, which can result in combustion and a decrease in performance. The high localized temperatures due to combustion may cause cracking of the electrolyte, oxidation of the metal substrate, or formation of non-conductive oxidized layers, leading to cell failure. The requirement for gas tightness and low thickness is a major challenge in the production of SOFC electrolytes.

1.3.3 SOFC cathodes

Cathodes for SOFCs have to possess many properties. First, cathode materials must have high electrical conductivity, be chemically stable in oxidizing environments, possess sufficient catalytic activity for oxygen reduction, and be chemically compatible with the electrolyte and interconnect materials. Furthermore, the thermal expansion coefficient of the cathode materials must be close to that of the other cell layers, i.e., anode and electrolyte, to decrease stresses due to thermal expansion mismatch. In addition, the cathode must have a good microstructure for catalytic activity. A high surface area, i.e., high TPB length, is required to increase reaction rates and minimize activation losses, and sufficient porosity is required to allow rapid diffusion of the oxidant gas to the reaction sites. Cathodes are commonly fabricated with an open porosity of 30% to 40% to allow adequate gas diffusion. Finally, the cathode must possess mechanical strength to withstand stresses arising from thermal mismatches with the other cell layers.

Most metals are oxidized in SOFC operation temperatures in the presence of oxygen, and therefore cannot be utilized as the electronic conductor in the cathode. Some metals can be utilized for this purpose, for example, platinum. However, this use results in significant cost increase, which makes the application of platinum as a cathode material impractical. Additional candidates for SOFC cathodes are electronically conductive oxides such as strontium doped lanthanum manganite (LSM, $La_{1-x}Sr_x)MnO_{3-y}$), and mixed ionic/electronic conducting (MIEC) oxides such as the perovskite $La_{0.8}Sr_{0.2}Co_{0.8}Fe_{0.2}O_{3-y}$ (LSCF). [8]. However, many of these candidate materials react with typical electrolyte materials at electrolyte firing temperatures

(1400°C); therefore, cathode material selection is frequently limited by compatibility issues with other fuel cell components [8].

1.4 Manufacturing of SOFCs

1.4.1 Manufacturing of SOFCs by wet ceramic processing

SOFC manufacturing by wet ceramic processing utilizes multiple processes to manufacture the cell. Tape casting is commonly used to manufacture Ni based SOFC anodes for the planar stack design, in which commonly the anode provides the mechanical support and therefore is the thickest layer among all SOFC layers in the anode-supported cell architecture ([9], [10] and [11]). This process utilizes formulated slurry comprising ceramic powders, NiO and YSZ, and a liquid system. The liquid system includes solvent, binder, plasticizer, and a deflocculant or wetting agent. After preparation, the slurry is spread to a controlled thickness with a doctor blade of a tape caster. The thickness of the tape is controlled by the blade gap.

After the tape is cast, it is moved to a dryer to remove the solvent. The other cell layers are then deposited onto the NiO-YSZ tape, commonly by a chemical or physical process such as spray pyrolysis, screen printing, or electrochemical vapor deposition. After deposition of all cell layers, the tape with the deposited layers is densified at elevated temperatures [12]. Figure 1.3 shows tape casting processing of an SOFC layer.

Figure 1.3: Tape casting processing of an SOFC layer

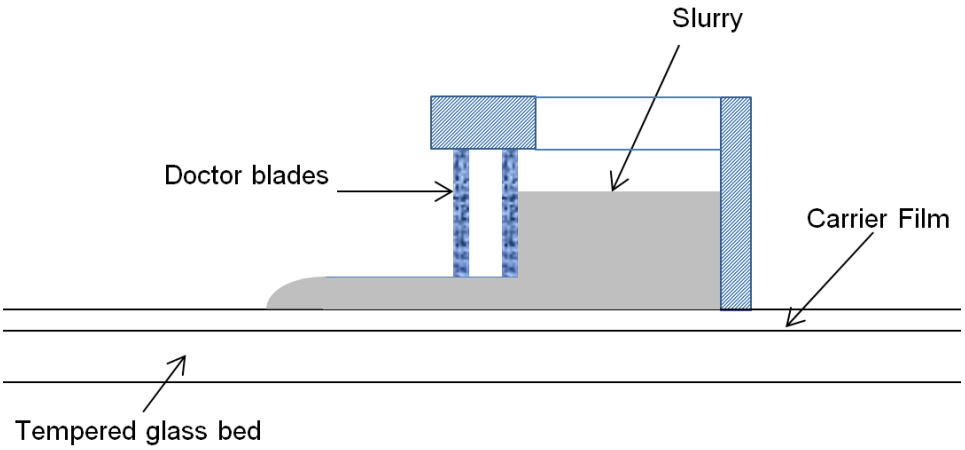

Utilization of tape casting to manufacture SOFC anodes has two main advantages. First, in the tape casting process, fine nano-size ceramic powders can be utilized to obtain a high surface area anode, which is important to obtain a high surface area of reaction rates and high electrochemical performance. Second, organic pore former can be added to the slurry to obtain the desired porosity. The pore former is then burned out during the firing step, leaving pores.

Despite these advantages, tape casting processing has several drawbacks. The complex multi-step processing procedures are time consuming and require significant capital costs, particularly when scaled up for mass production as the volume of cell production increases due to the long processing time and the need for enlarging production rates through the use of parallel production lines. An additional cost increase stems from the need to utilize multiple separate instruments, such as tape caster or extruder, screen-printer, and one or more furnaces are required for the multiple steps of the wet ceramic technique. In addition, high sintering temperatures increase the likelihood of inter-reactions between adjacent cell layers or of metal support oxidation in

metal-supported cells. Moreover, tape casting of planar cells of more than 25cm X 25cm can result in large total shrinkage or thermal expansion mismatch strain, often leading to macro-cracks, severe warping, or cell fracture during high-temperature firing steps. In addition, the choice of materials to manufacture cermet electrodes is limited to materials that can be co-sintered during the firing steps, i.e., having sufficiently close melting , allowing them to be co-sintered, without fully melting the low melting temperature material. In addition, the requirement for high temperature sintering in wet ceramic processing generally precludes the use of porous metallic layers as the structural supports for the SOFCs [13].

1.4.2 Manufacturing of SOFCs by plasma spray deposition

1.4.2.1 Advantages of plasma spraying

Plasma spray processing is a well-established surface coating technique developed in the 1960s. In plasma spraying, a plasma jet is created by flowing gases through high voltage electrode arc in a torch. The feedstock materials are fed into the plasma in a form of dry powders, suspensions, or precursor solutions. The particles are accelerated and melted or partially melted in the plasma jet, and then impact a substrate to form the coating. Plasma sprayed coatings are utilized for multiple applications, such as thermal barrier coatings (TPB) for turbine blades, wear resistant coatings for machinery, synthesis of powders and others ([14], [15] and [16]). Various plasma spray technologies have been studied recently as processing procedures for the manufacturing of SOFCs ([17], [18], [19], [20], [21], [22] and [23]) due to their potential to provide a simplified and cost-effective choice for fabricating SOFC components and cells in comparison to wet ceramic processing.

Plasma spraying has several advantages such as short processing time, material composition flexibility, and a wide range of controllable spraying parameters that can be used to adjust the properties of the coatings. Controlling the spraying and feedstock parameters during spraying allows control of the coating characteristics, creating the opportunity to vary the coating properties with thickness to obtain a functionally graded material (FGM) structure that may lead to better electrochemical performance and reduced thermal stresses ([20] and [21]). It also allows manufacturing of an entire cell in a fully-automated fabrication process ([17] and [24]), and spraying directly onto robust metallic interconnects, thus lowering material costs, with no requirement for sintering [24]. Nano-structured anodes have also been produced by plasma spraying of nano-agglomerated feedstock powder ([25] and [26]). This approach can provide more triple phase boundaries for the hydrogen oxidation reaction and contribute to the lowering of polarization losses. Plasma spray processing can also be scaled up easily for rapid, automated mass production, which may allow further reduction of manufacturing costs. Figure 1.4 shows a schematic diagram of plasma spray processing.

Figure 1.4: Schematic diagram of plasma spray processing

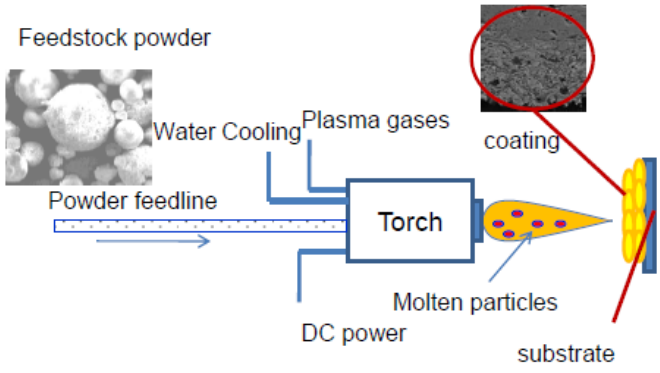

1.4.2.2 Principles of plasma spraying

1.4.2.2.1 Types of plasma torches

Plasma is generated in the torch utilizing two main methods, direct current (DC), or radio frequency (RF) induction. In direct current plasma torches, an arc is formed in between the cathode(s) and the anode(s) in the torch by applying a high DC voltage. Gases passing through the arc disassociate and ionize, thus forming the plasma. In an induction plasma torch, a generator supplies an alternating current (AC) of radio frequency to a coil in the torch. This alternating current induces an alternating magnetic field inside the coil. The alternating magnetic flux induces a voltage in the torch in accordance to Faraday's law, thus creating the plasma. Induction plasma torches are characterized by their large volume, low velocity and energy density, and their ability to provide the feedstock particles a relatively long in-flight heating time, on the order of 10 to 25 ms, compared to 0.5 to 1.0 ms in dc plasma spraying [27]. RF plasma spraying has been applied for the manufacturing of SOFCs [18].

RF torches, due to their electrodeless design, allow feeding of feedstock powder axially through the torch, unlike most DC torch designs, in which the feedstock powder must be fed radially. Axial feeding provides higher deposition efficiency and more homogeneous melting of the powder because the powder is fed directly into the plume axis, which is the hottest part of the plasma. One DC torch design, the Axial III torch (Mettech Corp. Inc., North Vancouver, BC Canada), used in this research, allows axial feeding of the powder. The design is rather complex because it requires radial arrangement of the electrodes.

In addition to axial feeding, RF torches do not have electrode erosion or contamination issues that typically occur with DC torches. This feature allows the application of widely versatile chemistry, including reducing, oxidative, or corrosive materials in RF torches.

Despite these advantages, the low particle velocities in RF plasma spraying can result in lower deposition efficiencies in comparison to axial injection DC plasma spraying, due to the longer residence time of the powder particle within the surrounding atmosphere resulting in resolidification of the particles and bouncing off of the substrate. One approach to reduce the residence time of the particles in the surrounding atmosphere is to decrease the standoff distance. However, this approach is limited because a decrease of standoff distance increases the heat flux to the substrate, which may cause melting of the substrate or sintering of the coating.

1.4.2.2.2 Atmospheric (APS) and Vacuum (VPS) plasma spraying

In addition to the type of torch applied (RF or DC), plasma spraying is characterized by the pressure of the surrounding atmosphere in which the process is taking place. Commonly, plasma spraying is conducted in air. Alternatively, it can conducted in an evacuated chamber. This reduced-pressure process is known as vacuum plasma spraying (VPS) or Low-Pressure Plasma Spraying (LPPS).

In VPS, the spray chamber is evacuated and then filled with inert gas and maintained at a low pressure (~100mbar). This low pressure allows coatings of reactive materials to be produced without oxidation. The high droplet impact velocities and low oxidation associated with VPS allow very dense coatings to be manufactured. Vacuum

plasma spraying is preferred to atmospheric plasma spraying (APS) for oxidation sensitive materials such as Ti alloys, and/or where improved adhesion and density is required. VPS has been applied for the manufacturing of low porosity SOFC electrolytes [23]. Due to the low porosity of coatings produced by VPS, it is less suitable for the production of SOFC electrodes. In addition, VPS is more costly in comparison to APS ([23] and [28]). Table 1.1 shows a comparison between plasma and feedstock parameters of the different plasma spray processes [29].

It can be seen in Table 1.1 that the plasma plume temperatures and velocities varies widely. This is because the plume's temperatures and velocities varies with the spraying parameters applied, such as torch current, plasma gas flow rates and plasma gas composition. In addition, plasma temperature and velocity varies within the plasma plume dependent on the distance from the torch nozzle and the jet axis. Therefore, a range of values is presented in Table 1.1.

It can also be noted in Table 1.1 that nitrogen is not used as plasma gas in both vacuum plasma spraying and radio frequency inductive plasma spraying. These two processes are applied normally for processing of reactive materials, so a reactive gas such as nitrogen in normally not applied in these processes.

Table 1.1: Plasma and feedstock parameters of different plasma spray processes

	Atmospheric plasma spraying (APS)	Vacuum plasma spraying (VPS)	Radio frequency (RF) inductive plasma spraying
Jet characteristics			
Jet temperature (K)	7,000-20,000[1]	2000-13,000[2]	2000-10,000[3]
Jet velocity (ms^{-1})	300-1000	200-600	20-80
Gas flow (slpm)	100-250	150-250	75-150
Gas types	Ar, He, N_2, H_2	Ar, He, H_2	Ar, He, H_2
Power input (kW)	40-200	40-120	40-200
Chamber pressure (kPa)	101	5-35[2]	101
Powder particles			
Particle temperature (max, °C)	>3800	>3800	>3800
Particle velocity (ms^{-1})	200-800	200-600	20-50
Material feed rate ($gmin^{-1}$)	50-150	25-150	20-50
Coating			
Density range (%)	90-95	90-99	95-99
Bond strength (MPa)	<68	>68	>68

1.4.2.2.3 Feedstock powder

A powder suitable for plasma spraying should exhibit good pouring properties. so that it can be fed into the torch without clogging the feeding lines. The powder particles should be a spheroid or similar shape. Recent studies utilized spray dried powder made of agglomerates of micron-sized powder to manufacture SOFC anodes by APS ([26] and [30]). Spray drying is a method of producing a dry powder from a liquid or slurry by rapidly drying with a hot gas, allowing the production of spherically shaped powders. These anodes exhibited better gas permeability and higher surface area, resulting in

[1] S.C. Snyder, L.D. Reynolds, J.R. Fincke, G.D. Lassahn, J.D. Grandy and T.E. Repetti, *Phys. Rev. E: Stat. Phys. Plasmas Fluids Relat. Interdisc. Topics* **50** (1994), pp. 519–525

[2] Y. Y. Zhao, P S Grant, B Cantor, Modelling and Simulation in Material Science and Engineering 8 (2000) 515–540

[3] J. Mostaghimi , P. Proulx, M. I. Boulos, Plasma Chemistry and Plasma Processing, 4 (1984) 199-217

43% lower polarization resistance and 34.5% higher power density compared with plasma sprayed anodes processed with commercially available non spray dried sintered and crashed feedstock powders.

1.4.2.2.4 Powder particle size

Feedstock powder particle size range and/or particle size distribution is an important parameter influencing the resulting coating microstructure. There are several techniques that aim to provide a single number that is indicative of the particle size. Powder particles are three dimensional objects not necessarily having a spherical shape. Therefore, to provide one single number indicative of the particle size, most analysis techniques assume that the material being reported is spherical and report the particle size as the diameter of an equivalent sphere having the same volume or other physical property as the particle being measured. The equivalent sphere varies dependent on the measuring technique. Figure 1.5 shows several possible equivalent spheres for a particle having irregular shape [31].

Figure 1.5: Equivalent spheres for a particle having irregular shape

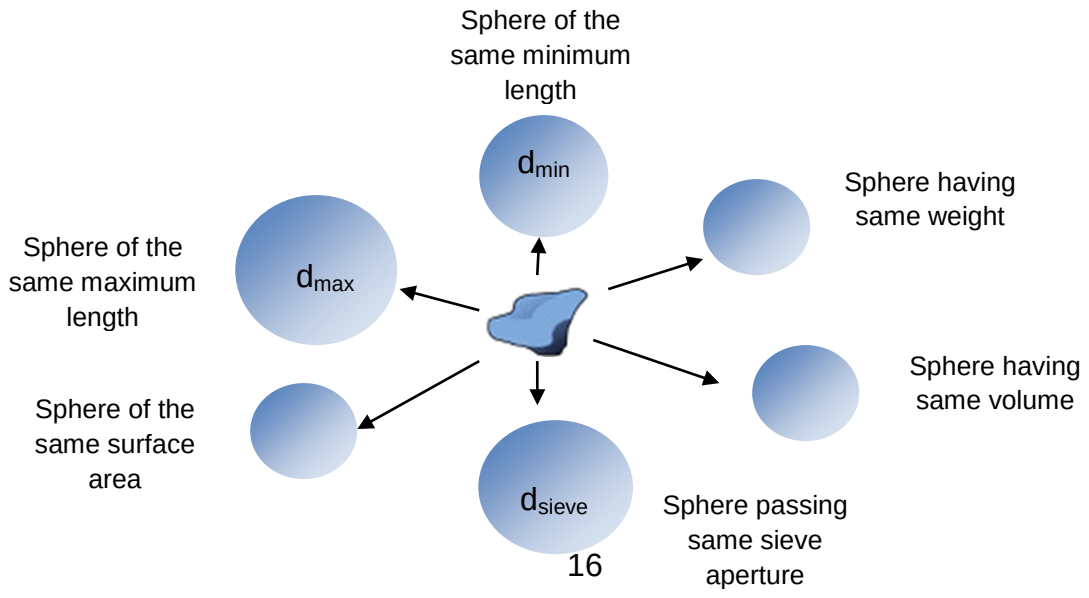

Two common particle size analysis methods are applied in this research, laser light scattering and the usage of sieves. In laser light scattering, a laser beam is aimed through a suspension of the powder. The beam hits a particle and is scattered at an angle dependent on the size of the particle. A series of detectors is used to measure the light intensities dependent on the diffraction angle. The resulting spectrum of intensities at a range of detector angles is used to calculate the distribution of the particle sizes present in the powder specimen. In the case of laser scattering, the diameter of the sphere that yields an equivalent light scattering pattern to the particle being measured is reported. In the work, the diameter of a sphere having the equivalent volume as the particles measured is reported.

Sieving is a common method used to obtain a specific range of particle sizes of a powder. In this method, sieves having different aperture sizes are stacked together, starting with the finest sieve on the bottom with the coarser sieves stacked on top. The powder is placed in the coarsest sieve, and the sieve stack is then shaken using a shaker. After sieving, the sieves are separated. The powder remaining in each sieve has a size range smaller than the upper sieve aperture size and larger than the lower sieve aperture size. This size range is typically indicated as –X + Y, with X representing the upper sieve aperture size, and Y representing the lower sieve aperture size. In the case of the sieved size range, the equivalent sphere radius will most likely be one of the particle's length, width, or height, dependent on the particle orientation while passing through the sieve aperture.

Some measuring techniques, such as light scattering, report the distribution of particle sizes in term of relative volume of a specific size range to the total powder

volume reported as a distribution histogram or by other statistical means. D_{50} is typically used to indicate the particle diameter corresponding to the midpoint in the size range, with D_{10} and D_{90} representing the sizes below which 10 % and 90% of the particles occur, respectively. Other measurement techniques, such as usage of sieves, report a particle size range but cannot report the distribution of the particle sizes within this range.

1.4.2.2.5 Plasma jet

In plasma spraying processing, plasma is created by dissociation and ionization of gas molecules due to the electrical energy input of the electrodes in the torch. The reverse process that occurs in the plasma provides the heat for fully or partially melting the particles of the sprayed materials. Commonly in plasma spraying, nitrogen, argon, helium or hydrogen are used to form the plasma. These gases can be divided into two groups – monatomic and diatomic gases. The process of plasma formation of a diatomic gas differs from the process of plasma formation of a monatomic gas. The difference consists in the fact that a diatomic gas both ionizes and dissociates, while a monatomic gas ionizes without disassociation. The two major reasons to use diatomic gases in plasma processing are to obtain plasmas of high energy content sand good thermal conductivity or to control the processing atmospheric chemistry.

In order to start the plasma in the torch, the gas must be ionized. This is done by applying a high voltage to the gas. Above a certain breakthrough voltage, electrons are extracted from the atomic core and the gas becomes ionized. The more energy

necessary for the first ionization of an atom, the more difficult it is to start the plasma, and the higher the breakthrough voltage [20].

With supply of energy from the electrodes in the torch, diatomic gases, such as N_2, dissociate into free atoms, as described by equation 1.1

$$N_2 + \text{energy} \rightarrow 2N \quad (1.1)$$

With a further increase in energy input, the free atoms ionize, as can be described in equation 1.2.

$$2N + \text{energy} \rightarrow 2N^+ + 2e^- \quad (1.2)$$

The reverse processes occur in the plasma, as can described in equation 1.3. This process provides the energy for heating the powder particles during spraying.

$$2N^+ + 2e^- \rightarrow 2N + \text{energy} \rightarrow N_2 + \text{energy} \quad (1.3)$$

In plasma spraying, nozzle exit velocities are typically on the order of 900–2000 ms^{-1} ([32] and [33]). Plasma jet temperatures generally vary between 7000°K and 20,000°K [34]. Both jet velocities and jet temperature are dependent on multiple spraying parameters, such as torch current, plasma gas composition, plasma gas flow rate, and nozzle size. Jet velocities and temperatures are not homogenous throughout

the plasma jet. Rather, they change dependent on the horizontal and vertical distance from the nozzle of the torch and the centreline of the plasma.

Figure 1.6 shows temperature contours in a plasma jet (a) without substrate and (b) with substrate, generated by numerical modeling analysis of a N_2-Ar plasma [35]. It can be seen that the jet temperature generally decreases in both the horizontal and vertical directions further from the torch exit and plasma central axis.

Figure 1.6: Temperature contours in a plasma jet (a) without substrate and (b) with substrate. Plasma parameters used for this model are: torch current=500A, torch voltage=40.2V, Ar flow rate=25slpm, N_2 flow rate= 3slpm[4]

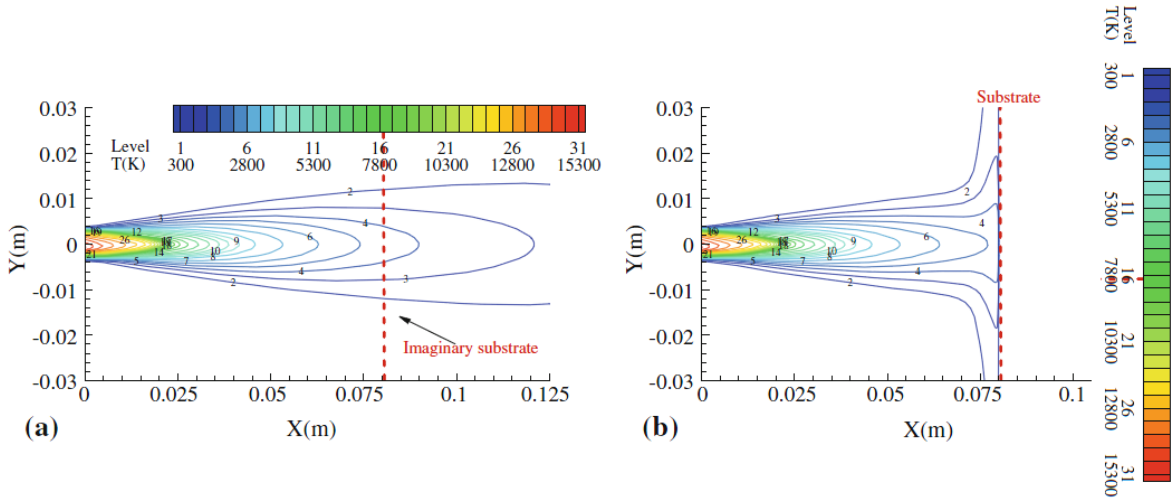

Figure 1.7 shows velocity contours in a plasma jet (a) without substrate and (b) with substrate generated by numerical modeling analysis of a N_2-Ar plasma [35]. In can be seen that the jet velocity generally decreases in both the horizontal and vertical directions further from the torch exit and from the plasma axis.

[4] Reprinted from Journal of Thermal Spray Technology 20: B. Selvan, K. Ramachandran, B.C. Pillai, and D. Subhakar Numerical Modelling of Ar-N2 Plasma Jet Impinging on a Flat Substrate, 534-548 Copyright (2011), with permission from Springer

Figure 1.7: Velocity contours in a plasma jet (a) without substrate and (b) with substrate. Plasma parameters used for this model are: torch current=500A, torch voltage=40.2V, Ar flow rate=25slpm, N_2 flow rate= 3slpm[5]. The color-scale applies for both images (a) and (b)

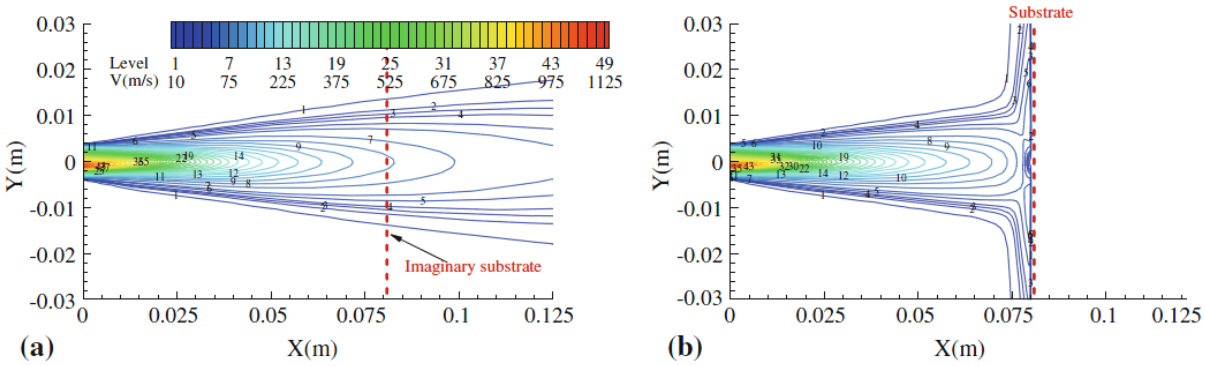

1.4.2.2.6 Properties of plasma gases

Argon is the most used primary plasma and shroud gas. It is a noble gas, and inert to all spray materials. Argon is the easiest commonly-available gas with which to form a plasma, and tends to be less aggressive on the spray equipment, electrodes, and nozzles than either nitrogen or hydrogen. For that reason, most plasma torches are started using pure argon. Argon creates relatively low temperature plasmas. It is used either alone or in mixtures with other gases to increase the plasma energy, and it has low thermal conductivity.

Nitrogen is one of the main gases used in thermal plasma spraying, due to its low cost and inert nature. It readily absorbs energy, with the potential to transfer that energy to the feedstock as described in Eq. (1.3), resulting in higher energy plasmas in

[5] Reprinted from Journal of Thermal Spray Technology 20: B. Selvan, K. Ramachandran, B.C. Pillai, and D. Subhakar Numerical Modelling of Ar-N2 Plasma Jet Impinging on a Flat Substrate, 534-548 Copyright (2011), with permission from Springer

comparison to argon. Hydrogen is mainly used as a secondary gas, usually to a maximum of 20 vol%. It increases heat conduction even in low concentrations (<5 vol%) and acts as an anti-oxidant. Helium is also mainly used as a secondary gas. It is inert to all spray materials. Due to its high cost, it is used only when hydrogen or nitrogen additions have disadvantageous effects, such as chemical reactions between hydrogen and the feedstock material. Like hydrogen, helium plasmas have high thermal conductivity.

Table 1.2 summarizes physical and chemical characteristics of plasma gases ([13] and [36]).

Table 1.2: Physical and chemical characteristics of plasma gases

Characteristics	Argon	Nitrogen	Hydrogen	Helium
Molar mass (g mol^{-1})	39.944	28.016	2.0156	4.0002
Specific mass at 0°C and 101.32Pa ($kg*m^{-3}$)	1.783	1.2505	0.0898	0.1785
Specific thermal capacity C_p at 20°C ($kJ*kg^{-1}*K^{-1}$)	0.511	1.046	14.268	5.233
Thermal conductivity at 0°C ($W*m^{-1}*K^{-1}$)	0.01633	0.02386	0.17543	0.14363
Ionization potential (V)				
One-stage ($A \rightarrow A^+ + e^-$)	15.75	14.53	13.60	24.58
Two-stage ($A^+ \rightarrow A^{++} + e^-$)	27.5	29.4	---	54.1

Due to the different properties of plasma gases, each gas will have different enthalpy at certain temperatures, as shown in Figure 1.8 [36]. It can be observed that at a given temperature both diatomic N_2 and H_2 have much higher energy content per volume than monatomic Ar or He.

Figure 1.8: Enthalpy of common plasma gases[6]

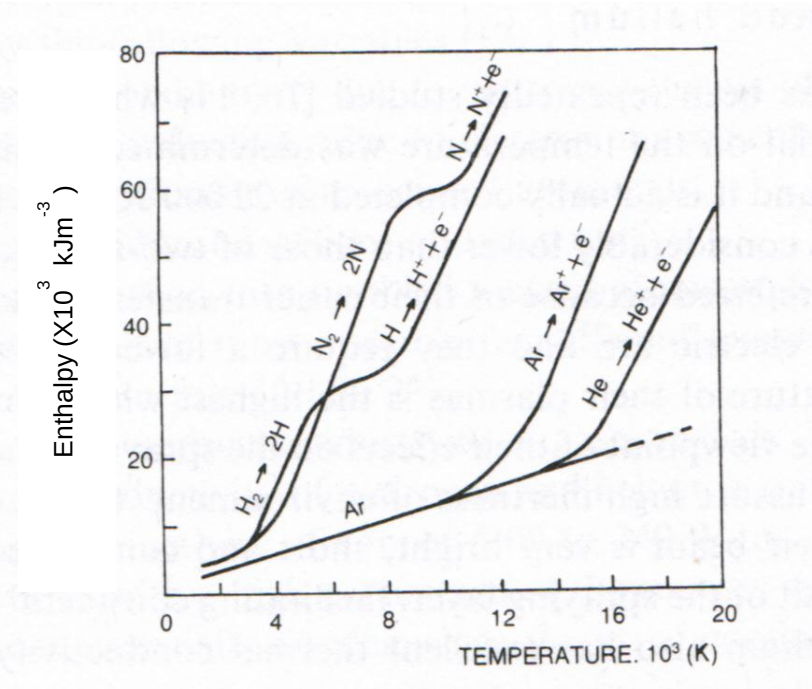

1.4.2.2.7 Formation of coating

In plasma spray processing, the feedstock materials are fed into the plasma jet in a form of a powder, suspension, or precursor solution. During flight, heat is transferred from the plasma jet to the particles, resulting in an increase of the particle temperature. The amount of heat being transferred to the particles within the plasma jet is determined by the physical and thermal properties of the sprayed material and plasma jet, as well as the time the particles reside in the plasma jet. The jet velocity, the physical properties of the individual particles, such as size and density, and the length of the plasma jet determine the residence time of the sprayed particles in the plasma jet,

[6] With kind permission from John Wiley & Sons Ltd : 'Plasma Spraying of Metallic and Ceramic Materials', D. Matejka, B. Benko, Figure 11, pp. 27

If the spraying distance is greater than the plasma jet length, the molten or partially molten particles cool and decelerate after leaving the jet due to the surrounding atmosphere, and then impact the substrate, potentially in a re-solidified state. During impact, their kinetic energy is transformed into thermal and deformation energy, resulting in a flattening of the molten or partially molten particle and formation of a splat, which solidifies into a lamellum within the coating. When particles are in contact with the substrate, heat is transferred from the particle to the substrate, resulting in rapid cooling and solidification of the splat. Splats deposited build up to form the coating. Plasma sprayed coatings form in a characteristic lamellar structure. Figure 1.9 graphically shows the formation of a plasma sprayed coating [37].

Figure 1.9: Formation of a plasma sprayed coating

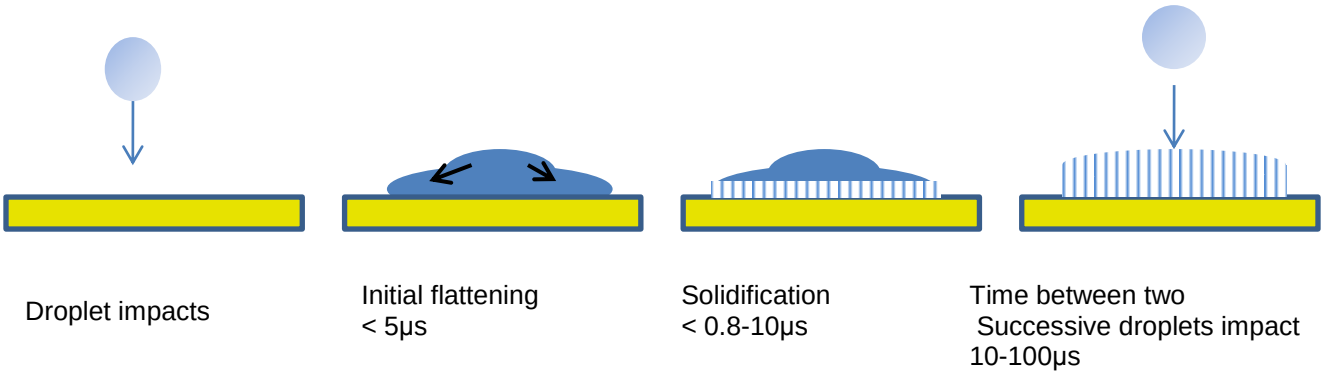

1.4.2.2.8 Deposition efficiency

The deposition efficiency of a plasma spray process is defined as the ratio between the weight of the material in the coating to that of the material fed to the plasma jet while the torch is in front of the substrate (material not fed to the substrate is referred to as overspray and contributes to a further loss of process efficiency beyond deposition efficiency losses). The deposition efficiency is affected by several factors.

The location of the powder inlet to the plasma jet has a large effect on the deposition efficiency. The highest efficiency is achieved when the powder is fed to the center of the plasma jet, at its hottest part. However, this solution is more complex from the point of view of torch design. In most cases, the powder is fed radially into the plasma near the exit nozzle. Radial feeding simplifies the torch design, because there is no need to provide space for powder feeding in between the torch electrodes. However, radial feeding has some drawbacks. Feedstock materials need to have a momentum comparable to that of plasma gases at the injection for proper in-flight particle treatment. Radial feeding may result in lower deposition efficiencies, because a portion of the powder may bounce off the plasma plume or pass through it instead of entering the jet. Powder that enters the jet may end up at the outer colder parts of the plasma. In both cases, the deposition efficiency will decrease. In the case of smaller feedstock, which can be applied for increased electrode surface area, the lower mass of particles needs to be compensated by higher velocities that tend to be too high for compatibility with a stable plasma [30].

Some torch designs, such as the Axial III torch (Mettech Corp, North Vancouver, BC Canada) applied in this research, allow feeding of the powder axially into the plasma. Axial feeding provides the advantage of feeding the powder directly into the hottest part of the plasma jet, thus allowing higher deposition efficiency in comparison to radial feeding. In addition, it allows the application of small particles without the need to provide them with sufficient momentum to enter the plasma jet.

In addition to the effect of powder feeding method, low deposition efficiencies can result from high vaporization rates of the deposited materials, or from material rebound,

which occurs when the particles have only partially melted or resolidified prior to impact. Several factors affect the particle temperature upon impact, which, in return, is correlated with the deposition efficiency. Jet velocity, jet length, the physical and thermal properties of the deposited materials, and the plasma thermal properties determine the exit temperature and velocities of the individual particles. Spraying distance, particle velocity exiting the jet and the physical and thermal properties of the sprayed material determine the time of contact with the surrounding atmosphere prior to impact. This will determine the particle temperature (its extent of melting) and velocity upon impact. Generally, lower jet exit velocities increase the residence time of the particles in the surrounding atmosphere. This may lead to resolidification of the particles and subsequently, the particles may bounce off upon impact with the substrate. In addition, smaller particles decelerate faster than larger particles; thus, their residence time in the surrounding atmosphere might be higher than that of larger particles. This again can result in a low temperature of a smaller particle upon impact and bouncing off the substrate. The deposition efficiency decreases with an increase in plume spread or with rotation of a planar sample holder.

1.4.2.2.9 Effect of particle size distribution

Powder particle size distribution has an important effect on the resulting coating morphology. First, the spraying of powders with particles of different sizes can result in overheating of the smaller particles, and evaporation of finer particles and insufficient heating of coarse particles may occur. Second, Smaller particles accelerate in the plasma jet and decelerate after leaving the plasma jet more easily than larger particles.

This characteristic of smaller particles may result in a larger distribution of velocities and temperatures upon impact with the substrate when a powder with a large particle size distribution is used as a feedstock. Therefore, a narrow particle size distribution is more desirable to manufacture plasma sprayed coatings [38].

1.4.2.2.10 Thermal effects of the substrate and the sprayed layer

The total heat transferred to the substrate during spraying consists of the heat transferred by the plasma jet and that transferred by the impacting particles. The total heat flux to the substrate increases linearly with the input to the torch, and decreases rapidly at greater spraying distance, as can be seen in Figure 1.10 [39].

Figure 1.10: Effect of standoff distance and torch output on heat flux to the substrate[7] [39]

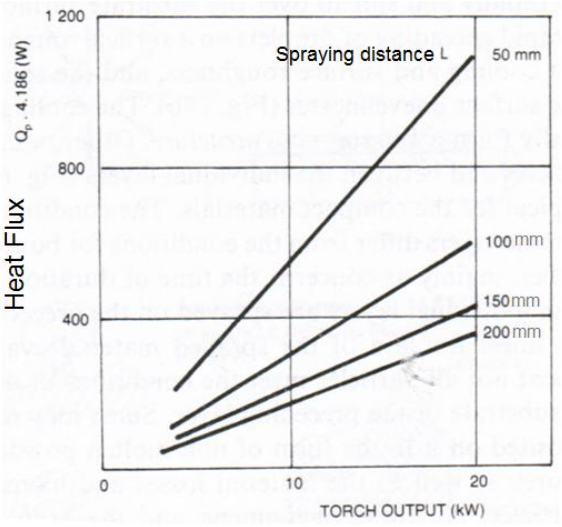

[7] With kind permission from John Wiley & Sons Ltd : 'Plasma Spraying of Metallic and Ceramic Materials', D. Matejka, B. Benko, Figure 20, pp. 40

Figure 1.11 shows the efficiency of heat transfer to the substrate as a function of spraying distance [39]. The efficiency is calculated as the ratio of total heat flux to the supplied torch power input. It can be seen that the heat transferred by the plasma jet to the substrate decreases considerably faster than the heat transferred from the particle material to the substrate with increasing spray distance. In order to prevent the formation of a molten pool on the surface, a sufficiently long standoff distance must be used to avoid excessive heat transfer to the substrate and the deposited coating.

Figure 1.11: Efficiency of heat transfer as a function of standoff distance[8] [39]

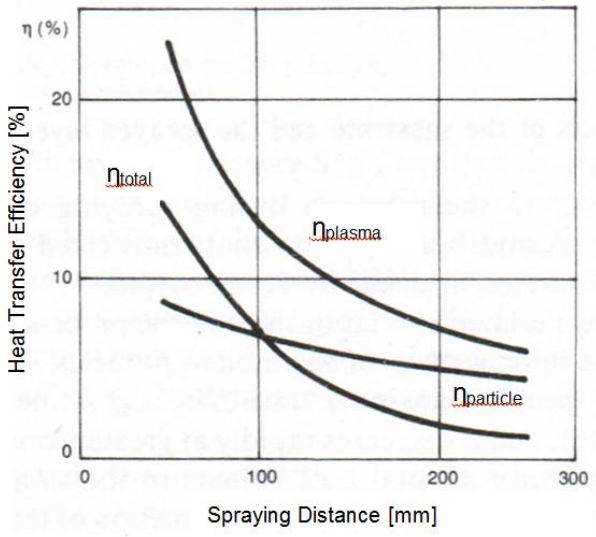

1.4.2.3 Challenges of plasma spray processing

Although plasma spraying might potentially allow a significant reduction in manufacturing costs of SOFCs, there are still technological challenges related to the production of SOFCs by plasma spraying, described in this section.

[8] With kind permission from John Wiley & Sons Ltd : 'Plasma Spraying of Metallic and Ceramic Materials', D. Matejka, B. Benko, Figure 21, pp. 40

1.4.2.3.1 Low porosity for SOFC electrodes

Plasma-sprayed coatings typically but not inherently have porosities in the range of 5-15 vol%. However, the different layers of an SOFC require porosities well above or well below this typical range. In SOFC electrodes, an adequate porosity of 30-40 vol% is required for minimizing mass transport losses. In contrast, SOFC electrolytes are required to be gas tight with no porosity.

Three strategies are typically applied with plasma sprayed SOFC anodes to obtain increased porosity. First, for typical Ni-YSZ oxides, NiO is commonly used as feedstock powder instead of Ni. After deposition, the non-electronically conductive NiO is reduced to Ni, and additional porosity is thereby obtained in the anode through the volume change, because NiO has a lower density (6.67 $grcm^{-3}$) than Ni (8.9 $grcm^{-3}$). For an anode with 30-40 vol% of Ni, the reduction step theoretically will increase the open porosity by 17-21 vol%. However, practically, part of the NiO phase will not be reduced to Ni if it is fully enclosed by YSZ, and sintering of Ni during reduction can decrease the amount of porosity introduced.

The second strategy applied to increase porosity in plasma sprayed anodes is to use plasma energy and velocity conditions such that the particles are partially melted rather than fully melted when they impact the substrate. However, this strategy will reduce the deposition efficiency of the powder. The deposition efficiency is the ratio between the weight of the powder deposited on the substrate to the weight of the powder fed to the substrate. Lower deposition efficiencies increase material costs, and make the process less cost effective. Deposition efficiency is especially important with the most costly materials applied in SOFCs, such as ceria. In addition, a lower degree

of melting of the materials reduces the adhesion of the anode materials to the electrolyte, which can affect anode performance by increasing interfacial resistances, and might increase the probability of failures such as anode delamination.

The third strategy applied to increase porosity in plasma sprayed anodes is to add pore former to the feedstock powder. Pore formers are organic material that is deposited with the feedstock powder and afterwards volatilizes during post-spraying thermal treatment, leaving behind porosity. These materials are commonly used in wet ceramic processing to introduce porosity. The use of pore formers in wet ceramic processing is particularly important for anode-supported SOFCs, where the anode is relatively thick and gas transport through the anode layer can significantly affect performance. However, pore formers are not commonly used with plasma spray processing, and only a few studies have documented the use of pore formers in plasma spraying ([40], [41], [42]). One challenge with spraying pore formers is their low melting temperature compared to that of the anode materials. These materials can volatilize either during flight or upon heating the substrate. In addition, some of the pore former may not volatilize during the post spraying thermal treatment when it is fully enclosed by other anode material. Pore former is required to have a sufficiently low volatilization temperature to avoid oxidation of the metallic substrates in plasma sprayed SOFCs during post spraying thermal treatment. However, a low volatilization temperature might not allow the pore former to survive the plasma. In addition, the pore former powder must be as spherical as possible to allow it to be fed to the torch.

A fourth strategy applied to increase porosity is to utilize with a precursor solution feedstock. This approach has been applied to produce highly porous cathodes. The

precursors react in the plasma to form the cathode materials. This process resulted in coatings with a unique microstructure in which needle shaped single crystals form a columnar structure of high open porosity. This microstructure is an ideal microstructure for SOFC electrodes, since it allows efficient vertical and horizontal gas migration paths and has a large quantity of reaction surface area [18].

1.4.2.3.2 Coarse microstructures for SOFC electrodes

SOFC anode performance is greatly affected by the active surface area available for the electrochemical reaction to occur. To achieve high surface area, wet ceramic processed anodes are often manufactured from nano-size powders. However, it is more challenging to deposit nano-size powders by plasma spray processing. Typical feedstock powder sizes used in plasma spray processing are between 25µm and 150µm. This powder size distribution often results in good deposition efficiencies but a coarse microstructure. Anode thickness for non-anode-supported SOFCs is typically 10µm - 50µm, and a very fine microstructure is typically used for the active anode layer. Therefore, to obtain a higher surface area, either smaller agglomerated particle sizes or feedstock powders where the powder is made of micron-sized agglomerates of nano-sized primary powder particles can improve the powder feedstock of plasma sprayed SOFC anodes. Agglomerated powders are typically produced by spray drying. Recent studies ([26] and [30]) utilized nano-agglomerated powders for the production of nano-structured Ni-YSZ anodes fabricated by pre-synthesized agglomerates of nano-particles. It was established that an enlarged reaction zone, provided by the high specific surface area of nanostructured anodes, and a finely porous microstructure, led to lower activation and concentration polarizations and enhanced cell performance

compared to conventional plasma sprayed cells [30]. These anodes exhibited better gas permeability, comparable high temperature conductivity, and 43% lower polarization and 34.5% higher power density compared with plasma sprayed anodes processed with non spray dried sintered and crashed commercially available feedstock powder. One disadvantage of spray dried powder is that presently it is more costly than non spray-dried powders.

An additional strategy to obtain finer microstructures by plasma spraying is to spray either powder in suspension or liquid precursors. However, these strategies require several adjustments to the spraying process, and the deposition rates are lower than for dry powders.

Finally, plasma spray processing can be used to fabricate engineered anodes constructed of an electrochemically active fine microstructured layer at the electrolyte interface and an electronically conducting layer deposited on top of the electrochemically active layer with coarser porosity to enhance mass transport near the anode fuel channels. This approach allows the maximization of anode performance by increasing the electrochemically active surface area and decreasing mass transport losses. This approach has several advantages, such as cost effectiveness and improved deposition rates. It can also be applied to produce optimized anodes for utilization of hydrocarbons.

1.4.2.3.3 Poor microstructure for SOFC electrodes

In plasma spraying, the electrode powders can be mixed and co-deposited to form a coating. Due to the differences between the melting temperatures and heat capacity of the electrode materials, both materials will not typically have the same

degree of melting during spraying. This situation can result in the need to fully melt the materials in the coating in order to obtain the highest deposition efficiencies possible, which negatively affects the porosity of the electrode and therefore the electrode performance. In addition, some materials, such as LSM, decompose during deposition with H_2 in the plasma gas [43]. It may be challenging to find compromise spray conditions that sufficiently melt the high melting temperature materials such as YSZ, but do not vapourize low melting temperature materials such as CuO or decompose less stable materials such as LSM. In addition, the requirement of sufficient electronic conductivity and the resultant percolation threshold of approximately 30 vol% of the solid volume constrain the minimum amount of the electronic conductor at the electrode, which typically is the lower melting temperature material of the electrode composite. This requirement makes it harder to obtain sufficient porosity.

1.4.2.3.4 Production of dense electrolytes

SOFC electrolytes must be dense and thin, to minimize ohmic losses while maintaining gas tightness. This requirement is harder to achieve with plasma spraying in comparison to wet ceramic processing. Plasma spraying utilizes micron size feedstock powder in comparison to the nano size powder utilized in wet ceramic processing. Traditional plasma spray configurations use powder feedstock typically between 25 and 150 μm in diameter that are delivered by a carrier gas. This feed configuration results in a somewhat coarse microstructure of laminae of flattened splats and interlaminar pores with poor control over microstructures and porosity. One possibility to obtain better microstructures for SOFC electrolyte is to modify the plasma

spray process to allow liquid feedstock delivery. Liquid feedstock delivery allows micron to sub-micron sized particles to be suspended in a carrier liquid such as water or ethanol and sprayed directly. However, significant modifications to the plasma spray system are required, and much work is involved to optimize the suspension by choosing the best suspending liquid, solid concentration, and dispersant ([24], [44], [45], [46] and [47]).

1.4.2.3.5 Integration of cell layers by plasma spraying

One of the major advantages of production of SOFCs by plasma spraying is that this manufacturing process allows the production of cells in one integrated process. However, the requirements of porous electrodes and dense electrolyte may require modifications of the plasma spraying process between the different layers. One approach that was used in the literature was to utilize a triple torch reactor chamber [48] in which the cell three layers have been deposited successively by changing only the feedstock and the chamber pressure, thus obtaining the required porosity. These process steps can be easily automated. An additional approach reported in the literature was to apply vacuum plasma spraying (VPS) to manufacture the cell layers. The cells layers were deposited sequentially on a porous metallic substrate [18]. A functionally graded material structure (FGM) of the electrode was suggested to allow increased TPB length and reduced thermal expansion mismatch at the electrolyte-electrode interface. Denser electrolytes were obtained by applying supersonic nozzles resulting in high particle impact velocities [18] or by utilizing suspension plasma spraying, in which the sprayed particles are suspended in liquid to allow the utilization of fine sized particles.

This approach resulted in dense electrolytes ([24], [44], [45], [46] and [47]).

An additional approach reported in the literature was to apply APS (atmospheric plasma spray) to deposit sequentially the cell layers. This is achieved by modifying the spraying and feedstock parameters for each cell layer [49].

1.4.2.4 Cost analysis of plasma spraying and wet ceramic processing

One of the major motivations for plasma spray processing of SOFCs is substantial cost reduction in comparison to wet ceramics processing for scaling up to mass production. There are several factors for the reduced cost. First, wet ceramic processing requires few different types of equipment during the process, such as tape casters, screen printers, and furnaces. Plasma spraying allows manufacturing of SOFCs in one integrated process utilizing one plasma spray torch, and substrate holder, and can be automated easily by adding a robot. Second, plasma spraying has much higher deposition rates in comparison to wet ceramics. Therefore, increasing of production volumes with wet ceramics requires large capital costs. Third, wet ceramic processed cells typically utilize thick anodes or electrolytes or cathodes as mechanical supports. This approach is more costly in comparison to metal substrate supports that can be more readily used when the cells are fabricated by plasma spraying. Table 1.3 shows cost comparisons for production of 30cm x 30cm planar cells with a total annual production volume of 200MW [50].

Table 1.3: Cost comparison for production of 30cm x 30cm planar cells with a total annual production volume of 200MW, in $/kW

200 MW/year	Wet Ceramic	Powder APS	Suspension APS	Powder VPS	Suspension VPS
Equipment	9.92	17.8	17.9	137.5	137.7
Energy	4.53	10.3	10.3	19.3	19.3
Land	0.31	2.76	2.76	2.76	2.76
Labor	56.7	6.47	6.47	6.47	6.47
Materials	147.0	71.4	75.5	73.7	77.9
Total	218.5	108.7	112.9	239.8	244.1

The cost can be further reduced when 1m x 1m cells are produced. Such size is not suitable for production with wet ceramic processing, due to warping and other problems during firing of cells with such size. Table 1.4 shows cost comparisons for production of 1m x 1m planar cells by various plasma spraying processes with a total annual production volume of 200MW. [51]

Table 1.4: Cost comparison for production of 1m x 1m planar cells with a total annual production volume of 200MW, in $/kW

200 MW/year	Powder APS	Suspension APS	Powder VPS	Suspension VPS
Equipment	8.90	8.92	66.0	66.1
Energy	5.22	5.23	9.78	9.8
Land	1.33	1.33	1.33	1.33
Labor	3.44	3.44	3.44	3.44
Materials	58.3	61.6	59.5	62.9
Total	77.2	80.6	140.1	143.5

1.5 Characterization of SOFCs

Several examination methods are available to characterize SOFCs to examine the quality and performance of the manufactured SOFCs and their components, These methods include examination of the microstructure of the cell layers, phase and composition analysis, gas permeation, mechanical strength, and electrochemical characterization.

Microstructural examination methods such as scanning electron spectroscopy (SEM) or optical microscopy allow the observation of the microstructure of the different cell layers, provide insight about the processing parameters and their effect on the microstructure, and aid in the diagnosis and detection of failure mechanisms. SEM can be used to determine the thickness of cell layers, the extent of melting of the materials, degree of mixing of the phases, and porosity. These observations can be used to improve and refine the manufacturing process. In addition, SEM allows detection of failure mechanisms such as cracks or delamination. Undesirable phenomena such as segregation of the materials in a composite electrode can also be detected.

The cell component porosity can be measured by a porosimeter, such as a mercury intrusion porosimeter. Image analysis can be also utilized for determination of electrode porosity.

Normally, the anode and cathode are composites. Energy-dispersive X-ray (EDX) analysis can be used to detect the relative amounts (by volume, atomic, or weight %) of each phase. In addition, EDX mapping can be used to determine the degree of mixing of the different phases.

X-ray diffraction (XRD) can be used to determine the phases of a cell layer. x-ray diffraction, the intensity of the diffracted x-ray is measured as a function of the detector angle in accordance to Bragg's law. X-Ray diffraction can also be applied to quantify the relative amounts of each phase in the sample.

Gas permeability tests can be used to determine the gas tightness of the electrolyte. In addition, gas permeability tests can be used to gain insight about the ease of gas permeation into the electrode.

.The mechanical behavior of the cell components may be determined by using well-established methods such as hardness testing, dilatometry, and others.

Electrochemical performances are normally measured in steady state and transient conditions. In steady state, polarization curves, i.e. the cell voltage versus the current, can be obtained. These curves give insight to the extent of losses of open circuit voltage and polarization. DC models can be utilized to distinguish between the different overpotential loss mechanisms, i.e., activation, ohmic and mass transport overpotential [52]. Steady state measurements can also be applied for long term detection of degradation of cell performance.

Complementary to steady state characterization by continuous methods are measurements under transient conditions utilizing techniques such as current interruption or impedance spectroscopy. Current interruption is conducted by stopping the flow of current. In such case, the ohmic losses immediately reduce to zero, while the charge double layer takes time to disperse. This method allows distinguishing between ohmic overpotential losses and time-dependent overpotential losses such as activation and mass transport polarizations.

In addition to current interruption, electrochemical impedance spectroscopy (EIS) is commonly used to gain more insight about the individual contributions of dissipative mechanisms to the overall overpotential at specific voltage or current operating conditions and to distinguish them from the purely resistive effects. A particular dissipative mechanism can be distinguished from other dissipative mechanisms by EIS only when its relaxation time is sufficient different from the others. EIS cannot distinguish between phenomena having identical relaxation times.

In impedance spectroscopy, a sinusoidal perturbation voltage or current having a small amplitude is imposed on the cell over a wide range of frequencies while the impedance response of the cell is measured. Linear response is required in EIS to obtain impedance data without error. However, electrochemical cells are highly non-linear. Therefore, a sufficiently small perturbation amplitude is required for quasi-linear impedance response and to reduce measurement error. In practice, the trade-off between linearity and signal-to-noise ratio has to be taken into account. The perturbation signal amplitude should be small enough to approach quasi-linear conditions for the response. However, it also has to be large enough to produce a response that can be measured above the background electrical noise levels. If the signals are too small, they could be buried in noise, resulting in low accuracy. Therefore, the amplitude should be adjusted to compromise between a high S/N (signal/noise) ratio and the linearity of the system response for any particular case [53]. Measuring an EIS spectrum takes time, especially in the low-frequency region. To validate the impedance spectrum, the system must be in steady state while impedance measurements are being taken. A common cause of problems in EIS measurements

and their analysis is drift in the system. For example, the cell can change through growth of an oxide layer, cracking of electrolytes or the electrode, changes of contact force between the current collector mesh and the electrodes, temperature changes, and more. Standard EIS analysis tools may give wildly inaccurate results for a system that is not at a steady state. A common practice to reduce errors resulting from non-steady state behavior is to let the cell reach a steady state by keeping the cell at a sufficient dwell time at the temperature and potential at which EIS is measured. [54]

System parameters such as gas environment, operation temperature, or cell polarization can be modified to allow the identification of the observed EIS features ([55], [56] and [57]). The system can then be analyzed in terms of equivalent circuits, an electronic analog reproducing the frequency response of the cell. An equivalent circuit is composed of a series of individual circuit elements corresponding to particular physical or chemical processes in the cell [58].

The impedance of electrochemical systems is normally presented by Bode or Nyquist (Cole-Cole) plots. In a Bode plot, both the amplitude and phase angles are drawn versus the frequency. In a Nyquist plot, the imaginary component of the complex impedance is drawn versus the real component of the complex impedance. Typically, the impedance response of an electrochemical process having specific relaxation times will appear as a semi-circular arc or depressed semi-circular arc in the Nyquist plot. In a case where few processes exist in the system, few arcs will appear. These arcs may overlap, dependent on how much the relaxation times of the different processes differ [59]. Figure 1.12 shows a Nyquist plot of an electrochemical system under pure kinetic control. Here, R_{el} is the ohmic resistivity of the system, C_d or C_{dl} is the double layer

capacitance and R_{ct} or R_p is the charge transfer or polarization resistance, respectively. The high frequency x-axis intercept R_{el} is the purely resistive component of the impedance. The low frequency x-axis intercept is the total resistance, i.e. the addition of the ohmic and polarization resistance contributions (R_{el} and R_p, respectively). The frequency at the peak of the arc is the reciprocal of the relaxation time τ, which equals R_pC_{dl}. An electronic equivalent circuit for this system is shown in Figure 1.13.

Figure 1.12: Nyquist plot of an electrochemical cell under pure kinetic control

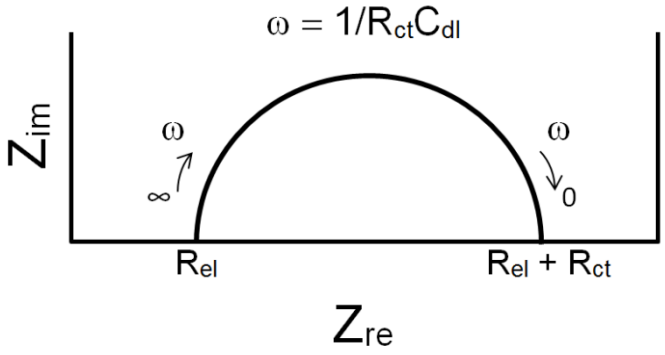

Figure 1.13: An electronic equivalent circuit for the system

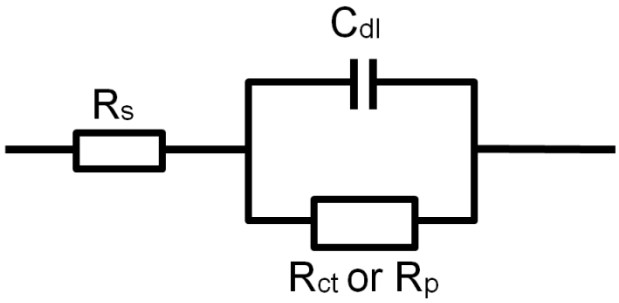

1.6 Fueling SOFCs with hydrocarbons

1.6.1 Utilization of HC fuels by internal reforming

When using HC fuels such as methane, the fuel is typically converted by steam reforming to CO and H_2, which are then consumed electrochemically within the fuel cell, or in the case of CO, reacted with steam to form CO_2 and H_2 through a water gas shift reaction. The reforming reaction can take place externally, in a reformer placed prior to the fuel cell inlet. This configuration, however, increases the overall cost and complexity of the system. Reforming of the fuel in a high temperature SOFC system can also take place within the fuel cell itself, utilizing a reforming catalyst, commonly nickel, in the SOFC anode. This process is known as internal reforming. Internal reforming eliminates the requirement for an external reformer and therefore simplifies the balance of plant system and reduces costs. In addition to reduced costs, internal reforming is endothermic for methane, and therefore it can assist in thermal management of the cell. However, steam reforming of petroleum-based hydrocarbons such as naphtha is typically less endothermic, and can become exothermic when the temperature is lowered below, for example, 600 °C [60].

Although internal reforming simplifies the SOFC balance of plant, it is still limited in practice due to technological issues. Experiments on internal methane steam reforming have shown that the strong activity of the nickel anode results in a marked temperature reduction in a very localized reaction zone that may lead to steep thermal gradients and thermal stresses [61]. Another disadvantage of steam reforming is that the reforming reaction has a high temperature requirement. When the fuel is reformed by steam, high equilibrium conversions require high temperatures. For example, the

equilibrium conversion of methane for a H_2O/CH_4 ratio of one at 1 bar is only 37% at 600 °C, 68% at 700 °C, and 87% at 800 °C, and for a H_2O/CH_4 ratio of two at 1 bar is 62% at 600 °C, 77% at 700 °C, and 100% at 800 °C. A higher H_2O/CH_4 ratio increases the extent of reformation of CH_4 to H_2, but it further dilutes the fuel and thereby decreases the overall cell efficiency. If reforming is to be performed internally in an SOFC, the high temperature requirement for equilibrium conversion limits the choice of materials that can be used to construct the fuel cell, since 700 °C is at the working limit for common metals [62]. Operation of SOFCs at low temperatures (LT-SOFC, 500–700 °C) may reduce material costs and sealing problems. However, the low conversion efficiencies of the steam reforming reaction at low temperatures lead to a reduction in cell efficiency. Although an operating SOFC is not at equilibrium and the reaction is driven forward by the removal of reaction products and the renewal of fuel supply, the efficiency is decreased when conversion of the fuel is not energetically favored. An additional disadvantage of steam reforming is the large amount of steam that is needed to suppress carbon deposition when utilizing HC fuels other than methane [63]. Moreover, it has been shown that even at high steam to carbon ratios (>~3.5), in the case of internal reforming of ethane and ethylene, the power generation of SOFCs deteriorates with time due to carbon deposition [64]. Carbon deposition reduces the cell performance by blocking the anode reaction sites [65] and damaging the microstructure of nickel in the anode.

1.6.2 Utilization of HC fuels by direct oxidation

These disadvantages of internal reforming encourage current research attempts searching for a direct oxidation mechanism to utilize HC fuels rather than internal

reforming, with particular emphasis on development of coking resistant anode materials ([4], [66], [67], [68], [69], [70] and [71]).

When HC fuel is directly oxidized in SOFC anode, it can be either partially oxidized to carbon monoxide and hydrogen (Eq. 1.4 and 1.5), or fully oxidized to carbon dioxide and water (Eq. 1.6 and 1.7), or undergo a mixture of partial and full oxidation.

$$CH_4 + ½O_2 \rightarrow CO + 2H_2 \quad (1.4)$$

$$C_nH_{2n+2} + ½nO_2 \rightarrow nCO + (n+1)H_2 \quad (1.5)$$

$$CH_4 + 2O_2 \rightarrow CO_2 + 2H_2O \quad (1.6)$$

$$C_nH_{2n+2} + (1.5n+0.5)O_2 \rightarrow nCO_2 + (n+1)H_2O \quad (1.7)$$

Carbon deposition can also occur on the anode surface (Eq. 1.8 and 1.9), dependent on the operation conditions and anode materials. Coke formation occurs by cracking of the hydrocarbon to the corresponding alkene, followed by subsequent formation of a carbonaceous overlayer, which undergoes further dehydrogenation to form coke [72], or by the Bouduard reaction (eq. 1.8) or by reaction of CO with hydrogen (eq. 1.9)

$$2CO \rightarrow C + CO_2 \quad (1.8)$$

$$CO + H_2 \rightarrow C + H_2O \quad (1.9)$$

1.6.3 Anodes for direct oxidation of HC fuels

Direct oxidation of HC fuels may reduce the thermal gradients created by internal reforming and improve fuel conversion efficiency, particularly with heavier hydrocarbons than methane. However, when HC fuel is directly utilized on conventional nickel-based

anodes, carbon deposited on the anode material due to a secondary cracking reaction blocks the reactants from reaching the reaction sites, degrades the nickel microstructure over time, and dramatically decreases the fuel cell performance and stability. Previous studies show that nickel can be utilized in direct oxidation of methane between 500°C and 700°C without carbon formation, but it is unlikely with higher hydrocarbons, since the temperature window for pyrolysis will be lower and carbon formation more severe [73]. This drives research attempts to find alternatives to the use of nickel in SOFC anodes for direct oxidation of hydrocarbon fuels.

Recent studies suggested several approaches to obtain carbon tolerant anodes. One approach is to manufacture the anode of ceramic material without a metallic phase. The ceramic material utilized in direct oxidation anodes has the role of both the electrical conductor and the reaction catalyst. Although such anodes have good thermal stability and good tolerance towards carbon deposition, their performance is typically poor because they have lower electrical conductivity and catalytic activity in comparison to metals, In addition, they are more costly and sometimes inter-react with other fuel cell components [74], [75] and [76]).

An additional approach to obtain carbon tolerant anodes is to utilize a composite of a metallic electronic conductor and ceramic ionic conductor and catalyst ([1], [4], [62], [63], [66], [67] [77], [78], [79], [80], [81], [82] and [83]). This approach allows much better electronic conductivity and lower ohmic losses in comparison to anodes manufactured of ceramic electronic conductors.

In recent studies ([77], [85] [86], [87] [88]), [89], [90], [*91*], [92], [93], [94] and [95]) copper has been suggested as an alternative to nickel as the electronic conductor

in SOFC anodes. Copper has been used as the metal for inclusion in the anode due to its high electrical conductivity and relatively low catalytic activity for hydrocarbon cracking [77]. Although copper has shown excellent tolerance towards hydrocarbon fuels and avoidance of carbon deposition, copper based anodes suffer from poor performance due to their limited catalytic activity, and poor thermal stability due to the low melting temperature of copper.

In copper based anodes, copper does not appear to have any catalytic function and the oxidation reaction at the triple phase boundaries (TPBs) relies on the addition of other components, primarily ceria. In recent studies ([86] and [87]), the addition of doped ceria has been shown to play an important role in improving anode performance, through improved catalytic activity and mixed ionic–electronic conductivity, which increases reaction surface area. It was demonstrated that copper/ceria and copper/doped-ceria anodes exhibit increased performance compared to that of copper-YSZ anodes [67].

Although copper has shown excellent resistance towards carbon deposition, copper-based anodes tend to be unstable at high temperature due to the relatively low melting temperature and high surface energy of copper, resulting in rapid sintering of the copper and loss of electrode conductivity at temperatures above 800 °C [88].

1.6.4 SOFC anodes based on copper–cobalt for direct oxidation of hydrocarbon fuels

In order to increase the performance of copper based anodes further, the addition of more catalytically active metals other than copper, having melting

temperatures higher than that of copper has been suggested ([96], [97], [98] and [99]). It has been shown that the addition of cobalt to copper based anodes results in increased performance and better thermal stability without severe carbon deposition. Cells produced with $Cu_{(50)}Co_{(50)}$ (on a weight basis) metallic phase demonstrated no degradation in performance after a 500hr test with CH_4. Anodes with Co content as low as 10wt% of the Cu-Co metallic phases have been demonstrated to have significant increases of performance relative to anodes with Cu only [100]. Anodes based on copper–cobalt mixtures processed by impregnation of aqueous metal salts into pre-sintered porous YSZ structures were found to be effective at suppressing carbon formation. For this system, the two metals do not form a solid solution, but rather exist in the form of two separate phases. It has been shown that the copper segregates at the copper-cobalt surface, due to its lower surface free energy (1.96 Jm^{-2}) relative to that of cobalt (3.23 Jm^{-2}). Through this mechanism, copper-cobalt bimetallic surfaces have been shown to have catalytic properties that are very different from those of the individual metals. Because the copper apparently coats the cobalt, even bimetallic compositions containing small amounts of copper were found to strongly suppress carbon formation.

One additional strategy suggested to obtain high performance copper based anodes is to apply a bi-layered anode structure ([101], [102] and [103]). Here, a thin functional/active layer is deposited onto the electrolyte, and it is optimized for increased catalytic activity. Namely, it contains highly catalytically active materials and utilizes a fine microstructure, which increases the total area of reaction sites. A non-catalytically active conduction/diffusion layer is deposited onto the functional/active layer and

functions primarily as a current collector/gas diffusion layer, with no role in enhancing catalytic activity. The non-catalytically active conduction/diffusion layer is designed to have high porosity to reduce mass transport losses. Figure 1.14 shows SEM micrograph of bi-layered anode

Figure 1.14: SEM micrograph of Bi-layered anode[9]

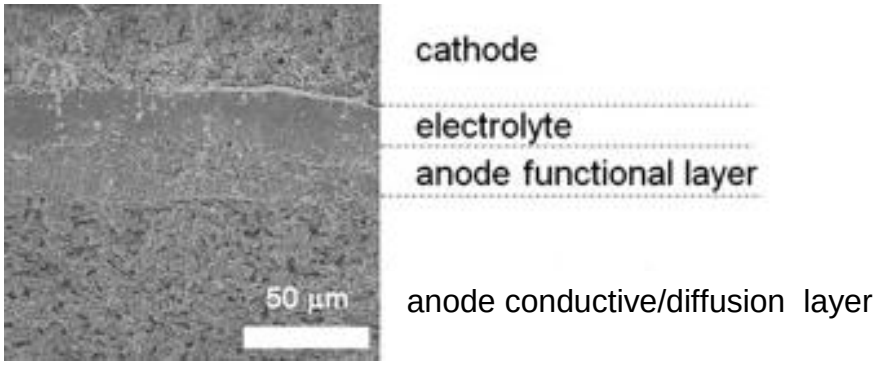

Despite the advantages of copper-based anodes for direct oxidation, they are manufactured presently using a multi-step wet ceramic technique that requires even more processing and firing steps than needed to make nickel-based anodes by wet ceramic processing, which makes them less attractive for mass production.

Figure 1.15 shows a typical wet ceramic manufacturing process of Cu-based anodes [86]. In this process, aqueous solutions of nitrate salts are impregnated into a pre-sintered porous YSZ matrix ([77], [86.] and [88]). This procedure is used because the low melting temperature of copper oxide compared to that of nickel oxide prevents

[9] Reprinted from Electrochemistry Communications 16: Bi Lei, Fabbri Emiliana, Traversa Enrico, 'Effect of anode functional layer on the performance of proton-conducting solid oxide fuel cells (SOFCs)', p 37-40. Copyright (2012) with permission from Elsevier

co-sintering of an anode layer containing copper oxide at a sufficiently high temperature to densify the YSZ electrolyte. This procedure adds further complexity to the wet ceramic manufacturing process, especially since multiple impregnation and firing steps are needed to obtain adequate connectivity of the anode metal phase. Table 1.5 and Table 1.6 show performance data of cells fabricated with wet ceramic processed Cu and Cu-Co anodes, respectively. The cell performances are reported as polarization resistance, which is the impedance interfering with electrochemical reaction and diffusion. Lower polarization resistance indicates better cell performance. In addition, the cell performance is shown in terms of power density. In this case, the power density is affected by the polarization impedances of both cathode and anode, and by the total ohmic resistances of the cell layers and contacts with the current collector.

Figure 1.15: Typical wet ceramic processing of Cu based anodes[10]

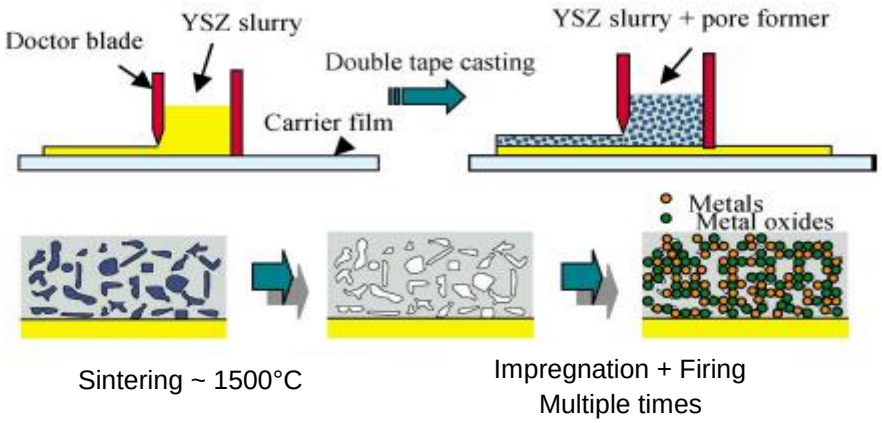

[10] Reprinted from Solid State Ionics 152-153: C Lu,W.L Worrell,C Wang,S Park,H Kim,J.M Vohs,R.J Gorte, 'Development of solid oxide fuel cells for the direct oxidation of hydrocarbon fuels', p 393elo7. Copyright (2002) with permission from Elsevier

Table 1.5: Performance data of Cu based anodes processed by wet ceramic methods

Research Group	Main Researchers	Anode composition	Cell Performance in H_2	Ref
Uni. of Pennsylvania	J.M. Vohs, R. J. Gorte	16 vol% Cu, 12 vol% CeO_2, balance YSZ	$R_{p,cell}$ = 1.0-2.7 Ωcm^2 (700°C) P = 0.10-0.25 Wcm^{-2}	[66]
	J. M. Vohs, R. J. Gorte	23 vol% Cu, 10 vol% CeO_2, balance SDC	$R_{p,cell}$ = 0.55 Ωcm^2 (650°C) P = 0.12 Wcm^{-2} (650°C)	[86]
	S. McIntosh, J. M. Vohs, and R. J. Gorte	20 wt% Cu and 10 wt% CeO_2, balance YSZ	$R_{p,anode}$ = 0.8 Ωcm^2 (750°C) Anode characteristic frequency = 4 Hz	[78]
Yonsei University, Seoul	J. Lee, E.W. Park, S.H. Hyun	30 vol% Cu/ and 30 vol% GDC, balance YSZ	P = 0.15 Wcm^{-2} (800°C)	[104]

Table 1.6: Performance data of Cu-Co based anodes fabricated by wet ceramic methods

Research Group	Main Researchers	Anode composition	Cell Performance in H_2	Ref
Uni. of Pennsylvania	J. M. Vohs, and R. J. Gorte	15 wt % Cu 15 wt% Co 15 wt % CeO_2 Balance YSZ	$R_{p,anode}$ = 0.17 Ωcm^2 (800°C) Anode characteristic frequency = 25 Hz	[100]
Uni. of Pennsylvania	J. M. Vohs, and R. J. Gorte	20 wt% metal (Cu and Co) 10 wt% CeO_2 Balance YSZ	$P_{Cu(90)Co(10)}$ = 0.31 W cm^{-2} (600°C) $P_{Cu(50)Co(50)}$ = 0.33 W cm^{-2} (600°C)	[1]

1.6.5 Plasma spray processing for the production of Cu based SOFC anodes

To date, plasma spraying has been applied to manufacture nickel-based SOFC anodes, and these anodes have been tested successfully in working cells ([105] and [24]). In addition, Cu–YSZ and Cu-Co-YSZ layers have been plasma sprayed in air utilizing radial feeding to a DC torch onto stainless steel coupons ([106] and [107]).

However, these layers have not been tested in fuel cells and their performances in hydrogen and hydrocarbon atmospheres have not been examined. In addition, these layers have not been optimized to perform as anodes by adequate control of the composition of the coating to obtain a solid volume fraction above 30% of the metallic phase to allow full percolation and thus to obtain sufficient electronic conductivity of the anode. Cu-Co anode performance is greatly dependent on the processing technique, and the characteristics of wet ceramic processed Cu-Co based anodes would not necessarily be similar to those of Cu-Co based anodes produced by plasma spraying. Production of Cu-Co based anodes by impregnation of metal salts produces nano-size particles and allows nano-scale mixing of the Cu and the Co. In contrast, powder plasma spraying commonly utilizes micron-scale particles, resulting in coarser-scale mixing of phases compared to anodes produced by wet ceramic processing. The physical distribution of both materials influences the ability of the Cu to diffuse into the Co and segregate at the surface of the Co phase. In addition, plasma spraying is characterized by rapid solidification of the plasma sprayed splats that form a coating. Cooling rates of the splats are in the range of 10^6 K s^{-1} to 10^7 K s^{-1} [108]. Wet ceramic processes are characterized by much slower cooling rates. The slower cooling rates of wet ceramic processes allow more time for Cu to diffuse into the Co. Due to the differences between the wet ceramic and plasma spray processes, it is not clear whether the partial coverage of Co by Cu observed in Cu-Co based anodes produced by impregnation of metal salts will occur with plasma sprayed Cu-Co based anodes.

In addition, it is more beneficial to replace the YSZ with ceria or doped ceria, for example, samaria doped ceria (SDC, $(CeO_2)_{1-x}(Sm_2O_3)_{0.5x}$) or gadolinia doped ceria

(GDC, $(CeO_2)_{1-x}(Gd_2O_3)_{0.5x}$), as ceria or doped ceria enhances the catalytic activity in Cu based anodes [77]. Moreover, It is advantageous to co-spray cupric oxide (CuO), cobalt monoxide (CoO) and SDC or GDC rather than Cu, Co and SDC or GDC due to the higher melting temperature of CuO and CoO ((1227 °C) for CuO [109] and 1830°C for CoO [110]) compared to the respective metals and also to allow increased porosity due to the reduction of CuO and CoO.

The primary challenge in making Cu based anodes by plasma spraying is the large difference between the melting temperature of CuO and ceria (1227 °C for CuO [109] and 2480°C for ceria [111]), which makes it difficult to co-deposit these materials. Co-deposition of materials with a large melting temperature difference, such as tungsten carbide–cobalt coatings, has been conducted previously by plasma spraying [112]. However, that application does not require coatings with significant porosity, so both materials can be co-deposited in a high-energy plasma that fully melts both materials, resulting in dense coatings. However, the requirement for high porosity of SOFC anodes for good diffusivity makes it more difficult to co-deposit materials with a large difference between the melting temperatures in a coating having a porous structure.

1.7 Thesis objectives

This thesis explores experimentally the application of air plasma spray processing for the production of Cu and Cu-Co based SOFC anodes for direct oxidation of hydrocarbon fuels. This work focuses on the development of plasma sprayed Cu and Cu-Co based anode layers and electrochemical tests of the anode layers in working cells.

A first objective of this thesis is to understand the relationship between spraying and feedstock parameters, the resulting coating crystallography and microstructure, and anode performance for the SDC/CuO material set.

A second objective of this thesis is to understand the relationship between spraying and feedstock parameters, the resulting coating crystallography and microstructure, extent of carbon deposition, and anode performance for the SDC/CuO/CoO and GDC/CuO/CoO material sets.

A third objective of this thesis is to understand the effect of microstructure on performance and degradation of Cu-Co-SDC anodes.

1.8 Experimental methodology

1.8.1 Input materials

This work aims to produce SOFCs by plasma spraying in one integrated process, where the layers are developed in parallel by different students. Input materials to fabrication of full cells include cell layers that are not within the scope of investigation of this work.

During the early stage of this work, YSZ electrolyte substrates were utilized in fabrication of the cells. However, it was found that these electrolytes easily break during plasma spraying of electrodes, so electrolyte substrates were replaced by 2.54 mm diameter porous AISI SS430 disk substrates (Mott Corporation, Farmington, CT, USA). Mechanically mixed spray dried and calcined 48.2 wt% lanthanum strontium manganite ($(La_{0.8}Sr_{0.2})_{0.98}MnO_{3-y}$, LSM) and 51.8 wt% 8 mol% yttria-stabilized zirconia (YSZ) powders (Inframat Advanced Materials, Farmington, CT, USA) were used to fabricate the cathode layers by applying plasma spraying parameters developed by a previous

student [113]. YSZ electrolytes were deposited by suspension plasma spraying of aqueous suspensions of non-spray dried 8 mol% YSZ powder (Inframat Advanced Materials, Farmington, CT, USA) utilizing plasma spraying parameters developed by another student ([24], [45], [46] and [47])]. Cu/doped ceria and Cu-Co/doped ceria anodes were deposited onto the YSZ electrolytes.

1.8.2 Experimental set-up

1.8.2.1 Substrate holder design

This work involved design of custom made equipment to allow manufacturing of SOFCs by plasma spraying. The manufacturer's set-up of the plasma spray apparatus used in this research included a turntable to allow mounting of substrates for plasma spray coating, to which substrate holders for spraying full cells onto 2.54 cm diameter disks had to be added. In addition, substrate temperature measurements were needed, since the substrate temperature has an important effect on the resulting microstructure of the coating. Therefore, as part of this work, a substrate holder was designed and built. This substrate holder allows plasma spraying of cathodes and electrolytes that cover the entire area of the substrate, which is required to avoid leakage of gas through the electrolyte during electrochemical testing of the cells. In addition, it allows real time measurement of the substrate back surface temperature during plasma spraying. This substrate holder was manufactured by the machine shop of the National Research Council for Fuel Cell Innovation (NRC-IFCI). Details of the substrate holder are given in Appendix A.

1.8.2.2 SOFC test station

SOFCs manufactured by plasma spraying were electrochemically tested utilizing a custom made test station designed and built during this thesis project, which has also been used to test cells during other students' projects. Details of the custom-made test station are given in Appendix B.

1.8.2.3 Reduction/CH_4 tube furnace

A reduction/CH_4 tube furnace was used in this work for reduction and CH_4 exposure experiments. This thesis project included the design of the tube fixtures and the integration of gas mass flow controllers.

1.8.3 Feedstock powder development and characterization

At an early stage of this work, SDC powder was produced by calcining of ball milled cerium carbonate and samarium acetate precursors. Non spray dried CuO powder was utilized with the calcined SDC to produce anode coatings. Later during this work, the synthesized powder was replaced by spray dried agglomerates of micron-sized powder having a spherical shape to facilitate flowability for plasma spraying. To avoid break-up of the powder during feeding, which clogs the feed lines, these powders were calcined at various temperatures. The effect of the calcining temperature on the break-up of the powder was analyzed by measuring the particle size of each powder using a laser light scattering particle size analyzer before and after feeding. Based on these results, optimized calcination procedures were determined for each material.

1.8.4 Cu-SDC anode coating development strategy

In order to understand the relationship between the coating microstructure and crystal structure with the plasma spraying process parameters, screening tests were conducted. In plasma spray processing, particle temperature and velocity are key factors for the resulting microstructure. However, due to the lack of available equipment to monitor in-flight particle temperature and velocity, it was not possible to determine quantitatively the effect of plasma parameters on the in-flight particle temperatures and velocities. Therefore, the relationship between the spraying parameters and the resulting microstructures was studied by Scanning Electron Microscopy (SEM) observation of the coatings and by determination of the deposition efficiency of each material. X-Ray Diffraction (XRD) was utilized to analyze the phases existing in the coatings.

The goal at an early stage of this work was to identify plasma spraying parameters to allow partial melting of both SDC and CuO, and thus to increase the coating porosity, while keeping the required phase structure of the anode materials. The goal also includes the achievement of sufficiently high deposition efficiency of the doped ceria and of the metallic precursor phases, so that the anode is cost effective. However, it was found that the CuO is fully melted over a wide range of plasma spraying parameters tested, even with low energy plasmas, so it was not possible to co-deposit both materials without complete melting of the CuO. Therefore, a complete statistical study of the plasma spraying parameters was not performed and focus was instead made on identifying and applying strategies to obtain high performance anodes within the constraint of a fully melted CuO feedstock.

The first strategy applied was to identify plasma spraying parameters that will lead to partial melting of doped ceria, thus preserving its micron-sized morphology, allowing high catalytic activity due to its high surface area.

The second strategy applied was to reduce the feedstock particle size to the minimum that is still possible to feed to the torch to allow a high surface area anode to be fabricated with a high TPB length. To attain this goal, custom made feedstock powder with low particle size was purchased. This powder was made of agglomerates of micron-sized powder.

1.8.5 Development of Cu-Co-GDC coatings for use as SOFC anodes

After Cu-SDC coatings were developed and electrochemically tested, the addition of Co was investigated due to its potential for increasing anode performance. These studies focus on understanding the relationship between the plasma and feedstock parameters and the resulting phase structure, coating microstructure, and material composition of Cu-Co-GDC coatings produced of CuO, CoO, and GDC feedstock powders. These relationships were used to obtain Cu-Co-GDC coatings with varying Co loadings and 40 vol% of metallic phase sprayed onto Cu substrates. The relationship between the Co content within the coating and the extent of carbon deposition was studied by exposure to CH_4 at elevated temperature, followed by measurement of the weight gain. After exposure to CH_4, the coatings were analyzed by SEM for carbon fibers or residue.

1.8.6 Development of monolayer and bi-layered anodes with different feedstock powder particle sizes

To understand better the relationship between feedstock powder particle size and anode microstructure and electrochemical performance, Cu-Co-SDC anodes were produced of coarse and fine feedstock powders. In addition, a bi-layered anode structure was investigated. Bi-layered anodes were processed of fine Cu-Co-SDC anode functional layers and coarse Cu-YSZ anode conductive layers. These anodes were characterized for microstructure and phase composition, and were optimized to contain 40 solid vol% of metallic phase within the coating.

1.8.7 Electrochemical testing

Electrochemical testing was conducted to characterize Cu-SDC and Cu-Co-SDC anodes. Either glass and ceramic paste seals were applied for these tests. Polarization resistance of full cells was obtained by impedance spectroscopy at open circuit voltage (OCV) and at polarizations of 0.7V and 0.5V above reference. The cathode contribution to the overall polarization resistance was subtracted at OCV to obtain the anode polarization resistance. Polarization resistance was measured at various temperatures to obtain the activation energy of the anode. Degradation studies were performed by measuring the change of polarization resistance over 30 hrs of operation at 700°C.

1.9 Summary of chapters

The work completed in this project has been reported in five chapters. Chapter 1 consists of background information on SOFCs, direct oxidation of hydrocarbon fuels, and manufacturing of SOFCs by plasma spraying. Chapter 2 presents feedstock powder preparation and preliminary screening experiments conducted with ceramic and

metal substrate supports. This work was the first time direct oxidation anode material coatings were produced by plasma spraying and reported in the open literature. The relative deposition efficiency of the anode materials, crystal structure, and microstructure of the plasma sprayed anode layers were investigated over a wide range of spraying parameters. Chapter 3 describes electrochemical testing of plasma sprayed metal supported full cells and electrolyte supported symmetrical cells utilizing fine Cu-SDC anodes. Chapter 4 continues with coating development work on Cu-Co-GDC anode coatings. The behavior of these anodes when exposed to methane is investigated over a range of Co loadings. Chapter 5 continues with the development of SOFC full cells utilizing coarse and fine Cu-Co-SDC mono-layers, and Cu-Co-SDC/Cu-YSZ bi-layered anodes. Feedstock and spraying conditions utilized to produce the cells are presented along with their corresponding microstructures and phase compositions. Electrochemical performance of each anode is investigated along with a long term degradation study.

Chapter Six presents the overall conclusions and recommendations for future work stemming from this thesis.

1.10 Unique contributions of this thesis project

This work's contribution to the body of knowledge is the development of Cu-SDC and Cu-Co-SDC anodes produced by plasma spraying by understanding the relationship between feedstock and processing parameters, coating characteristics, and electrochemical performance. The methodology developed in this study overcomes the limitations of a slow multi-step wet ceramic processing technique by which these anodes are currently manufactured, and allows these anodes to be processed in a one-

step and rapid process that can be scaled up and automated for mass production. The first peer-reviewed publication originating from this work was the first to report the production of Cu-SDC layers by plasma spraying, and the second peer reviewed publication stemming from this work is the first, and so far only, published work demonstrating the application of plasma spraying to produce Cu-SDC and Cu-Co-SDC anodes electrochemically tested within a working cell.

2. Plasma spray deposition of CuO-SDC coatings for use in SOFC direct oxidation anode layers

Atmospheric plasma spraying (APS) was used to produce porous composite coatings containing $Ce_{0.8}Sm_{0.2}O_{1.9}$ (SDC) and Cu utilizing an axial injection DC plasma torch (Axial III Series 600 DC plasma torch, Northwest Mettech Corp., North Vancouver, Canada). Two different CuO and SDC powder types were investigated as feedstock for co-deposition by APS, namely non-spray-dried CuO and synthesized SDC powders, and commercially available spray dried powders made of agglomerates of micron-sized particles. A range of plasma conditions was examined for the production of composite coatings from pre-mixed SDC and CuO powders. Plasma gas compositions were varied to obtain a range of plasma temperatures. After reduction in H_2, coatings were characterized for crystal structure, composition and microstructure using X-ray diffraction (XRD), energy dispersive X-ray spectroscopy (EDX), and scanning electron microscopy (SEM), respectively.

2.1 Experimental procedure

2.1.1 Material preparation

2.1.1.1 YSZ substrate preparation by tape casting

Yttria-stabilized zirconia (YSZ) electrolyte substrates for the deposition of Cu-SDC coatings were prepared by mixing 60wt% YSZ powder (Tosoh, 8 mol % Y_2O_3), 12wt% ethyl alcohol, 12wt% toluene, 5wt% PVB, and 7wt% butyl benzyl phthalate. The mixture was ball milled for several hours and tape cast. The tape was cut and sintered at 1400˚C to produce dense circular electrolyte supports. The electrolyte supports were

sand blasted prior to plasma spraying to create a coarse surface in order to allow better adhesion of the coating to the surface.

2.1.1.2 Non spray dried powders

Samaria doped ceria (SDC, $Ce_{0.8}Sm_{0.2}O_{1.9}$) was synthesized by mixing cerium carbonate and samarium acetate precursors (Inframat Advanced Materials, Connecticut, USA) in the appropriate cation ratios. The mixture was ball milled with 40wt% ethanol for 48 hours. The ball milled mixture was then calcined in air at 1500°C for 6 hrs.

The SDC powder was then sieved to a narrower size range between 45µm and 75µm utilizing a shaker (Ro-Tap® RX-29 Sieve Shaker, W.S Tyler™, Mentor OH USA). The sieves are stacked in order of sizewith the sieves having the smallest openings on the bottom. The sieves are then placed in a shaker. Sieving is conducted by shaking of the powder in the sieves until the amount of powder retained in each sieve becomes more or less constant. A small amount of powder is sieved in each round to avoid clogging of the sieves and allow passing of the powders through the sieves without interference. The sieved particle size range is commonly written as +minimum size – maximum size or –maximum size + minimum size, meaning the particle size is greater than or equal to the minimum particle size determined by the finer sieve size and it is less than or equal to the maximum size defined by the coarser sieve size. For example, the above particle size range is written as +45-75µm or

-75+45 µm.

2.1.1.3 Spray dried agglomerates of micron-sized particles

Following the use of non-spray-dried powders, all subsequent coating fabrication was conducted utilizing commercially available feedstock powders of CuO and SDC ($Ce_{0.8}Sm_{0.2}O_{1.9}$) (Inframat Advanced Materials, Farmington, CT, U.S.A.). The powders were flowable spray dried agglomerates of micron-sized particles with a spherical shape.

Spray dried powders tend to break up during feeding to the plasma torch, clogging the feedlines. In order to avoid the break-up of the powder, the CuO and SDC spray dried powders were calcined at various temperatures. To determine the extent of powder break up, the calcined CuO and SDC powders were fed through the feed hopper and collected. Particle size analysis of the fed powders was conducted using a wet dispersion laser light scatting particle size analyzer (Mastersizer 2000, Malvern Instruments, Worcestershire, U.K.). After calcining profiles were determined, the as-received coarse CuO and SDC powders were calcined and then sieved to a narrower size range of +32-45μm.

2.1.2 Plasma spray processing

The APS system used in these experiments (Axial III Series 600 DC plasma torch, Northwest Mettech Corp., North Vancouver, Canada) contains a torch in which powder is injected axially ensuring that virtually all of the powder injected passes through the hottest part of the plasma jet. Powders were delivered to the torch with Ar carrier gas using powder feeders (MPF Thermico, Dortmund, Germany). The APS system further consisted of a custom built substrate-mounting turntable for both generating horizontal substrate motion relative to the torch and for the cooling of the

substrates in air. A type 'K' thermocouple was spring loaded to the back of the substrate, with the signal carried from the rotating substrate holder through a slip ring to allow substrate temperature monitoring. An X-Y manipulator (Miller Thermal Inc, Appleton, WI, USA) was used to move the plasma torch vertically. Figure 2.1 schematically depicts the experimental set-up. A detailed description of this experimental set-up is given in appendix A.

Figure 2.1: Plasma spray experimental setup

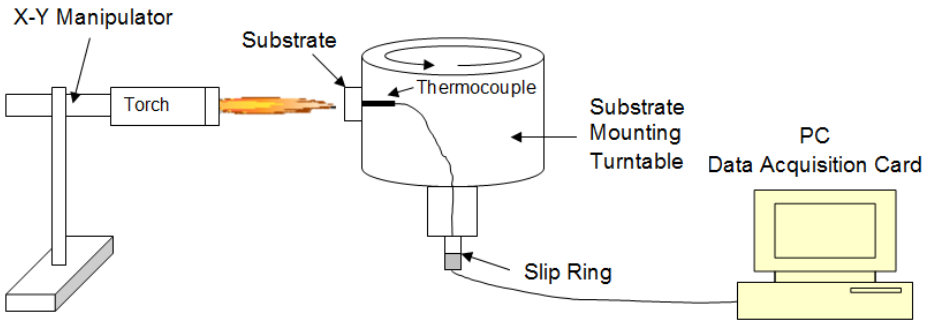

Figure 2.2 shows particle injection geometry of the Axial III torch. Unlike most DC plasma torches in which the powder is injected radially into the plasma jet, the Axial III torch configuration allows axial injection of the powder. This is achieved by a patented torch design in which 3 anodes and cathodes are arranged radially at 120°C angles, allowing the feeding tube to be located at the plasma jet axis. The torch current for each cathode is roughly $^{1}/_{3}$ of the total current.

Figure 2.2: Particle injection geometry of the Axial III Torch[11]

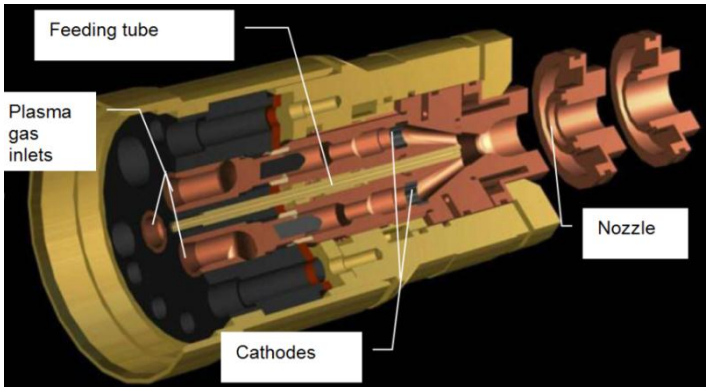

Initially, screening tests were carried out with mixed non-spray-dried CuO (Inframat Advanced Materials, particle size $d_{0.5}$ = 9.05µm) and synthesized SDC powders mixed in a weight ratio of 1:1. The dry mixed powders were plasma sprayed from a single hopper onto a YSZ electrolyte support substrate. Table 2.1 shows spraying and feedstock conditions used to produce the coatings utilizing as-received CuO and synthesized SDC powders. Table 2.2 shows the spraying and feedstock parameters varied during the APS deposition experiments. Not all of the power produced by the torch is retained in the plasma due to the flow of cooling water that prevents the torch from overheating. The difference between the torch power and the enthalpy flow rate removed from the torch in the cooling water stream is the retained plasma power. As the torch power increases, the retained power in the plasma also increases, but at a slower rate. To determine the plasma power, the enthalpy transferred to the cooling water in the torch is subtracted from the total power delivered to the torch. Torch efficiency is determined as the ratio between the plasma power and the torch power.

[11] With kind permission of NorthWest Mettech Corp., North Vancouver, BC, Canada

Table 2.1: Spraying and feedstock conditions used to produce all coatings utilizing as-received CuO and synthesized SDC powders

Parameter	Value
Powder feed-rate (g min^{-1})	16
Carrier gas flow-rate (slpm)	15
Spraying distance (mm)	150
SDC particle size (μm)	-75+45
CuO particle size (μm)	-25
Nozzle diameter (mm)	12.7
Weight Ratio CuO/SDC	1
Substrate	YSZ
Robot traverse speed (m sec^{-1})	4.25
Plasma gas composition (%N_2)	50
Plasma gas composition (%Ar)	50

Table 2.2: Spraying parameters used for a range of CuO-SDC composite coatings utilizing as-received CuO and synthesized SDC feedstock powders

Run	Plasma Gas Flow Rate (slpm)	Arc Current (A)	Torch Power (kW)	Plasma Power (kW)	Torch Efficiency (%)
#1	160	720	75.6	59.6	78.8%
#2	180	720	78.8	63.6	80.8%
#3	180	600	70.0	56.3	80.4%
#4	160	600	64.5	50.4	78.2%
#5	140	600	61.0	46.4	76.1%

Following the co-deposition of synthesized SDC and CuO, all subsequent coating fabrication was performed by plasma spraying of spray dried SDC and CuO powders. Due to the lack of in-flight particle temperature and velocity diagnosis equipment, a full parametric study was ruled out in this stage. Plasma gas composition was chosen as the major plasma spraying parameter to be modified, due to its major effect on the plasma power.

Screening tests were carried out with CuO and SDC powders mixed with a weight ratio of 1:1.2 SDC to CuO. Due to the wider particle size distribution available,

and identical particle size range of -45+32μm was applied for the CuO and SDC powders. A narrow particle size distribution is recommended for plasma spray processing since the spraying of powder of wide size distribution causes overheating and eventually evaporation of finer size fractions and insufficient heating of coarser size fractions may occur [114].

The plasma gas composition was changed for each of the coatings. Deposition of coatings on metal supports was carried out onto sandblasted 2.54 cm diameter 1mm thick type 430 stainless steel (SS430) disks. The coatings were reduced after deposition in a 90:10 vol% N_2 -H_2 mixture at 700°C for 12 hrs. Table 2.3 shows spraying and feedstock conditions used to produce CuO-SDC anode coatings. Table 2.4 shows the plasma gas composition and the corresponding torch and plasma powers and the torch efficiency.

Table 2.3: Plasma spray process parameter values for production of CuO-SDC anode coatings utilizing spray dried powders

Parameter	Value
Powder feed rate (g min^{-1})	32
Carrier gas flow rate (slpm)	15
Spraying distance (mm)	100
SDC particle size (μm)	-45+32
CuO particle size (μm)	-45+32
Weight ratio SDC/CuO	0.83
Vertical traverse speed (m sec^{-1})	4.25
No. of vertical passes	40
Torch current (A)	600
Plasma gas flow rate (slpm)	220
Nozzle diameter (mm)	12.7
Substrate	SS430

Table 2.4: Plasma gas composition and the corresponding torch and plasma powers and torch efficiency

Plasma gas composition	Torch power [kW]	Plasma power [kW]	Torch efficiency
20% N_2 / 80% Ar	58.2	49.3	84.8%
40% N_2 / 60% Ar	69.8	58.3	83.6%
60% N_2 / 40% Ar	87.6	72.6	82.9%
80% N_2 / 20% Ar	98.4	81.5	82.9%

2.1.3 Coating characterization

X-ray diffraction (XRD) analysis of the coatings was performed using a Brucker D8-Discovery diffractometer (Brucker AXS Inc.) with Cu Kα radiation at 0.01°s^{-1} both before and after reduction to determine the phase structure dependence on spraying and feedstock parameters. Energy dispersive X-ray spectroscopy (EDX, Hitachi High Technologies America, Pleasanton, CA) was performed to calculate the volume fraction of Cu present in the coatings. Scanning Electron Microscopy (SEM, S3500N, Hitachi High Technologies America, Pleasanton, CA) imaging of the coatings was performed to observe the porosity and uniformity of the microstructures.

2.2 Results and discussion

2.2.1 Feedstock powder morphology and crystal structure

2.2.1.1 Synthesized SDC

Figure 2.3 shows an XRD pattern of the reacted ball milled cerium carbonate and samarium acetate after heating, showing that the materials react to form single-phase $Ce_{0.8}Sm_{0.2}O_{1.9,}$ without other phases present.

Figure 2.3: XRD pattern of reacted ball milled cerium carbonate and samarium acetate

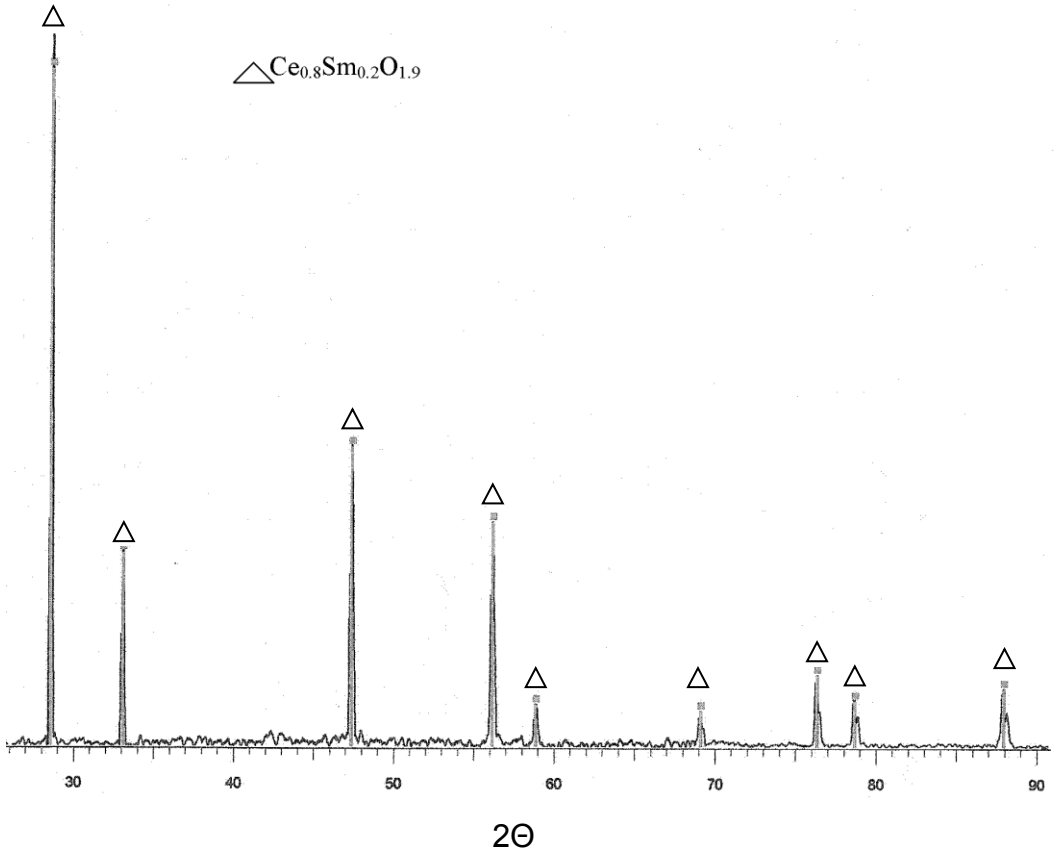

2.2.1.2 Feedstock characterization of non-spray-dried powders

Figure 2.4 shows the particle size distribution of the calcined synthesized SDC. The analysis showed a particle size range of 0.25µm-550µm, with $d_{0.1}$=3.33µm, $d_{0.5}$=39.7µm, and $d_{0.9}$=205µm.

Figure 2.4: Particle size distribution of the calcined synthesized SDC

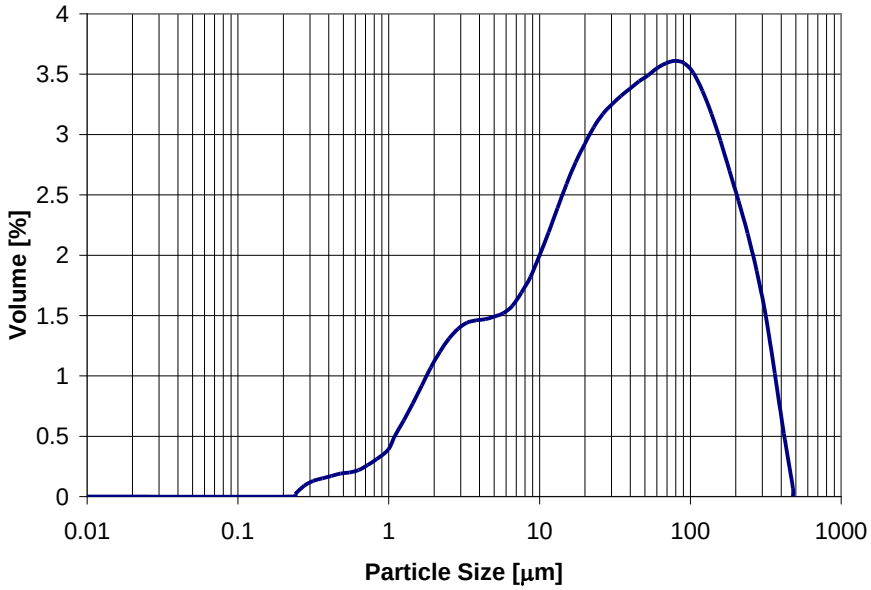

Figure 2.5 shows an SEM micrograph of the synthesized SDC powder sieved to +75-108μm. It can be seen that the particles have an irregular non-spherical shape, with a large relative volume of smaller particles (<75μm) that form larger agglomerates. These agglomerates appear to break easily into smaller particles, resulting in a non-homogenous particle size distribution.

Figure 2.5: SEM micrograph of the synthesized SDC powder sieved to +75-108µm

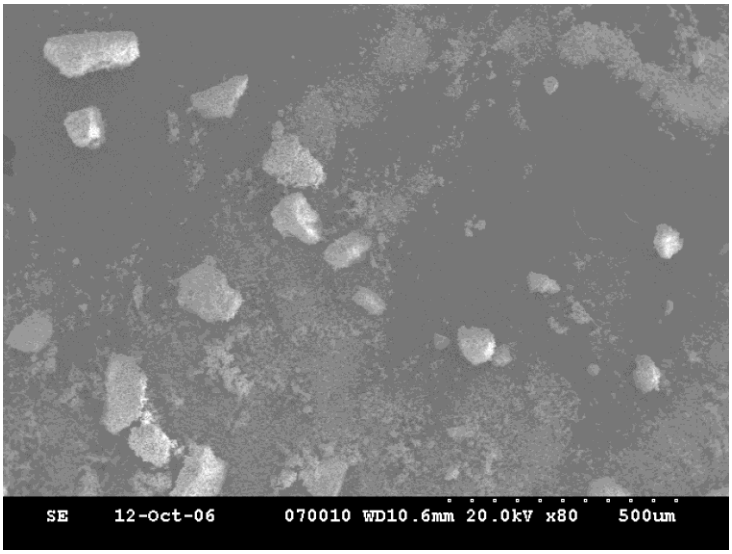

Figure 2.6 shows the particle size distribution of the CuO powder as received. The CuO powder particle size demonstrates a narrow range of $d_{0.1}$=3.82µm, $d_{0.5}$=9.05µm, and $d_{0.9}$=18.5µm.

Figure 2.6: Particle size distribution of the CuO powder as received

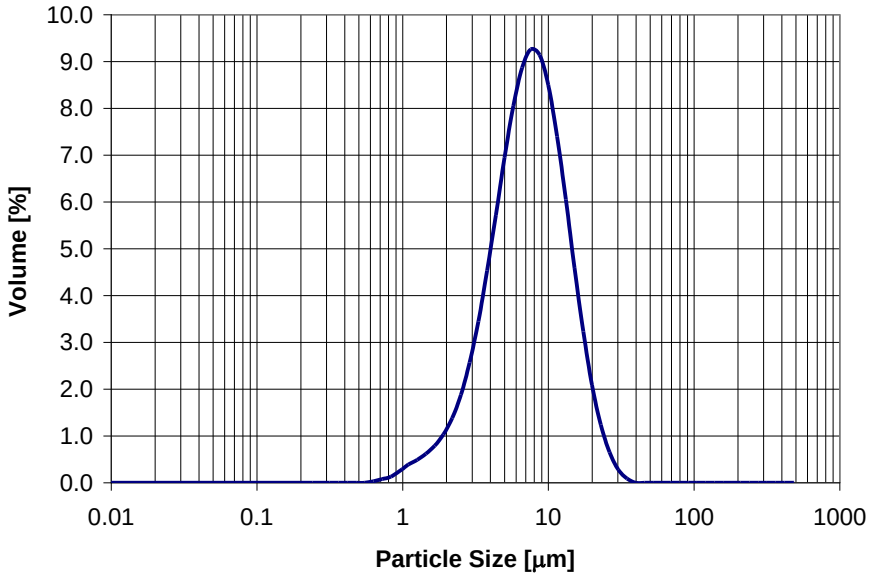

Figure 2.7 shows an SEM micrograph of the CuO as-received powder. It can be seen that the particles have an irregular non-spherical shape.

Figure 2.7: SEM micrograph of the CuO powder as received.

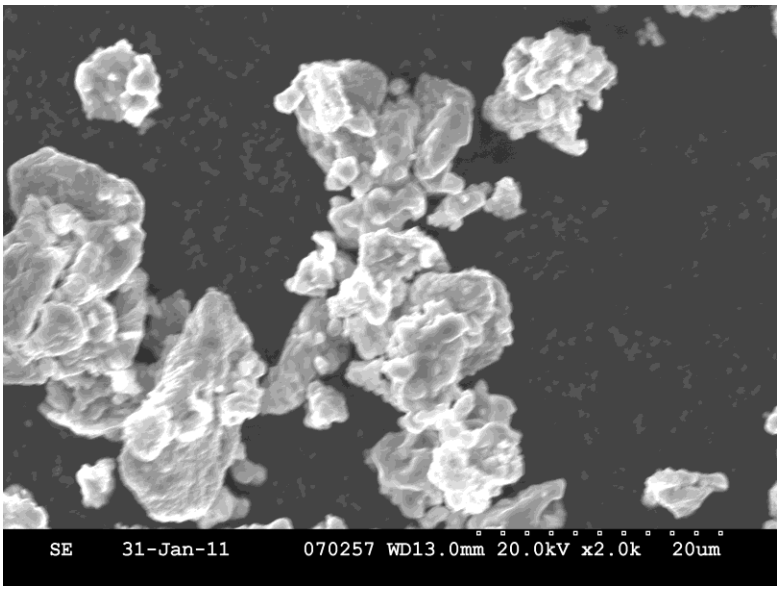

2.2.1.3 Feedstock characterization of spray dried powders

Figure 2.8 shows particle size distributions of spray dried CuO powder as received and calcined at various temperatures before and after feeding through the plasma spray torch feed hopper. The break-up during feeding can be seen as an increase of the particle size distribution curve at smaller particle sizes and decrease at larger particle sizes. The spray dried CuO as-received and calcined at 800°C breaks up during feeding to a much greater extent than CuO calcined at 850°C. The particle size distribution of the spray dried CuO after feeding is asymmetric, demonstrating that at least a portion of the agglomerated particles break up during feeding.

Additional calcining experiments have shown that spray dried CuO powder calcined at 900°C undergoes partial sintering, and therefore was not feedable. Based on these results, a calcining temperature of 850°C was chosen to treat the spray dried CuO powder.

Figure 2.8: Particle size distributions of spray dried CuO powder as received and calcined at various temperatures before and after feeding through the feed hopper

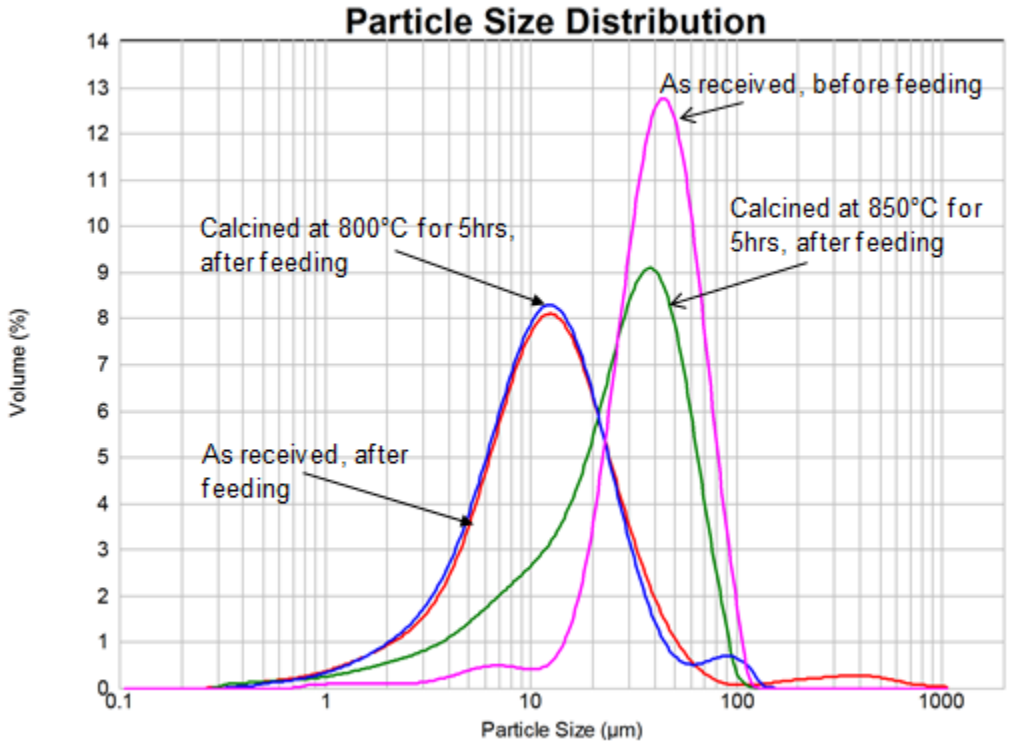

Figure 2.9 shows particle size distributions of spray dried SDC powder as received and calcined at various temperatures before and after feeding through the hopper. The break-up during feeding can be seen as an increase in volume of particles having a smaller diameter on the particle size distribution curve. The spray dried SDC as-

received breaks up during feeding, resulting in a larger portion of fine particles than SDC calcined at 1200°C or 1350°C. Spray dried SDC powder calcined at 1350°C was found to be highly packed and hard to sieve. Therefore, calcining temperatures higher than 1350°C were not examined. Based on these results, a calcining temperature of 1350°C was chosen to treat the spray dried SDC powder prior to spraying due to the smaller volume of broken particles in comparison to SDC powder calcined at 1200°C

Figure 2.9: Particle size distributions of spray dried SDC powder as received and calcined at various temperatures before and after feeding through the hopper

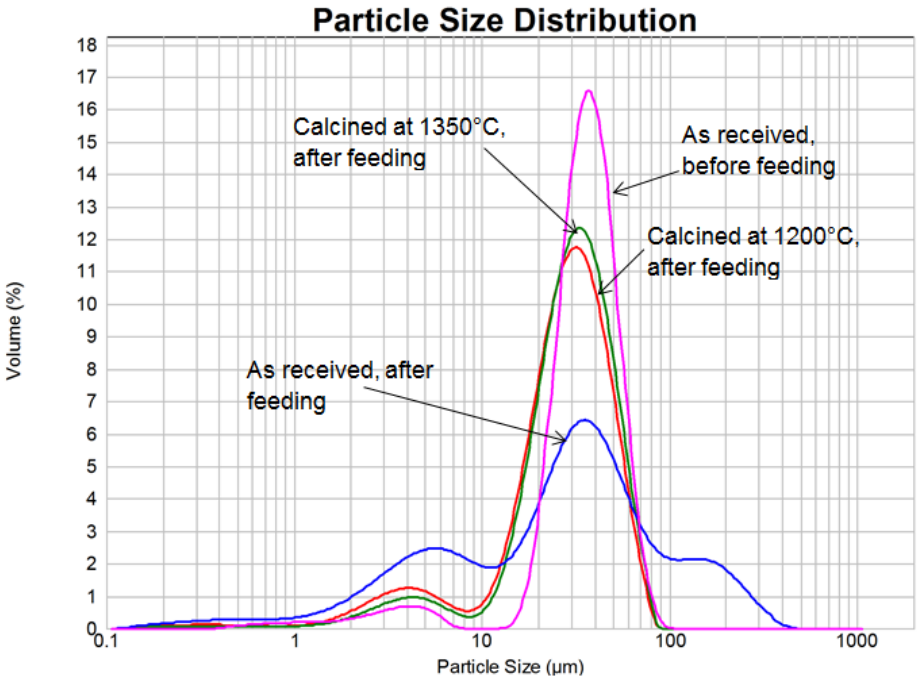

Figure 2.10 and Figure 2.11 show SEM micrographs of spray dried CuO and SDC feedstock powders, respectively. Unlike non-spray-dried powders, the spray dried powders have approximately spherical shapes that make them flowable for APS.

Figure 2.10: SEM micrograph of CuO spray dried powder

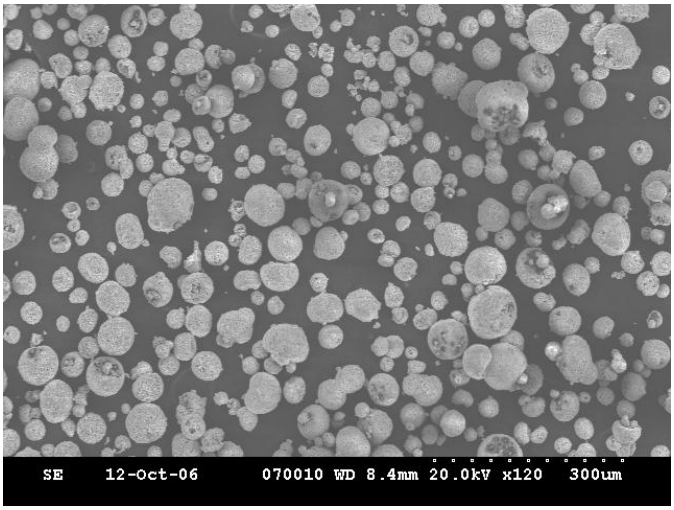

Figure 2.11: SEM micrograph of SDC spray dried powder

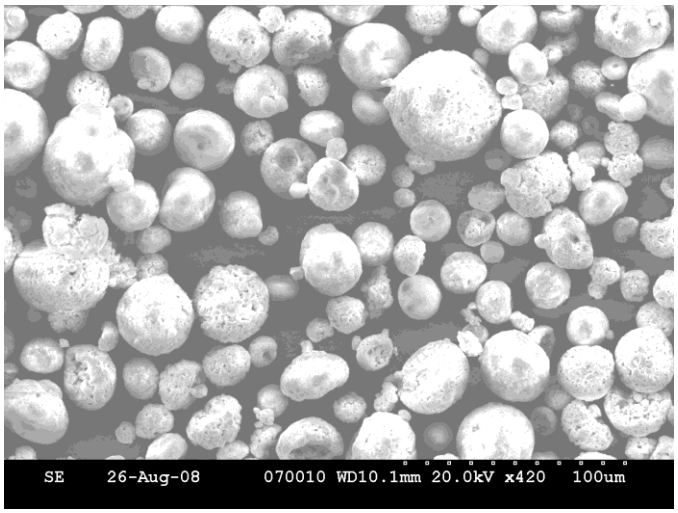

2.2.2 Microstructural analysis

2.2.2.1 Screening tests with non spray dried powders

Figure 2.12 shows a cross section SEM micrograph of the CuO-SDC coating produced using the plasma conditions of run #1 in Table 2.2. The SDC appears brighter in SEM in comparison to the CuO. It can be seen that the coating forms distinct layers of the two materials. Also, the CuO is much more melted than the SDC, forming thinner splats. Figure 2.13 shows an EDX mapping of a cross section of the coating produced with the set of conditions of run #1 in Table 2.3. It can be seen that a Cu-rich layer forms near the interface with the electrolyte, with low SDC content in that region, with alternating layers rich in CuO and in SDC through the coating thickness. Formation of separate layers may occur due to separation of the powders in the vibrating hopper, or due to powder clogging due to the non spherical geometry of the powders. This microstructure is not desirable for SOFC anodes, in which both materials have to be homogenously mixed, to allow sufficient contact areas between the SDC, Cu and the electrolyte, and for sufficient percolation of the Cu. Inhomogeneous mixing might affect the anode performance by increasing ohmic and activation losses.

Figure 2.12: Cross-section SEM micrograph of coating produced in run #1

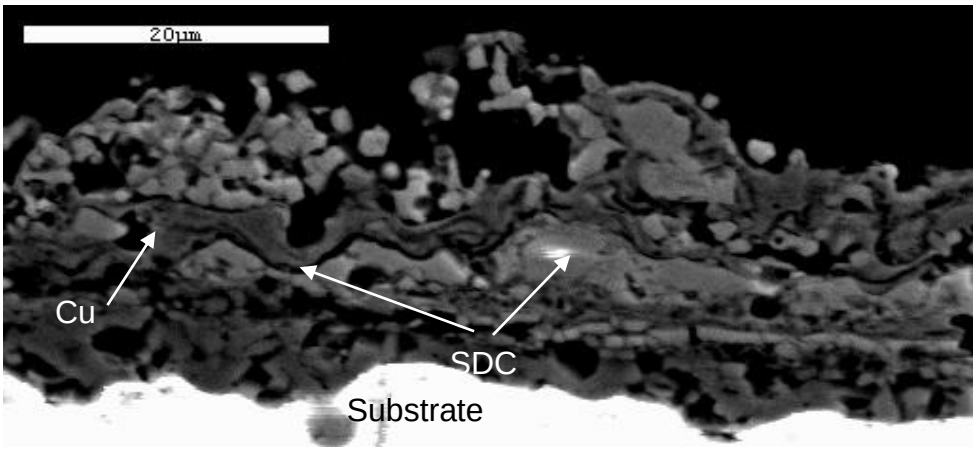

Figure 2.13: EDX map of a cross section of the coating produced with the set of conditions in run #1

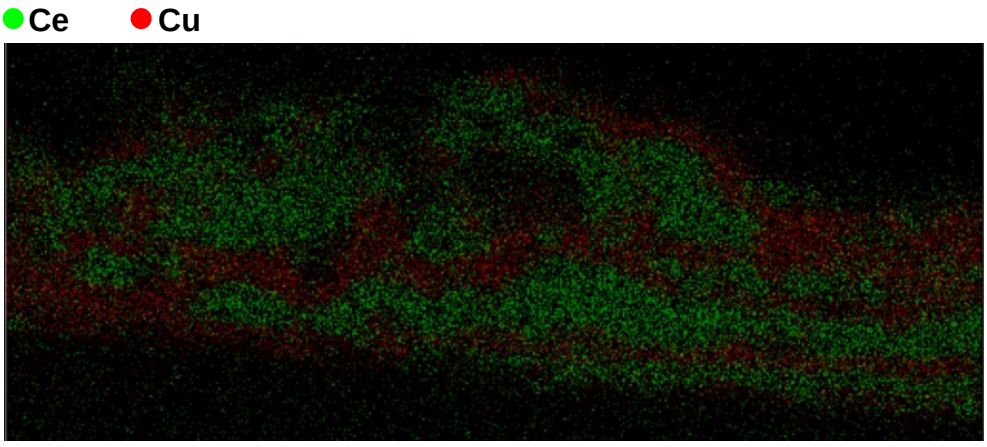

2.2.2.2 Screening tests with spray dried powders

2.2.2.2.1 XRD of plasma sprayed CuO-SDC coatings

Figure 2.14 shows XRD patterns of coatings produced from CuO-SDC feedstock powders, before and after reduction. Peak intensities are measured in arbitrary units. The crystal structure of the SDC remained cubic over the entire range of spraying conditions. This makes it possible to further optimize the microstructure because SDC can be sprayed within a wide spraying envelope. In high energy plasmas with plasma gas composition of N_2-Ar 60%-40% and 80%-20%, the CuO remained monoclinic. For lower energy plasmas with plasma gas composition of N_2-Ar 40%-60% and 20%-80%, partial reduction of CuO to Cu_2O was observed. The XRD patterns of the coatings after reduction in a 10%-90% H_2-N_2 mixture confirmed that the CuO and Cu_2O were fully reduced to cubic Cu.

Peak intensities vary with the plasma gas composition.. It can be observed that the relative peak intensities, i.e. normalized to the highest-intensity peak, of the as-

sprayed CuO and Cu_2O decrease with the increase of N_2 content in the plasma, while the relative peak intensity of the as-sprayed SDC increases with the increase of N_2 content in the plasma. This result suggests that the ratio between SDC and CuO/Cu_2O in the coating increases with the increase of N_2 content in the plasma. This observation reflects the effect of N_2 content on the absolute deposition efficiency of these materials. Generally, a higher N_2 content results in a higher plasma torch electrode voltage, which results in higher energy plasmas. In APS, if the particles are not sufficiently melted prior to impact, they will likely bounce off the surface, resulting in lower deposition efficiency compared to particles that are fully melted upon impact with the substrate. In such a case, an increase in plasma energy will increase the deposition efficiency of this material, whereas if the particles have partially evaporated, it will decrease the deposition efficiency due to the material loss. In that case, a decrease in plasma energy will increase the deposition efficiency of the material. The absolute deposition efficiency of the CuO, which has a lower melting temperature than SDC (1227 °C for CuO[109] and 2480°C for ceria [111]), decreases with the increase of N_2 in the plasma. This can likely be attributed to a higher degree of evaporation of the CuO. The absolute deposition efficiency of the SDC, having a higher melting temperature than the CuO, increases with the increase of N_2 in the plasma. This can be attributed to a higher degree of melting of the SDC.

Figure 2.14: XRD patterns of coatings produced from CuO-SDC feedstock powders using various plasma gas compositions.

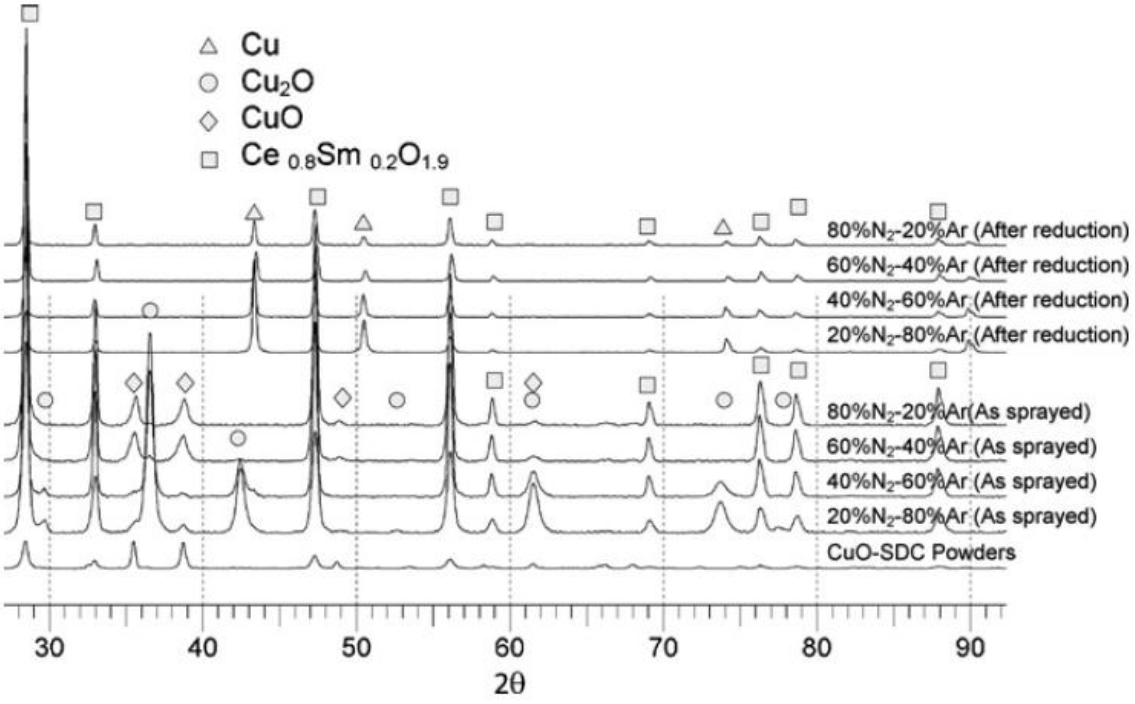

2.2.2.2.2 Relative deposition efficiency of CuO in CuO-SDC coatings

One challenge in producing CuO/SDC composite anode coatings by APS is achieving the desired composition, 40 vol. % of Cu in the solid phases after reduction, due to the differences in deposition efficiency between the two materials for a given set of plasma conditions. The relative deposition efficiency is determined as the ratio between the weight ratio of CuO to SDC in the coating to the weight ratio of CuO to SDC in the feedstock powders.

The molar ratios of the Ce and Cu in the coating are determined by EDX. Since both SDC and CuO contain oxygen, it is not possible to utilize EDX to directly derive the relative molar ratios of SDC and CuO. After EDX analysis of Ce and Cu compositions,

the molar ratios of SDC and CuO in the coating are derived using the physical constants in Table 2.4 and Equation 2.1 to Equation. 2. 2

Equation 2.1 shows the Kröger-Vink notation of formation of SDC solid solution. In this notation, M denotes dopant ion, V vacancy, e‘ negative charge, $h^{\bullet}$ positive charge. This reaction implies that when *x/2* moles of dopant oxide (M_2O_3) are added, cation sites are filled with *x* moles of dopant cation (M^{3+}) and *1-x* moles of host cation (Ce^{4+}), while anion sites are filled with *2-x/2* moles of host anion (O^{2-}) and x/2 moles of anion vacancies (V). Therefore, a predictable concentration of oxygen vacancies can be introduced into the crystal by controlling the concentration of the dopant added.

$$xMO_{1.5} + (1-x)CeO_2 \longleftrightarrow xM'_{Ce} + 0.5xV_O^{\cdot\cdot} + (1-x)Ce_{Ce} + (2-0.5x)O_O \tag{2.1}$$

Equation 2.2 shows the molar mass of $Ce_{1-x}Sm_xO_{2-x/2}$, where x is the concentration of Sm in the solid solution. The molar ratio of the Sm_2O_3 in the SDC powder used to produce the coatings is 10 mol%, i.e., x = 0.2. Using Eq. 2.1 with x=0.2, the molar mass of SDC ($Ce_{0.8}Sm_{0.2}O_{1.9}$) is 172.56 g mol^{-1}.

$$M_{Ce_{1-x}Sm_xO_{2-\frac{1}{2}x}} = (1-x)M_{Ce} + XM_{Sm} + (2-\tfrac{1}{2}x)M_O \tag{2.2}$$

Eq. 2.2 and Eq. 2.3 show the relative weight of SDC and CuO in the coating, respectively, where Ce(mol%) is the molar ratio of Ce in the coating obtained by EDX , Cu(mol%) is the molar ratio of Cu in the coating obtained by EDX, and M_{CuO} is the molar mass of CuO

$$W_{\mathrm{Ce_{1-x}Sm_xO_{2-\frac{1}{2}x}}}(wt\%) = \frac{Ce(mol\%)\frac{1}{1-x}M_{Ce_{1-x}Sm_xO_{2-\frac{1}{2}x}}}{Ce(mol\%)\frac{1}{1-x}M_{Ce_{1-x}Sm_xO_{2-\frac{1}{2}x}} + Cu(mol\%)M_{CuO}} \quad (2.3)$$

$$W_{CuO}(wt\%) = \frac{Cu(mol\%)M_{CuO}}{Ce(mol\%)\frac{1}{1-x}M_{Ce_{1-x}Sm_xO_{2-\frac{1}{2}x}} + Cu(mol\%)M_{CuO}} \quad (2.4)$$

Table 2.5 shows the molar mass of elements and sprayed materials used to determine the relative deposition efficiency.

Table 2.5: Molar mass of elements and sprayed materials

Material	Molar mass g mol^{-1}	References
CuO	79.545	[109]
SDC ($Ce_{0.8}Sm_{0.2}O_{1.9}$)	172.56	*Calculated*
Cu	63.546	[115]
Ce	140.116	[116]
Sm	150.36	[117]
O	15.9995	[118]

The relative deposition efficiency is determined as the ratio between the weight ratio of CuO to SDC in the coating to the weight ratio of CuO to SDC in the feedstock powders, as shown in Equation 2.1.

$$Rel.D.E = \frac{\left(\frac{CuO_{coating}}{SDC_{coating}}\right)}{\left(\frac{CuO_{feedstock}}{SDC_{feedstock}}\right)} \quad (2.1)$$

Figure 2.15 shows the relative deposition efficiency of CuO to SDC. It can be seen that the relative deposition efficiency of CuO to SDC decreases with the increase of N_2 content within the plasma. Since CuO has a much lower melting temperature than SDC, hotter plasmas will lead to a greater extent of evaporation of the CuO, which reduces the deposition efficiency of CuO, and in parallel, a higher degree of melting of the SDC, which increases the deposition efficiency of SDC. Therefore, the deposition efficiency of CuO will decrease relative to that of SDC, as can be seen in Fig. 2.15.

Figure 2.15: CuO deposition efficiency relative to that of SDC with varying N_2 content

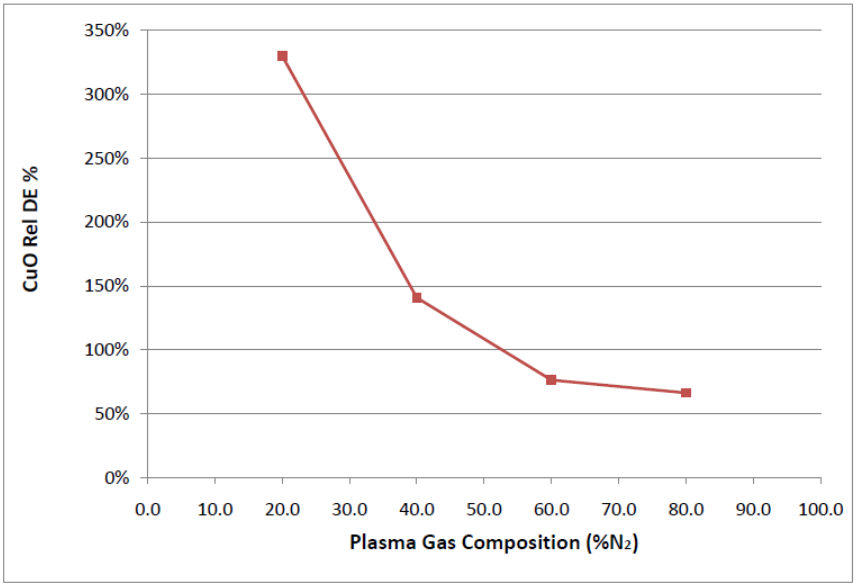

2.2.2.2.3 Surface SEM

Figures 2.16 and 2.17 show SEM micrographs of coatings produced in high and low plasma energy conditions, respectively. Over the spraying conditions examined, the CuO tends to melt easily to form thin, fairly dense layers within the coating. Figure 2.16 shows a coating formed in a high-power (81.5 kW) plasma. The CuO phase is well

melted and forms splats that spread over the less melted SDC particles. Figure 2.17 shows a coating formed in a lower-power plasma (58.3kW). It can be seen that the CuO is very highly melted, even with the lower-power plasma. It can also be seen that the spray dried SDC agglomerates break up into smaller particles during the spraying process. This is likely a result of a combination of low particle temperature and high particle velocity at the time of impact with the substrate. EDX mapping showed that although the CuO and SDC in the coatings are well mixed on the mm scale, the coatings are not homogenous and the SDC and CuO are not well mixed on the µm scale. It is not clear whether the SDC agglomerates break up upon entering the plasma or whether the droplets only partially melt in the plasma, leading to breaking up of the particles upon impact with the substrate, but clusters of SDC remain intact in the coatings. The SDC particles in the coating show a wide size distribution, from sub-micron to tens of microns.

Figure 2.16: CuO-SDC coating formed in high (81.5 kW) plasma power conditions

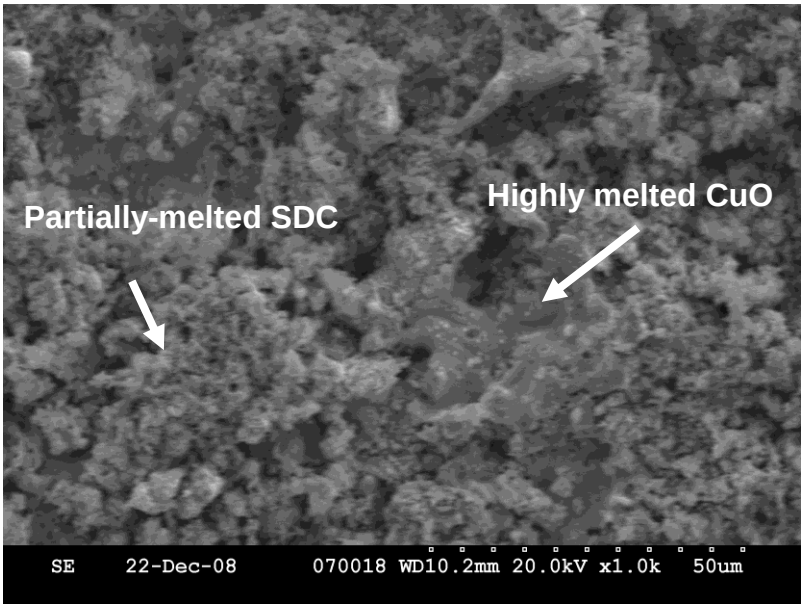

Figure 2.17: CuO-SDC coating formed in low (58.3 kW) plasma power conditions

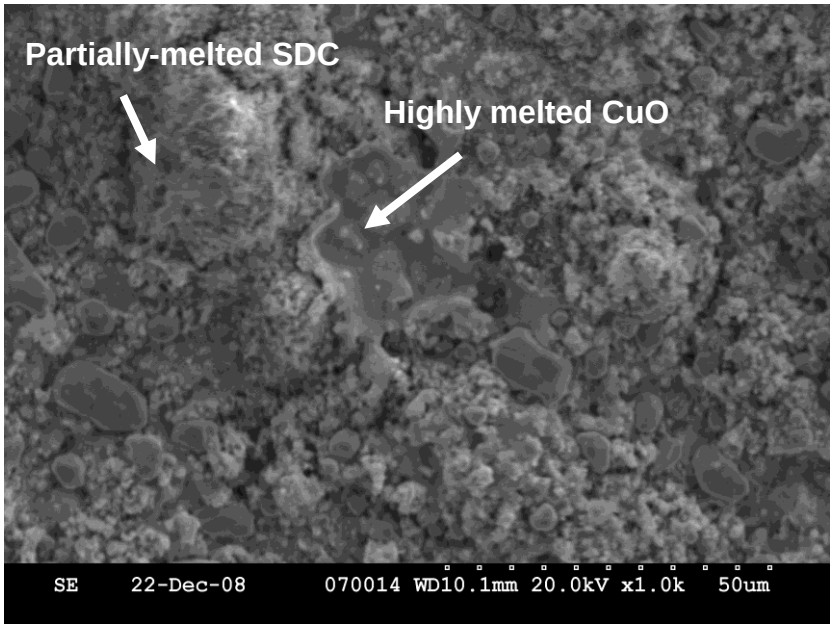

2.3 Conclusions

SDC powder was produced by reaction and calcining of precursors. APS of synthesized SDC powder and commercially available CuO powder resulted in non-homogenous coatings and stratified CuO and SDC layers.

Calcining profiles for spray dried agglomerates of CuO and SDC powders were determined by measuring particle sizes of each powder prior to and after feeding through the hopper. These powders were successfully co-deposited by APS to form composite coatings. XRD patterns confirm that the SDC remain cubic and the CuO remains monoclinic over a wide range of spraying conditions. EDX measurements indicate that both materials are present in the coating, with the relative deposition efficiency of CuO compared to that of SDC decreasing with increasing N_2 content over

the conditions studied. The CuO in the composite coatings has sufficient porosity to allow full reduction to Cu after spraying, thus demonstrating the feasibility of using plasma spraying with CuO and SDC as starting powders for the production of composite Cu-SDC anode coatings.

3. CuO-SDC coatings for use as anode functional layers in direct oxidation SOFCs

This chapter deals with electrochemical testing of Cu-SDC anode functional layers. Fine spray dried CuO and SDC powders were utilized to produce homogeneously mixed anode coatings with high-surface-area microstructures. Symmetrical electrolyte supported cells with CuO-SDC anode layers were fabricated by air plasma spraying, followed by in-situ reduction of the CuO to Cu. Full cells utilizing CuO-SDC anode layers were deposited on SS430 porous substrates and produced in one integrated process. The cells were tested electrochemically with hydrogen fuel at various temperatures, and their impedances were measured over a range of frequencies. The resulting area-specific polarization resistances were 21.8 Ωcm² for electrolyte supported symmetrical cells at 723°C and 4.8 Ωcm² for SS430 porous substrate supported full cells at 712°C.

3.1 Experimental procedure

3.1.1 Material preparation

3.1.1.1 YSZ substrate preparation by axial pressing

YSZ substrates were prepared by pressing 4g of YSZ powder (Inframat Advanced Materials, CT, USA, d_{50} = 1.58μm) into pellets with a 32mm die. This method is preferred for laboratory-scale anode characterization compared to tape casting because it results in YSZ substrates with coarser surfaces than tape cast substrates. Coarse surfaces allow better adhesion of the plasma sprayed coatings to the surface. In addition, axially-pressed YSZ substrates remain flat during the sintering step, unlike

tape cast YSZ substrates, which tend to curve during sintering. In addition, it was found that axially-pressed substrates withstand thermal shock better than tape cast substrates, and tend to break less frequently during plasma spraying. The pellets were sintered into substrates at 1400°C for 4hrs, resulting in 1” diameter pellets. The sintered YSZ pellets were sand blasted prior to spraying to create a coarse surface to provide better adhesion of the coating to the surface. After sand blasting, the surfaces were cleaned with acetone to remove any residue.

3.1.2 Plasma spraying

3.1.2.1 Production of symmetrical cells with Cu-SDC anode functional layers

Anode coatings were deposited symmetrically on both sides of YSZ substrates, using a custom made mask to obtain concentric anodes. Fine spray dried CuO (d_{50} = 8.2µm) and SDC (d_{50} = 2.5µm) (Inframat Advanced Materials, Connecticut, USA) sieved to -25µm and mixed in a weight ratio of 1.5:1 SDC to CuO were utilized to produce anode functional layers with high surface areas.

To obtain full percolation in porous composite anodes, the volume fraction of the Cu in the solid phases of the anode was targeted at 40%, in keeping with the observed upper percolation threshold range of the metallic phase for Ni-YSZ anodes [119]. The symmetrical cell anode layer coatings produced were reduced in H_2 at 700°C for 5 hrs. Table 3.1 shows experimental plasma spray process parameters for anode production in symmetrical cells. Figure 3.1 shows an electrolyte-supported symmetrical cell.

Table 3.1: Plasma spray process parameter values for production of anode coatings for symmetrical cells

Parameter	Values
Powder feed rate (g min^{-1})	18
Carrier gas flow rate (slpm)	15
Spraying distance (mm)	100
SDC particle size (μm)	-32+25
CuO particle size (μm)	-25
Weight ratio SDC/CuO	1.5:1
Vertical traverse speed (m sec^{-1})	4.25
No. of vertical passes	40
Torch current (A)	540
Plasma gas flow rate (slpm)	180
Vol.% nitrogen (balance Ar)	50
Nozzle diameter (mm)	12.7
Torch power [kW]	64.6
Plasma power [kW]	51.5
Torch efficiency [%]	79.7%
Substrate	YSZ

Figure 3.1: Electrolyte supported symmetrical cell

3.1.2.2 Plasma spraying of Cu-SDC functional layers on metal substrates

Due to the performance and mechanical limitations introduced by electrolyte-supported cells, porous metallic substrates were integrated into subsequent cells as a substitute for the YSZ electrolyte supports. Commercially available 2.54 cm diameter porous SS430 disks (Mott grade 5, Mott Corporation, Farmington, CT, USA) with a

thickness of approximately 1mm were used as the metallic substrates. One such substrate is shown in Figure 3.2.

Figure 3.2: Porous SS430 metal substrate

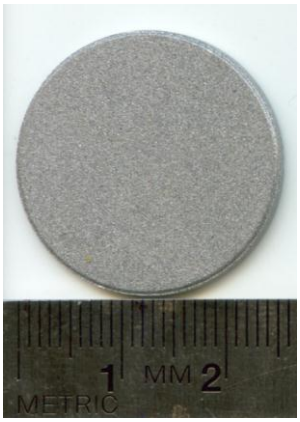

SS430 was chosen due to it its low thermal expansion coefficient (11.9 μm m^{-1} $°C^{-1}$ at 650°C), which allows a better thermal expansion match between the substrate and the cathode-electrolyte-anode layers than Hastelloy X alloy (15.6 μm m^{-1} $°C^{-1}$ at 700°C) , which has been previously utilized as the substrate material ([105] and [120]). A cathode layer was formed by spraying mechanically mixed LSM-YSZ powders (Inframat Advanced Materials) onto the substrate using conditions developed previously [113]. Fine YSZ powder (Inframat Advanced Materials) suspended in water was used to form the electrolyte on top of the cathode using conditions reported elsewhere ([24] and [45]). CuO and SDC powders were mixed with a weight ratio of 1.67:1 SDC to CuO. This powder mixture was sprayed through a mask onto the YSZ layer to form an anode layer. The coatings were reduced after deposition in a N_2-H_2 mixture (10%H_2) at 700°C for 12 hrs. Table 3.2 shows experimental plasma spray process parameters for the cathode and electrolyte. Table 3.3 shows experimental plasma spray process parameters used to produce the anode.

Table 3.2: Experimental plasma spray process parameters for cathode and electrolyte production

Parameter	Values	
	cathode	***electrolyte***
Feedstock	48.2 wt% LSM /51.8 wt% YSZ powder	23.7 wt% YSZ aqueous suspension
Particle size	−45+32µm /−32+25 µm	1.6 µm (d_{50})
Powder feed rate (g min^{-1})	40	38.1[12]
Carrier gas flow rate (slpm)	11.7	n/a
Spraying distance (mm)	100	80
Vertical traverse speed (m sec^{-1})	4.25	4.25
No. of vertical passes	60	50
Torch current (A)	549	750
Plasma gas flow rate (slpm)	250	220
Vol.% nitrogen (balance Ar)	76.7	80
Nozzle diameter (mm)	9.5	12.7
Pre-heat temperature (°C)	300	325

Table 3.3: Experimental plasma spray process parameters for anode production

Parameter	***anode***
Feedstock	37.5 wt% CuO / 62.5 wt% SDC
Particle size	2.5 µm (d_{50}) (SDC) / 8.2 µm (d_{50}) *(CuO)*
Powder feed rate (g min^{-1})	40
Carrier gas flow rate (slpm)	15
Spraying distance (mm)	100
Vertical traverse speed (m sec^{-1})	4.25
No. of vertical passes	40
Torch current (A)	600
Plasma gas flow rate (slpm)	220
Vol.% nitrogen (balance Ar)	40
Nozzle diameter (mm)	12.7
Torch power [kW]	70.6
Plasma power [kW]	58.8
Torch efficiency [%]	83.3
Pre-heat temperature (°C)	300

[12] of solids in suspension

3.1.3 Coating characterization

Energy dispersive spectroscopy (EDX) was performed to determine the volume fraction of Cu present in the coatings. SEM imaging of the coatings was performed to observe the porosity and uniformity of the microstructures.

3.1.4 Electrochemical testing

Symmetrical cell testing was performed using an SOFC test station (AMI, Canada, and AMEL, Italy) and an FRA and potentiostat (Solartron 1260 and 1470E, UK) after in-situ reduction in H_2 at 569°C of the anodes. The test station design includes a thermocouple that measures the temperature close to the cell. Figure 3.3 shows the test station set-up.

Figure 3.3: AMI-AMEL test station set-up

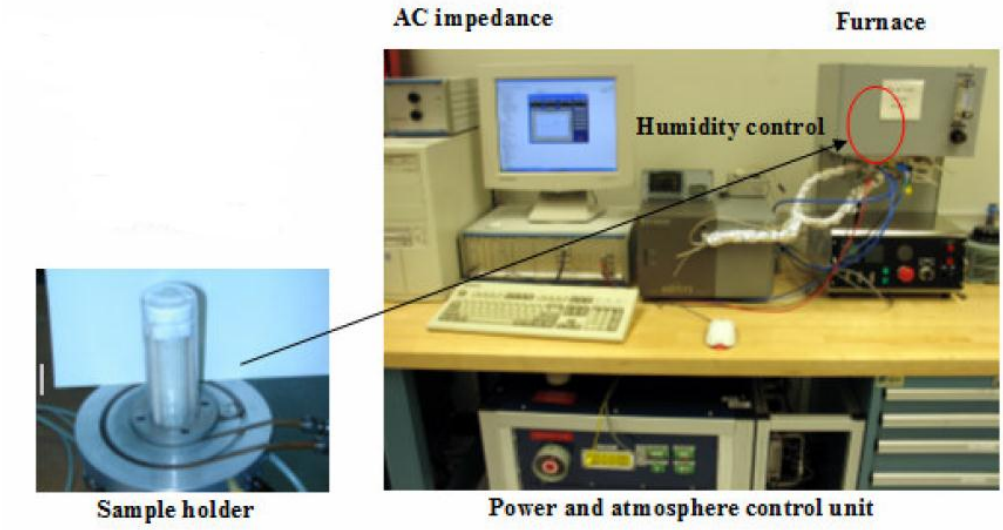

The symmetrical cell was tested in dry hydrogen flowing at 100 sccm at temperatures ranging from 569ºC to 772ºC, in approximately 50ºC increments with 3ºC min^{-1} ramp rates between temperatures. Impedance spectroscopy at open circuit conditions was conducted at cell temperatures of 569ºC, 620ºC, 672ºC, 723ºC, and 772ºC over the frequency range of 2mHz to 1MHz, with 50mV rms voltage perturbation amplitude. The measurements were repeated several times during 90 min holds at each temperature.

The CuO-SDC anodes in full cells were tested with a custom made test station described in detail in appendix B. Initially, the cells were reduced in-situ with a humid (3% H_2O) H_2-N_2 mixture (10%H_2) at a total flow rate of 100 sccm for 13 hrs at 700°C. The cells were then tested in a humid (3% H_2O) H_2-N_2 mixture (20% H_2) at a total flow rate of 200 sccm at temperatures ranging from 550ºC to 700ºC, in approximately 50ºC increments with 1ºCmin^{-1} ramp rates between temperatures. Impedance spectroscopy at open circuit voltage (OCV) and at 0.7V (polarized condition) was conducted utilizing potentiostatic mode at cell temperatures of 562ºC, 612ºC, 672ºC, and 712ºC over the frequency range of 1mHz to 1MHz, with 50 mV rms voltage perturbation amplitude. Polarization curves were obtained from OCV to 0.3V. After testing with H_2, the cells were exposed to CH_4 for 12 hrs. After the cells were cooled down, they were examined by EDX to search for carbon residue.

3.2 Results and discussion

3.2.1 Microstructural analysis

3.2.1.1 Microstructural analysis of symmetrical cell

After analyzing the results from the screening tests in Ch.2, further modifications were made to the spraying and feedstock conditions. The CuO particle size was decreased to reduce the size of the splats of the highly melted CuO particles and to improve the extent of mixing with the SDC to improve the microstructure. The SDC particle size was decreased to allow the coatings to be sprayed with a lower plasma power in order to produce coatings on YSZ substrates without breaking them due to thermal shock and to increase the surface area for reaction. The plasma gas flow rate was reduced to allow higher residence times of the particles in the plasma and therefore better melting of the SDC particles.

Figure 3.4 shows a cross section SEM micrograph of a coating produced with the set of spraying parameters and conditions listed in Table 3.1, after reduction with H_2. It can be seen that decreasing the SDC and CuO particle sizes and applying a low plasma gas flow rate resulted in coatings with uniform, porous, and well mixed microstructures with the desired characteristics of anodes: fairly high surface area, porosity, and extensive CuO-SDC mixing and contact. Figure 3.5a and Figure 3.5b show EDX maps of the Cu and Ce, respectively, confirming that the CuO and SDC phases are fairly well mixed.

Figure 3.4: Cross section of an anode coating produced for a symmetrical cell with the set of spraying parameters and conditions shown in Table 3.1.

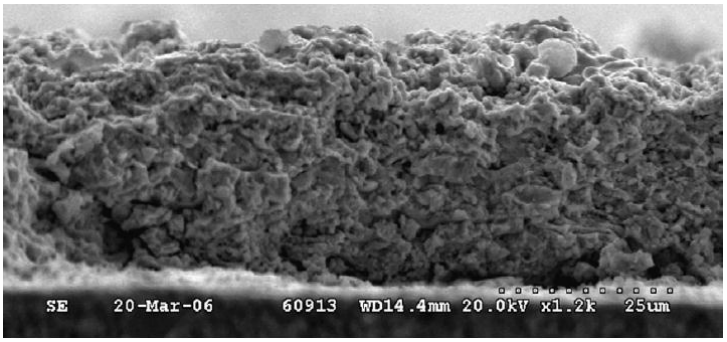

Figure 3.5: EDX map of (a) Cu and (b) Ce in a coating produced with the set of spraying parameters and conditions listed in Table 3.1

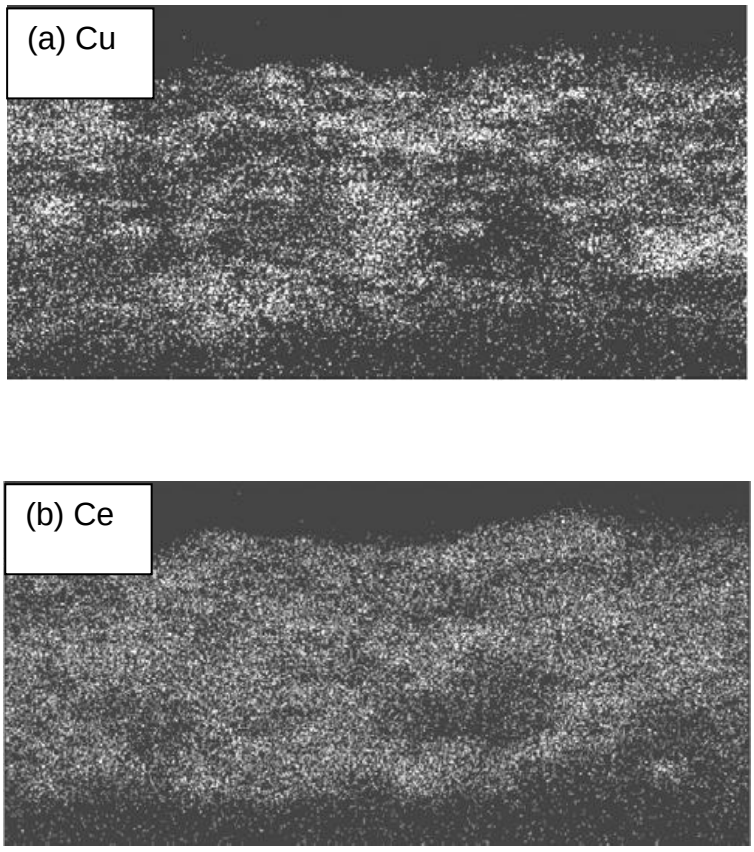

Eq. 3.1 shows the volume fraction of Cu. Here, X_{Ce} and X_{Cu} are the molar fractions of Ce and Cu, respectively. M_{Cu} and M_{SDC} are the molar masses of Cu and SDC ($Ce_{0.8}Sm_{0.2}O_{1.9}$) obtained from Table 2.4. ρ_{Cu} and ρ_{SDC} are the densities of Cu and SDC ($Ce_{0.8}Sm_{0.2}O_{1.9}$), respectively. These densities appear in Table 3.4. The volume fraction of Cu in the coatings after reduction determined by EDX and Eq. 3.1 was 39.8vol%.

$$V_{Cu}(vol\%) = \frac{M_{Cu}X_{Cu}\rho_{Cu}^{-1}}{M_{Cu}X_{Cu}\rho_{Cu}^{-1} + 1.25M_{SDC}X_{Ce}\rho_{SDC}^{-1}} \quad (3.1)$$

Table 3.4: Physical constants of elements and sprayed materials

Material	Density g cm^{-3}	References
SDC $(CeO_2)_{0.8}(Sm_2O_3)_{0.2}$	7.134[1]	[121]
Cu	8.96	[115

3.2.1.2 Microstructural analysis of metal substrate cell

Figure 3.6 shows an SEM micrograph of a metal supported cell cross section. As seen in the SEM micrograph, the anode is porous, with a thickness of approximately 20µm. The use of fine SDC and CuO particles resulted in a fine microstructure with fairly high surface area.

Figure 3.6: Cross section of metal-supported cell

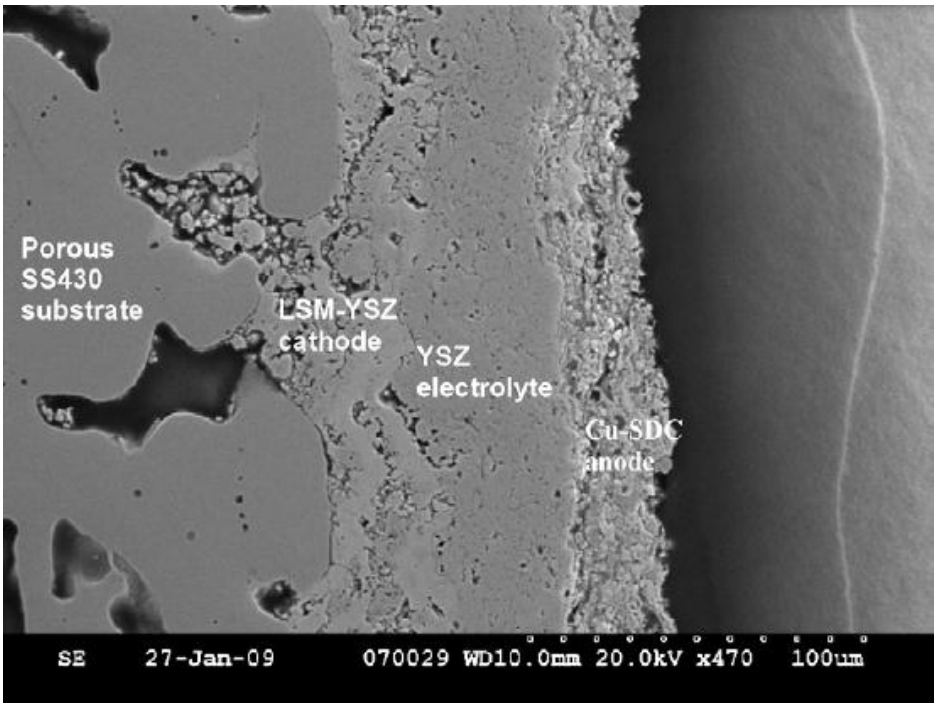

An EDX map of Cu and Ce in the anode is shown in Figure 3.7a and Figure 3.7b, respectively. From the maps, it can clearly be seen that the Cu and SDC phases are well mixed.

Figure 3.7: EDX map of (a) Cu and (b) Ce in a Cu-SDC anode functional layer in a metal-supported cell

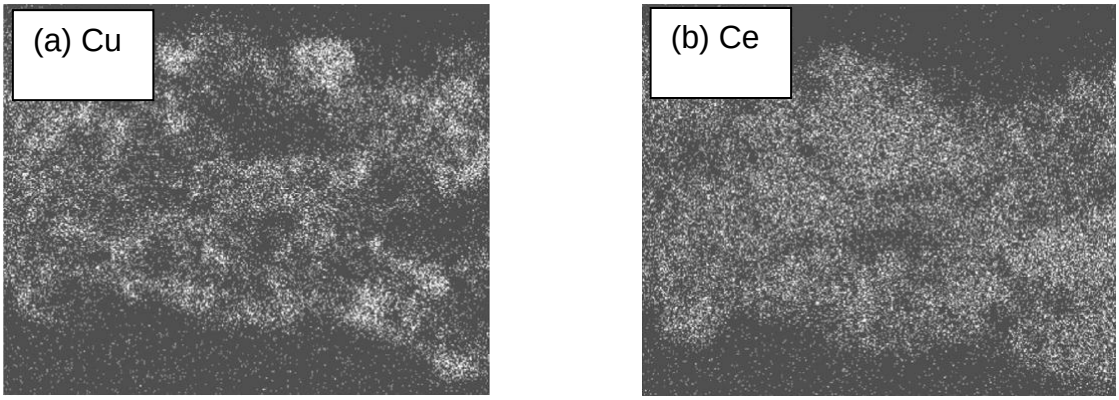

EDX measurements determined that the volume fraction of Cu in the coatings after reduction was 35 vol%. EDX of the cell after testing in methane revealed no carbon residue on the anode surface.

3.2.2 Electrochemical performance

3.2.2.1 Symmetrical cell electrochemical performance

Figure 3.8 shows the impedance spectra of the symmetrical cell at 723°C and 772°C. Each impedance spectrum shown was obtained after 30 min of dwelling at the specific temperature. Impedance values are normalized to electrode area. The high frequency x-intercept in the impedance plots is the ohmic losses of the cell layers, i.e. two anodes and electrolyte, and the ohmic losses due to contact resistance between the cell and the test station's current collecting Pt meshes. The diameter of the semi-circular arc in the impedance plots is the polarization resistance, i.e., the impedance interfering with electrochemical and mass transport processes in the anode.

The area-specific polarization resistance (ASR_p) for each anode is shown in Table 3.5 for all temperatures tested, assuming that each anode in the symmetrical cell has the same polarization resistance. The ASR_p is higher than in Cu-based cells manufactured by wet ceramic processing. The reader can refer to Table 1.4 for polarization resistance values of wet ceramic processed Cu-based anodes. The fairly high area-specific polarization resistance is at least in part due to the extremely low catalytic activity of the Cu in the anode layer, and partly due to the need for further microstructural refinement.

Figure 3.8: Impedance spectra of a symmetrical cell at OCV

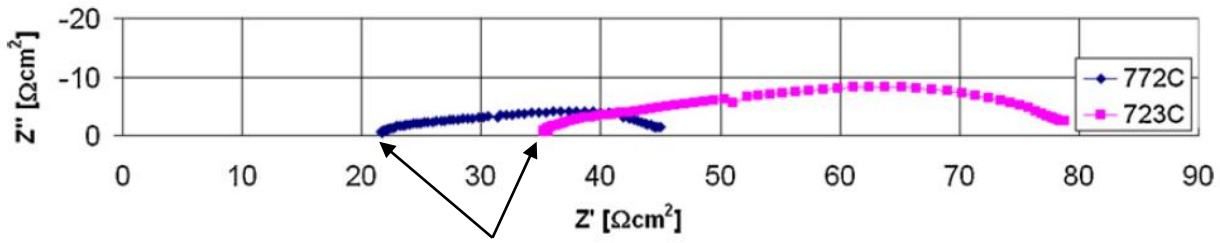

High frequency X-intercepts

Table 3.5: Area-specific polarization resistances of a symmetrical electrolyte-supported cell

ASR_p (Ωcm^2) at OCV	
T[°C]	***Anode***
772	12.4
723	21.8
672	38.5
620	67.4

3.2.2.2 Metal-supported cell electrochemical performance

Polarization curves of the metal-supported cell at temperatures from 600°C to 700°C are shown in Figure 3.9. The power densities are lower in comparison to wet ceramic processed cells reported elsewhere ([66], [86] and [95]). The open circuit voltage, i.e. the Y-intercept of the polarization curves, was 862.5mV at 700°C, which is lower than the Nernst voltage (980mV at 700°C, 20% H_2 and 20.95% O_2). This can be attributed to leaks either through the electrolyte or seal, reducing the fuel and oxidant concentrations at the anode and cathode, respectively.

Figure 3.9: Polarization curves of a metal-supported cell

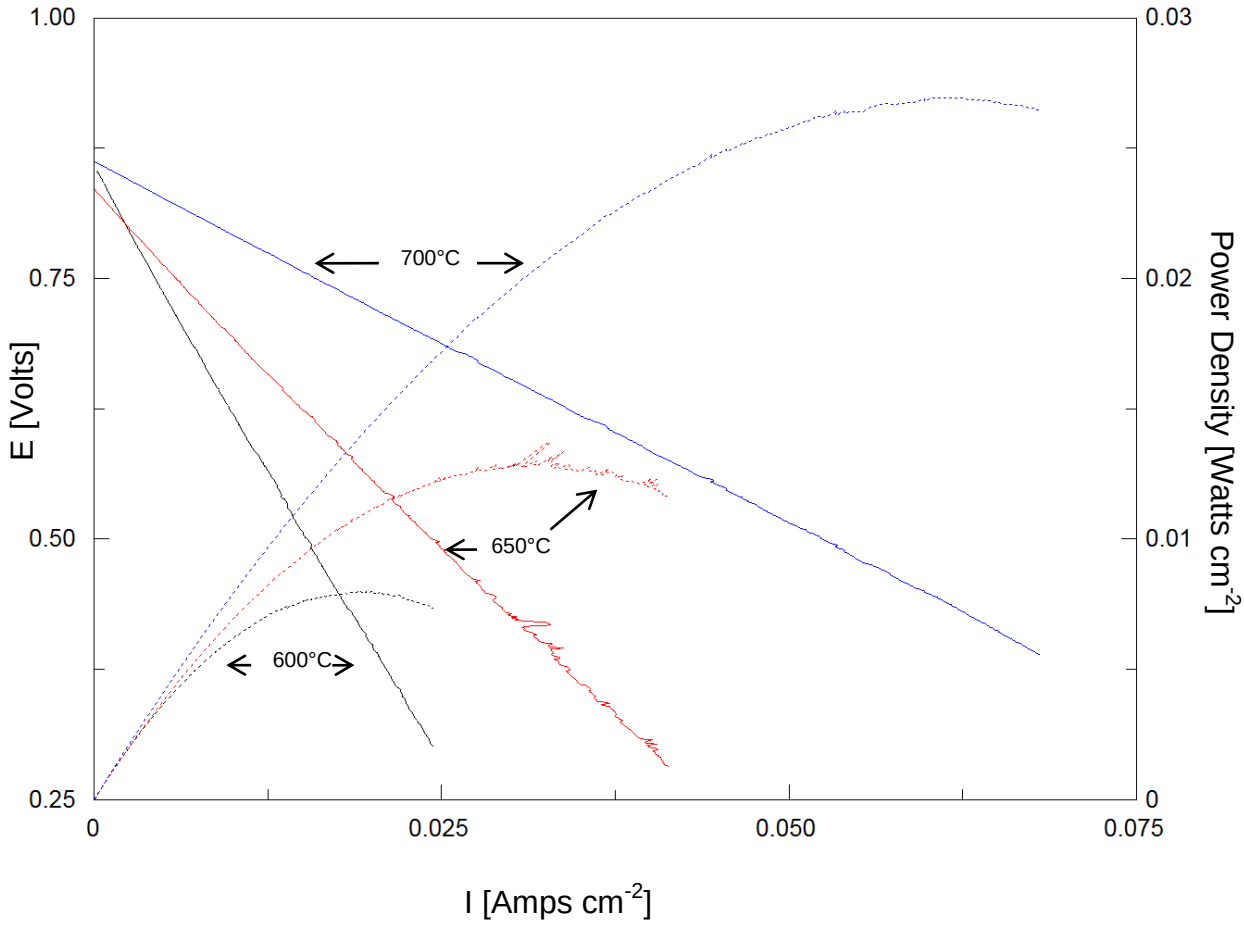

Impedance spectra were conducted in potentiostatic mode rather than galvanostatic mode due to the low current produced by the cell to minimize error due to non-linear effects.

Nyquist impedance plots at cell polarizations of 0.7V (a) and OCV (b) can be seen in Figure 3.10. Three overlapping arcs can be detected, for example, in the Nyquist plot at OCV and 650°C. This can be attributed to processes having 3 different relaxation times. However, in metal-supported cells with thin electrolytes, it is not possible to separate the individual contributions to the overall polarization resistance of the anode and of the cathode directly from the plots. Both polarization resistances and

ohmic resistances were higher than values of wet ceramic processed anodes reported in the literature [66].

Figure 3.10 Nyquist plots at cell polarizations of (a) 0.7V and (b) OCV at various temperatures.

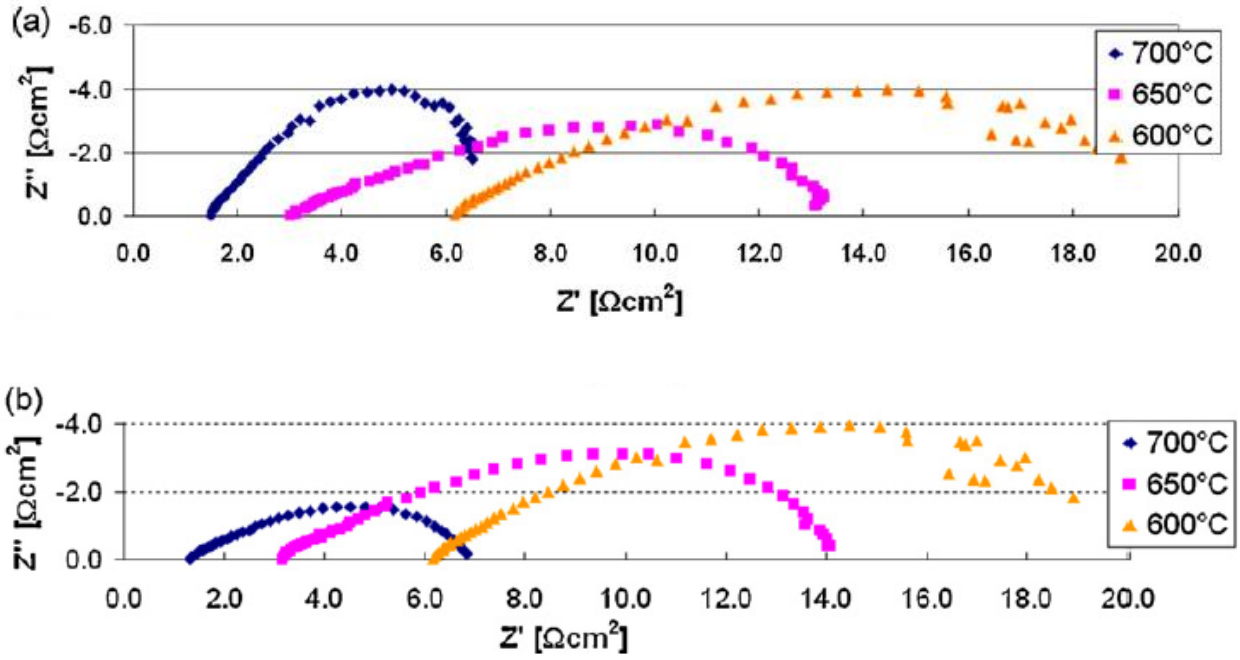

Table 3.6 shows the polarization resistances obtained by EIS testing of the metal-supported cell and the corresponding cathodic polarization resistance [113], anodic polarization resistance from electrolyte-supported symmetrical cells, and anodic polarization resistance calculated for the anodes in the metal-supported full cells. The anodic polarization resistance was higher than that of wet ceramic processed anodes reported in the literature [78].

Table 3.6: Area-specific polarization resistances of the metal-supported cells

ASR_p (Ωcm^2) at OCV			
T(°C)	**Full cell**	**Cathode**	**Calculated Anode**
712	5.51	0.73	4.78
660	10.9	1.34	9.55
610	15.9	2.55	13.4
560	27.6	5.26	22.3

Corresponding Arrhenius plots of the cell polarization resistances determined from the EIS testing of the metal-supported cell at OCV are shown in Figure 3.11, along with results from cathode–cathode symmetrical cell testing reported in the literature using the same cathode processing parameters [113]. Arrhenius plots of the anode–anode symmetrical cell testing results are also shown in Figure 3.11, along with calculated values of ASRp from the metal supported cell tests, calculated from the full cell impedance values at OCV and the symmetrical cell cathode ASRp values. Activation energies for the four configurations were found to be 0.90eV for the anode–anode symmetrical cell, 0.91eV for the cathode–cathode symmetrical cell, 0.69eV for the calculated anode ASRp in a metal supported cell, and 0.72 eV for the metal-supported full cell. Other works have reported similar values of the activation energy, such as Risø thin electrolyte Ni-YSZ anode supported cells, with activation energies of 0.6eV-0.8eV [122].

An Arrhenius plot of the metal supported cell ohmic resistance is also shown in Figure 3.11. The activation energy of the ohmic resistance of the metal-supported cell was found to be 1.0eV. This value is similar to values reported in the literature for plasma sprayed electrolytes [123].

Figure 3.11: Arrhenuis plots of the metal-supported cell, metal-supported cathode–cathode symmetrical cell [113], and electrolyte-supported anode–anode symmetrical cell. ASR given in units of Ωcm^2.

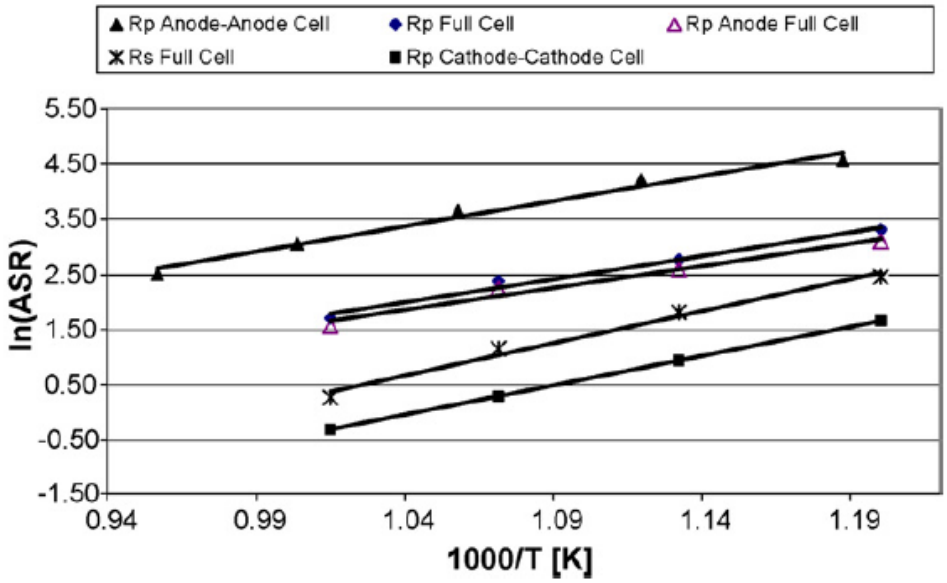

3.3 Conclusions

Cu-SDC anode coatings have been fabricated and tested in electrolyte-supported symmetrical cell and full metal-supported cell configurations. CuO and SDC powders were sprayed simultaneously onto YSZ electrolyte supports or electrolyte coatings on metal-supported cathodes and subsequently reduced in hydrogen to produce Cu-SDC anode layers on test substrates, electrolyte supported symmetrical cells, and metal-supported full cells. Using fine powder feedstock, well-mixed coatings with 35-40 vol. % Cu were fabricated, and a calculated anode polarization resistance of 4.78 Ωcm^2 was obtained with the Cu-SDC anodes at 712^{o}C in metal-supported cell tests.

4. Plasma sprayed Cu-Co-GDC anode coatings with various Co loadings

This chapter deals with the development of Cu-Co-GDC coatings produced of CuO, Co_3O_4 and GDC feedstock powders. Screening tests were conducted to identify the effect of plasma gas composition on the coating phase structure, microstructure, and absolute deposition efficiency of each material. Then, using the absolute deposition efficiency, feedstock mixing ratios were determined to produce anode coatings with Cu-Co weight ratios of Cu(100)Co(0), Cu(90)Co(10), Cu(70)Co(30), and Cu(50)Co(50). These coatings were reduced with a 50 % N_2 / 50% H_2 gas mixture at 700°C. After reduction, coating porosity and gas permeability were evaluated. Finally, carbon deposition behavior was examined by measuring weight gain of the coating after exposure to CH_4 at 700°C for 3hrs.

4.1 Experimental procedure

4.1.1 Material preparation

In this work, commercially available feedstock powders of CuO, Co_3O_4 and GDC ($Ce_{0.8}Gd_{0.2}O_{1.9}$, Inframat Advanced Materials, Farmington, CT, USA) were used to produce the coatings. These powders are spherical spray dried agglomerates of micron-sized powder.

In order to prevent the breakup of the spray dried agglomerates during feeding, the CuO and GDC as-received powders were heated to various temperatures utilizing the profiles shown in Table 4.1. The calcined powders were then sieved into narrower size fractions, with the sieved powder in the size range of -45μm + 32 μm being used for

the spraying experiments. Table 4.1 shows the particle size distribution, calcining temperature, and calcining time of the calcined powders.

Table 4.1: Particle size distribution and calcining temperature and time of calcined powders

Powder	Particle Size [µm]			Calcining Temperature [°C]	Calcining Time [h]
	$D_{0.1}$	$D_{0.5}$	$D_{0.9}$		
CuO	14.5	34.5	61.6	850	5
Co_3O_4[1]	17.1	38.4	70.2	1100	5
GDC	23.3	36.7	58.0	1350	5

[1] Co_3O_4 decomposes to CoO when heated above 950°C

4.1.2 Plasma Spray Processing

Air plasma spraying of CuO-CoO-GDC coatings was implemented using the set-up shown in Chapter 2. In order to allow good adhesion of the plasma sprayed coatings, substrates were pre-heated to 300°C by the torch prior to deposition. Substrate temperature was monitored during the spraying process to ensure that it did not exceed 500°C.

Preliminary screening tests were carried out with CuO, CoO and GDC powders. The plasma gas composition was changed for each of the coatings. Deposition was carried out onto commercially available 2.54 cm diameter porous SS430 disk substrates (Mott Corporation, Farmington, CT, USA) with a thickness of approximately 1mm. Table 4.2 shows experimental plasma spray process parameters used for all coatings. Table 4.3 shows experimental plasma spray process parameters varied for each coating.

Following the identification of usable plasma and feedstock parameters, CuO-CoO–GDC coatings were deposited onto commercially available 2.54cm diameter

1.6mm thick Cu disk substrates for carbon deposition tests, and on the SS430 porous substrates (media grade 2, Mott Corporation, Farmington, Connecticut, U.S.A.) for gas permeability measurements. Initial powder weight ratios were determined for each of the coatings to obtain coatings with Co weight fraction in the Cu-Co phases of 0, 0.1, 0.3 and 0.5 and a volume fraction of 40% of the metallic phases in the coating among the solid phases. The coatings were reduced after deposition in a N_2–H_2 mixture (50% H_2) at 700°C for 6 h.

Table 4.2: Experimental plasma spray process parameters used for all coatings

Parameter	Value
Carrier gas flow rate (slpm)	15
Spraying distance (mm)	100
Vertical traverse speed (ms^{-1})	4.25
Torch current (A)	690
Plasma gas flow rate (slpm)	250
Nozzle diameter (mm)	12.7
CuO, CoO and GDC particle sieve fraction size (μm)	-45μm +32μm

Table 4.3: Experimental plasma spray process parameters used for each of the coatings

Parameter	Value				
	Screening Tests	Run#1	Run#2	Run#3	Run#4
Powder feed rate (g min^{-1})	31.5	36.1	24.1	20.9	25.5
Powder Feed Time (sec)	38.0	99.8	70.0	100	100
Vol.% nitrogen (balance Ar)	20, 40, 60 and 80	40	40	40	40
Torch Power [kW]	70.3, 84.6, 104.2 and 117.5	84.6	84.6	84.6	84.6
Plasma Power [kW]	61.1, 72.2, 88.7 and 99.6	72.2	72.2	72.2	72.2
Torch Efficiency [%]	86.9%, 85.3%, 85.1% and 84.7%	85.3%	85.3%	85.3%	85.3%

Parameter	Value				
	Screening Tests	Run#1	Run#2	Run#3	Run#4
Powder weight	33.3 wt% GDC 33.3 wt% CuO 33.3 wt% CoO	45.5 wt% GDC 54.5 wt% CuO	54.6 wt% GDC 40.4 wt% CuO 4.90 wt% CoO	54.9 wt% GDC 28.6 wt% CuO 16.5 wt% CoO	53.8 wt% GDC 21.0 wt% CuO 25.3 wt% CoO

4.1.3 Coating characterization

4.1.3.1 Phase and elemental composition

X-ray diffraction (XRD) analysis of the coatings was performed both before and after reduction to determine the phase structure dependence on spraying and feedstock parameters. When peak shift magnitude had to be identified with high accuracy to avoid errors resulting from tilting or misalignments of the sample, Al_2O_3 powder was put on the coatings and used for calibration of the x-ray detector position. Energy dispersive spectroscopy (EDX) was performed to determine the volume fraction of Cu and Co present in the coatings and the weight ratios of the Cu and the Co.

4.1.3.2 Porosity evaluation

Porosity of the coatings was characterized by two methods – image analysis and permeation testing. For the image analysis, coatings were mounted in epoxy resin, sectioned and polished. To minimize pull-outs that introduce errors to the calculated porosity, coatings were examined by optical microscopy between each polishing step. Polished cross-section images of each coating were taken by SEM. Ten images were taken for each coating, at 0.50 mm intervals along the length of the coating. The images were taken at 3000x magnification, with corresponding analysis areas of 42.7 x 32.0 μm^2. To clearly distinguish between solid and pore when image analysis software is

utilized, image brightness was reduced and contrast increased to create SEM images predominated by black and white with minimal areas of grey. Grey areas were predominantly present within the boundaries between solid and pores as the white color characterizing the solids transitioned to the black color characterizing the pores. Image analysis was performed utilizing ImageJ software (National Institutes of Health, USA). To minimize error, an image analysis procedure was developed that included determination of the range of possible porosities and a best estimate value of porosity. The lower bound of porosity was determined by setting a grey scale threshold such that no solid phases that can be identified visually in the coating are included within the porosity estimate. The upper bound on porosity was determined by setting a grey scale threshold such that all pores that can be identified visually are included within the porosity estimate. A best estimate porosity value was determined by setting a grey scale threshold such that it corresponds well with the extent of the pore phase that can be visually identified.

Helium permeation measurements were performed using an in-house designed jig in order to measure the gas permeability of the deposited layers. The supply of helium gas was regulated by a pressure controller (Alicat Scientific,model PCD-5PSIG-D, Tucson, AZ, USA). The flow through the sample was then measured at the outlet of the jig by a mass flow meter (Alicat Scientific, model MC-500SCCM-D/5M 5IN N_2, Tucson, AZ, USA). To determine the thickness required for the permeability coefficient calculations, fifteen SEM images were taken at equal intervals of 0.5mm along the coating cross-section length and 15 thickness measurements were taken at equally

spaced intervals across the coating in each of the images, and then averaged. Figure 4.1 schematically depicts the gas permeability measurement setup.

Figure 4.1: Gas permeability measurement setup

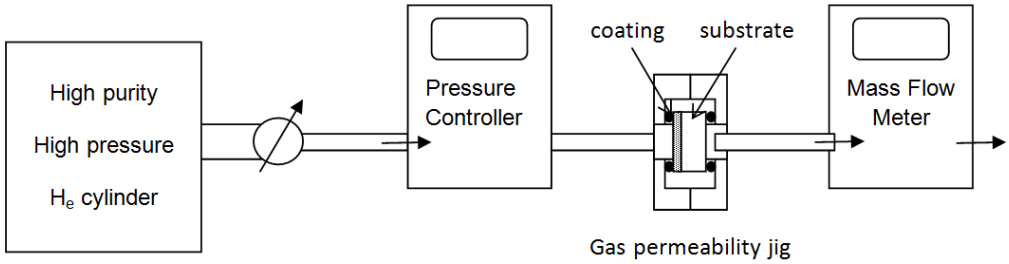

4.1.4 Carbon deposition

Carbon deposition was analyzed by measuring the weight gain of CuO-GDC and CuO-CoO-GDC coatings plasma sprayed onto 2.54mm diameter Cu disks and exposed to 100% CH_4 at 700°C. First, the coatings were reduced and the reduced coating weight was measured. Then, the coatings were heated in a 80% N_2 / 20% H_2 mixture at a rate of 1°C min^{-1} to 700°C and then exposed to dry 100% CH_4 for 3 hrs. After exposure to CH_4, the gas mixture was changed to a reducing mixture of 99.5% N_2 / 0.5% H_2 and the coatings were cooled at a rate of 1°C min^{-1} to room temperature. SEM analysis of the coatings was performed to detect carbon residue.

4.2 Results

4.2.1 Powder morphology

Figure 4.2 shows a high magnification scanning electron microscopy (SEM) image of an as-received CuO agglomerate of micron-sized particles. It can be seen that the primary particle size is on the order of 1µm.

Figure 4.2: Scanning electron microscopy micrograph of as-received CuO agglomerate

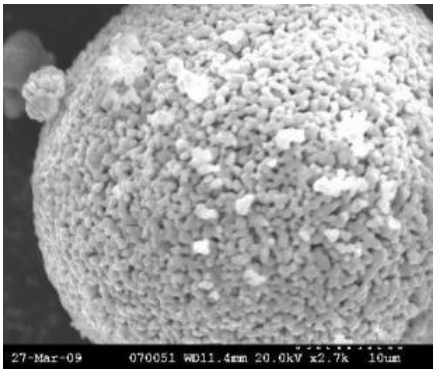

To determine the effect of the calcining step on the agglomerated powder, the calcined powder was examined by SEM. Figure 4.3 shows SEM micrographs of the spray dried powder agglomerates after the calcining step. The micron-sized particles are coarser relative to the non-calcined agglomerates. The primary particle size of the CuO and CoO increased from approximately 1µm to approximately 3µm for CuO, and fto 5-10 µm for CoO. The primary particle size of GDC remained on the order of 1µm.

Figure 4.3: SEM images of calcined (a) CuO (b) CoO and (c) GDC spray dried powders

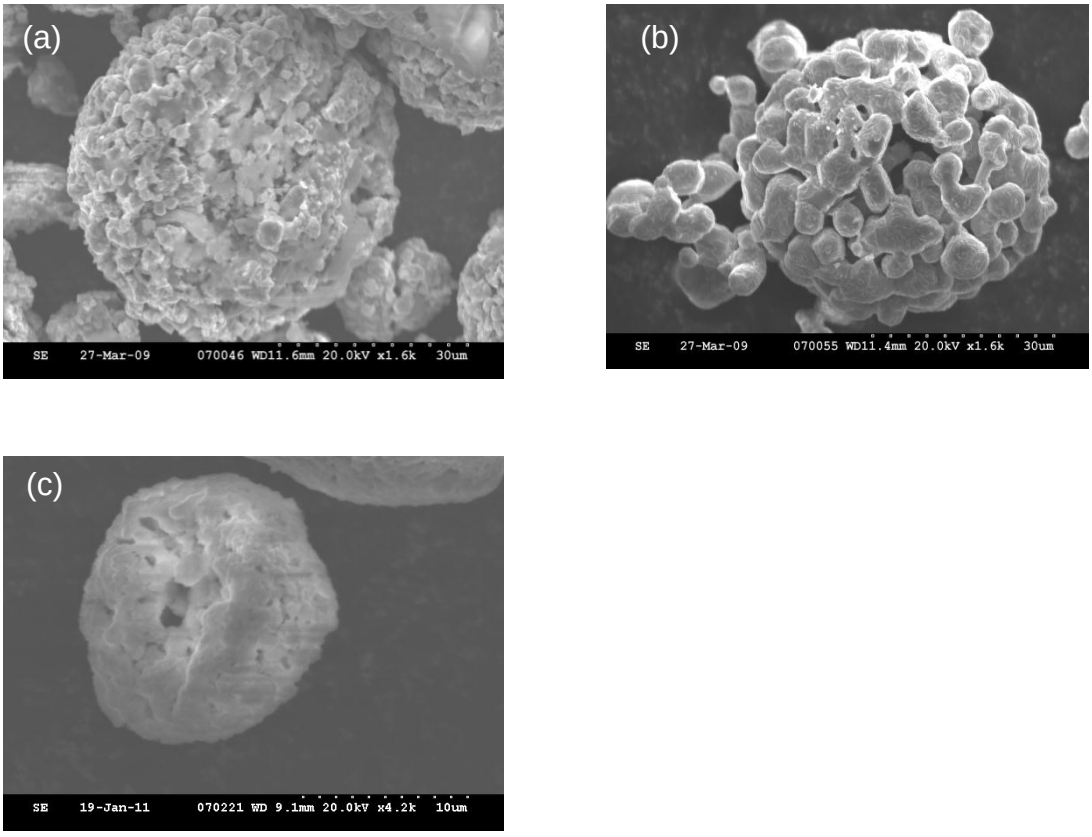

4.2.2 Microstructural analysis

4.2.2.1 Microstructural analysis of screening test coatings

Figure 4.4 shows XRD patterns of coatings produced from CuO-CoO-GDC feedstock powders. The crystal structure of the GDC coatings was cubic fluorite over the entire range of spraying conditions. This result is similar to results obtained with SDC powder. Partial reduction of CuO to Cu_2O cannot be detected in the pattern because the Cu_2O and CoO peaks overlap.

Figure 4.4: XRD of CuO-CoO-GDC coatings produced with N_2 content of (a) 20% (b) 40% (c) 60% and (d) 80%

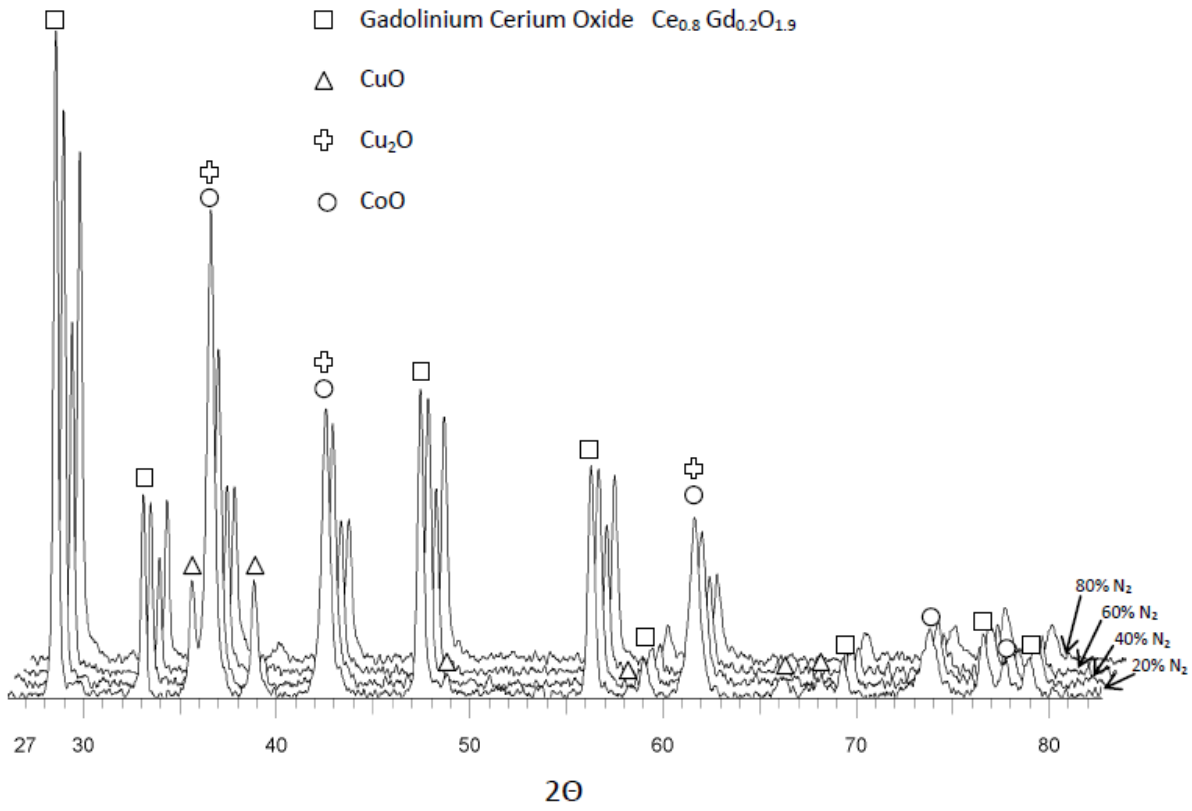

The main difficulty in co-depositing CuO, CoO and GDC composite coatings by APS is achieving sufficient porosity. The melting temperatures of these materials are 1227°C for CuO [109], 1830°C for CoO[110] and 2480°C for ceria [111]. The large difference between the melting temperature of CuO and GDC makes it difficult to co-deposit these materials with sufficient porosity for optimized anode performance. With the CuO-SDC coatings presented in Chapters 2 and 3, it was demonstrated that the CuO is highly melted for a wide range of APS parameters tested, even with low energy plasmas. Therefore, the strategy applied here to obtain sufficiently porous coatings is to

identify APS parameters that will lead to partial melting of the GDC. Partial melting of the agglomerated micron-sized GDC particles allows increased porosity, and in addition, allows the GDC to keep its finely structured morphology to some extent, which increases the anode surface area and improves its performance [33]. This is especially important due to the dual role of GDC in Cu-GDC anodes, in which the Cu only plays a role as an electronic conductor, while the GDC functions as the catalyst towards oxidation of H_2 and CH_4 as well as a mixed ionic-electronic conductor. An additional challenge in co-depositing CuO-CoO-GDC coatings is achieving the desired relative solid volume of metallic phases of 40% in the coating to allow full percolation of the metallic phases and thus to obtain sufficient electronic conductivity of the anode. Finally, spraying parameters must allow the CuO and CoO to be sufficiently melted to allow fine-scale mixing and possible covering of the Co by Cu after the CuO and CoO have been reduced.

Plasma spraying is a manufacturing process in which the feedstock powder is injected into the plasma jet, where powder particles absorb thermal and kinetic energy from the plasma jet and are then deposited onto a substrate in a fully or partially molten state to form a coating. Plasma jet temperature and velocity affect how well the powder is deposited. These conditions vary according to the physical properties of the plasma sprayed material, such as its melting temperature and heat capacity. Insufficiently melted plasma sprayed particles will bounce off the substrate upon impact, thus resulting in a lower absolute deposition efficiency. In the case of high energy plasmas, particles may evaporate or volatize, thus resulting in lower absolute deposition efficiency. Due to the difference between the melting temperatures, densities, and heat

capacities of the CuO, CoO and GDC materials, each of these materials will have specific deposition efficiency for given set of spraying parameters.

Eq. 4.1 shows the molar mass of GDC. The powder used in this study was $Ce_{0.8}Gd_{0.2}O_{1.9}$

$$M_{GDC(Ce_{0.8}Gd_{0.2}O_{1.9})} = 0.8M_{Ce} + 0.2M_{Gd} + 1.9M_{O} \tag{4.1}$$

Eq. 4.2 to Eq. 4.4 show the relative weights of CuO, CoO and GDC, respectively. Here, Ce(mol%), Cu(mol%) and Co(mol%) are the respective molar fractions of Ce, Cu and Co obtained by EDX. M_{CuO}, M_{CoO}, and $M_{GDC}$are the respective molar masses of CuO, CoO and GDC.

$$W_{CuO}(wt\%) = \frac{Cu\ (mol\%)M_{CuO}}{Ce\,(mol\%)\frac{1}{0.8}M_{GDC} + Cu\,(mol\%)\ M_{CuO} + Co(mol\%)M_{CoO}} \tag{4.2}$$

$$W_{CoO}(wt\%) = \frac{Co\ (mol\%)M_{CoO}}{Ce\,(mol\%)\frac{1}{0.8}M_{GDC} + Cu\,(mol\%)\ M_{CuO} + Co(mol\%)M_{CoO}} \tag{4.3}$$

$$W_{GDC}(wt\%) = \frac{Ce\ (mol\%)\frac{1}{0.8}M_{GDC}}{Ce\,(mol\%)\frac{1}{0.8}M_{GDC} + Cu\,(mol\%)\ M_{CuO} + Co(mol\%)M_{CoO}} \tag{4.4}$$

The absolute deposition efficiency is calculated for each material as the weight ratio between the powder deposited onto the substrate per unit area of the substrate times the area over which powder is delivered to the drum and the powder fed to the plasma torch, as seen in Eq (4.5).

$$Absolute\ D.E = \frac{\Delta W_{substrate} A_{drum}}{W_{powder} A_{substrate}} X_i \quad (4.5)$$

where $\Delta W_{substrate}$ is the substrate weight gain, W_{powder} is the weight of the fed powder, A_{drum} is the total sprayed area, $A_{substrate}$ is the substrate area and X_i is the weight percent of a material in the coating. X_i is determined using Eq. 4.2 to 4.4.

Using the deposition efficiencies of the materials, the initial powder ratios can be adjusted to control the composition of the APS coating and thus to obtain the desired metallic volume fraction of 40 vol% and also to obtain the desired weight ratios of the Cu and Co in the coatings.

Figure 4.5 shows the plasma power versus the N_2 content in the plasma gas. It can be seen that the plasma power increases with increasing N_2 content in the plasma gas. Previous studies showed that augmenting the N_2 content in the N_2-Ar plasma gas will increase the arc voltage and heat transfer ability of the plasma jet and consequently, the plasma power ([50]).

Figure 4.5: Effect of the N_2 content in the plasma on the plasma power

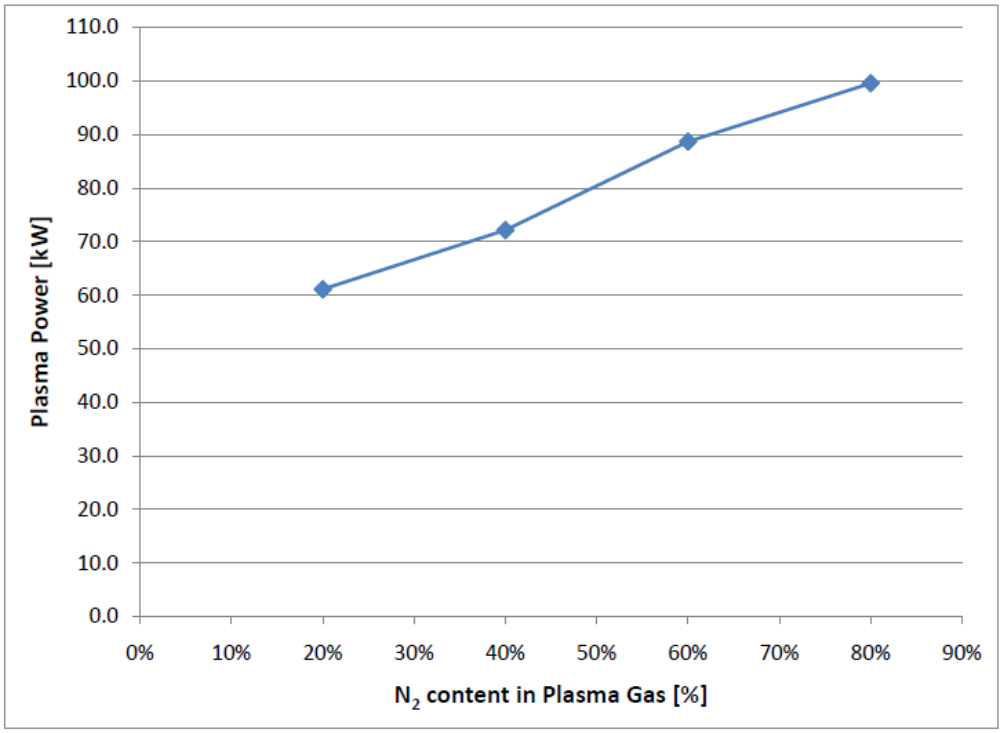

Figure 4.6 shows the absolute deposition efficiencies of the GDC, CuO, and CoO as a function of the N_2 content in the plasma gas. In plasma spray processing, lower deposition efficiencies can result from high vaporization rates of the deposited materials or from material rebound, which occurs when the particles have only partially melted or have re-solidified prior to impact. It can be observed that the deposition efficiency of the CuO decreases with the increase of N_2 content in the plasma gas throughout the entire range of plasma gas composition examined. This decrease can be attributed to partial evaporation of the CuO during flight. The deposition efficiencies of the CoO and the GDC increase sharply when the N_2 content in the plasma is changed from 20% to 40%, and then more gradually when the N_2 content in the plasma is changed from 40% to 60%. This can be attributed to a higher degree of melting of these materials with the

increase of plasma energy. When the N_2 content is changed from 60% to 80%, a decrease of the deposition efficiencies of the CoO and the GDC is observed. This might be attributable to increased plasma velocity, resulting in decreased residence time of the particles in the plasma, or to higher evaporation rates of these materials due to the higher plasma energy with 80% N_2.

Figure 4.6: Absolute deposition efficiencies of CuO, CoO and GDC plasma sprayed with different plasma gas compositions

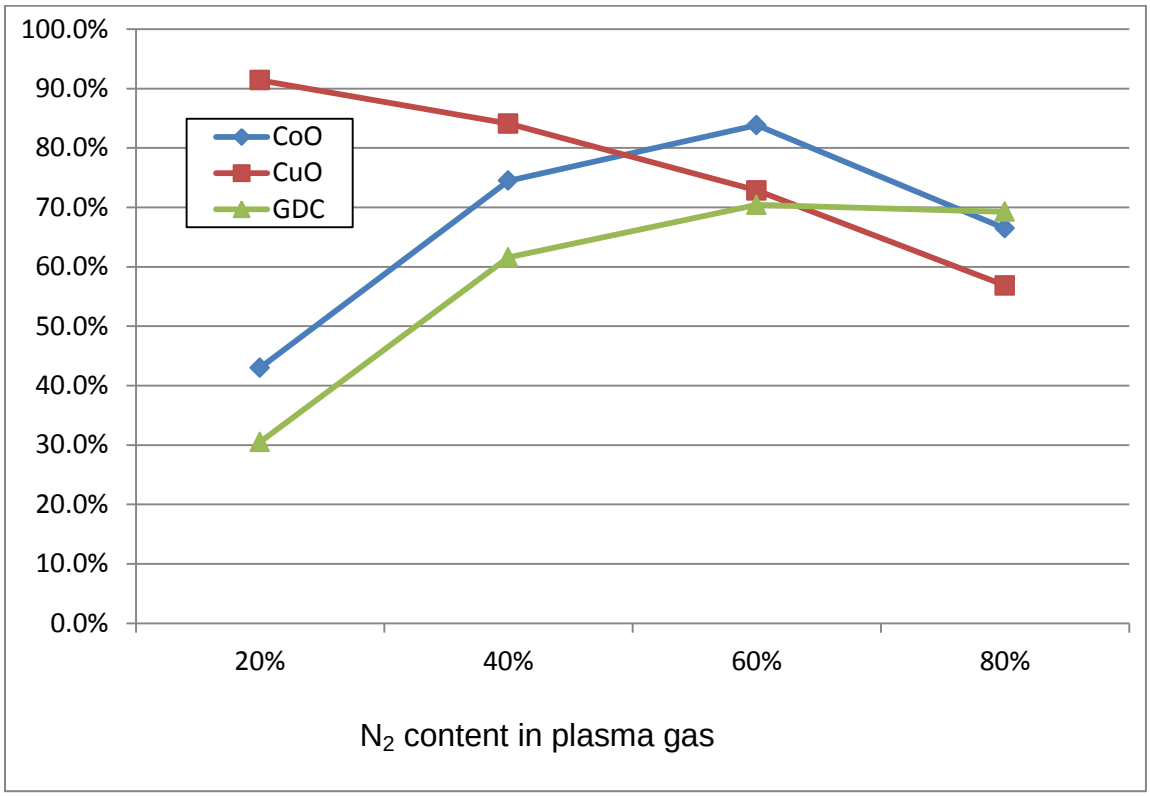

Figure 4.7 shows surface SEM micrographs of coatings produced with 40% N_2 and 80% N_2. The coating produced with 40% N_2 is homogenous and the fine structure of the GDC particles is preserved. The coating produced with 80% N_2 is less

homogenous, and cauliflower-like clumps are evident, surrounded by highly melted splats. The surface clumps were on the order of the size of the starting agglomerate of micron-sized particles. This observation suggests that the surface clumps may have been caused by unmelted or partially melted agglomerates of micron-sized GDC. Such non-homogenous coatings could potentially be attributed to the affect of a higher particle velocity upon impact with the substrate, and the corresponding shorter residence time available for complete melting of the particles. Other studies have demonstrated that the velocity of Ar-H_2 plasmas increases with an increase of H_2 content [51]. In addition, the absolute deposition efficiency of GDC decreases with an increase of N_2 content in the plasma from 60% to 80%. This result occurs despite the increase of plasma power. Therefore, this decrease may be attributable to a lower residence time of the particles in the plasma, due to a higher velocity. An increased impact kinetic energy results in thinner splats of the low melting temperature material, i.e, CuO, and unmelted particles of the higher melting temperature material, i.e, GDC, potentially explaining the less-homogenous coatings produced at higher plasma powers.

Figure 4.7: APS coatings produced with (a) 40% N_2 and (b) 80% N_2

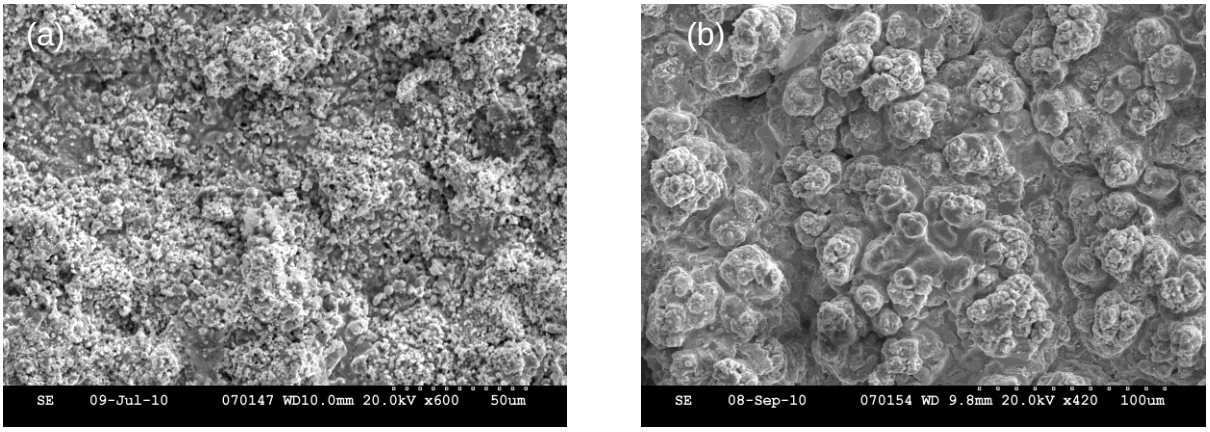

Figure 4.8 shows the relative deposition efficiencies of CuO:CoO, CuO:GDC, and CoO:GDC. The relative deposition efficiency is calculated for each pair of materials as the ratio between the absolute deposition efficiency of the lower melting temperature material to the absolute deposition efficiency of the higher melting temperature material. The relative deposition efficiencies decrease for each pair of materials with the increase of N_2 content in the plasma throughout the entire range of N_2 content. This indicates that the effect of material loss due to evaporation increases as plasma power increases, while material loss due to bouncing off the substrate of partially melted particles caused by insufficient melting is more dominant at low plasma powers.

Figure 4.8: Relative deposition efficiencies of CuO, CoO and GDC plasma sprayed with different plasma gas compositions

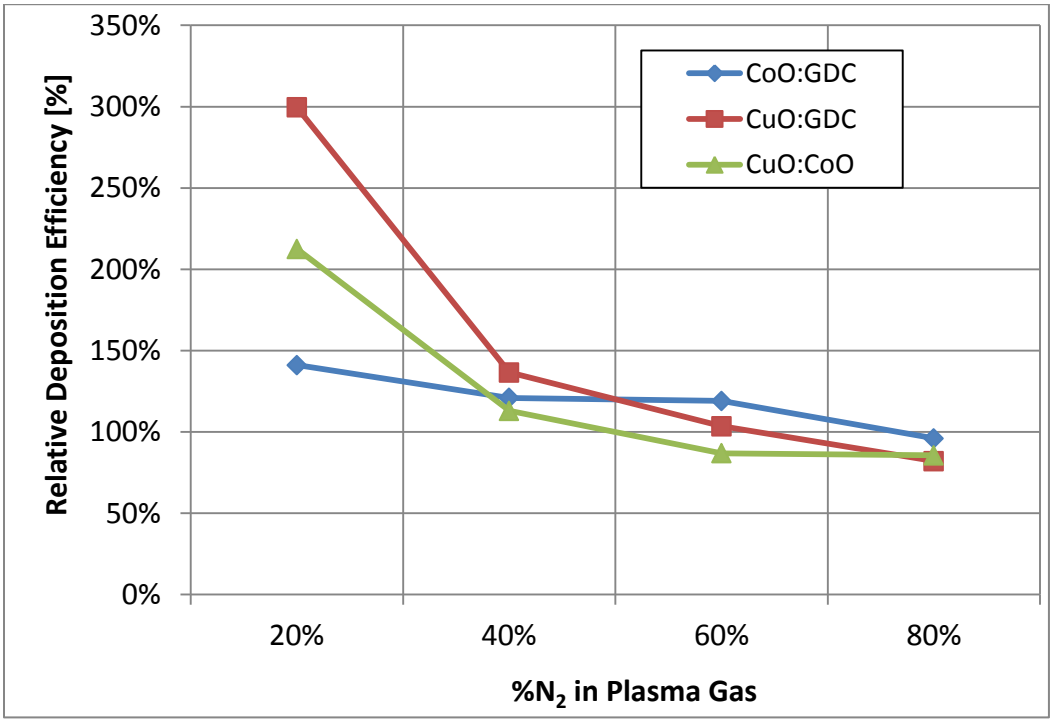

4.2.2.2 Microstructural analysis of Cu-Co-GDC coatings

Based on the absolute deposition efficiency of GDC and SEM micrographs obtained during the screening tests, a plasma gas composition of 40% N_2 / 60% Ar was used for subsequent coating deposition to allow sufficient melting of the CuO and CoO so that they can mix together to obtain resistance to carbon deposition, as suggested by wet-ceramic processed anode results reported elsewhere [25]. In addition, this plasma gas composition was chosen to allow deposition of partially-melted GDC particles with an absolute deposition efficiency of 64%. Due to the high cost of GDC, it is desirable to utilize plasma spray conditions that maximize the deposition efficiency of GDC subject to other constraints, such as the need to introduce adequate porosity. Moreover, the

screening experiments demonstrated that a lower N_2 content in the plasma resulted in homogenous coatings, while a higher N_2 content in the plasma resulted in non-homogeneous coatings. Using the absolute deposition efficiency, feedstock powder ratios were determined with the goal of producing CuO-CoO-GDC coatings with Co content of 0%, 10%, 30% and 50% by weight in the Cu-Co phases. The coatings were produced utilizing the spraying conditions shown in Tables 4.2 and 4.3.

Eq. 4.7 to Eq. 4.9 show the target weight ratios between the CuO:CoO, CuO:GDC, and CoO:GDC in the coatings using the molar masses, the desired volume fraction of metallic phases in the coatings and the desired weight ratio of the Cu and the Co. Here, W_{CuO}, W_{CoO} and W_{GDC} are the respective weights CuO, CoO and GDC in the coating, M_{CuO}, M_{CoO}, and M_{GDC} are the respective molar masses of CuO, CoO and GDCM_{Cu}, M_{Co} are the respective molar masses of Cu and Co, ρ_{Cu}, ρ_{Co} and ρ_{GDC} are the respective densities of Cu, Co and GDC, V is the desired volume fraction of metallic phases in the coating, and r is the relative weight of Co in the Cu-Co metallic phases.

$$\frac{W_{CuO}}{W_{CoO}} = \frac{(1-r)M_{CuO}M_{Co}}{rM_{Cu}M_{CoO}} \tag{4.7}$$

$$\frac{W_{CuO}}{W_{GDC}} = \frac{v\varphi_{Co}\varphi_{Cu}M_{CuO}(1-r)}{\varphi_{GDC}M_{Cu}(1-v)(\varphi_{Co}(1-r)+\varphi_{Cu}r)} \tag{4.8}$$

$$\frac{W_{CoO}}{W_{GDC}} = \frac{v\varphi_{Co}\varphi_{Cu}M_{CoO}r}{\varphi_{GDC}M_{Co}(1-v)(\varphi_{Co}(1-r)+\varphi_{Cu}r)} \tag{4.9}$$

These ratios were obtained for Co weight fractions of 0.1, 0.3, and 0.5, and a volume fraction of the metallic phase of 40 vol%. These ratios then were divided by the relative deposition efficiency of each pair of materials to obtain the weight ratio of the

feedstock powders. Table 4.4 shows physical constants of the sprayed materials and their reduced forms. Table 4.5 shows calculated feedstock weight ratios to obtain coatings with 40 vol% of metallic phases among the solid phases and varying Co loadings.

Table 4.4 Physical constants of sprayed materials

Material	Density g cm^{-3}	Molar mass g mol^{-1}	References
CuO	6.31	79.545	[109]
CoO	6.44	74.932	[110]
GDC ($Ce_{0.8}Gd_{0.2}O_{1.9}$)	7.248[13]	173.775[14]	
Cu	8.96	63.546	[115]
Co	8.66	58.933	[125]

Table 4.5: Calculated feedstock weight ratios to obtain coatings with 40 vol% of metallic phases among the solid phases and varying Co loadings

Cu-Co composition	Cu(100)Co(0)	Cu(90)Co(10)	Cu(70)Co(30)	Cu(50)Co(50)
Weight ratio	49.1 wt% GDC / 50.9 wt% CuO/	49.1 wt% GDC / 45.8 wt% CuO/ 5.2 wt% CoO	49.0 wt% GDC / 35.6 wt% CuO/ 15.4 wt% CoO	48.9 wt% GDC / 25.4 wt% CuO/ 25.7 wt% CoO

Energy dispersive spectroscopy (EDX) was performed on the coatings to determine the volume fraction of Cu and Co present in the coatings and the weight ratios of the Cu and Co; the results are shown in Table 4.6. Due to the presence of oxygen in all sprayed materials, EDX was performed to quantify atomically Ce, Cu, and Co. Then, using the physical properties of the materials shown in Table 4.4, the relative

[13] Kondakindi Rajender Reddy, Kunal Karan, , Journal of Electroceramics 15 (2005) 45–56

[14] Calculated

volumes and weights of Cu, Co, and GDC in the coating were determined. The volume fractions and weight ratios are close to the targeted values.

Table 4.6: Relative volume of metallic phases to solid phases in the coatings and relative weight of Co in the Cu-Co phases

Parameter	Run#1	Run#2	Run#3	Run#4
Compositions measured in coatings by EDX among the cations present in the coating (mol%)	74.5 mol% Cu/ 24.1 mol% Ce 5.50 mol% Gd	8.00 mol% Co/ 64.5 mol% Cu/ 21.7 mol% Ce/ 5.80 mol% Gd	18.7 mol% Co/ 48.9 mol% Cu/ 26.3 mol% Ce/ 6.00 mol% Gd	37.9 mol% Co/ 35.5 mol% Cu/ 21.2 mol% Ce/ 5.30 mol% Gd
Volume fraction of metallic phases in coating (vol%)	41.3%	44.4%	37.9%	44.8%
Co content within metallic phases (%wt)	N/A	10.3%	26.2%	49.8%

Figure 4.9 shows cross section SEM micrographs of coatings produced in (a) Run #1, (b) Run #2, (c) Run #3, and (d) Run #4. The non-conductive SDC appears lighter in SEM images, while the conductive Cu and Co appear darker. It can be seen that the anode materials are well mixed and that the GDC particles were partially melted during plasma spraying, thus introducing porosity to the anode. Figure 4.9 (a) shows a Run #1 coating, which is composed of Cu and GDC without Co. It can be seen that the GDC was partially melted, and some of the GDC particles retained their fine-structured morphology. The Cu was partially melted or highly melted, resulting in thin splats. Three types of porosity can be observed: fine pores, resulting from the fine-structured morphology of the SDC particles, oval-shaped pores, resulting from microstructural features of the partially melted sprayed particles and gaps between subsequently sprayed particles, and planar porosity, which is observed near metallic particles and can be attributed to the decrease in volume due to reduction of metal oxide to metal.

Figure 4.9: Cross section SEM micrographs of coatings produced in (a) Run #1 (b) Run #2 (c) Run #3 and (d) Run #4

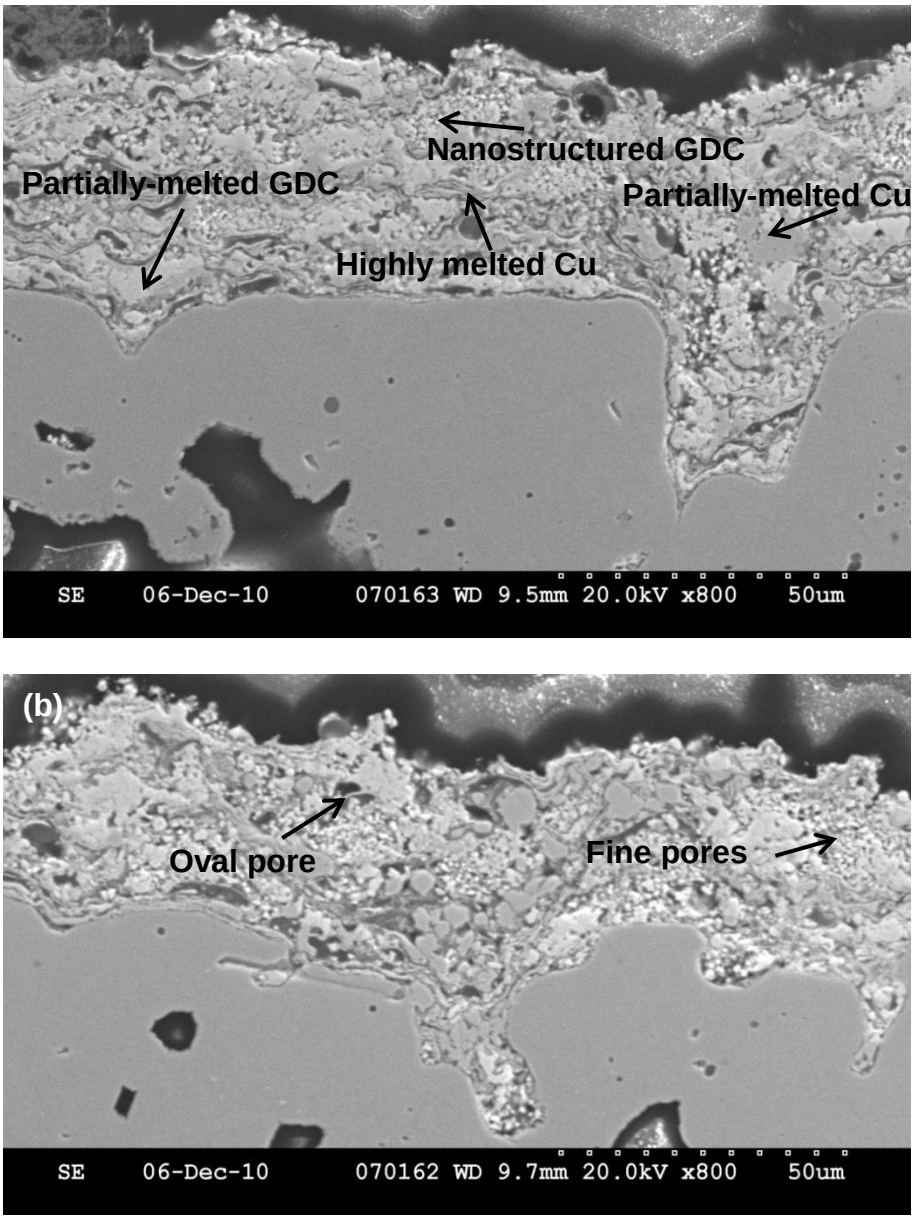

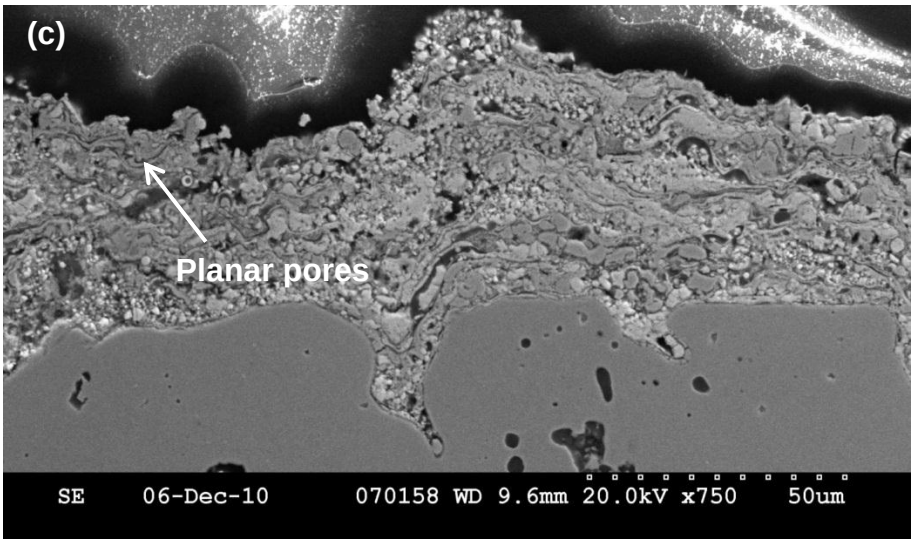

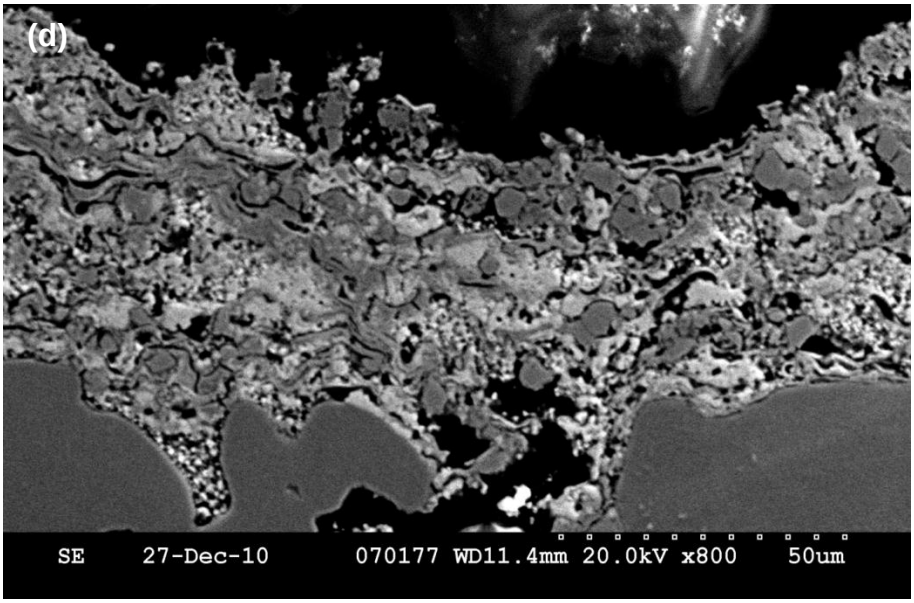

Figure 4.10 shows XRD patterns of as-sprayed CuO-CoO-GDC coatings produced with the spraying parameters in Table 4.2 and 4.3 and of reduced Cu-Co-GDC coatings. XRD patterns of the as-sprayed coatings show that the GDC remained cubic. XRD patterns after reduction demonstrate that the CuO and CoO have been reduced completely to Cu and Co.

Figure 4.10: XRD patterns of coatings produced from CuO-CoO-GDC powders sprayed with 40% N_2 – 60% Ar plasma. *Y*-axis represents X-ray intensity in arbitrary units.

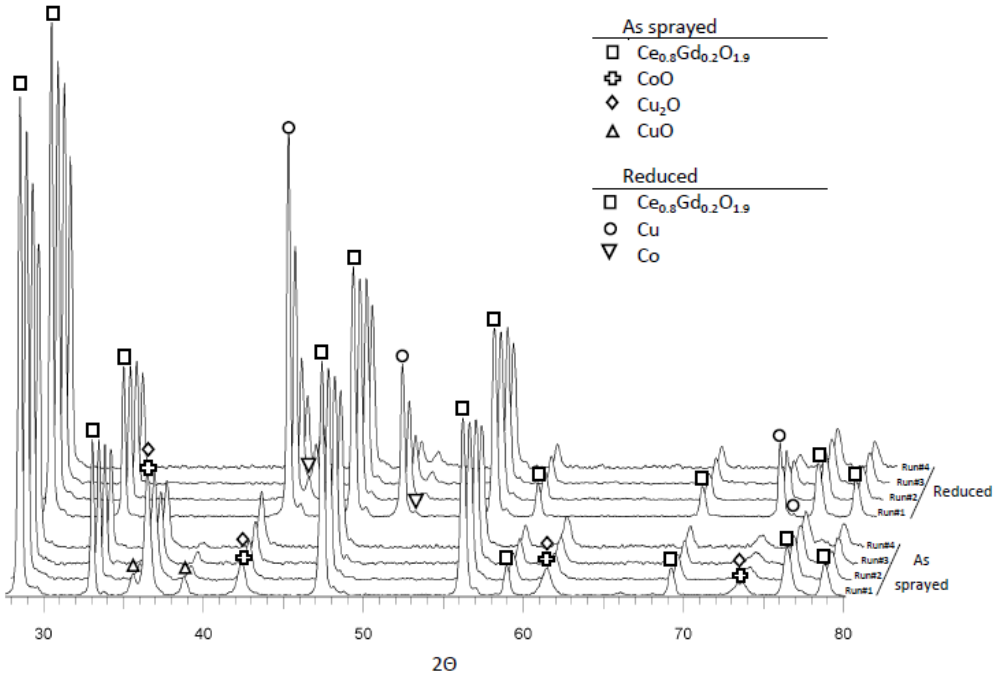

Figure 4.11 shows XRD patterns of Cu-Co coatings from 42° to 45°. From the XRD patterns it is clear that the Cu and the Co peaks are shifted from their theoretical values. Previous studies utilizing wet ceramic processing to produce Cu-Co based anodes showed that a shift of the Cu peak to a higher angle was present. In [1] it is reported that a shift in peak position may indicate probable dissolution of the Cu into the Co. However, the phase diagram of Cu and Co demonstrates that the maximum dissolution of Co in Cu is 0.71% ([126] and [127]). Due to the low solubility of these materials, it is more likely that the shift of the peaks is due to residual stress in the coating. Previous studies have shown that during plasma spray processing, a high level of in-plane tensile stress can develop within each splat during quenching after

solidification, because thermal contraction of the splat is constrained by the underlying solid [128]. Dependent on the orientation of the crystal lattice, these in-plane stress can cause an increase or a decrease of d-spacing between atomic planes, thus shifting the XRD peak to a lower or a higher incident angle.

Figure 4.11: XRD patterns of Cu-Co-GDC coatings sprayed with 40% N_2 – 60% Ar plasma. *Y*-axis represents X-ray intensity in arbitrary units.

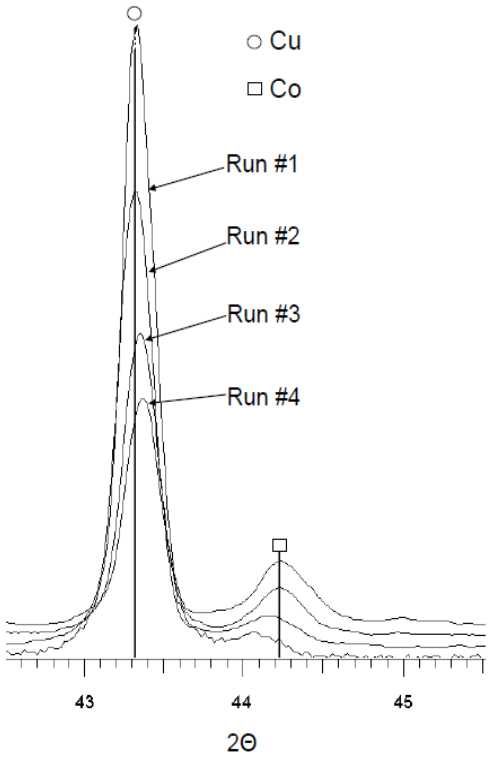

4.2.2.3 Porosity evaluation of Cu-Co-GDC coatings

4.2.2.3.1 Image analysis

Figures 4.12 and 4.13 show an SEM micrograph of a coating cross section and binary digitized images, respectively. Porosity is determined by adjusting the grey scale threshold for the image with image analysis software until the pore phase identified by

the software matches the pore phase that can be identified visually in the micrograph. Light grey solid features and dark grey pores can be identified in the image.

Figure 4.13(a) shows a digitized binary image of the lower bound estimate of porosity, obtained by setting the grey scale threshold such that no solid feature that can be visually identified is included. However, it can be observed that the some of the pore features with bright hues of grey grey that are identified visually in Figure 12 are not identified as pores in Figure 4.13(a).

Figure 4.13(b) shows a digitized binary image of the upper bound estimate of porosity, obtained by setting the grey scale threshold such that all porous features that can be visually identified are included. Binary image includes only black for pores or white for solid phases, without any hues of grey. It can be observed that the some of the solid features having darker hues of grey that are visible in Figure 4.12 are not identified as solids in Figure 4.13(b).

Figure 4.13(c) shows an image overlay of Figure 4.13(a) (purple) and 4.13(b) (blue), visually demonstrating the extent of differences between the grey scale thresholds that lead to the estimates of minimum and maximum porosities.

Figure 4.14 shows a digitized binary image obtained with a grey scale threshold selected between the values shown in 4.13(a) and 4.13(b), resulting in an estimate of the porosity that corresponds well with the extent of the pore phase that can be visually identified in the micrograph.

Figure 4.12: Coating cross section SEM micrograph

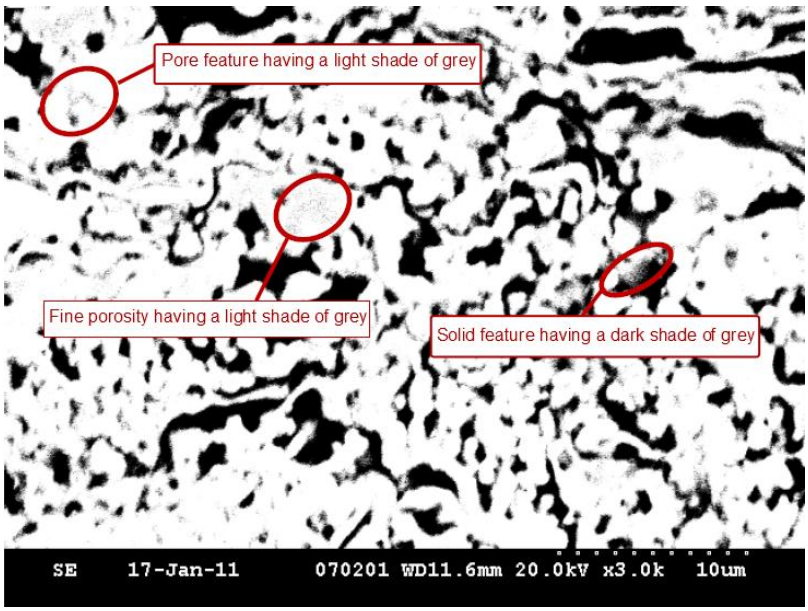

Figure 4.13: Digitized binary images of (a) minimum estimated porosity (b) maximum estimated porosity and (c) image overlay of minimum (purple)and maximum (blue plus purple) estimates of porosity

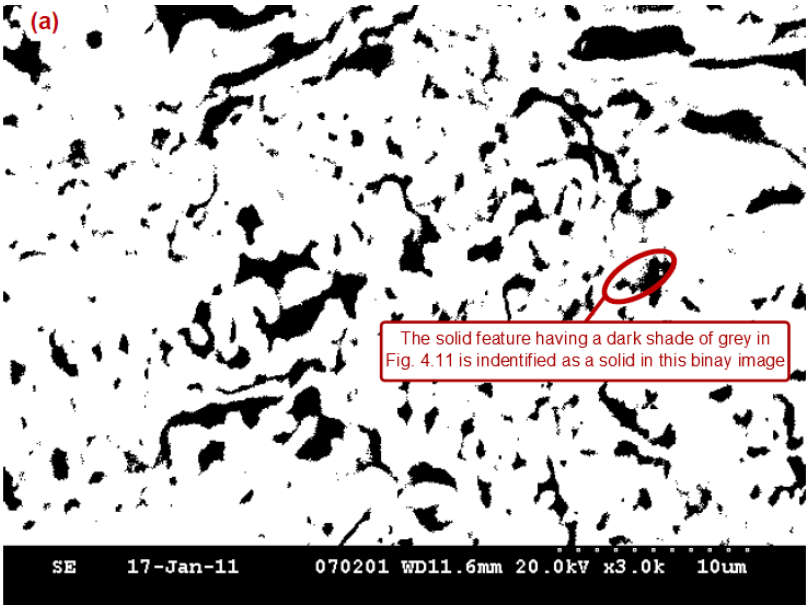

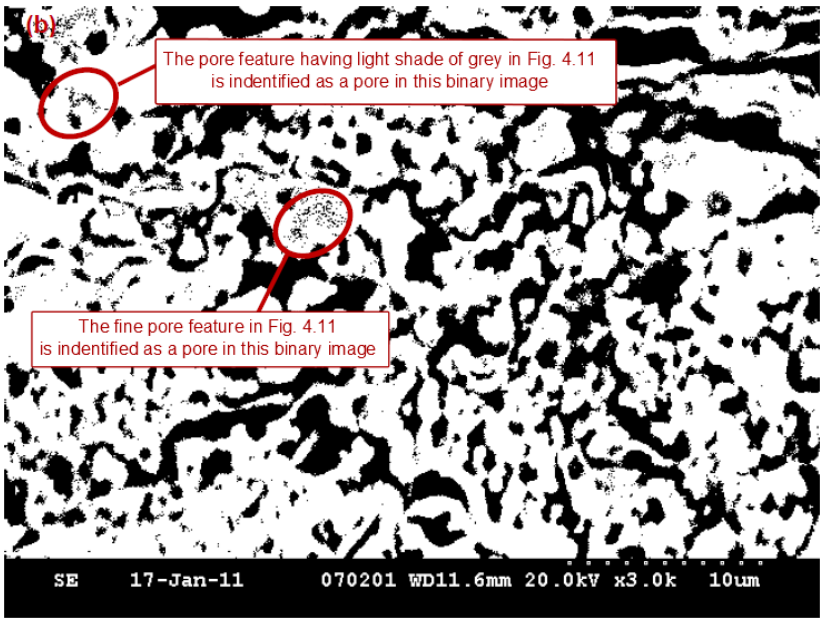
(b)
The pore feature having light shade of grey in Fig. 4.11
is indentified as a pore in this binary image
The fine pore feature in Fig. 4.11
is indentified as a pore in this binary image
SE 17-Jan-11 070201 WD11.6mm 20.0kV x3.0k 10um

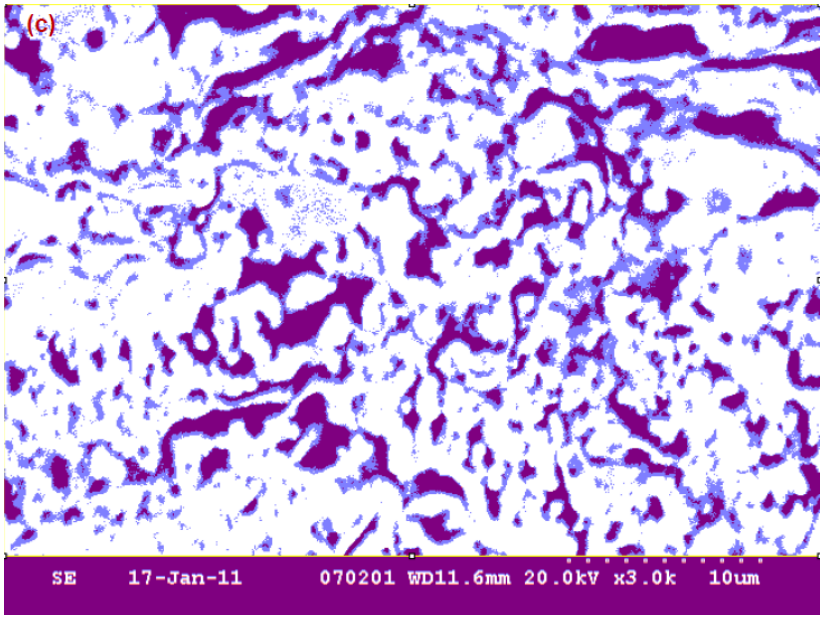
(c)
SE 17-Jan-11 070201 WD11.6mm 20.0kV x3.0k 10um

Figure 4.14: Digitized binary image of best estimate of porosity

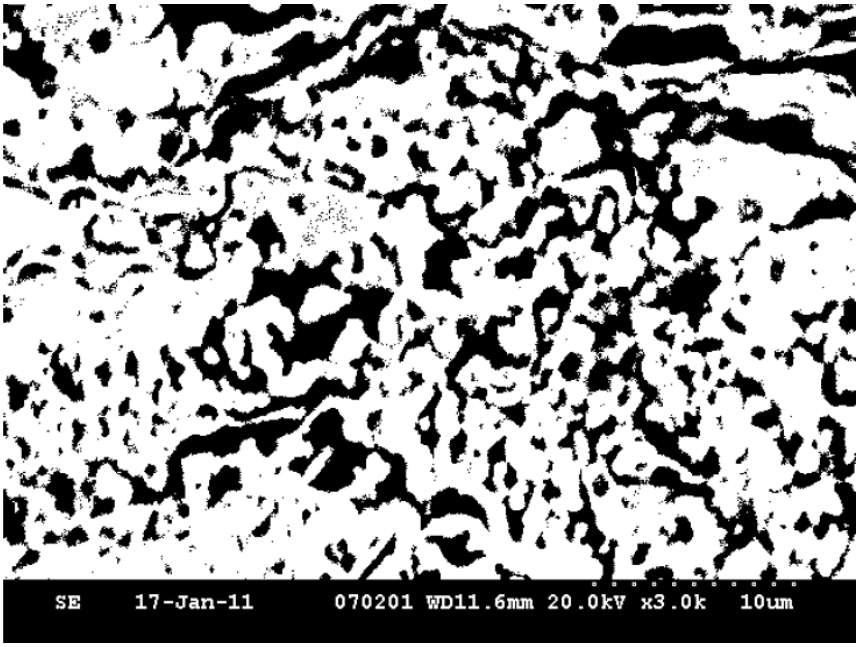

Figure 4.15 shows porosity values of Cu-Co-GDC coatings with different Co loadings obtained by image analysis using optimized grey scale thresholds, The error bars show the minimum and maximum porosity estimates.

Figure 4.16 shows average porosities obtained by image analysis using optimized grey scale thresholds and the calculated theoretical porosity values due to reduction of CuO and CoO to Cu and Co. The theoretical porosity was determined by the relative molar values obtained by EDX.

The error calculated for image analysis is determined for each run as the statistical error of the porosities obtained utilizing optimized grey scale thresholds with significance level $\alpha=0.05$ based on the sample size $n=10$ and standard deviation. For the theoretical porosity, the error is calculated considering the measurement error of EDX of 3%.

The total porosities calculated by image analysis utilizing optimized grey scale thresholds are within the range of 20% to 30%. These values are higher than the range reported by others for plasma spray processing of Cu-Co-YSZ SOFC anode coatings ([12]). This can be attributed to the utilization of CuO and CoO feedstock powders and the porosity gain due to reduction of CuO and CoO to Cu and Co. The porosity values are higher than typical plasma sprayed coating porosities, which are in the range of 5-15 vol%.

Figure 4.15: Porosity of Cu-Co-GDC coatings with different Co loadings obtained by image analysis utilizing optimized grey scale thresholds

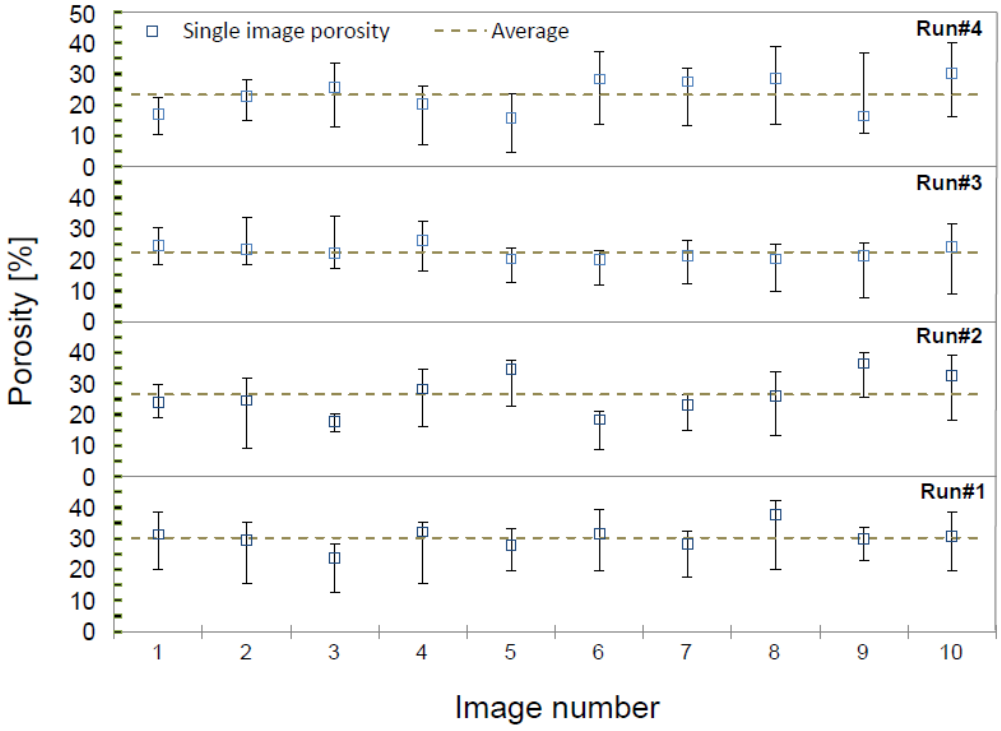

4.2.2.3.2 Gas permeability

The gas flux through the sample can be related to the layer permeation using Darcy's law (Eq. (4.1)):

$$\Phi_{gas} = \frac{Q}{A} = \frac{-\kappa}{\mu}\left(\frac{P_b - P_a}{L}\right) \tag{4.1}$$

Here, Φ is the volumetric gas flux (m sec^{-1}), Q is the flow rate ($m^3 s^{-1}$), κ is the permeability (m^2), A is the cross-sectional area to flow (m^2), ($P_b - P_a$) is the pressure drop (Pa), μ is the dynamic viscosity (Pa s), and L is the length over which the pressure drop takes place (m).

The normalized gas permeance Λ is related to the gas flux through the sample and the resulting pressure drop using Eq. (4.2)

$$\Lambda = {d\Phi_{gas}}\Big/{\left|dp_{app}\right|} \tag{4.2}$$

In the case of two layers, substrate and anode, having pressure drops of Δp_1 and Δp_2 and fluxes Φ_1 and Φ_2, the total pressure drop Δp_t is related to each layer's pressure drop using Eq. (4.3), and the total flux Φ_t is related to each layer's flux using Eq. (4.4),

$$\Delta p_t = \Delta p_{substrate} + \Delta p_{anode} \tag{4.3}$$

$$\Phi_t = \Phi_{substrate} = \Phi_{anode} \tag{4.4}$$

Algebraic manipulation of Eq. (4.1) to Eq. (4.4) yields the anode permeability (Eq. (4.5)).

$$\kappa_{anode} = \mu_{gas} L_{anode} \left(\frac{1}{\frac{1}{\Lambda_t} - \frac{1}{\Lambda_{substrate}}} \right) \tag{4.5}$$

It can be realized from Eq. 4.5 that the anode permeability is derived indirectly from the normalized permeance of the substrate, and the total permeance of the anode and substrate together. The normalized permeance in each case is calculated by applying various pressure drops and measuring the gas flow rates, which are then converted to gas fluxes. Least-squares fitting is used to derive the normalized gas permeance.

Figure 4.16 shows gas permeability coefficient values of Cu-Co-GDC coatings with different Co loadings. Table 4.7 shows permeability values of anode cermets reported by other studies, for comparison purposes.

Figure 4.16: Gas permeability coefficient of Cu-Co-GDC coatings with different Co loadings

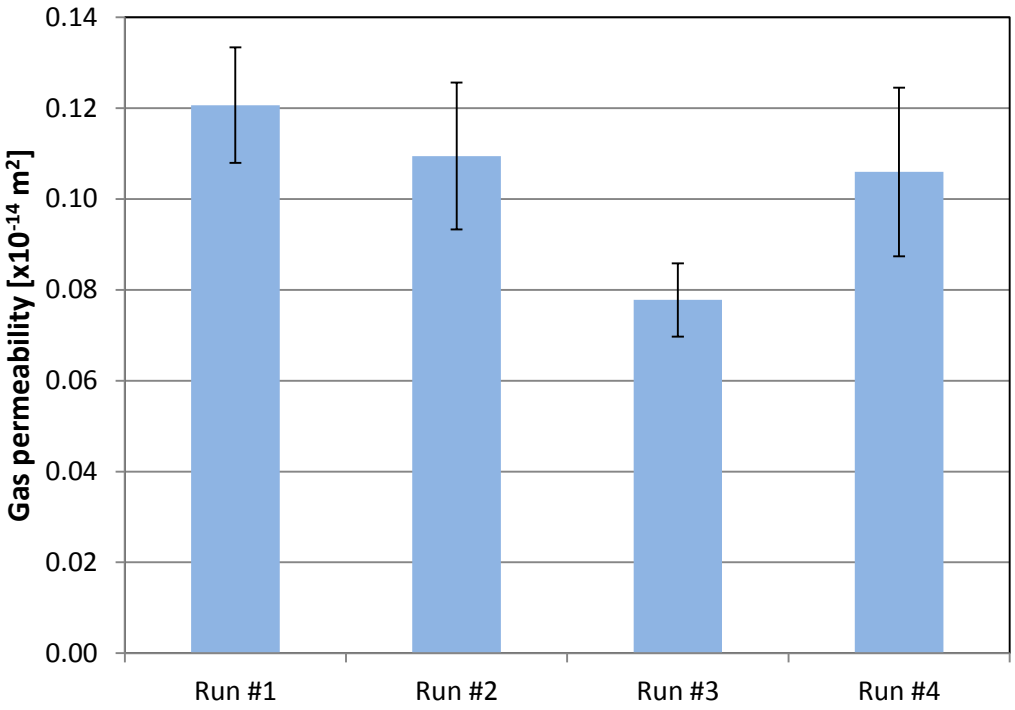

Table 4.7: Gas permeability values of anode cermets

Manufacturing process	Anode material	Gas Permeability [10^{-14} m^2]	Reference
Tape casting	Ni-YSZ	6.00	[129]
APS	Ni-YSZ (nano agglomerated powder)	3.60	[30]
APS	NiO-YSZ (conventional powder)	0.90	[30]
APS	CuO-CoO-GDC	0.08-0.12	This work

The gas permeability coefficient values are lower relative to Ni-YSZ coatings produced in other studies utilizing NiO-YSZ pre-synthesized agglomerates of nano-particles, and they agree well with the porosity values obtained by image analysis. Both total porosity and gas permeability values do not correlate with the amount of Co present in the coating. Although CoO has a higher melting temperature than that of

CuO, under the plasma energy conditions applied to deposit these coatings, the CoO does not have a role in generating increased porosity due to its extent of melting.

4.2.3 Carbon Deposition

EDX analysis of the coatings after 3 hours of exposure to 100% CH_4 at 700°C showed that carbon is deposited on the coatings. SEM analysis of the coatings did not detect any visible evidence of carbon, i.e, carbon fibers or particles. Figure 4.17 shows EDX scans of coatings produced in (a) run #1 (Cu(100)Co(0)) (b) run #2 (Cu(90)Co(10)) (c) run #3 (Cu(70)Co(30)) and (d) run #4 (Cu(50)Co(50)). It can be observed that the carbon peak intensity increases relative to the other peaks when the Co content in the coating is increased, which indicates the presence of carbon in the coating and the tendency of Co to increase the amount of carbon deposited. Figure 4.18 shows surface SEM micrographs of coatings produced in (a) run #1 (Cu(100)Co(0)) (b) run #2 (Cu(90)Co(10)) (c) run #3 (Cu(70)Co(30)) and (d) run #4 (Cu(50)Co(50)). No carbon fibers or particles are visible.

Figure 4.17: EDX scans of coatings produced in (a) run #1 (b) run #2 (c) run #3 and (d) run #4 after 3hr exposure to CH_4 at 700°C

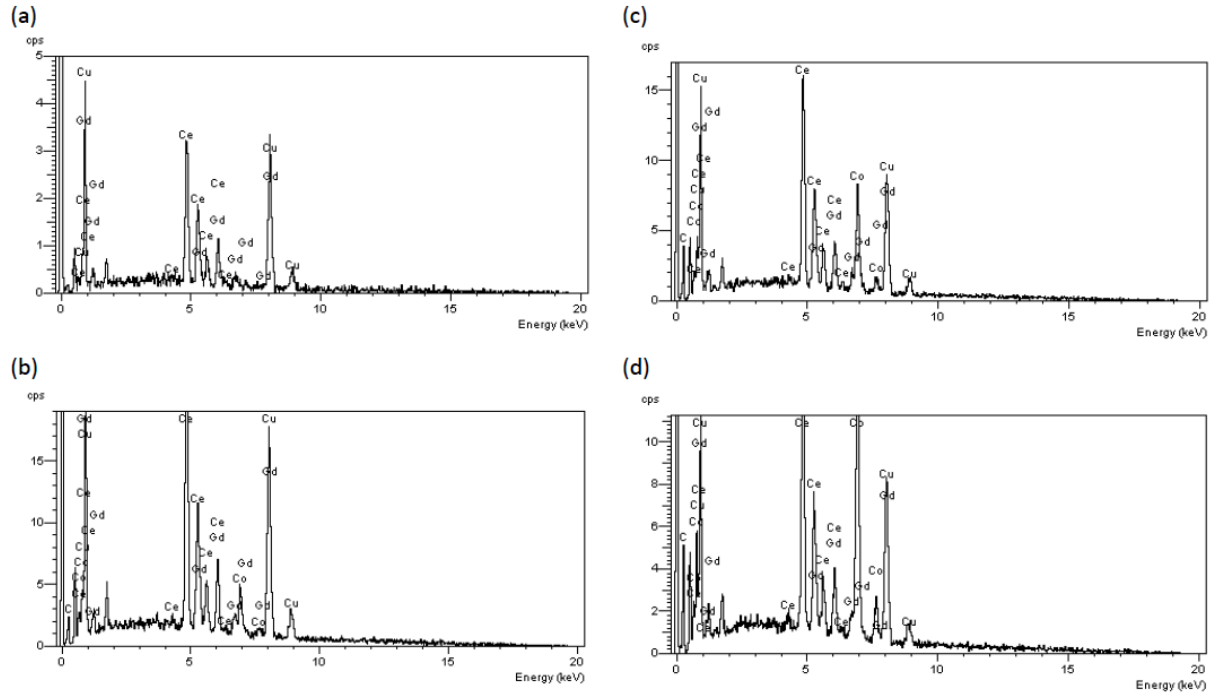

Figure 4.18: SEM micrographs of coatings produced in (a) run #1 (b) run #2 (c) run #3 and (d) run #4 after 3hr exposure to CH_4 at 700°C

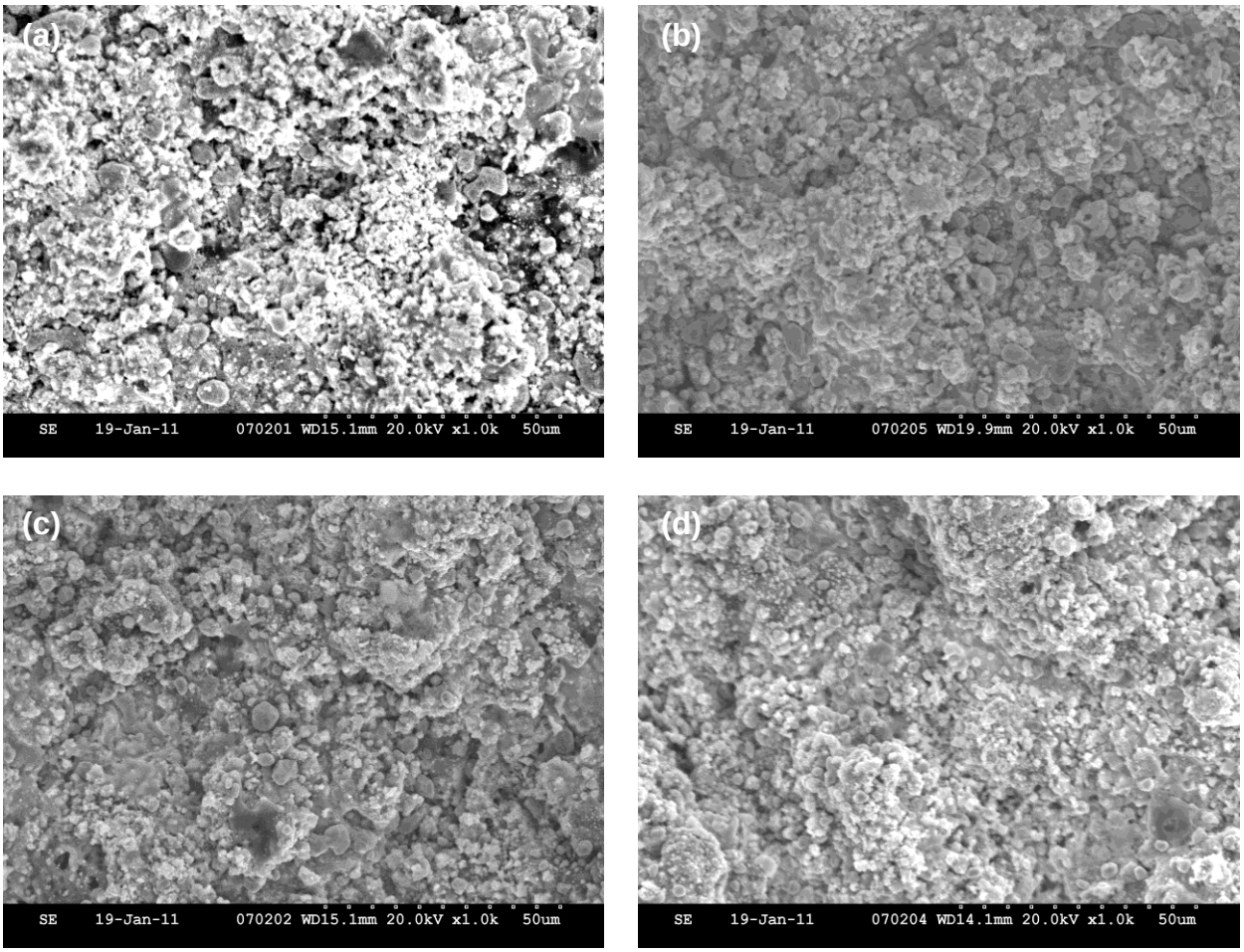

Table 4.8 shows carbon formation data on Cu-Co-GDC coatings with various Co loadings after exposure to dry CH_4 at 700°C for 3hrs. The error is calculated by using the general formula for propagation of uncertainty shown in Eq. 4.6

$$\Delta f = \pm\sqrt{\sum_{i=1}^{n}\left(\frac{\partial f}{\partial x_i}\right)^2(\Delta x_i)^2} \qquad (4.6)$$

Eq. 4.7 is used to calculate the carbon weight fraction relative to the coating weight from the measured weights, where W_{sub} is the weight of the substrate, W_{red} is the total weight of the substrate and the coating after reduction, and W_t is the total weight of the substrate, the reduced coating and the deposited carbon.

$$W_c(W_{sub,}W_{red}, W_t) = \frac{W_t - W_{red}}{W_{red} - W_{sub}} \tag{4.7}$$

Eq. 4.8 shows the propagation of uncertainty error function for the calculated carbon weight, where Δw is the measurement precision of the scale, i.e. 0.01mg, and Δr is the resulting error.

$$\Delta r = \pm\sqrt{\left(\frac{1}{W_{red} - W_t}\right)^2 \Delta w^2 + \left(\frac{W_t - W_{sub}}{(W_{red} - W_t)^2}\right)^2 \Delta w^2 + \left(\frac{W_t - W_{red}}{(W_{red} - W_t)^2}\right)^2 \Delta w^2} \tag{4.8}$$

It can be seen in Table 4.8 that the amount of carbon increases with increasing Co content in the coating. These results are comparable to those of carbon deposition experiments on Cu-Co based coatings produced by wet ceramic processing reported previously [100]. However, the extent of carbon deposition is related to the surface area of the Co and the ability of the CH_4 to permeate into the coating. Due to the low porosity measured for these coatings, it is possible that the low carbon deposition is partially due to low diffusivity of CH_4 into the coating or due to low surface area of the cobalt phase.

The carbon formation was not high (<2.0 wt%) in the samples that were tested. However, these coatings were exposed to CH_4 for a short term of 3 hrs and therefore this result may not indicate that these anodes will be carbon tolerant in a long term fuel

cell operation. To better project these anodes' tendency towards carbon deposition it would be more precise to use the rate at which carbon is deposited rather than the weight gain within the short term exposure. The rate at which carbon is deposited is relatively high and it might indicate that these anodes will experience more significant carbon deposition that might degrade the performance of these anodes in actual steady state fuel cell operation.

Table 4.8: Carbon content in Cu-Co-GDC coatings

Sample	wt % of carbon	Carbon deposition rate (%wt hr^{-1})
Cu(100)	<0.1%	<0.03%
Cu(90)Co(10)	0.43% ± 0.16%	0.14% ± 0.05%
Cu(74)Co(26)	1.30% ± 0.08%	0.43% ± 0.03%
Cu(52)Co(48)	1.92% ± 0.08%	0.64% ± 0.03%

4.3 Conclusions

Cu-Co-SDC coatings were produced by air plasma spraying of CuO, CoO and GDC agglomerates of micron-sized particles. Adequate control of coating composition was achieved by determining the initial feedstock powder ratios required by using the absolute deposition efficiency of each material. A set of plasma spray parameters was identified to produce coatings with different Co loadings in which the GDC is partially melted and keeps its fine structured morphology during plasma spraying. XRD patterns indicated possible interdiffusion of Co and Cu. Co does not seem to have a role in increasing coating porosity due to its extent of melting under the APS conditions applied in this study. The coatings demonstrated excellent comparable stability against carbon formation, comparable to that of previously-fabricated wet ceramic produced anodes of

similar composition from the literature, but were made with a simpler, single-step deposition process.

5. Electrochemical performance of plasma sprayed Cu-Co-SDC monolayer and Cu-Co-SDC/Cu-YSZ bi-layered anodes manufactured from coarse and fine feedstock powders

This chapter deals with manufacturing and electrochemical testing of Cu-Co-SDC monolayer anodes utilizing coarse and fine feedstock powder, and of fine feedstock Cu-Co-SDC/coarse feedstock Cu-YSZ bi-layered anodes, utilizing the APS parameters developed in the study reported in the previous chapter. The absolute deposition efficiency of each coating was calculated and used to obtain Cu-Co-SDC coatings with 40 vol% of metallic phases and approximately 5 wt% of Co within the metallic phases . These coatings were reduced with a 90 % N_2 / 10% H_2 gas mixture at 700°C for 3 hrs. After reduction, coating microstructure, phase composition, material composition, porosity and gas permeability were evaluated. Full cells utilizing coarse feedstock and fine feedstock Cu-Co-SDC monolayer anodes and Cu-Co-SDC/Cu-YSZ bi-layered anodes were manufactured. The cells were tested electrochemically in hydrogen over the temperature range of 550°C to 700°C, and their impedances were measured. The cells were then held at 700°C for 30hrs, and their impedances were obtained as a function of time for degradation analysis.

5.1 Experimental procedure

5.1.1 Material preparation

Commercially available CuO, Co_3O_4, 8 mol% yttria stabilized zirconia ($(ZrO_2)_{0.92}(Y_2O_3)_{0.08}$) and 10 mol% samaria doped ceria (SDC, $Ce_{0.8}Sm_{0.2}O_{1.9}$) powders (Inframat Advanced Materials, Farmington, CT, U.S.A.) were used to produce the anode layers.

Two different SDC powder batches were used in this study: coarse and fine powder batches. Coarse SDC powders were used to produce coarse feedstock Cu-Co-SDC anode layers and fine SDC powders were used to produce fine feedstock Cu-Co-SDC anode layers. The feedstock powders were spherical micron-sized spray dried agglomerates flowable for plasma spraying.

To avoid break-up of the powders, the powders were calcined at various temperatures. Particle size analysis of the fed powders was conducted using a wet dispersion laser light scatting particle size analyzer (Mastersizer 2000, Malvern Instruments, Worcestershire, U.K.). Table 5.1 shows the powder particle size distributions and the calcining temperatures used for each powder.

Table 5.1: Particle size distributions and calcining temperatures

Powder (batch)	Particle Size [µm]			Calcining Temperature [°C]	Calcining Time [h]
	$D_{0.1}$	$D_{0.5}$	$D_{0.9}$		
CuO (Coarse)	14.5	34.5	61.6	850	5
Co_3O_4[1] (Coarse)	17.1	38.4	70.2	1100	5
YSZ (Coarse)				1350	5.5
SDC (Coarse)	22.4	33.2	42.1	1350	5
SDC (Fine)	5.10	15.2	35.2	1350	5

[1] Co_3O_4 decomposes to CoO when heated above 950°C

SDC powder was sieved to narrower particle size distributions of +32µm - 45µm and -32µm utilizing the coarse feedstock and fine feedstock powders, respectively. CuO and CoO powder was sieved to narrower particle size distributions of +32µm - 45µm and -25µm for the coarse and fine feedstock, respectively. The YSZ feedstock powder was sieved to a narrower particle size distribution of +32µm - 45µm. The feedstock powder sieved to a particle size range lower than -32µm will be referred to here as “fine”

feedstock and feedstock powder sieved to particle size greater than 32μm and lower than 45μm will be referred to as “coarse” feedstock.

5.1.2 Plasma spray processing

The atmospheric plasma spray system used for these experiments (Axial III Series 600 DC plasma torch (Northwest Mettech Corp., North Vancouver, Canada) contains a torch in which powder is injected axially between the three electrode pairs, utilizing the set-up described in Appendix A.

Commercially available 2.54 cm diameter porous SS430 disks (media grade 2, Mott Corporation, Farmington, CT, USA) with thickness of approximately 1mm were used as the metallic substrates. A cathode layer was formed by spraying mechanically mixed LSM-YSZ powders (Inframat Advanced Materials) onto the SS430 substrate using plasma and feedstock conditions reported elsewhere [43]. Fine YSZ powder (Inframat Advanced Materials) suspended in water was used to form the electrolyte on top of the cathode using plasma and feedstock conditions reported elsewhere ([24] and [45]). Symmetrical cathode-cathode cells were produced by spraying a cathode layer on top of the electrolyte. Table 5.2 shows experimental plasma spray process parameters for production of cathode and electrolyte layers.

Table 5.2: Plasma spray process parameter values for production of cathode and electrolyte layers

Parameter	Values	
	Cathode	***Electrolyte***
Feedstock	48.2 wt% LSM /51.8 wt% YSZ powder	23.7 wt% YSZ aqueous suspension
Particle size	−45+32µm /−32+25 µm	1.6 µm (d_{50})
Powder feed rate (g min^{-1})	40.0	38.1[1]
Carrier gas flow rate (slpm)	11.7	n/a
Spraying distance (mm)	100	80
Vertical traverse speed (m sec^{-1})	4.25	4.25
No. of vertical passes	60	50
Torch current (A)	549	750
Plasma gas flow rate (slpm)	250	220
Plasma gas composition	76.7% N_2 / 23.3% Ar	80% N_2/15% Ar / 5% H_2
Nozzle diameter (mm)	9.5	9.5
Pre-heat temperature (°C)	300	300-350

[1] of solids in suspension

Anode layers were formed by spraying mechanically mixed powders utilizing the plasma spray process parameters shown in Table 5.3. Preliminary screening tests were conducted by air plasma spraying of the feedstock powders onto SS430 porous substrates (media grade 2, Mott Corporation) and pre-sprayed cathode-electrolyte layers to obtain the absolute deposition efficiency of each feedstock material. The absolute deposition efficiency was used to determine feedstock mixing ratios that will result with the desired anode composition. These coatings were optimized to contain 40 vol% of metallic phases and approximately 5 wt% of Co within the Cu-Co phase. To determine anode gas permeability, 25.4mm diameter anode layers were sprayed onto SS430 porous substrates (Mott grade 2, Mott Corporation). For SEM and porosity characterization and electrochemical testing, anode layers were sprayed onto the cathode-electrolyte layers. To form a bi-layered anode, an anode layer containing CuO,

CoO, and SDC fine feedstock powder was deposited initially followed by deposition of a Cu-YSZ anode conducting layer produced from coarse CuO-YSZ feedstock. These powder mixtures were sprayed through a mask onto the YSZ electrolyte layer to form 11.1mm diameter anodes. To allow better understanding of the cathode contribution to the overall cell performance, an additional cell with symmetrical cathodes was manufactured utilizing identical spraying and feedstock parameters that were utilized to spray cathodes onto the Mott MG2 SS430 substrates. Following the deposition, the coatings were reduced in a N_2-H_2 mixture (10% H_2) for 3hrs.

Table 5.3: Plasma spray process parameter values for production of monolayer and bi-layered anodes

Parameter	Values						
	Screening tests			*1" Button Cells*			
				Monolayer Anode		*Bi-layered Anode*	
	Coarse feedstock CuO-CoO-SDC	***Fine feedstock CuO-CoO-SDC***	***Coarse feedstock CuO-YSZ***	***Coarse feedstock Anode***	***Fine feedstock Anode***	***Functional layer***	***Conducting layer***
Feedstock (sprayed on SS430 substrate)	40.8 wt% CuO / 2.6 wt% CoO / 56.6 wt% SDC	29.5 wt% CuO / 11.8 wt% CoO / 58.8 wt%SDC	40 wt% CuO / 60 wt% YSZ	40.8 wt% CuO / 2.6 wt% CoO / 56.6 wt% SDC	44.1 wt% CuO / 2.70 wt% CoO / 53.2 wt% SDC	44.1 wt% CuO / 2.70 wt% CoO / 53.2 wt% SDC	43.2 wt% CuO / 56.8 wt% YSZ
Feedstock (sprayed on YSZ electolyte)	40.8 wt% CuO / 2.6 wt% CoO / 56.6 wt% SDC	29.5 wt% CuO / 11.8 wt% CoO / 58.8 wt% SDC	40 wt% CuO / 60 wt% YSZ	46.7 wt% CuO / 2.92 wt% CoO / 50.4 wt% SDC	47.1 wt% CuO / 2.75 wt% CoO / 50.2 wt% SDC	47.1 wt% CuO / 2.75 wt% CoO / 50.2 wt% SDC	27.8 wt% CuO / 72.2 wt% YSZ
Particle size	−45+32µm	−25µm CuO/ −25µm CoO/ -32µm SDC	−45+32µm	−45+32µm	−25µm CuO/ −25µm CoO/ -32µm SDC	−25µm CuO/ −25µm CoO/ -32µm SDC	−45+32µm
Powder feed rate (g min^{-1})	36.1	24.6	43.8	40.8	31.0	31.0	41.7
Carrier gas flow rate (slpm)	15	15	15	15	15	15	15
Feeder drum speed (rpm)	6.0	6.0	5.0	6.0	6.0	6.0	5.0
Spraying distance (mm)	100	100	100	100	100	100	100
Vertical traverse speed (m sec^{-1})	4.25	4.25	4.25	4.25	4.25	4.25	4.25
Spraying time (sec)	50	50	50	50	70	23.2	50.0
Torch current (A)	690	690	690	690	690	690	690
Plasma gas flow rate (slpm)	250	250	250	250	250	250	250
Vol.% nitrogen (balance Ar)	40	40	40	40	40	40	40
Nozzle diameter (mm)	12.7	12.7	12.7	12.7	12.7	12.7	12.7
Pre-heat temperature (°C)	300	310	295	300	310	310	310

5.1.3 Coating characterization

Phase analysis was carried out by X-ray diffraction (XRD) (Brucker D8-Discovery diffractometer,Brucker AXS Inc., with Cu Kα radiation at 0.01°s^{-1}. Energy dispersive spectroscopy (EDX) was performed to determine the volume fraction of Cu and Co present in the anode coatings. Scanning Electron Microscopy (SEM, Hitachi High Technologies America, Pleasanton, CA/ USA) imaging of the coatings was performed to observe the porosity and uniformity of the anode microstructures.

Porosity of reduced anodes was determined by statistical image analysis of cross section SEM micrographs of polished samples using ImageJ software. Coatings were mounted in epoxy resin, sectioned and polished. To minimize pull-outs that introduce errors to the calculated porosity, coatings were examined by optical microscopy between each polishing step. After the coatings had been polished, ten images were taken for each coating at 0.50 mm intervals along the length of the coating. The images were taken at 3000x magnification with corresponding analysis areas of 42.7 x 32.0 μm^2. When an electrolyte layer was present in part of the image, it was omitted with the image analysis software. To clearly distinguish between solid and pore, the contrast was increased and brightness reduced to obtain images predominated by black (pore) and white (solid), utilizing the procedure described in chapter 4.

Permeability coefficients of reduced anodes were determined using Darcy's law, in which a constant transverse air flow causes a pressure drop across a resistance, i.e. the thickness of the anode layer, using the set-up described in Chapter 4. To obtain the thickness required for the permeability coefficient calculation, fifteen images were taken at equal intervals of 0.5 mm along the coating.

Following the microstructural analysis of anode coatings, single cells were manufactured utilizing coarse feedstock and fine feedstock Cu-Co-SDC anode monolayers, and fine feedstock Cu-Co-SDC/coarse feedstock Cu-YSZ bi-layered anodes.

5.1.4 Electrochemical testing

Cell testing was performed using an SOFC test station (AMI, Canada) and an FRA and potentiostat (Solartron 1260 and 1470E, UK). The test station design includes a thermocouple that measures the temperature close to the cell. Glass felt was utilized to facilitate the sealing. To allow the glass felt to melt and produce a seal, the cells were heated utilizing the heating profile shown in Table 5.4

Table 5.4: Heating profile used to form a glass seal.

Step	Rate (°C min^{-1})	Duration (Hr)	End Temperature (°C)
Ramp	1.0	--	150
Dwell	--	1.0	150
Ramp	1.0	--	500
Dwell	--	2.0	500
Ramp	3.0	--	740
Dwell	--	5.0	740
Ramp	5.0	--	700
Dwell	--	5.0	700
Ramp	5.0	--	770
Dwell	--	0.5	770
Ramp	5.0	--	700

All cells were tested utilizing identical testing profiles. After the glass seal sintering profile was completed, in-situ reduction of the Cu-Co-SDC anodes was conducted in a dry H_2-N_2 gas mixture (20% H_2) at a total flow rate of 200 sccm for 2 hrs.

After reduction, the cells were cooled down to 550°C at a rate of 3°C min^{-1} with approximately 50°C decrements and 1 hr of dwell time at each temperature. Impedance spectroscopy at open circuit conditions and at 0.7V polarization was conducted at each temperature over the frequency range of 1mHz to 1MHz, with 50mV rms voltage perturbation amplitude. Polarization curves were obtained from OCV to 0.3 V. All tests utilized the anode and cathode gas flows shown in Table 5.5.

To test degradation of cell performance, the cells were heated to 700°C at a rate of 3° $Cmin^{-1}$ and dwelled for 1 hr. Impedance spectroscopy at open circuit conditions and at 0.7V polarization was than conducted at time intervals of 0.5 hr over the frequency of 1mHz to 1MHz, with 50mV rms voltage perturbation amplitude for 26-40hrs. In between impedance measurements, cell current was measured at a terminal voltage of 0.7V.

To facilitate subtraction of the cathode contribution to the overall polarization resistance, symmetrical cathode tests were conducted utilizing an identical temperature profile and air flow rate of approximately 500ccm for each cathode. Impedance spectroscopy at open circuit conditions was conducted over the frequency range of 1mHz to 1MHz, with 50mV rms voltage perturbation amplitude. Equivalent circuit fitting was performed utilizing Z-View software (Scribner Associates Inc., Southern Pines, NC, USA). After the cells were cooled down, they were sectioned and examined by SEM.

Table 5.5: Anode and cathode gas flows and compositions

Parameter	Value
Anode gas composition (vol %)	20% H_2, 80% N_2
Anode gas flow (sccm)	200
Cathode gas composition (vol %)	Air (79% N_2, 21% O_2)
Cathode gas flow (sccm)	200

5.2 Results and Discussion

5.2.1 Microstructural analysis

5.2.1.1 Microstructural analysis of screening test coatings

The calculated absolute deposition efficiencies of the CuO, CoO, SDC and YSZ phases sprayed onto pre-deposited cathode and electrolyte layers are shown in Figure 5.1. The deposition efficiencies of fine CuO, CoO, and SDC powders are lower than those of coarse CuO, CoO, and SDC powders, where the CuO has the largest difference, and the SDC the smallest. This result is expected, due to a higher proportion of evaporation of the fine powder relative to that of the coarse powder. The absolute deposition efficiency of the coarse CuO powder deposited with CoO and SDC is identical to that of CuO powder deposited with YSZ. This suggests that the absolute deposition efficiency of each of the materials present in the feedstock may be independent of the other materials co-deposited in the case where deposition efficiency is not limited by the extent of melting of the particles, as is the case for CuO, but rather by volatilization of the feedstock at higher plasma powers

It can also be observed from Figure 5.1 that the SDC has a much higher absolute deposition efficiency than that of the YSZ. YSZ has a higher melting temperature than SDC (2710°C for zirconia[131], and 2480°C for ceria [111]). In addition, the heat capacity of zirconia in the solid state is lower than that of ceria (56.2 $Jmol^{-1}K^{-1}$ for ZrO_2 and 61.6 $Jmol^{-1}K^{-1}$ for CeO_2). Moreover, the density of YSZ is lower than that of SDC (5.96 g cm^{-3} for YSZ and 7.22 g cm^{-3} for SDC). It is possible that YSZ experiences a lower residence time in the plasma in comparison to SDC for similarly-sized particles, because similarly-sized particles are lighter and may therefore accelerate to a higher

velocity in comparison to those of SDC. These factors may contribute to the lower extent of melting of YSZ compared to the extent of melting of SDC sprayed under identical plasma parameters. The difference could also result from different particle size distributions within the same sieve size fraction.

Figure 5.1: Absolute deposition efficiencies of the CuO, CoO, SDC and YSZ phases

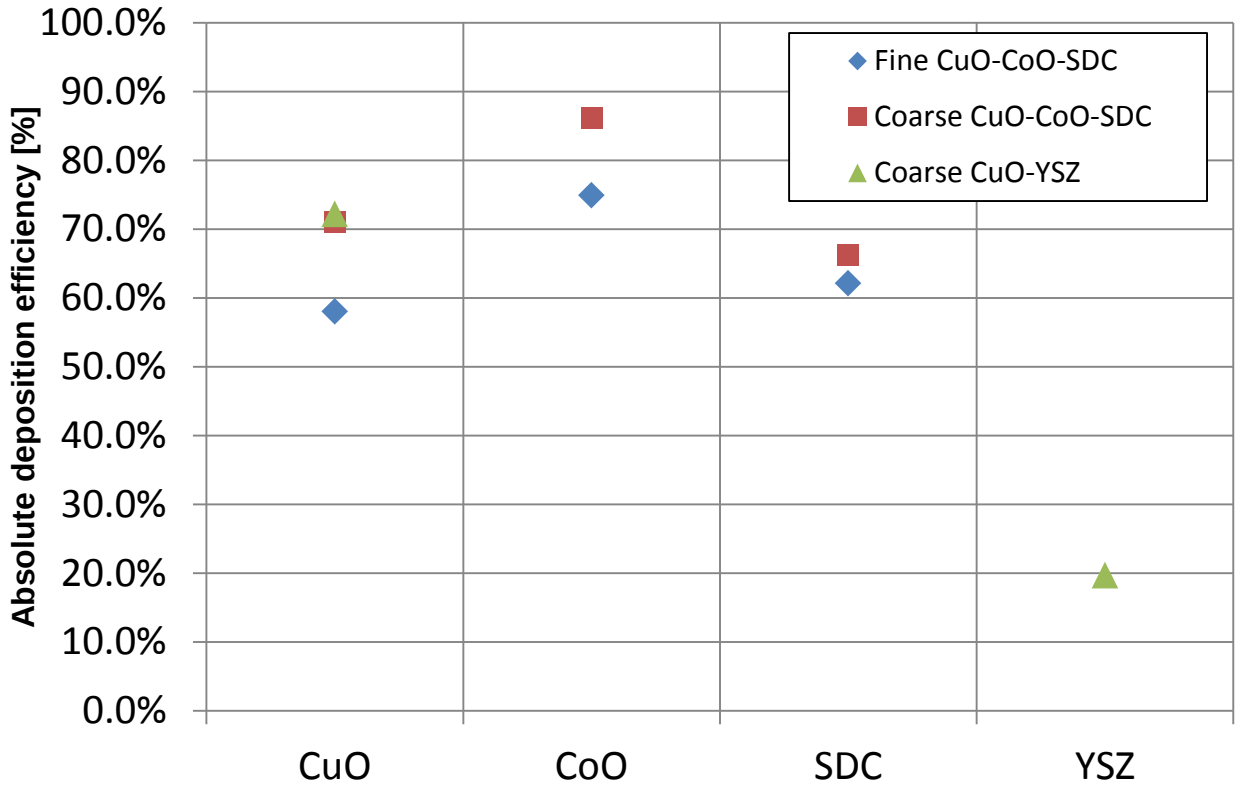

The relative deposition efficiencies of the CuO, CoO, SDC and YSZ are regarded as the ratio of the absolute deposition efficiencies for any pair of materials; i.e. CuO:CoO, CuO:SDC, CoO:SDC, and CuO:YSZ. The relative deposition efficiency is

then used to determine the initial feedstock weight ratios required to obtain the target values of 40 vol% of metallic phases in the anode, and 5 wt% of Co within the Cu-Co phases. Mixing ratios of the feedstock powders are shown in Table 5.3

5.2.1.2 Microstructural analysis of anode coatings

Energy dispersive spectroscopy (EDX) was performed on the coatings after reduction to determine the volume fraction of Cu and Co present in the coatings and the weight ratios of the Cu and Co. The results are shown in Table 5.6. The volume fractions and weight ratios are close to the targeted values. It can be seen in Table 5.6 that feedstock mixing ratios are different for the SS430 substrates alone and for YSZ electrolytes on cathodes on the metallic substrates. The differences are due to the dependence of absolute deposition efficiency on the substrate material, thermal conductivity, and surface roughness. Therefore, initial feedstock powder mixing ratios were adjusted corresponding to the substrate used.

Table 5.6: Volume fraction of metallic phases in the coatings and the weight fraction of Co in the Cu-Co phases

Parameter	Substrate					
	SS430 (Mott MG2) substrate			Suspension electrolyte		
	Coarse feedstock CuO-CoO-SDC	**Fine feedstock CuO-CoO-SDC**	**Coarse feedstock CuO-YSZ**	**Coarse feedstock CuO-CoO-SDC**	**Fine feedstock CuO-CoO-SDC**	**Coarse feedstock CuO-YSZ**
Feedstock powder relative weights	40.8 wt% CuO / 2.6 wt% CoO / 56.6 wt% SDC	44.1 wt% CuO / 2.70 wt% CoO / 53.2 wt% SDC	43.2 wt% CuO /56.8 wt% YSZ	40.8 wt% CuO / 2.6 wt% CoO / 56.6 wt% SDC	44.1 wt% CuO / 2.70 wt% CoO / 53.2 wt% SDC	27.8 wt% CuO / 72.2 wt% YSZ
EDX analysis	Co 4.20 mol%/ Cu 70.4 mol%/ Ce 25.4 mol%	Co 4.70 mol%/ Cu 72.4 mol%/ Ce 22.9 mol%	Cu 72.5 mol%/ Zr 27.5 mol%	Co 5.70 mol%/ Cu 72.0 mol%/ Ce 22.3 mol%	Co 5.90 mol%/ Cu 67.8 mol%/ Ce 26.4 mol%	Cu 74.0 mol%/ Zr 26.0 mol%
Solid volume fraction of metallic phases in coating (vol%)	36.3%	39.4%	43.1%	40.3%	35.1%	42.8%
Co content within metallic phases (wt%)	5.24%	5.7%	---	6.87%	7.46%	---

Figure 5.2 shows SEM cross section micrographs of (a) a coarse feedstock Cu-Co-SDC layer (b) a fine feedstock Cu-Co-SDC layer, and (c) a coarse feedstock Cu-YSZ coating, all sprayed onto YSZ electrolytes. The electronically insulating SDC and YSZ phases are the brighter materials in the images of the anode composites. Both in the coarse feedstock Cu-Co-SDC coating and in the fine feedstock Cu-Co-SDC coating, partial melting of the SDC is evident. In the coarse feedstock coating, the SDC partially preserves its finely-structured morphology. This structure is not observed as frequently in the fine feedstock coating. The metallic phases, comprising Cu and Co, are highly melted, but partially melted metallic particles are also evident in the coating. It can be observed that the extent of melting is higher in the fine feedstock coating. In the fine

feedstock coating, the splats are thinner compared to the splats of the coarse feedstock coating. This observation is expected due to the use of identical spraying parameters for feedstock powders sieved to different size fractions. Three types of porosity can be observed: Fine pores, resulting from the finely structured morphology of the SDC particles, oval shaped pores, resulting from the microstructural features of the sprayed particles and gaps between subsequently sprayed particles/splats, and planar porosity, which is observed near metallic particles and can be attributed to a decrease in volume due to reduction of metal oxide to metal.

It can be observed in Figure 5.2 that the Cu-Co-SDC coating produced by coarse feedstock powders is less homogeneous than the Cu-Co-SDC coating produced from fine feedstock powder, in which the materials are more homogenously mixed.

In the Cu-YSZ coating, shown in Figure 5.2(c), it can be observed that the YSZ keeps its finely-structured morphology to a greater extent than the SDC in Figure 5.2(a), with both having the same feedstock powder sieve fraction size range of -45 + 32 µm. This is due to the higher extent of melting of SDC in comparison with the YSZ. The lower extent of melting visible from the morphology of the YSZ phase in the coating is consistent with the lower absolute deposition efficiency of YSZ in comparison to that of SDC.

Figure 5.2: Cross section SEM micrographs of (a) coarse Cu-Co-SDC, (b) fine Cu-Co-SDC and (c) coarse Cu-YSZ coatings

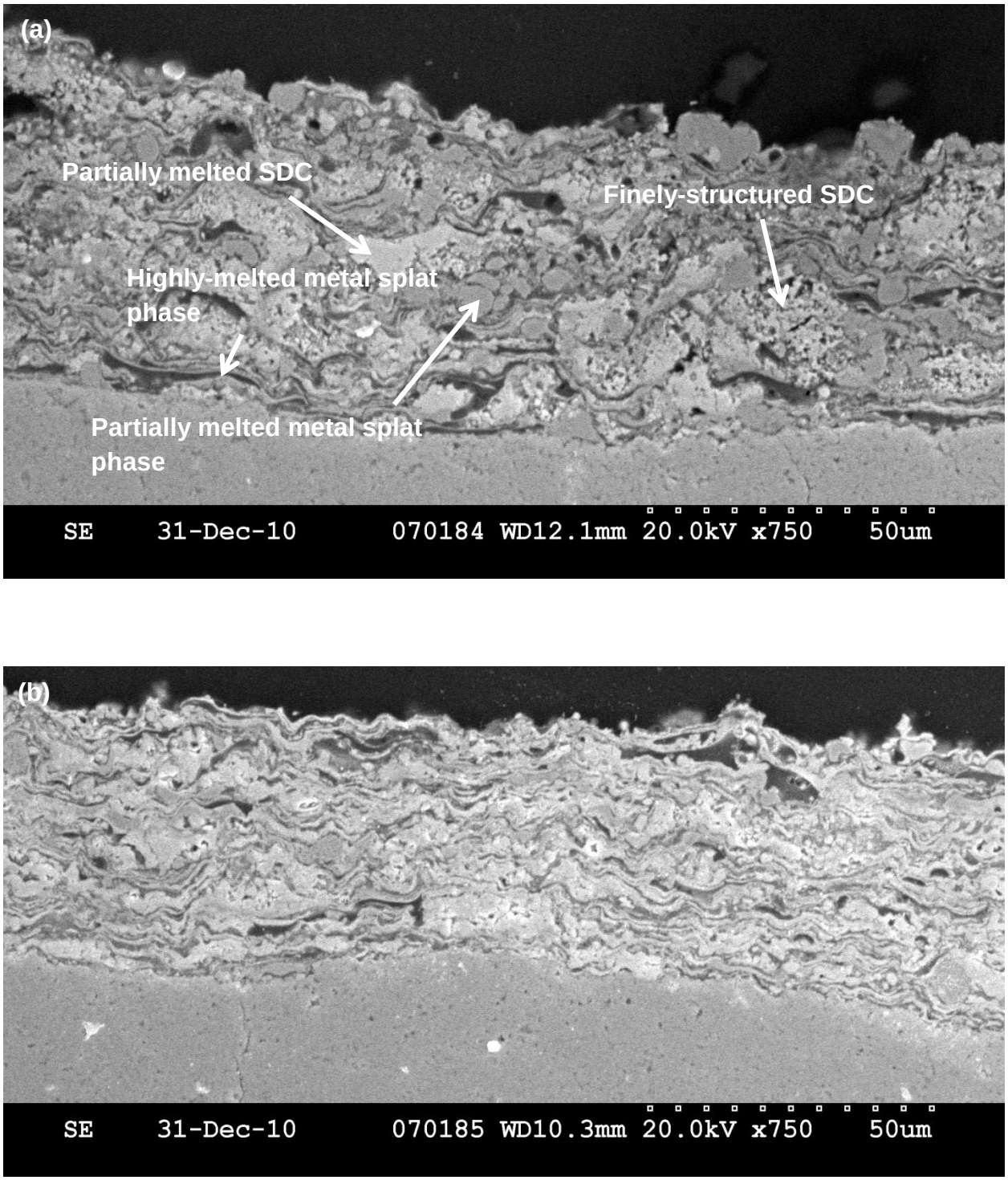

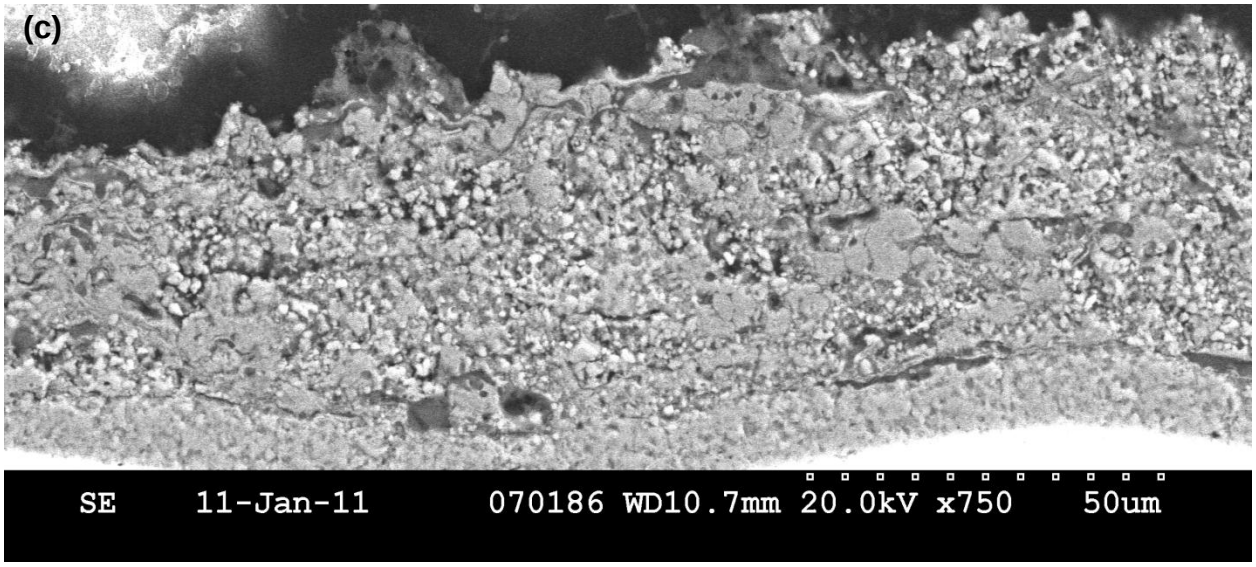

Image analysis was performed on cross section SEM micrographs of the coarse feedstock Cu-Co-SDC, fine feedstock Cu-Co-SDC, and coarse feedstock Cu-YSZ coatings, using the method described in Chapter 4. Figure 5.3 show image analysis of coarse feedstock Cu-Co-SDC, fine feedstock Cu-Co-SDC, and coarse feedstock Cu-YSZ anode layers. The error bars indicate the porosity range obtained by using the procedure described in chapter 4.

The total porosities of all coatings were in the range of 13.0 to 22.4 vol%, which is lower than the desired opened porosity for SOFC anodes of 40 vol%. Both coarse feedstock Cu-Co-SDC and coarse feedstock Cu-YSZ anode layers porosities were higher than that of fine feedstock Cu-Co-SDC anode layers. This can indicate that partial melting of coarse powders resulting with increased porosity in comparison to a higher degree of melting of fine feedstock powders which result with decreased porosity. In addition, the Cu-YSZ anode layers porosity was higher than that of coarse

feedstock Cu-Co-SDC, which can indicate lower degree of melting of YSZ particles in comparison to SDC particles. This results is consistent with absolute deposition efficiencies of these materials.

Figure 5.3: Image analysis of coarse feedstock Cu-Co-SDC, fine feedstock Cu-Co-SDC, and coarse feedstock Cu-YSZ anode layers

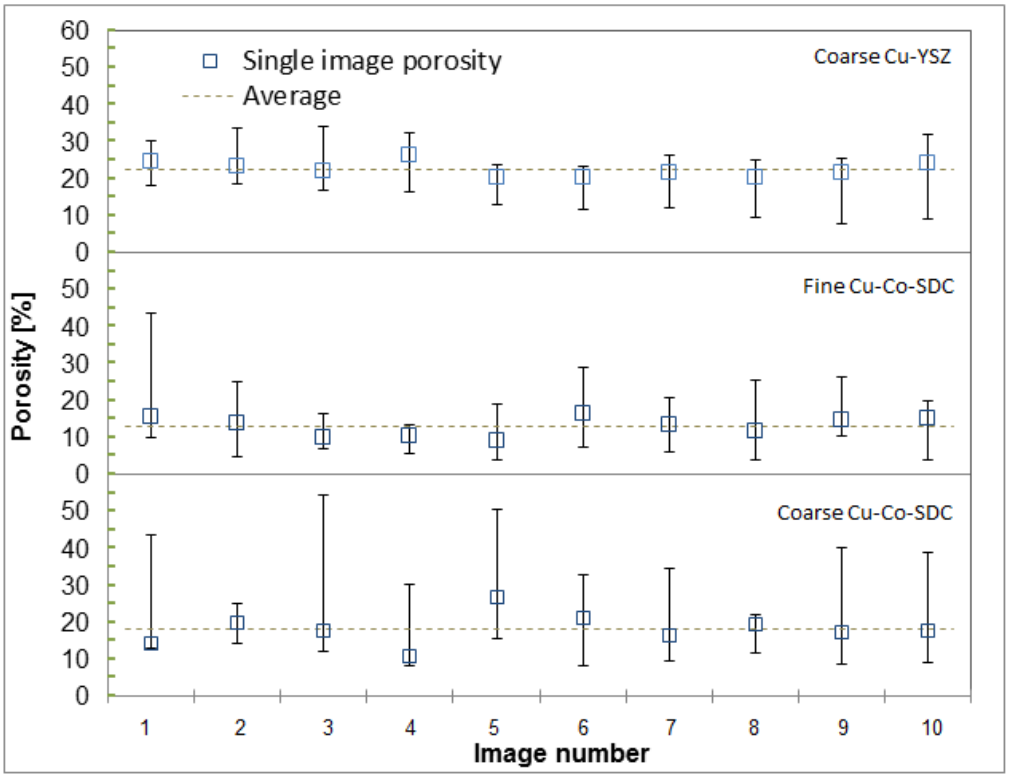

Permeability coefficients of reduced anode coatings are shown in Figure 5.4. Gas permeability coefficient values are lower relative to Ni-YSZ coatings produced in other studies utilizing nanostructured NiO-YSZ powders injected radically to DC plasma torch (F4 torch, Medicoat, Mägenwil, Switzerland) [30]. In chapters 2 and 3, it was demonstrated that the CuO is highly melted even with low energy plasmas. This is likely

the cause of the low gas permeability coefficient, compared to NiO-YSZ anodes manufactured by plasma spraying.

Figure 5.4: Permeability coefficients of reduced anode coatings

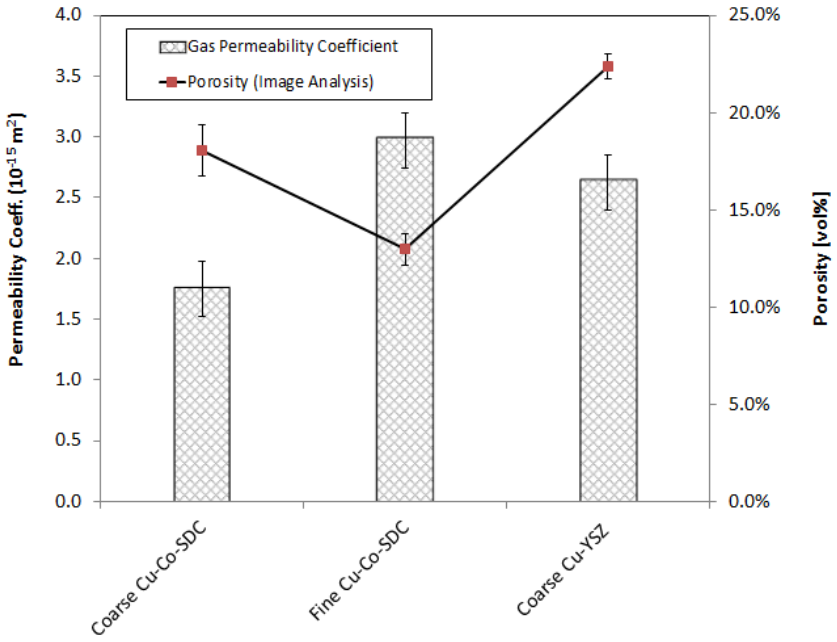

The gas permeability coefficients do not correlate directly with the porosity values obtained by image analysis. This discrepancy can be explained by noting that open porosity is not the only factor determining the permeability through a porous medium. Gas transport is also affected by the tortuosity factor of the microstructure. In addition, the difference between the open porosity and the total porosity determined by image analysis may not be negligible for low values of total porosity. Image analysis measures the total porosity, including closed porosity. Closed porosity can be created due to geometric shape mismatch between splats. The gas permeability coefficient is dependent on the open porosity, though which the gas can flow. The coarse feedstock

coating has higher porosity values and lower gas permeability values in comparison to the fine feedstock coating. This may indicate a higher portion of closed porosity in the coarse feedstock coating, or a higher tortuosity of the pore space compared to the coatings with lower total porosity. An additional parameter that affects the gas permeability values is the coating thickness. In theory, gas permeability coefficient is not affected by the coating thickness, since the coating thickness is considered in the calculation. However, due to the surface roughness of the substrate, 5.2µm for Mott media grade 2 ([24] and [44]) substrates, pinholes in the coating may be present if the coating is not sufficiently thick. This may increase the measured gas permeation, and subsequently, the calculated gas permeability coefficient. The average thicknesses of the fine feedstock Cu-Co-SDC, coarse feedstock Cu-Co-SDC, and of the coarse feedstock Cu-YSZ coatings were 54.1±6.45, 54.5±4.42, and 39.9±3.74, respectively, at a confidence level of α=0.05. The Cu-YSZ layer is the thinnest of the three types of layers. It is possible that pinholes were present in the Cu-YSZ layer as a result of its lower thickness, which made its gas permeability coefficient appear artificially higher than the value corresponding only to the coating microsctructure due to those concentrated defects.

5.2.1.3 Phase analysis of anode layers in full cells

Figure 5.5 shows XRD patterns of anode layers produced from CuO, CoO, SDC and YSZ feedstock powders, before and after reduction with H_2 at 700°C. It can be observed that the crystal structure of the SDC remained cubic. During spraying, the CuO was partially reduced to Cu_2O. In the case of bi-layered anodes, SDC peaks of the anode functional layer under the Cu-YSZ conducting layer can be observed. No new

phases resulting from inter-reactions between the two layers are apparent. In the case of fine feedstock and coarse feedstock anodes, the Cu_2O, CoO and CuO were fully reduced to Cu and Co. In the case of bi-layered anodes, no CuO was detected, and a low-intensity peak of Cu_2O can be observed in the reduced coatings at 36.7°. Note that all anodes were reduced under identical conditions. This result demonstrates that one of the layers of the bi-layered anode may have exhibited less open porosity in comparison to the coarse and fine feedstock anode monolayers, causing less access of oxide metals to the reducing H_2.

Figure 5.5: X-ray diffraction of fine feedstock Cu-Co-SDC, coarse feedstock Cu-Co-SDC, and bi-layered anodes

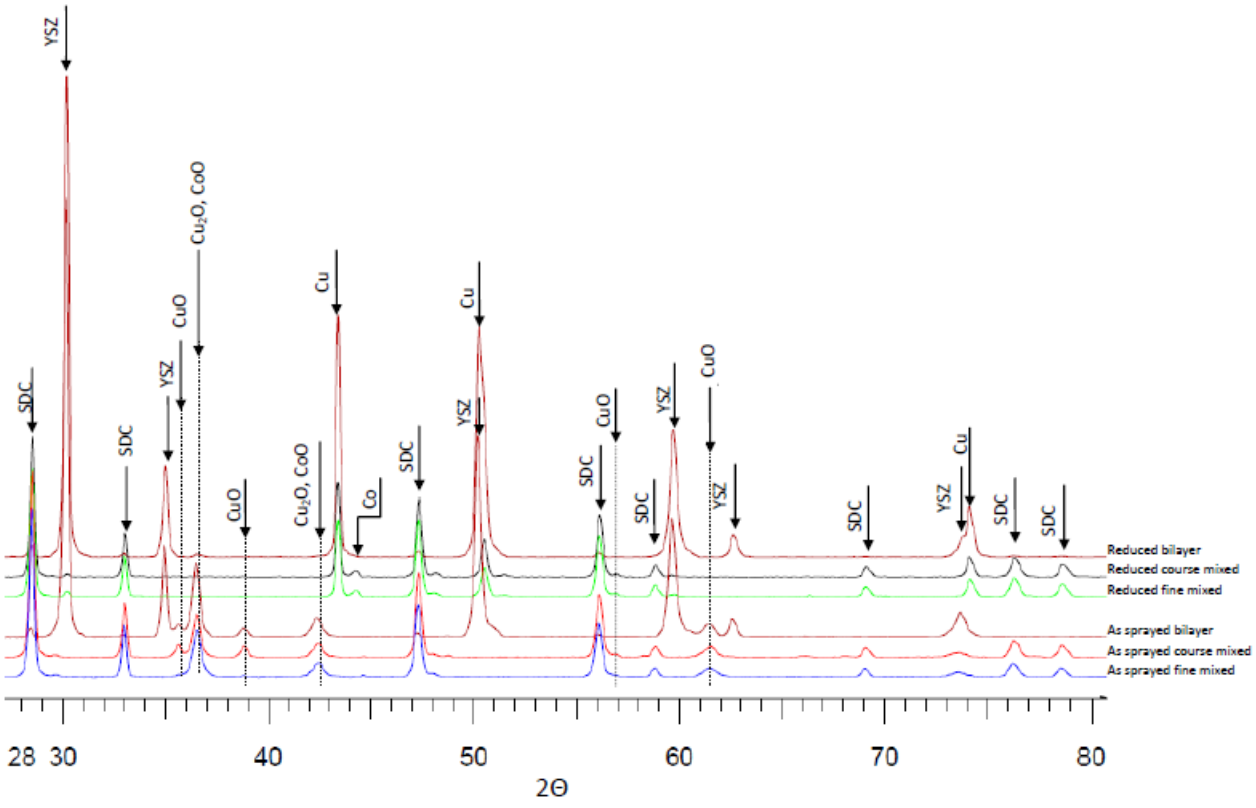

5.2.2 Cell testing

5.2.2.1 Open circuit voltage

The performance of single cells with coarse feedstock Cu-Co-SDC anodes, fine feedstock Cu-Co-SDC anodes, and fine feedstock Cu-Co-SDC/coarse feedstock Cu-YSZ bi-layered anodes was measured at temperatures between 550°C to 700°C with H_2-N_2 mixtures (20% H_2) with a total flow rate of 200 sccm at the anode and 200 sccm of air at the cathode. The open circuit voltage of each cell is shown in Table 5.7. The open circuit voltages of all cells were lower than the open circuit voltage values predicted by the Nernst equation of 1052 mV at atmospheric pressure and with identical reactant gas compositions. This result can be explained by leakage through the plasma sprayed electrolytes or through the glass seals, or both, which causes a decrease of the open circuit voltage. When the H_2 concentration at the anode was increased beyond 20%, a rapid decrease of the open circuit voltage was observed for all cells. This result demonstrates the presence of leaks through the electrolyte or glass seals and subsequent combustion. Therefore, all tests were conducted with H_2-N_2 mixtures at the anode with 20% H_2.

Table 5.7: Open circuit voltage at 700°C with H_2-N_2 mixture (20% H_2)

Time after reduction (Hrs)	Open circuit voltage at 700°C, H_2-N_2 mixture (20% H_2) [mV]		
	Coarse feedstock cell	Fine feedstock Cell	Bi-layered cell
1.0	821	887	865
10.0	908	892	851
26.0	740	892	851

The open circuit voltage did not degrade substantially in cells with fine feedstock anodes or with bi-layered anodes. However, the coarse anode cell demonstrated substantial degradation of the open circuit voltage with time after reduction. Post-testing examination of this cell by SEM revealed that the porosity of the substrate near the cathode was blocked by a layer with Cr. This observation can be attributed to rapid chromium oxide formation in the SS430 substrate pores caused by high localized temperatures due to combustion resulting from leaks through cracks at the electrolyte or seals.

5.2.2.2 Impedance spectroscopy of full cells at various temperatures

Impedance spectroscopy was used to characterize the variation of the cell performance with temperature. Impedance spectra measured near OCV using a four-probe configuration are shown in Figure 5.6 for (a) a coarse feedstock Cu-Co-SDC anode (b) a fine feedstock Cu-Co-SDC anode (c) a fine feedstock Cu-Co-SDC/ coarse feedstock Cu-YSZ bi-layered anode. In these spectra, the highest frequency real-axis intercept determines the cell ohmic resistance, R_s, and the lowest frequency real-axis intercept determines the total cell resistance, R_t. The width of the impedance arcs on the real axis is the polarization resistance, R_p, which includes the reaction and mass transport resistances of both the anode and cathode.

Figure 5.6: Impedance spectra of cells with (a) coarse feedstock Cu-Co-SDC anode (b) fine feedstock Cu-Co-SDC anode and (c) fine feedstock Cu-Co-SDC/ coarse feedstock Cu-YSZ bi-layered anode.

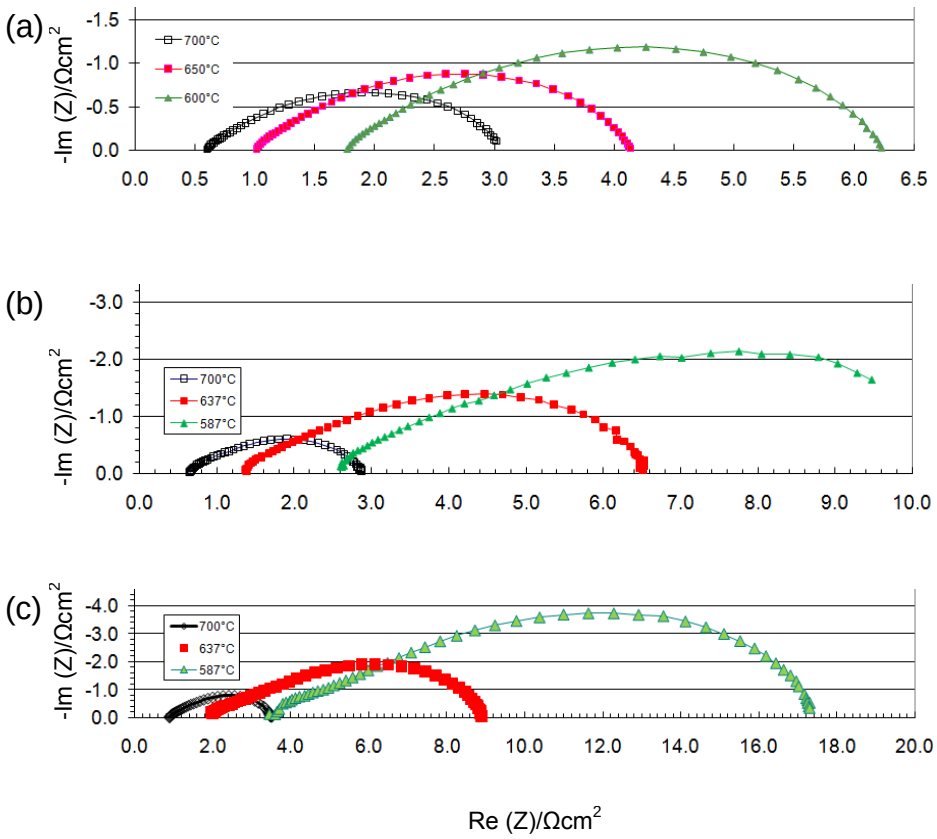

5.2.2.3 Impedance spectroscopy of cathode symmetrical cell

Impedance spectroscopy was used to identify the contribution of the cathode to the total polarization resistance of the full cells, utilizing an identical testing profile as that used for the full-cell tests, but using different single-cell testing hardware and sealing procedures. Impedance spectra measured at OCV using a four-probe configuration are shown in Figure 5.7.

Figure 5.7: Impedance spectra of cathode-cathode symmetrical cell

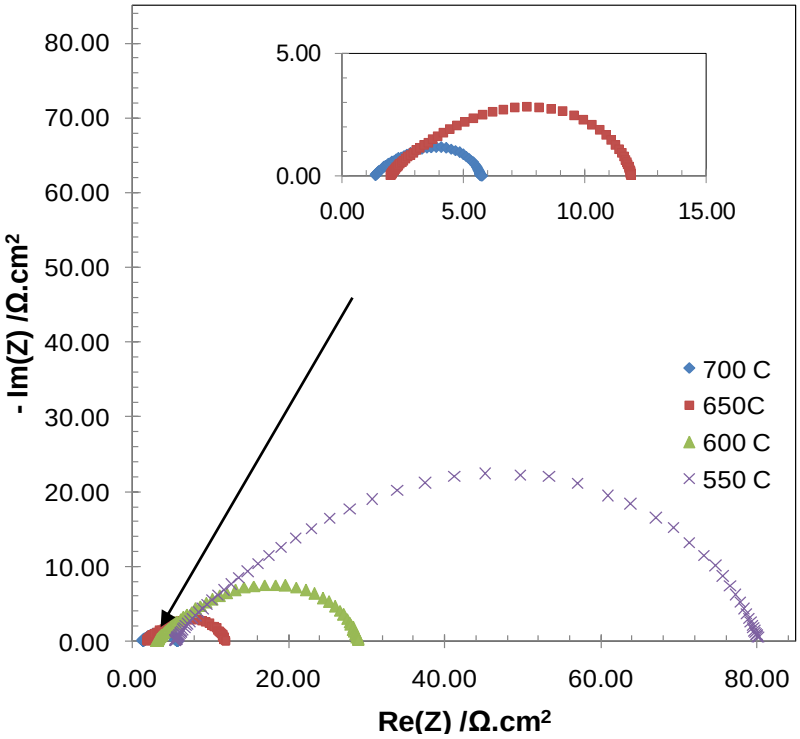

In an attempt to separate the contribution of each individual cathode to the total polarization resistance, equivalent circuit fitting was performed utilizing an equivalent circuit model shown in Figure 5.8, where CPE denotes a constant phase element. The fitting results are shown in Table 5.8. It can be seen that the contributions of each cathode modeled by a CPE-Rp element are not identical. This difference may result from differences of the microstructure of each individual cathode due to spraying of the cathode layers onto SS430 porous substrates and onto YSZ electrolytes previously deposited on the other cathode. Surface roughness and thermal conductivity are different for SS430 porous substrates and for the electrolyte, causing both layers to

have different microstructures and potentially different compositions. The differences may also result from more than one process in the cathode, having the presence of different time contants, for example, charge transfer and gas transport.

Figure 5.8: Equivalent circuit model used for cathode symmetrical cell fitting

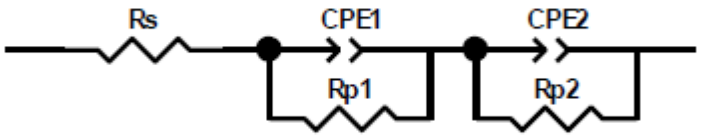

Table 5.8: Equivalent circuit fitting results for symmetrical cathode cell

Temperature /°C	Rs/Ω.cm^2	Rp_1 /Ω.cm^2	Rp_2 /Ω.cm^2	R_pl /Ω.cm^2
700	1.36	1.38	3.04	4.41
650	1.98	2.01	8.19	10.20
600	3.15	4.44	22.05	26.49
550	5.50	12.75	62.97	75.71

5.2.2.4 Polarization resistance of full cells

The resistances of cells with coarse feedstock anode, fine feedstock anode, and bi-layered anode are summarized in Table 5.8. At 700°C, the cell with the bi-layered anode had the lowest polarization resistance and the cell with the coarse feedstock anode had the highest Rp.

It can be seen that the total polarization resistance of the coarse-anode cell is lower than the polarization resistance of both cathodes obtained by equivalent circuit modeling shown in Table 5.8. This discrepancy may be caused by differences in microstructure between the cathodes sprayed with identical parameters, causing the cathodes on the surface of the symmetrical cells farthest from the substrates to have

higher polarization resistances than the cathodes applied at the substrate interface of both the symmetrical and full cells. In addition, discrepancies between test stations may also cause differences in the calculated polarization resistance values. Because the cathode polarization resistances obtained from symmetrical cell tests are higher than the total cell resistance of the coarse cell, it is not possible to obtain the individual contributions of the anode and cathode by subtracting the cathode polarization resistance from the total polarization resistance. Additional work to quantify the differences in test station hardware and their impact on measurements of cell performance as well as differences in microstructure of identically-processed electrodes on opposite sides of a cell electrolyte is required to further diagnose the causes for the discrepancies between the cathode symmetrical cell tests and the full cell tests.

Table 5.9: Cell resistances at different temperatures

Cell	Temperature (°C)	Anode thickness (μm)	R_s (Ωcm^2)	R_t (Ωcm^2)	$R_{p,cell}$ (Ωcm^2)
Coarse feedstock Cu-Co-SDC monolayer	700	93.4±6.20	0.60	3.02	2.42
	650		1.01	4.15	3.15
	600		1.77	6.27	4.51
	550		3.21	9.84	6.62
Fine feedstock Cu-Co-SDC monolayer	700	71.25±5.72	0.64	2.87	2.23
	637		1.38	6.49	5.10
	587		2.60	9.80	7.20
	546		4.36	21.50	19.00
Fine feedstock Cu-Co-SDC / coarse feedstock Cu-YSZ bi-layered	700	29.9±1.9 (functional layer) 39.8±4.8 (conductive layer)	0.90	2.87	1.98
	637		1.96	6.49	4.50
	587		3.38	17.88	14.50
	546		5.52	26.20	20.71

Arrhenius plots of the series and polarization resistance are shown in Figure 5.9

(a) and Figure 5.9 (b), respectively. The activation energy of the ohmic resistance R_s is similar to values reported in the literature for APS YSZ electrolytes [123]. The activation energies of the polarization resistances differ to a large extent between the cells. However, these values differ between cells in the literature as well [122].

Figure 5.9 (a): Arrhenius plot for (a) series resistance (R_s) and (b) polarization resistance of all cells

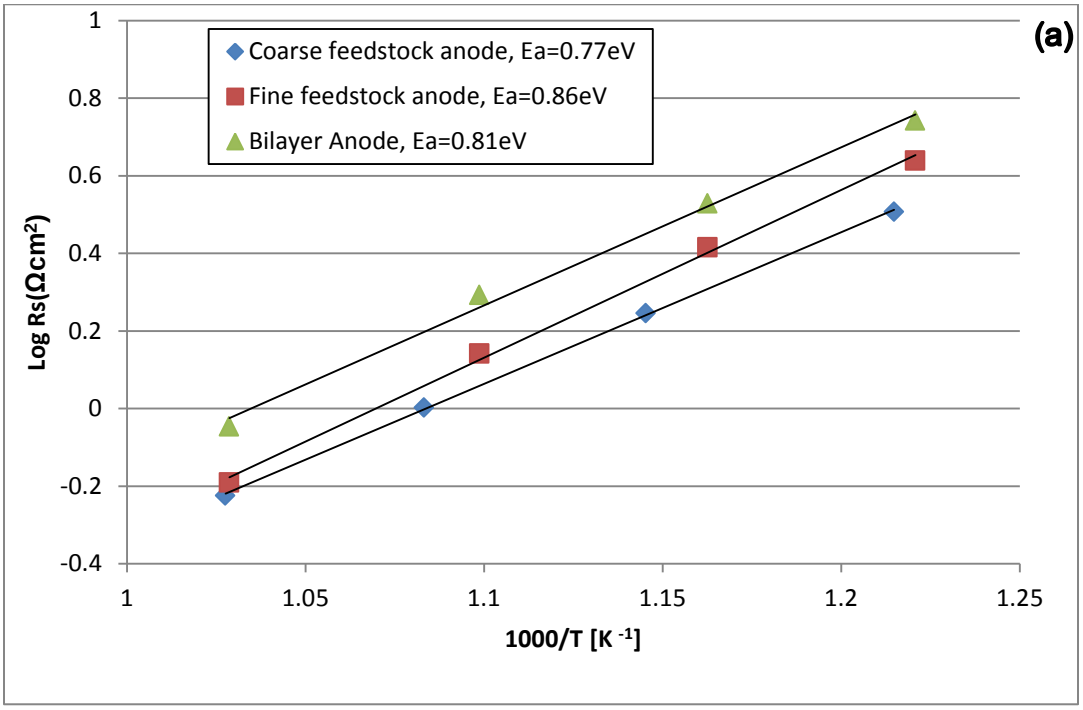

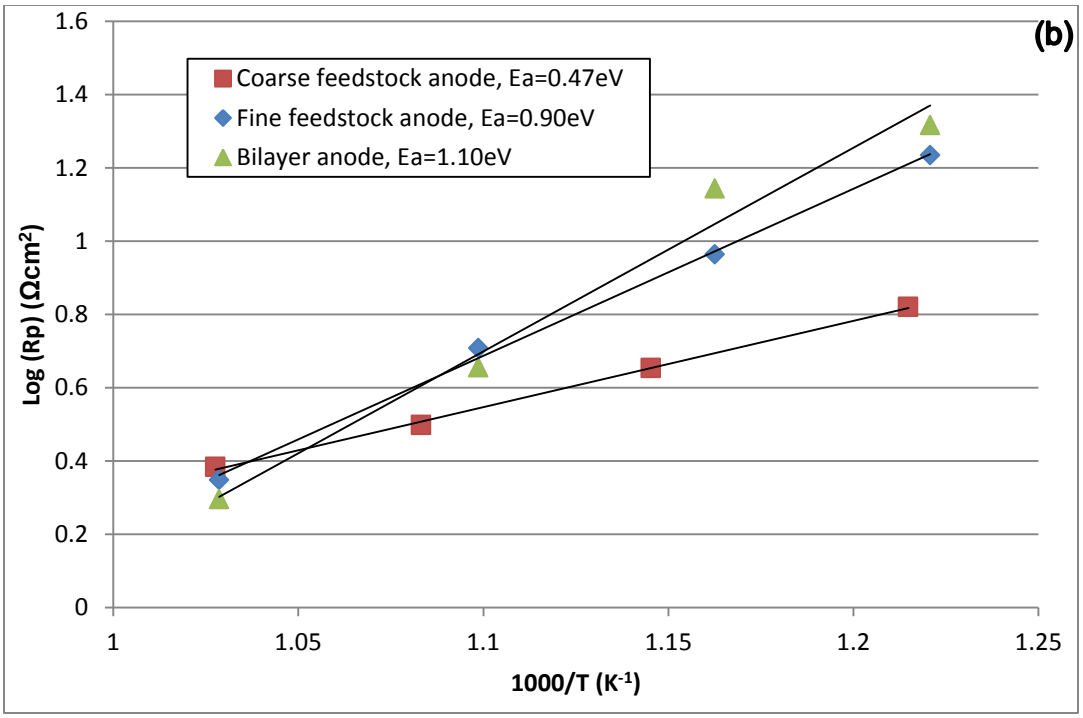

Polarization and power density curves of the full cells at 700°C are shown in Figure 5.10. All cells exhibit fairly high activation and ohmic losses, as demonstrated by the low current densities of all cells. In addition, it can be seen that the bi-layered cell is highly mass transport limited, since its polarization curve demonstrates mass transport limitations at an overpotential of approximately 400 mV, whereas the coarse and fine feedstock anode cells do not demonstrate obvious mass transport limitations as dominant loss mechanisms in the polarization curves. These results agree with the image analysis results, where the coarse feedstock Cu-YSZ layer was the least porous of the three layer types, with a total porosity of approximately 11 vol%. Note that the fuel had a H_2 concentration of 20% in these tests. The lower the concentration of the fuel at the anode, the higher the mass transport resistance observed in the full cell, in general. The mass transport limitations observed with 20% H_2 are likely to be more severe than those that would be observed with pure hydrogen fuel at the anode; however, the cells

could not be tested in pure hydrogen for these experiments. Nevertheless, it is likely that some mass transport limitations are present in the anodes tested, due to their fairly low porosities.

Figure 5.10: Polarization curves of cells with coarse feedstock monolayer anode, fine feedstock monolayer anode, and bi-layered anode at 700°C.

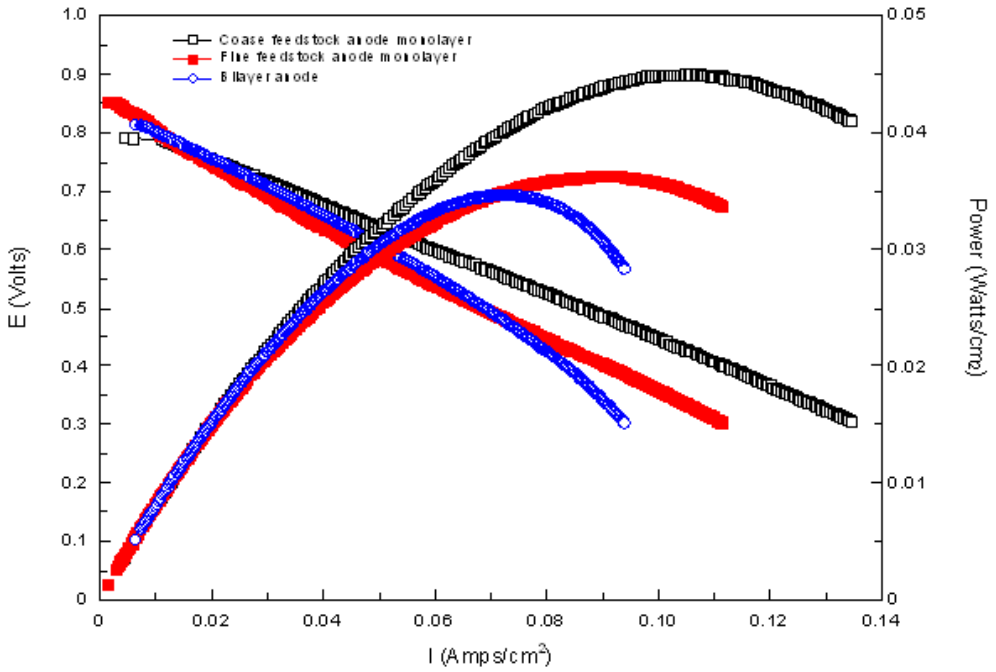

To better understand the extent of mass transport limitations at these operation conditions, impedance spectra of all cells were measured at OCV and at 0.7V. Figure 5.11 shows polarized cell impedance spectra of cells with (a) coarse feedstock anode (b) fine feedstock anode and (c) bi-layered anode taken at 700°C 10hrs after reduction of the cells. It can be seen that the polarization resistances of cells with the coarse feedstock anode and bi-layered anode increase with increased polarizations. The higher impedances at increasing polarization can be related to mass transport limitations or to

gas conversion, in which the concentration of reactant changes through the anode layer. [57. It is apparent that the anode approaches the diffusion limit condition at an overpotential of 208mV for the coarse feedstock cell and at 151mV for the bi-layered cell, resulting in the expansion of the corresponding impedance spectral arcs, which can be seen at the low frequency region of the impedance spectra. This result suggests increased polarization due to fuel starvation or slow desorption and evacuation of the reaction products. The high frequency impedance does not seem to be affected by the operating voltage. With the fine feedstock cell, the effect of mass transport is not noticeable, demonstrating that the fine feedstock cell is less mass transport limited. In addition, the fine feedstock anode is thicker than both the coarse feedstock anode and bi-layered anode, which provides further evidence that the fine feedstock anode is the least mass transport limited in its microstructure.

Figure 5.11: Impedance spectra of cells with (a) coarse feedstock anode (b) fine feedstock anode and (c) bi-layered anode at OCV and at 0.7V polarizations

(a)

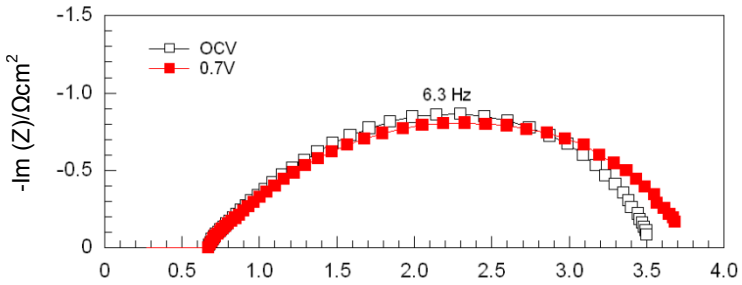

(b)

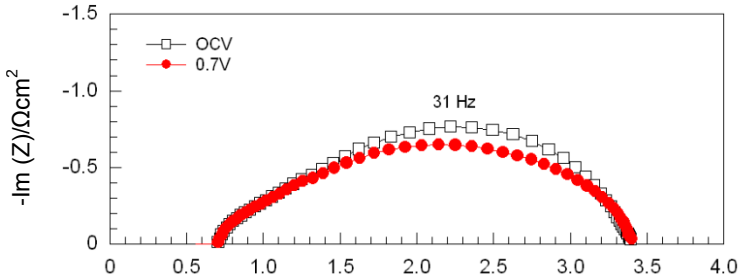

(c)

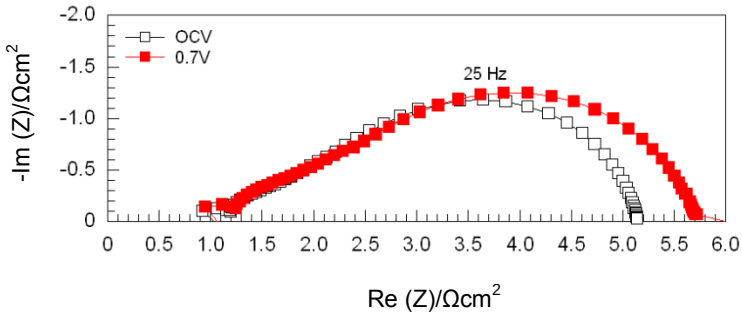

5.2.2.5 Cell degradation analysis

To detect degradation of performance of each cell with time, impedance spectra of the cells were taken at open circuit voltage while the cells were dwelled for several hours at 700°C, as shown in Figure 5.12 for cells with (a) coarse feedstock anode monolayers, (b) fine feedstock anode monolayers, and (c) bi-layered anodes. All spectra demonstrated an increase of both series and polarization resistances. In addition, all cells demonstrate a stabilization of the increase of polarization resistance, where the polarization resistance increased at a decreasing rate with time. It can be seen in Figure 5.12 that the increase of polarization resistance is associated with the low frequency arc. The high frequency arcs of the spectra seem to remain identical during the time dwell.

Figure 5.12: Impedance spectra at OCV for cells with (a) coarse feedstock monolayer anodes (b) fine feedstock anode monolayers and (c) bi-layered anodes dwelled at 700°C for different dwell times after reduction.

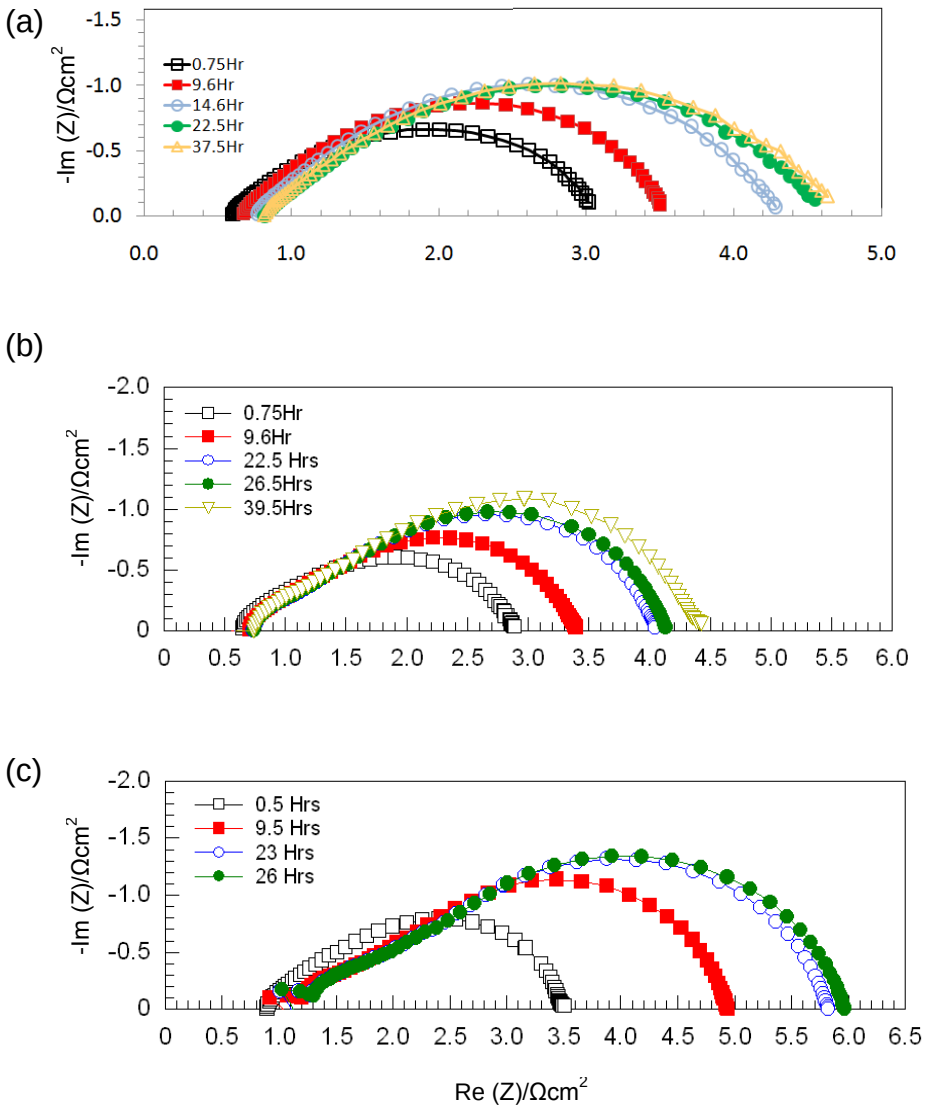

Figure 5.13 shows normalized series and polarization resistances of (a) coarse cell (b) fine cell and (c) bi-layered cell over time extracted from the impedance spectra measured while the cells were dwelled at 700°C for several hours. Both polarization and series resistances of all cells seem to stabilize over time.

Figure 5.13: Normalized series and polarization resistances over time of (a) coarse feedstock cell, (b) fine feedstock cell, and (c) bi-layered cell dwelled at 700°C for several hours

(a)

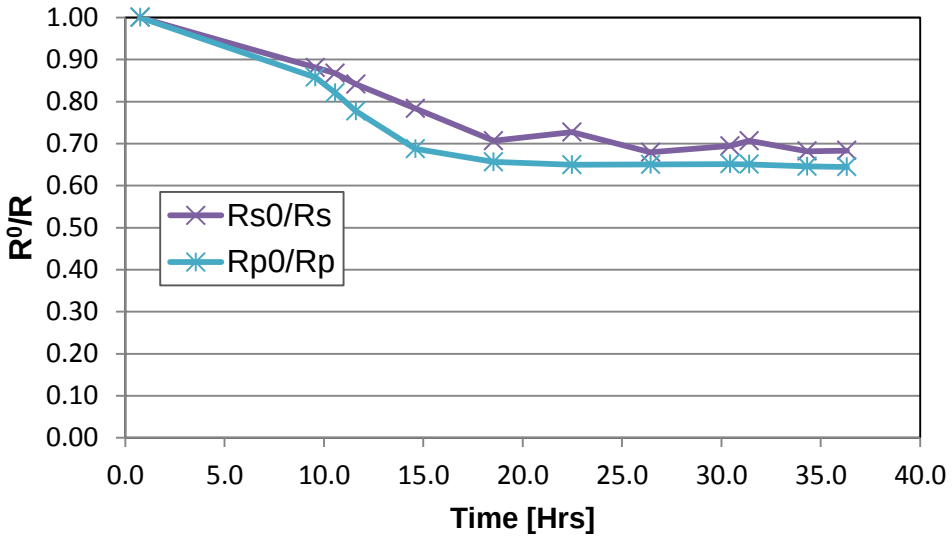

(b)

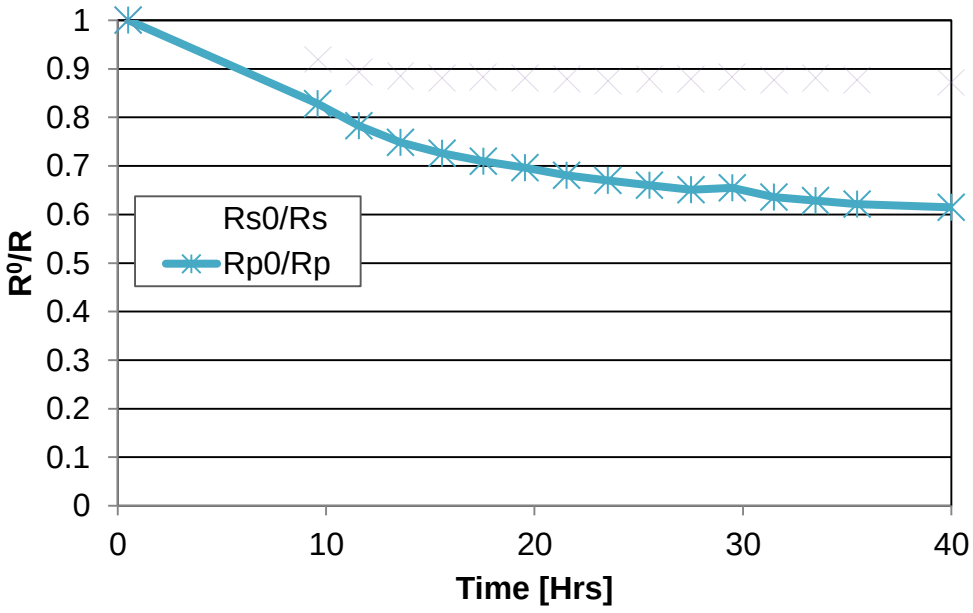

(c)

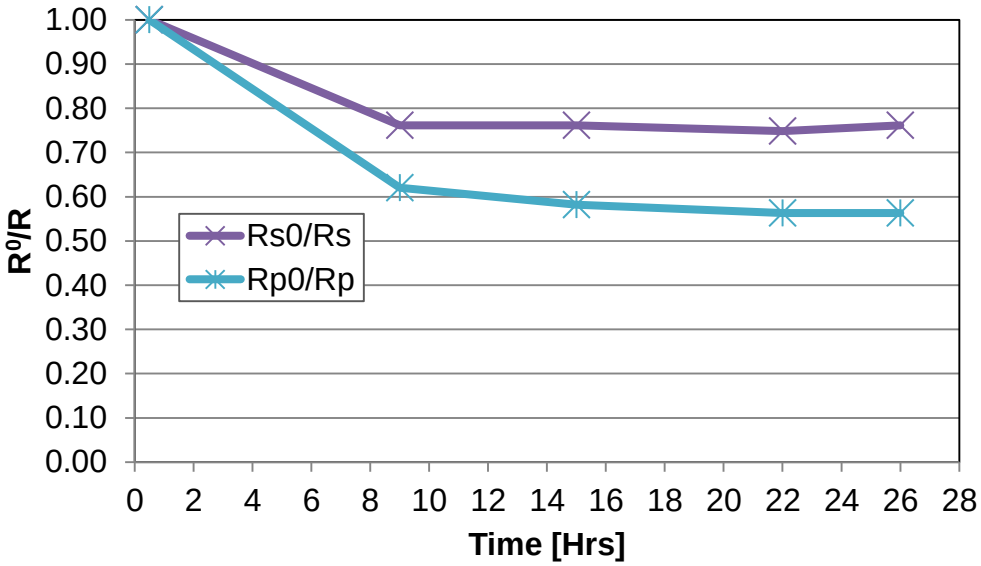

At this point of the research, there are no experimental data regarding possible degradation of individual cell layers. The total degradation as reflected by the increase of polarization resistance can be related to several mechanisms. At this point we can only point out possible mechanisms related to the anode. It has been demonstrated by other studies that Cu based anodes operated at 700°C experience degradation of performance due to sintering of the Cu, resulting in coarsening of the Cu particles and loss of conductivity [130]. This results in loss of electronic conductivity, which increases ohmic resistance if the Cu phase was originally bordering on being not fully percolated, and with loss of TPB length due to detachment of Cu particles from the ionic conductive phase, i.e. SDC, which increases polarization resistance. To overcome this problem, modifications to the wet ceramic manufacturing process were introduced [65].

To test the hypothesis that degradation occurs through microstructural changes in the anodes, impedance spectra of the 3 types of cells were taken after several hours of operation at OCV and at 0.7V. Figure 5.14 shows impedance spectra of cells with (a)

coarse feedstock, (b) fine feedstock monolayer anodes and (c) bi-layered anode. Unlike the spectra of the cells with coarse and fine feedstock anode obtained during the beginning of the test, which did not demonstrate a decrease of the low frequency arc at polarized conditions compared to those at OCV, these spectra of the same cells demonstrated decreased impedance at polarization of 0.7V in comparison to impedance obtained at OCV. This result demonstrates an improvement of mass transport of those two types of cells, which suggests that a microstructural change may be occurring at the anode. There may also be partial reduction/activation of the cathodes occurring in the cells, which would reduce the total Rp of the cells over time.

Figure 5.14: Impedance spectra of cells with (a) coarse feedstock anode (b) fine feedstock anode and (c) bi-layered anode at OCV and at 0.7V obtained after 26 and 26.5 hours of operation

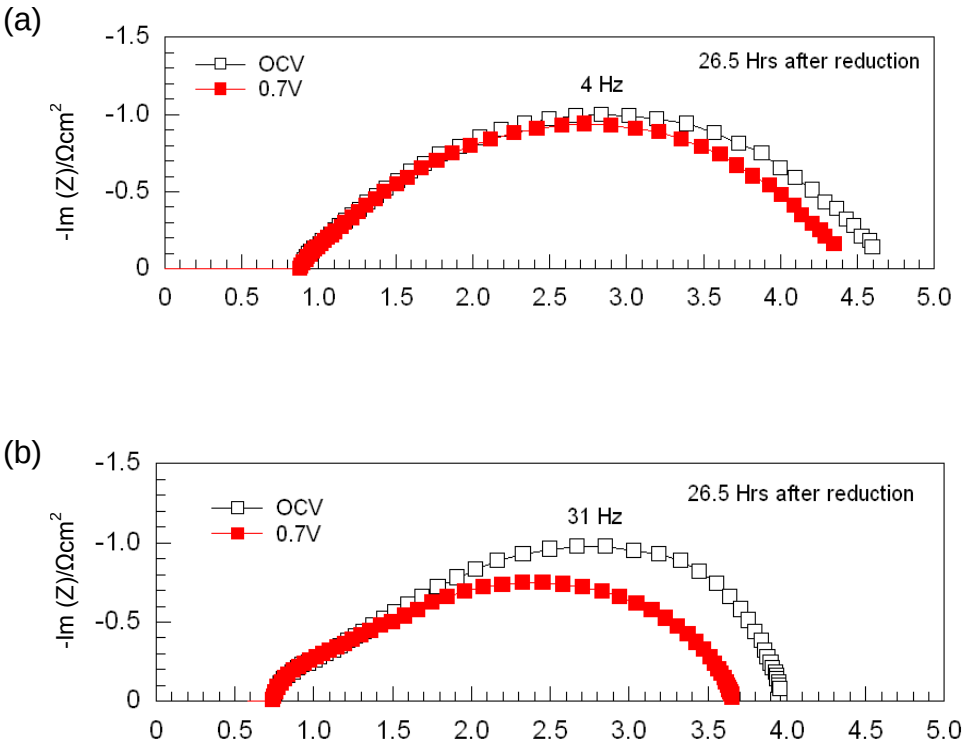

(c)

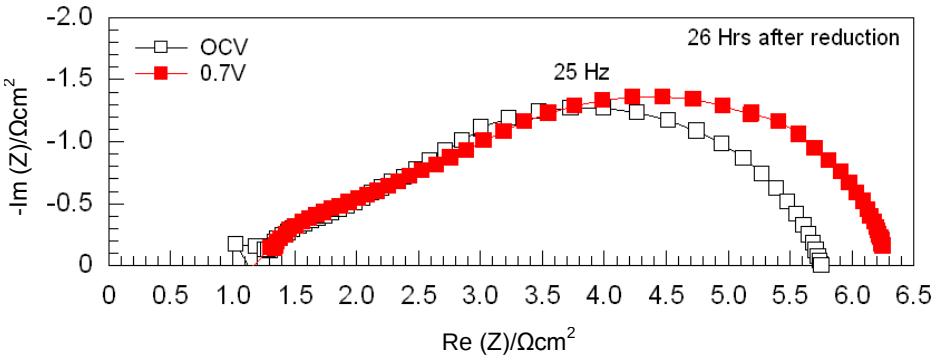

Unlike the coarse and fine feedstock cells, the bi-layered cell does not demonstrate a similar decrease of the low frequency arc diameter when the cell is polarized. This result can potentially be attributed to the initial low porosity of the Cu-YSZ conducting layer, as determined by image analysis. It is apparent that the microstructural change is not sufficiently large to result in a decrease of the low frequency arc diameter of the impedance spectrum when the cell is polarized.

5.2.3 Post-testing examination

5.2.3.1 Cell microstructure

A cross section SEM micrograph of a cell with fine feedstock anode after cell testing is shown in Figure 5.15. The microstructure looks more porous in comparison to the reduced fine feedstock anode coating shown in Figure 5.2(b). Figure 5.16 shows (a) a zoomed image of the tested fine feedstock anode and (b) a corresponding EDX map. Based on the EDX map, Cu and SDC particles can be identified in the coating. It can be seen in Figure 5.16(a) that the indicated Cu particle is detached from the SDC particle above it, and that there is empty volume surrounding the particle. It seems that a Cu particle has undergone partial sintering, as suggested by the pore volume surrounding

the particle. The original fine feedstock coating had splats that appeared to be in close contact with adjacent splats. The coating was less porous, and no isolated particles were observed having surrounding pore volume. The splats in the anode after testing are still attached to the surrounding particles, but with less material connecting them. This result indicates that the Cu particles may have partially detached from the surrounding particles during testing due to sintering.

Microsturcutral degradation of cermet anodes in SOFC is usually attributed to some kind of Ostwald ripening [132]. This mechanism might be assisted by a release of residual stresses that result from the PS processing. As the splats hit the substrate and rapidly cool and solidify, they are constrained mechanically by the underlying splats as their volume contracts due to the cooling. This constraint results in tensile residual stress, as pointed out in other studies [128]. The residual stress will cause a tendency of the CuO or Cu particles to contract during long operating times at elevated temperatures. Since the melting temperature of Cu is lower than that of CuO, once the cells have been heated and the CuO has been reduced to Cu, the Cu will be closer to its melting temperature than CuO, allowing higher mobility of the Cu phase compared to the CuO formed during coating deposition. Then, the residual stresses may cause the Cu to detach from the surrounding particles.

Figure 5.15: SEM micrograph of polished cross section of fine feedstock anode tested for 40hrs

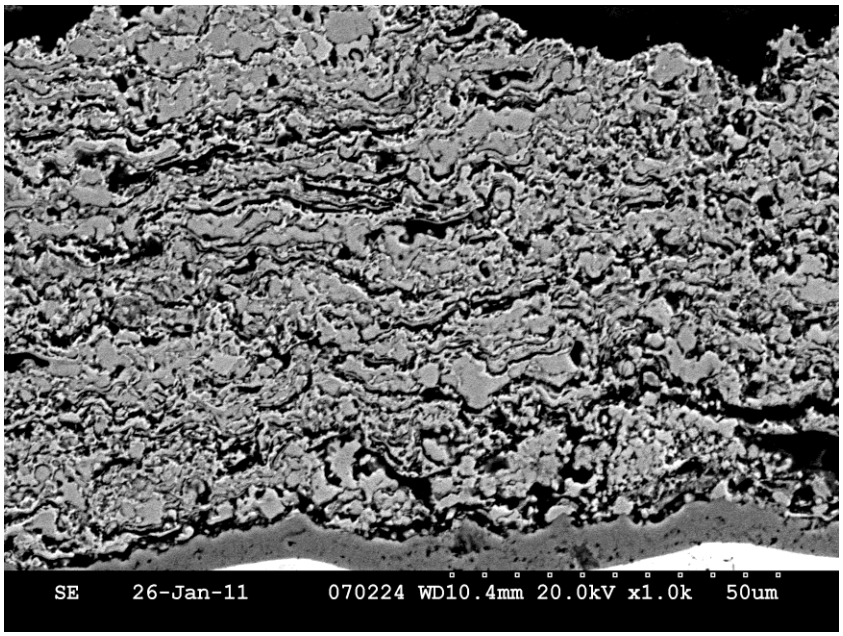

Figure 5.16: High magnification (a) SEM micrograph and (b) corresponding EDX map of polished cross section of fine feedstock anode tested for 40hrs

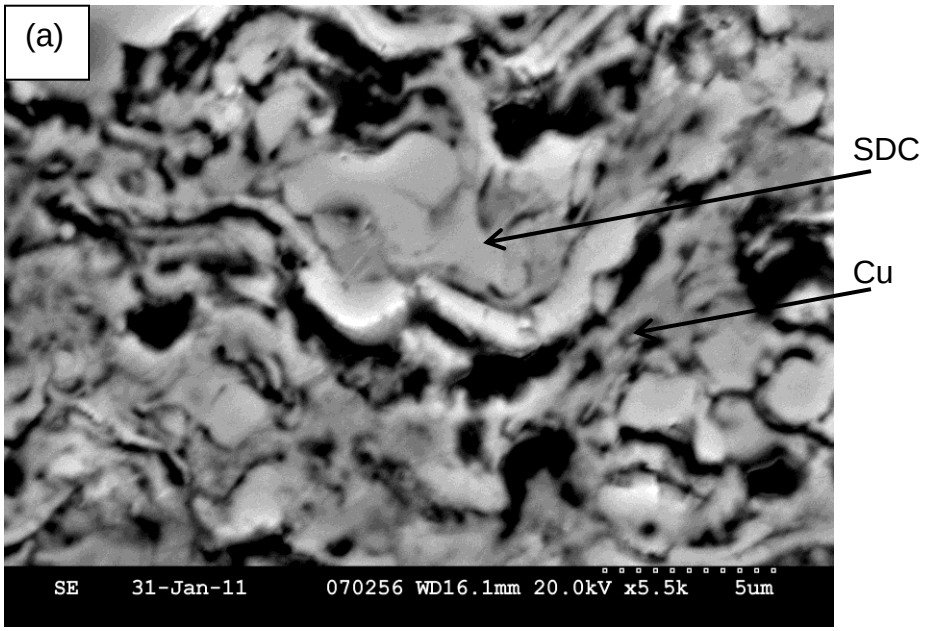

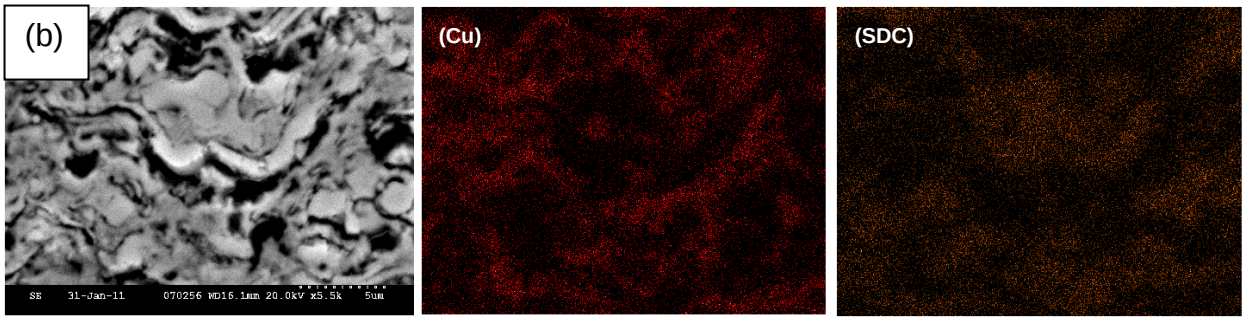

A cross section SEM micrograph of a tested cell with a coarse feedstock anode is shown in Figure 5.17. The non-conductive SDC looks brighter in SEM and the conductive Cu looks darker. It can be observed that a large number of the Cu particles have porosity surrounding them, and they are disconnected from the matrix in the plane of the micrograph, which was not observed in micrographs of the coating prior to testing. Figure 5.19 shows a high magnification SEM micrograph of a polished cross section of a tested cell with a coarse feedstock anode. The dark areas are either pores or pores filled with epoxy resin. It seems that the Cu particles undergo sintering and detach at least partially from the surrounding particles, resulting in some empty volume surrounding the Cu particles, and a less-connected conductive network of Cu compared to the anodes prior to cell testing.

Figure 5.17: SEM micrograph of a polished cross section of a coarse feedstock anode tested for 40hrs

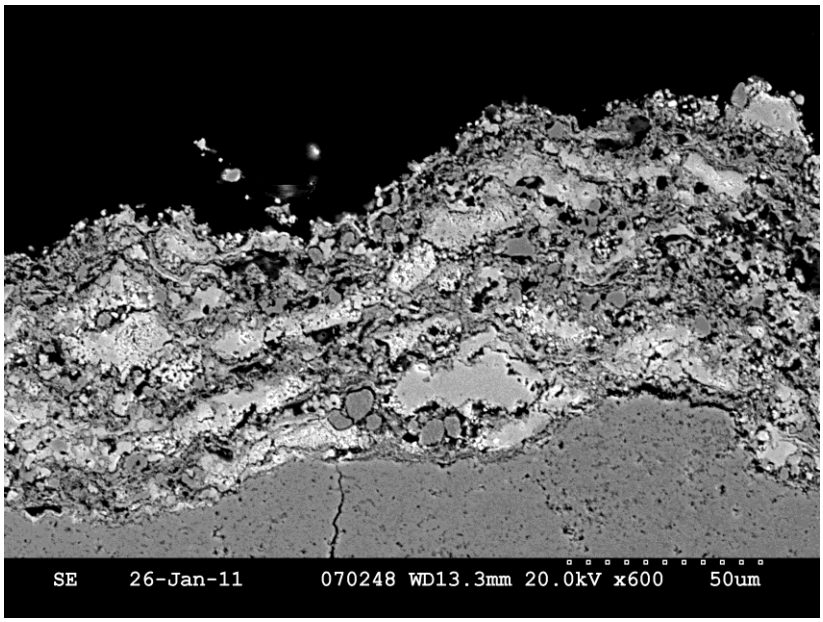

Figure 5.18: High magnification SEM micrograph of a polished cross section of a coarse feedstock anode tested for 40hrs

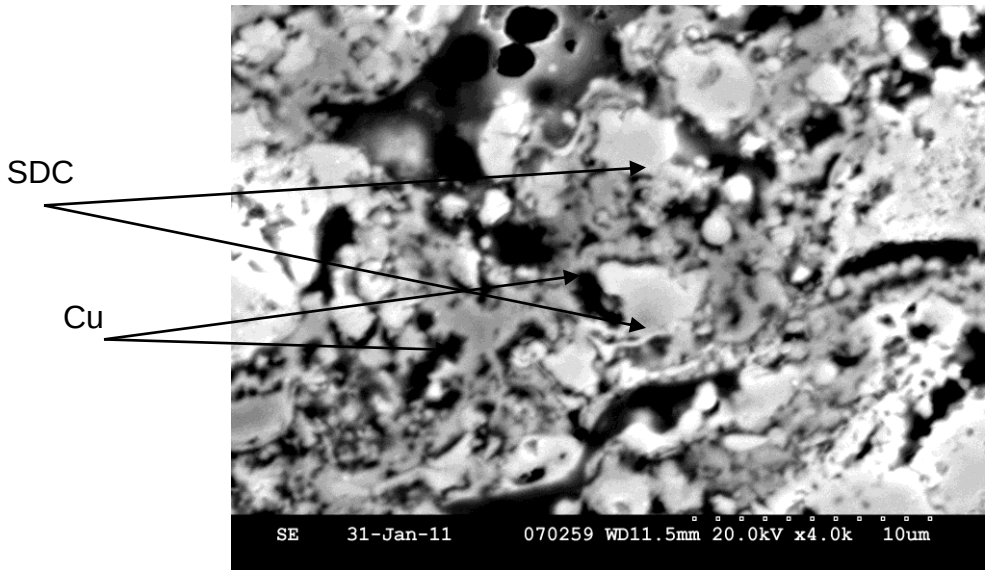

An SEM micrograph of a polished cross section of a tested cell with a bi-layered anode is shown in Figure 5.19. Unlike the other anodes, which demonstrated coarsening of the microstructure and high porosity, it seems that the Cu in the functional layer is highly sintered, resulting in reduced porosity. The conductive layer has a morphology with a fine pore structure due to the low extent of melting of the YSZ during fabrication. This observation agrees with the observed low absolute deposition efficiency of YSZ. One possible reason for the lack of increased porosity due to coarsening of the microstructure observed in the bi-layered anode cells, in contrast with the observations of the cells with fine and coarse feedstock monolayer anodes, is a possible stabilizing effect of the conductive layer, which makes the Cu less volatile, or due to a lower initial porosity, which leads to more densification during sintering at extended times at the operating temperature.

Figure 5.19: SEM micrograph of a polished cross-section of a bi-layered anode tested for 40hrs

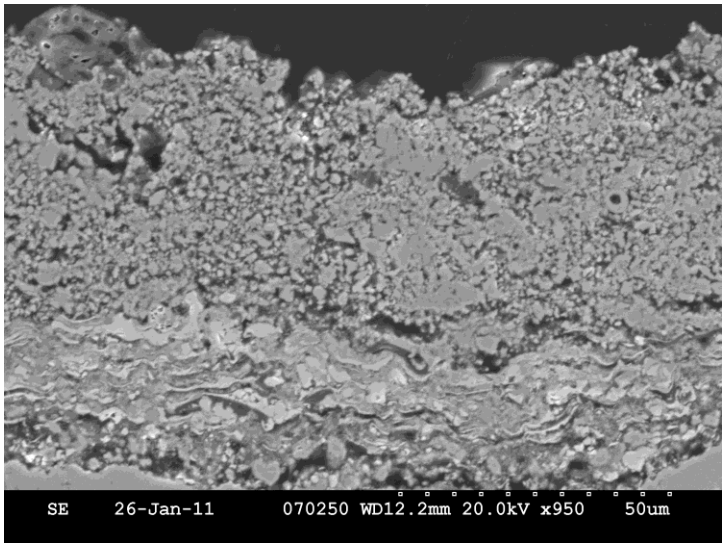

5.2.3.2 Local delamination

Figure 5.20 shows an SEM micrograph of a polished cross-section of a cell with a fine feedstock anode. Delamination of the anode is present locally, at a point at which the electrolyte has an irregular 'bump' in its shape. This delamination can occur when the anode is constrained mechanically while thermally expanding, thus creating localized stresses parallel to the anode-electrolyte interface that may cause delamination in areas of the anode where its geometry is not planar, but curved such as around a bump, due to the presence of localized stress concentrations. Such local delamination contributes to the overall degradation of performance, since a portion of the anode becomes inactive for electrochemical reaction. One possible cause for anode delamination is the heating rates of 5 °Cmin^{-1} required to form the glass seal. Due to the difference between the thermal expansion coefficients (CTEs) of YSZ (10.5-11.0X10^{-6} K^{-1} [133]) and of Cu (16.5X10^{-6} K^{-1} [134]), too-high heating rates may cause anode delamination due to the resulting thermal expansion mismatch. At this point, it is not clear whether the observed local delamination is an outcome of the applied heating rates during the test or was present after fabrication and prior to testing.

Figure 5.20: SEM micrograph of polished cross-section of a cell with a fine feedstock anode showing localized delamination

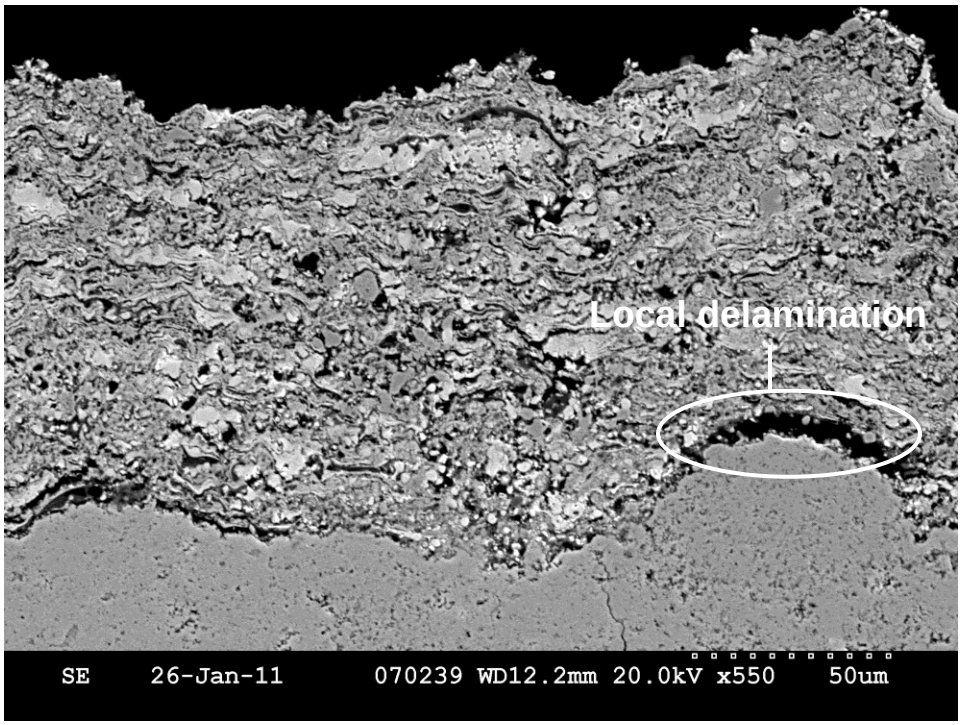

5.2.3.3 Substrate oxidation

SEM examination after the test of the SS430 porous substrate of the coarse cell demonstrated a loss of porosity, with Cr detected by EDX inside the substrate pores. This result can be caused by a local increase of temperature of the SS430 substrate resulting from combustion of gases leaking across the cell or its seals, leading to the rapid formation of a Cr_2O_3 layer on the stainless steel support. SEM micrographs on additional cross sections of the same cell did not show the same loss of porosity due to the formation of a chromia layer. This result indicates that the combustion occurred locally, likely resulting from gas leakage either through the electrolyte, through the seal, or through delaminated regions between cell layers. The formation of thick localized

chromia layers and their hypothesized origin due to leakage-induced combustion are in agreement with the lower open circuit voltage observed with this cell. Figure 5.21 shows an SEM micrograph of a polished cross section of a cell with a coarse feedstock anode with visibly blocked substrate porosity. Figure 5.22 shows an SEM micrograph of an additional polished cross section from a different location in the same cell without any visibly blocked substrate porosity.

Figure 5.21: Cross section micrograph of a cell with a coarse feedstock anode demonstrating blocked porosity in the substrate

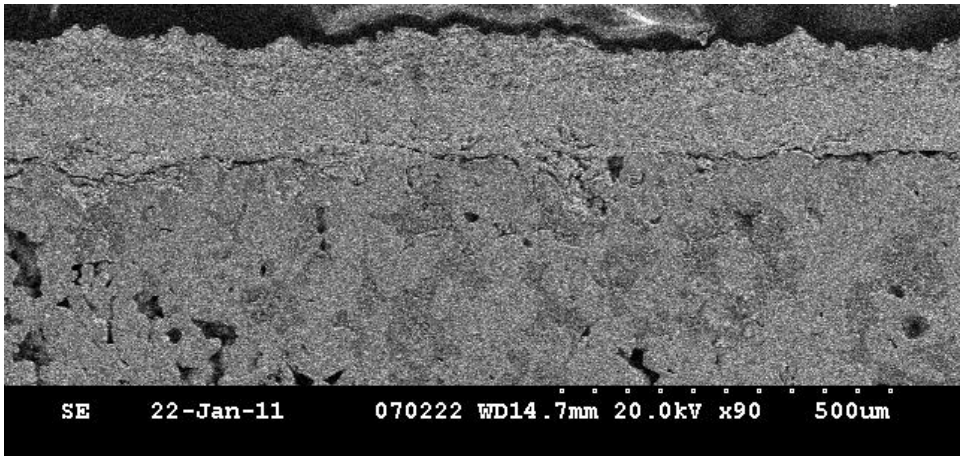

Figure 5.22: Cross section micrograph of the same cell as in Figure 5.21 from a different location, demonstrating open porosity in the substrate

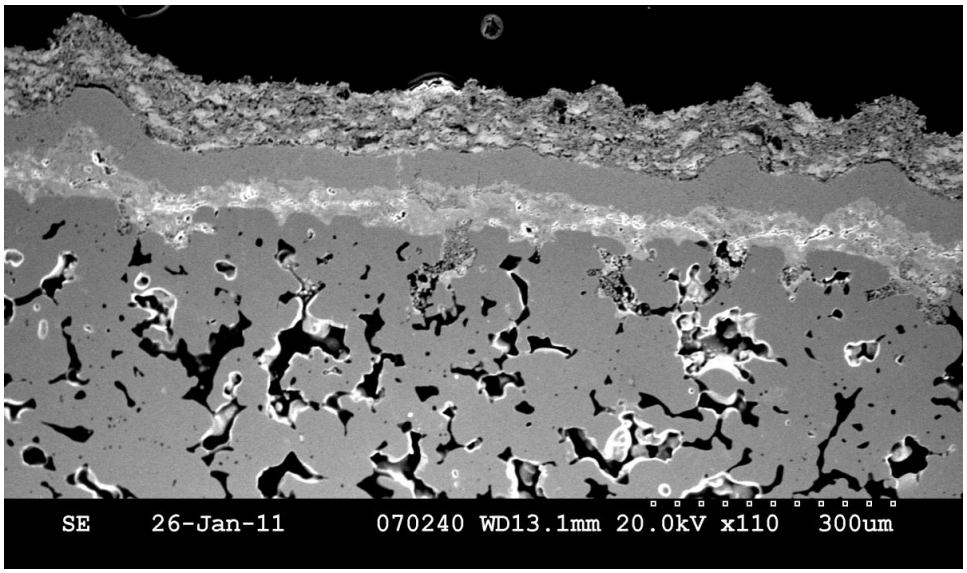

5.3 Conclusions

Cu based monolayer and bi-layered anodes were fabricated by air plasma spraying of coarse and fine feedstock powders. Cells were tested with 20% H_2/80% N_2 anode gas mixtures. Cells with coarse feedstock, fine feedstock and bi-layered anodes tested at 700°C exhibited power densities of 0.049 Wcm^{-2}, 0.036 Wcm^{-2}, and 0.034 Wcm^{-2}, respectively, and polarization resistances of 2.42 Ωcm^2, 2.23 Ωcm^2, and 1.98 Ωcm^2, respectively. Cells with coarse feedstock and bi-layered anodes demonstrated mass transport limitations, and cells with fine feedstock anodes were the least mass transport limited. Performance of all cells degraded with time. However, possible stabilization of the performance after several hours was observed. Cells undergo microstructural changes and possible sintering of Cu during extended operating times. Localized anode delamination was also observed after cell testing.

6. Conclusions

6.1 Analysis and integration of thesis results

This work aimed to investigate the production of Cu-SDC and Cu-Co-GDC/SDC anodes by PS. This work fits within the framework of the broader effort to utilize plasma spraying to fabricate SOFCs using a rapid deposition technique that can be easily automated for mass production, and the effort to utilize hydrocarbon fuels by direct oxidation in SOFC anodes. The material sets applied in this research presented a greater challenge than processing typical NiO-YSZ anodes, due to the large difference of melting temperatures between the copper oxide and the fluorite ceramic materials. This work aimed to develop an understanding of the deposition process of these materials sets by PS with the goal of obtaining the required anode characteristics: well mixed materials, high surface area, sufficient ionic and electronic conductivity, sufficient porosity, and proper crystal structure.

Due to the low catalytic activity inherent in copper-based anodes, one of the major focuses of this work was to increase the surface area of SDC in order to improve anode performance.

This work started with the investigation in Chapter 1, with the examination of feedstock powders and PS screening experiments over a broad range of plasma energy conditions. It was found that non-spray-dried powders tend to clog the feed lines during feeding to the plasma torch, and the resultant coatings have segregated Cu-SDC layers. Therefore, commercially available spray dried powders with spherical shapes were utilized for subsequent coating fabrication. These powders were agglomerates of nano-powders. There were two goals in applying these powders. First, it enabled the

feedstock powders to be fed without clogging. Second, the powder morphology allowed the manufacturing of finely-structured anodes, thus allowing an increased surface area of SDC and CuO compared to anodes fabricated from non-agglomerated powders. When fabricated anodes using the spray dried powders, it was found that the coatings were fairly homogenously mixed and no coarse-scale segregation of the layers was evident. The study suggested that segregation was due to clogging of the feedlines and not due to the different physical properties of the powders. It was also found that spray dried powders tend to break up during feeding and clog the feedlines. Therefore, calcining profiles were developed for each material. Since calcining coarsened the nanostructured powders, it was essential to determine calcination- profiles that would minimize the coarsening effect. To find the most desirable calcining profile, the non calcinced and calcined powder particle sizes were measured before and after feeding through the hopper. This approach developed in this study gave a good indication of the optimized calcining profile for each powder.

In chapter 1, feedstock powders were sprayed using a broad range of plasma powers. It was found that all materials remained crystalline during PS, and that SDC keeps it crystal structure during fabrication. This is an important result, given its role in the anode as a mixed conductor and also as a catalyst. This result also allows for a fairly wide spraying envelope of plasma energies. However, it was also found that the CuO is highly melted over the entire range of spraying parameters. It was not possible to co-deposit the CuO and SDC powders without completely melting the CuO. This result introduced a significant challenge, since the complete melting of the CuO during

deposition reduces the anode porosity compared to a structure in which both phases are partially melted upon deposition.

The approach of this work was therefore to accept the complete melting of the CuO as ‘given’, and to introduce the required porosity by adequate control of the PS parameters such that the SDC is only partially melted when it arrives at the substrate, but still sufficiently melted to produce a well-adhered coating. This requirement resulted in a narrower window of plasma spray parameters that can be applied compared to those that can be used to successfully deposit CuO alone. Since there was no instrumentation available to detect the effect of plasma parameters on the in-flight temperature and velocity of the particles, the study of the effect of plasma parameters on the coating characteristics was conducted by means of SEM, XRD, and EDX to determine the deposition efficiency, phase identity, and microstructure of the materials. This work aimed to keep the deposition efficiency as high as possible. Low deposition efficiencies are not desirable due to increased costs and potentially lower adhesion, with correspondingly higher electrical contact resistance.

After the initial coating fabrication studies, anode coatings were tested electrochemically in proof-of-concept cells, in the investigation presented in Chapter 3. The feedstock powder that was used for anode fabrication in full cells was sieved below 25μm in order to produce anodes with high surface area to be utilized as anode functional layers. Sieving of feedstock powders to isolate different size fractions was also utilized to produce bi-layered anode structures from feedstock powders having different average particle sizes, in order to evaluate the effects utilization such bi-layered structures on the cell performance. At an early stage of this work, sintered

electrolyte substrates were used to produce cells. It was found that sintered electrolytes easily break during fabrication due to thermal shock during spraying, thus limited the spraying conditions that could be used to only those resulting in low plasma powers. Later in this work, anodes were deposited on SS430 porous substrates, on which the cell layers were subsequently deposited in one process. The ability to use of metallic substrates is the primary benefit of PS processing in comparison to wet ceramic processing. It did require the development of the other cell layers conducted in parallel to this work, and therefore, it could not be used at an early stage of this work. The use of metallic substrates allowed the use of a broader spraying envelope for the fabrication of the anode layers. It was found that utilizing high plasma gas flow rates resulted in better coating microstructures and cell performances in initial studies of Cu-SDC anodes. The metal substrate cells had much lower polarization resistances than the YSZ electrolyte supported symmetrical cells, with 4.8 Ωcm^2 for anodes deposited on SS430 substrate-supported cells, in comparison to 21.8 Ωcm^2 for anode deposited on YSZ substrates, with both polarization resistances measured close to 700°C. This work suggests that the performance difference is due to the limitation of PS parameters that can be applied in the case of the YSZ electrolyte substrates, as well as the more rapid cooling of the coatings that solidify on thin ceramic layers deposited on metal supports, compared to on thick ceramic layers. In addition, the different substrate properties, i.e., thermal conductivity and surface roughness, resulted in better anodes with the SS430 substrates in comparison to those fabricated on the YSZ ceramic substrates, making the SS430 porous substrates a more desirable choice for PS of Cu-SDC anodes. The

anode coatings fabricated in metal-supported cells had fairly high surface areas, porosities, and extensive CuO-SDC mixing and contact.

After Cu-SDC layers were deposited, this work focused on the development of Cu-Co-SDC/GDC coatings, an investigation presented in Chapters 4 and 5. Co has been investigated due its potential advantage as a catalyst for direct oxidation, when it is combined with Cu. Studies with wet ceramic processed anodes showed that the Cu partially covers the Co, thus allowing the anode to have increased catalytic activity, but also partially resisting carbon deposition. In addition, Cu based anodes are thermally not stable, due to the low melting temperature of Cu. Other studies found that the addition of Co increased the thermal stability of Cu based anodes. The challenge with PS of Cu-Co-GDC anodes is to obtain sufficient mixing between the Cu and the Co. Mixing in PS occurs on a coarser scale than with wet ceramic processing. An additional challenge with PS deposition of Cu-Co-GDC anodes is the rapid cooling rates in comparison to the slow heating rates in wet ceramic processing, which makes it harder for the Cu to mix with the Co.

The development of Cu-Co-SDC/GDC anodes started with screening tests to examine the affect of plasma energy on coating properties and the absolute deposition efficiency. The plasma gas composition was chosen as the primary parameter of investigation, since it has a large influence over the plasma temperature and velocity. XRD analysis confirmed that all sprayed materials remain crystalline and that GDC remains cubic over the range of plasma gas compositions investigated. It was found that lower N_2 contents resulted in homogenous coatings, while higher N_2 contents resulted in non-homogenous coatings, in which the CuO is highly melted and the SDC

formed cauliflower-like clumps. This work attributes this behavior to high plasma velocities resulting from increased N_2 content in the plasma. This work suggests that high plasma velocities may not be desirable for spraying composite materials with a large range of melting temperatures, such as CuO and SDC, since it may result in non-homogenous coatings. The high impact speed resulted in thin splats of the low melting temperature material and unmelted clumps of the high melting temperature material. Low contents of N_2 were utilized applied to produce anode coatings to allow for partial melting of the feedstock

Further investigation included the calculation of the absolute deposition efficiency of coatings fabricated using various processing conditions. This work showed how the absolute deposition efficiency of each material varies with the plasma gas composition, and correlates to qualitative observations of the extent of melting of coating feedstock materials from SEM observation. This work also demonstrated how these data can be used to choose desired plasma gas compositions for the fabrication of composite coatings. Based on the absolute deposition efficiencies and microstructural analysis, plasma gas compositions were chosen to produce homogenous Cu-Co-GDC coatings.

Further investigation included the calculation and use of the relative deposition efficiency values to determine the feedstock mixing ratios required to produce coatings with the desired material composition. It was found that the relative deposition efficiency can be determined with high accuracy to obtain feedstock powder mixing ratios that result in the production of coatings with 40 solid vol % of the metallic phases and varying Co loadings that can be controlled.

The coatings produced with various Co loadings were investigated to determine porosity and permeation of the coatings. It was found that Co did not have a role in increasing porosity. The study suggested that this result was due to the high extent of melting of the CoO feedstock at the PS conditions used for coating fabrication. The coatings had relatively high porosities, ranging between 15 and– 20 vol%, in comparison to the typical porosity of plasma sprayed coatings, although these values are still lower than those typically utilized in the fabrication of SOFC electrode layers. This result demonstrated that by applying the approach of adjusting the PS parameters to obtain partial melting of the SDC, it was possible to obtain porous coatings despite the relatively low melting temperature of the CuO. Gas permeation constants were lower in comparison to values obtained by other studies with NiO-YSZ PS coatings. The study suggested that the low gas permeability in comparison to the extent of porosity was due to high gas phase tortuosity and possibly also to unreduced CuO or CoO enclosed by GDC phases.

To better understand whether the extent of mixing of Cu and Co is sufficient for the Cu to cover the Co, X-ray diffraction evaluation of the coatings was conducted. The study observed a shift of Cu peaks to higher angles, which indicated potential solid solution formation of Co with Cu. The study also observed that this shift was correlated to the amount of Co present in the coatings. This investigation was concluded by carbon deposition investigation of coatings with various Co loadings exposed to CH_4 at elevated temperatures. The study observed that carbon deposition did occur and was directly correlated with the amount of Co in the coatings. However, the total weight gain due to carbon deposition was similar to the values obtained during methane exposure

testing of anodes made by wet ceramic processing. This result demonstrated the feasibility of producing Cu-Co-GDC anodes by PS that can reduce the extent of carbon deposition compared to anodes containing Ni as the main electronically conductive and catalytically active phase.

To better understand the affect of microstructure on anode performance, anode coatings were produced with coarse and fine feedstock powders, in an investigation described in Chapter 5. It was originally hypothesized that anodes fabricated from coarser feedstock may exhibit better mass transport than anodes fabricated from fine feedstock, while the latter may provide increased surface area and better performance at low polarizations. Approximately 5 wt% of Co was used to fabricate anodes from different powder size feedstocks. Cu-Co-SDC monolayer anodes manufactured from coarse and from fine feedstock powders and Cu-Co-SDC/Cu-YSZ bi-layered anode were investigated for their initial microstructures, cell performances, and microstructural stability. Full cells were dwelled for several hours at operation temperatures to examine their performance stability over time. All cells demonstrated similar polarization resistances of approximately 2.0 Ωcm^2 in anode gas N_2-H_2 mixtures with 20% H_2. The study found that the fine feedstock anodes were the least mass transport limited among the three microstructures tested. This result contradicts the initial hypothesis that coarser feedstock powder would result in less severe mass transport limitations than the finer feedstock powder. The evident mass transport limitations made it hard to observe which anode had a higher surface area for the electrochemical reaction to occur, since all impedance spectra were similar, and it was not possible to separate the activation

polarization of the anodes alone from the total cell impedance. Further studies are required to clarify the reasons for the observed performances.

Degradation studies showed that all of the cell performances degraded with time. Both polarization and series resistances increased with time for all cells, but degraded at slower rates and approached stabilization of performance after several hours of testing. Examination of the cells after the tests showed the Cu detached from the surrounding particles due to sintering in some of the anodes. This behavior may be assisted by residual tensile stressed introduced during the PS process. This observation is consistent with results in other published studies, in which the Cu has been found to sinter over time in Cu-based anodes manufactured by wet ceramic processing methods.

The study concluded that it is possible to obtained well mixed microstructures with good contact between the different materials by PS, but that these anodes suffer thermal instability similarly to wet ceramic processed Cu-based anodes.

6.2 Project summary

This work demonstrated the application of a logical progression of experimental work to develop an understanding of the processing-microstructure-property-performance relationships of CuO-SDC, CuO-CoO-SDC/GDC, and CuO-YSZ anode materials fabricated by PS. It demonstrated that by adequate control and refinement of processing parameters and starting powders, it was possible to achieve coatings with properties not typical to the process. This work overcame processing challenges stemming from a material set having large differences between the melting temperatures of each material by focusing on obtaining partial melting of the higher

melting temperature material, i.e. SDC. The work thereby demonstrated the feasibility of obtaining homogenous Cu-SDC and Cu-Co-SDC/GDC anodes with performances comparable to those of Cu-based anodes processed by complex, multi-step wet ceramic processing techniques. To the author's knowledge, no study to date beside this work has demonstrated the manufacturing of Cu-SDC and Cu-Co-SDC/GDC anodes in working SOFCs by PS, and it was the first study to fabricate coatings of those materials sets.

6.3 Original contributions of this work

Major contributions to the general body of knowledge can be identified from this thesis work:

1. Understanding the relationship between process parameters and coating characteristics and electrochemical performances, to allow manufacturing of coatings with desired properties.

- Most PS coatings having low porosity. This work demonstrated that it is possible to obtain higher porosities by a careful choice of feedstock powder properties and adequate control of spraying parameters.

2. Demonstrating the feasibility of achieving sufficient mixing of CuO-CoO during deposition, thus allowing the Co to at least partly interdiffuse with Cu. This allowed the manufacturing of Cu-Co based anodes with a similar extent of carbon deposition as

anodes fabricated by a much more complex multi-step wet ceramic manufacturing process previously reported in the literature.

- To the author's knowledge, no other study to date has examined the carbon deposition behavior of PS Cu-Co based coatings for use in anodes.

3. Demonstrating the application of absolute deposition efficiency calculations to develop an understanding of the effects of process parameters on the coating properties.

4. Demonstrating the feasibility of producing bi-layered anode structures with a Cu-Co-SDC anode functional layer and a Cu-YSZ anode conducting layer.

5. Demonstrating the affect of starting powder particle size on the resulting coating and anode performance.

6. Identifying several potential causes of degradation of Cu-Co based anode performance over time.

6.4 Significance of this work

PS presents a rapid alternative to manufacturing of SOFCs by wet ceramic processing. It has several advantages over wet ceramic methods, such as compatibility with the use the of mechanically robust metallic cell supports, allowing reduced material cost and increased durability of SOFCs. It is more advantageous than wet ceramic

processing for early-stage scale-up towards mass production due to a more incremental cost structure and the ease of automating the process. However, to apply PS to manufacture SOFCs, it is essential to develop a good understanding of the effects of processing parameters on the coating characteristics. This work demonstrated the applicability of PS to process materials with a large range of melting temperatures by understanding the effect of PS parameters on the coating characteristics, and subsequent refinement of PS processing parameters to obtain desired coating characteristics and compositions. This work fits within the context of larger research efforts to make SOFCs more commercially available. An important aspect of this effort is the development of anodes for direct oxidation of hydrocarbon fuels. This work showed that a multi-step wet ceramic manufacturing process currently applied to manufacture Cu based anodes can be replaced by a simpler PS, allowing Cu based anodes with comparable performance to be manufactured in one simple step.

6.5 Future work

This work aimed to lay the foundation of production of Cu-Co based anodes by plasma spraying. It identified possible advantages but also challenges of fabricating such anodes. Future work needs to be conducted to address the challenges identified in the use of this material set for the fabrication of direct oxidation anodes.

6.5.1 Thermal stability

This work investigated degradation of Cu based anodes and suggested that sintering of Cu particles is one major cause for degradation of performance, and it

seemed that degradation occurs at decreased rates over time. Long term studies of anode performance are suggested to estimate to what extent performance degrades.

To enhance thermal stability, the introduction of materials other than Cu is suggested. Co has been shown to enhance anode stability in other studies. This work suggests that investigation of the effect of Co content on the thermal stability of Cu based anodes would be beneficial in conjunction with the results presented here on performances and carbon deposition rates.

6.5.2 Increased surface area

To further enhance anode performance, reduction of feedstock powder particle sizes is suggested. This reduction in feedstock size might require the investigation of suspension plasma spraying (SPS) or solution precursor plasma spraying (SPPS). Additional studies of the effect of introducing pore former during the anode fabrication process can allow for an increase in the anode porosity, potentially benefitting both the reaction surface area and the mass transport properties.

6.5.3 Increased porosity

This work demonstrated that Cu based anodes can be manufactured by PS with higher porosity in comparison to a typical PS process. However, this porosity is still lower than the desired porosity range of 30-40 vol%. This work suggests studying the addition of pore former to the feedstock powders to obtain increased porosity.

References

1. S. Lee, J. M. Vohs, R. J. Gorte, J. of the Electrochemical Society, 151 (2004) A1319-A1323

2. J. Molenda, K. Swierczek, W. Zajac, J. of Power Sources, 173 (2007) 657-670

3. S.C. Sighal, K. Kendall, "High Temperature Solid Oxide Fuel Cells: Fundamentals, Design and Applications", Elsevier Oxford 2003, pp. 150

4. M.D. Gross, J.M. Vohs, R.J. Gorte, J. of the Electrochemical Society, 154 (2007) B694-B699

5. D.W. Dees, T.D. Claar, T.E. Easler, D.C. Fee, and F.C. Mrazek, J. of the Electrochemical Society, 134 (1987) 2141-2146

6. A. Weber, E. Ivers-Tiffee, J. of Power Sources 127 (2004) 273-283

7. CRC Handbook of Chemistry and Physics, 91st Edition, 2010-2011, pp. 12:224

8. C. Sun, R. Hui, J. Roller, J. of Solid State Electrochemistry, 14 (2010), 1125–1144

9. C. Wang, L. Luo , Y. Wu, B. Hou, L. Sun, Materials Letters, 65 (2011) 2251–2253

10. J. Wang, D. Yan, J. Pu, B. Chi, L. Jian, International J. of Hydrogen Energy, 36 (2011) 7234-7239

11. S. H. Nien, C. S. Hsu, C. L. Chang, B. H. Hwang, Fuel Cells, 11 (2011) 178-183

12. N.Q. Minh, T. Takahashi, 'Science and technology of ceramic fuel cells', Elsevier 1995, pp. 291-293

13. R. Hui, Z. Wang, O. Kesler, L. Rose, J. Jankovic, S. Yick, R. Maric, D. Ghosh, J. of Power Sources, 170 (2007) 308–323

14. N. Curry, N. Markocsan, X. Li, A. Tricoire, M. Dorfman, J. of Thermal Spray Technology, 20 (2011) 108-115

15. J. R. Davis, 'Handbook of thermal spray technology', ASM International. Thermal Spray Society Training Committee (2004) pp. 171-208

16. J.H. Seo, J.S. Kim a, M.Y. Lee, W.T. Ju, I.T. Nam, Thin Solid Films, 519 (2011) 7111–7115

17. X.Q. Ma., H. Zhang, J. Dai, J. Roth, R. Hui, T.D. Xiao, D.E. Reisner, J. of Thermal Spray Technology, 14 (2005) 61-66

18. G. Schiller, R. Henne, M. Lang, M. Muller, Fuel Cells, 4 (2004) 56-61

19. S. Kim, O. Kwon, S. Kumar, Y.Xiong, C. Lee, Surface and Coatings Technology, 202 (2008) 3180-3186

20. R. Hui, Z. Wang, O. Kesler, L. Rose, J. Jankovic, S. Yick, R. Maric, D. Ghosh, , J. of Power Sources, 170 (2007) 308–323

21. R. Henne, J. of Thermal Spray Technology, 16 (2007) 381-403

22. R. Vaßen, H. Kaßner, A. Stuke, F. Hauler, D. Hathiramani, D. Stöver, Surface and Coatings Technology, 202 (2008) 4432 – 4437

23. M. Lang, T. Franco, G. Schiller, N. Wagner, J. of Applied Electrochemistry, 32 (2002) pp. 871-874

24. D. Waldbillig , O. Kesler, J. of Power Sources, 191 (2009) 320-329

25. C. Hwang, C. Yu, Surface and Coatings Technology, 201 (2007) 5954-5959

26. C. Hwang, C. Tsai, C. Lo, C. Sun, J. of Power Sources, 180 (2008) 132-142

27. H.I. Boulos, J. of Thermal Spray Technology, 1 (1992) 33-40

28. G. Renouard-Vallet, L. Bianchi, A.L. Sauvet, P. Fauchais, M. Vardelle, M. Boulos, F. Gitzhofer, Proceedings of the International Thermal Spray Conference (2004) p 132-137

29. J. R. Davis, 'Handbook of thermal spray technology', ASM International. Thermal Spray Society Training Committee (2004) pp. 54

30. A. Ansar, D. Soysal, G. Schiller, International J. of Energy Resources, 33 (2009) 1191–1202

31. H. G. Merkus, 'Particle Size Measurements: Fundamentals, Practice, Quality', 2009 Springer Science+Business Media

32. P. Fauchais, J.F. Coudert, M. Vardelle, A. Vardelle, A. Denoirjean, J. of Thermal Spray Technology, 1(1992) 117–128

33. J.F. Coudert, M.P. Planche, P. Fauchais, Plasma Chemistry and Plasma Processing, 15 (1995 47-70

34. S.C. Snyder, L.D. Reynolds, J.R. Fincke, G.D. Lassahn, J.D. Grandy, T.E. Repetti, Physical Review E - Statistical Physics, Plasmas, Fluids, and Related Interdisciplinary Topics 50 (1994 519–525

35. B. Selvan, K. Ramachandran, B.C. Pillai, and D. Subhakar, J. of Thermal Spray Technology, 20 (2011) 534-548

36. D. Matejka, B. Benco, 'Plasma Spraying of Ceramic and Metallic Materials', Wiley & Sons Chichester UK, pp. 27

37. P Fauchais, J. of Physics D: Applied Physics, 37 (2004) R86–R108

38. D. Matejka, B. Benko, "Plasma Spraying of Mettalic and Ceramic Materials", Wiley & Sons (1989), pp. 32

39. D. Matejka, B. Benko, "Plasma Spraying of Mettalic and Ceramic Materials", Wiley & Sons (1989), pp. 40

40. L. Tai and P.A. Lessing, J. of the American Ceramics Society, 74 (1991) 501-504

41. O.C. Kwon, C. Lee, S.Y. Hwang, Conference Proceedings ITSC 2007

42. H. Weckmann, A. Syed, Z. Ilhan, and J. Arnold, J. of Thermal Spray Technology, 15 (2006) 604-609

43. B.D. White, O. Kesler, Advanced Materials Research, 15-17 (2006) 299-304

44. D. Waldbillig, 'Aqueous suspension plasma spraying of yttria stabilized zirconia solid oxide fuel cell electrolytes', Thesis, (PhD), University of British Columbia 2010

45. Waldbillig, D., Kesler, O., Surface and Coatings Technology, 203 (2009) 2098-2101

46. Waldbillig, D., Kesler, O., Journal of Power Sources, 196 (2011) 5423-5431

47. Waldbillig, D., Kesler, O, Surface and Coatings Technology, 205 (2011) 5483-5492

48. H. C. Chen, J. Heberlein, R. Henne, J. of Thermal Spray Technology, 9 (2000) 348-353

49. X.Q. Ma, S. Hui, H. Zhang, J. Dai, J. Roth, T.D. Xiao, D.E. Reisner, Thermal Spray 2003: Advancing the Science & Applying the Technology, (Ed.) C. Moreau and B. Marple, pp. 163-168

50. D. Gallagher,'Process Cost Modelling of Solid Oxide Fuel Cell Manufacturing', M.Eng. Thesis, Department of Mechanical and Industrial Engineering, University of Toronto 2009, pp. 100

51. D. Gallagher,'Process Cost Modelling of Solid Oxide Fuel Cell Manufacturing', M.Eng. Thesis, Department of Mechanical and Industrial Engineering, University of Toronto 2009, pp. 104

52. A. Gebregergis, P. Pillay, D. Bhattacharyya, R. Rengaswemy, IEEE Transactions on Industrial Electronics, 56 (2009) pp. 139-148

53. Popkirov G.S, Schindler R.N, Electrochimica Acta, 40 (1995) 2511–17

54. X. Yuan , C. Song , H. Wang, J. Zhang, 'Electrochemical Impedance Spectroscopy in PEM Fuel Cells: Fundamentals and Applications', Springer London UK 2010, pp. 135

55. S. Primdahl , P. V. Hendriksen " High Temperature Electrochemistry: Ceramics and Metals", F. W. Poulsen, N. Bonanos, S. Linderoth, M. Mogensen and B. Zachau-Christiansen, Editors, 17th Risø International Symposium on Materials Science Roskilde, DK (1996), pp. 403-410

56. S. Primdahl, M. Mogensen, J. of the Electrochemical Society, 144 (1997) 3409-3419

57. S. Primdahl, M. Mogensen, J. of the Electrochemical Society, 145 (1998) 2431-2438

58. S. C Singhal, K. Kendall, 'High Temperature Solid Oxide Fuel Cells: Fundamentals, Design and Applications', Elsevier Oxford UK 2003, pp. 158

59. S. C Singhal, K. Kendall, 'High Temperature Solid Oxide Fuel Cells: Fundamentals, Design and Applications', Elsevier Oxford UK 2003, pp. 251-256

60. J. Larminie, A. Dicks, "Fuel Cells Systems Explained", Wiley Chichester, 2000, pp. 192-193

61. R. Peters, R. Dahl, U. Klüttgen, C. Palm, D. Stolten, J. of Power Sources, 106 (2002) 238–244

62. R. J. Gorte, S. Park, J. M. Vohs, C. Wang, Advanced Materials, 12 (2000) 1465-1469

63. S. McIntosh, R.J. Gorte, Chemical Reviews 104 (2004) 4845-4865

64. K. Eguchi, H. Kojo, T. Takeguchi, R. Kikuchi, K. Sasaki, Solid State Ionics, 152-153 (2002) 411-416

65. J. Maček, B. Novosel, M. Marinšek, J. of the European Ceramic Society, 27 (2007) 487-491

66. S. Jung, C. Lu, H. He, K. Ahn, R.J. Gorte, J.M. Vohs, J. of Power Sources, 154 (2006) 42-50

67. R.J. Gorte, J.M. Vohs, S. McIntosh, Solid State Ionics, 175 (2004) 1-6

68. X. Ye, S.R. Wang, J. Zhou, F.R. Zeng, H.W. Nie, T.L. Wen, J. of Power Sources, 196 (2011) 5499-5502

69. X. Ye, S.R. Wang, Z.R. Wang, L. Xiong, X.F. Sun, T.L. Wen , J. of Power Sources, 177 (2008) 419–425

70. S. Islam, J. M. Hill, J. of Power Sources, 196 (2011) 5091-5094

71. N. Ai, K. Chen, S. Jiang, Z. Lu, W. Su, International J. of Hydrogen Energy, 36 (2011) 7661-7669

72. S. C. Singhal, K. Kendall, 'High Temperature Solid Oxide Fuel Cells: Fundamentals, Design and Applications', Elsevier Oxford UK 2003, pp. 343

73. S.Park, R. J. Gorte, J. M. Vohs, Applied Catalysis A: General, 200 (2000) 55–61

74. S. Jiang, L. Liu, K. P. Ong, P. Wu, J. Li, J. Pu, J. of Power Sources, 176 (2008) 82–89

75. S.Q. Hui, A. Petric, Journal of the European Ceramic Society, 22 (2002) 1673-1681

76. S.W. Tao, J.T.S. Irvine, Nature Materials, 2 (2003) 320-323

77. R.J. Gorte, H. Kim, J.M. Vohs, J. of Power Sources, 106 (2002) 10–15

78. S. McIntosh, J. M. Vohs, and R. J. Gorte, J.l of the Electrochemical Society, 150 (2003) A1305-A1312

79. E. W.Park, H. Moon, M. Park, S. H. Hyun, International Journal of Hydrogen Energy, 34 (2009) 5537-5545

80. L. F. D'Elia Camacho, J. A. Moncada Vivas, Fuel, 88 (2009) 1970–1974

81. A. Hornés, P. Bera, M. Fernández-García, A. Guerrero-Ruiz, A. Martínez-Arias, Applied Catalysis B: Environmental, 111–112 (2012) 96–105

82. X. Ye, J. Zhou, S.R. Wang, F.R. Zeng, T.L. Wen, Z.L. Zhan, International J. of Hydrogen Energy, 37 (2012) 505-510

83. G. Chen, G. Guan, Y. Kasai, H. You, A. Abudula, J. of Solid State Electrochemistry, 16 (2012) 2071–207784. A. Fuerte, R.X. Valenzuela, M.J. Escudero, L. Daza, J. of Power Sources, 196 (2011) 4324–4331

85. X. Ye, S.R. Wang, Q. Hu, J.Y. Chen, T.L. Wen, Z.Y. Wen, Solid State Ionics, 180 (2009) 276-281

86. C. Lu, W.L. Worrell, J.M. Vohs, R.J. Gorte, J. of the Electrochemical Society, 150 (2003) A1357-A1359

87. S. Zhao, R.J. Gorte, Applied Catalysis A: General, 277 (2004) 129–136

88. M.D. Gross, J.M. Vohs and R. J. Gorte, J. of Materials Chemistry, 17 (2007) 3071-3077

89. L. F. D'Elia Camacho, J. A. Moncada Vivas, Fuel, 88 (2009) 1970–1974

90. N. Kaklidis, G. Pekridis, C. Athanasiou, G.E. Marnello, Solid State Ionics, 192 (2011) 435–443

91. M. Cimenti and J. M. Hill, Asia-pacific Journal of Chemical Engineering, 4 (2009) 45–54

92. X. Ye, S.R. Wang, Q. Hu, Z.R. Wang, T.L. Wen, Z.Y. Wen, Electrochemistry Communications, 11 (2009) 823–826

93. A.C. Tavares, B.L. Kuzin, S.M. Beresnev, N.M. Bogdanovich, E.Kh. Kurumchin, Y.A. Dubitsky, A. Zaopo, J. of Power Sources, 183 (2008) 20-25

94. N. E. Kiratzis, P. Connor, J. T. S. Irvine, J. of Electroceramics, 24 (2010) 270–287

95. J.-J. Lee, E.-W. Park and S.-H. Hyun, Fuel Cells, 10 (2010) 145–155

96. S. McIntosh, J. M. Vohs, R. J. Gorte, Electrochemical and Solid-State Letters, 6 (2003) p A240-A243

97. S.W. Jung, J. M. Vohs, and R. J. Gorte, J. of the Electrochemical Society, 154 (2007) B1270-B1275

98. M.D. Gross, J. M. Vohs, R.J. Gorte, Electrochimica Acta, 52 (2007) 1951-1957

99. A. Fuertea, R.X. Valenzuelaa, M.J. Escuderoa, L. Dazaa, J. of Power Sources, 196 (2011) 4324-4331

100. S.-K. Lee, K. Ahn, J. M. Vohs, R.J. Gorte, Electrochemical and Solid-State Letters, 8 (2005) A48-A51

101. M. D. Gross, J. M. Vohs, and R. J. Gorte, Electrochemical and Solid-State Letters, 10 (2007) B65-B69

102. J. S. Ahn, H. Yoon, K. T. Lee, M. A. Camaratta, E. D. Wachsman, Fuel Cells, 9 (2009) 643–649

103. N.P Brandon, D.J Brett, Philosophical Transactions of the Royal Society A, 364 (2006) 147-159

104. J.J. Lee, E.W. Park, and S.H. Hyun, Fuel Cells, 10 (2010) 145–155

105. R, Hui, J. Oberste Berghaus, C. Decès-Petit, W. Qu, S. Yick, J.-G. Legoux, C. Moreau, J. of Power Sources, 191 (2009) 371–376

106. A. Benyoucef, D. Klein, C. Coddet, B. Benyoucef, Surface and Coatings Technology, 202 (2008) 2202-2207

107. A.Benyoucef, D. Klein, O. Rapaud, C. Coddet, B. Benyoucef, J.of Physics and Chemistry of Solids, 70 (2009) 1487-1495

108. P. Fauchais, G. Montavon, M. Vardelle, J. Cedelle, Surface and Coatings Technology, 201 (2006) 1908–1921

109. CRC Handbook of Chemistry and Physics, 91st Edition, 2010-2011, pp. 4-62

110. CRC Handbook of Chemistry and Physics, 91st Edition, 2010-2011, pp. 4-60

111. CRC Handbook of Chemistry and Physics, 91st Edition, 2010-2011, pp. 4-57

112. J. Iwaszko, Z. Nitkiewicz, Materials and Manufacturing Processes, 17 (2002) 169-176

113. B.D. White, O. Kesler, L. Rose, J. of Power Sources, 178 (2008) 334–343

114. D. Matejka, B. Benko, “Plasma Spraying of Mettalic and Ceramic Materials”, Wiley & Sons (1989), pp. 31

115. CRC Handbook of Chemistry and Physics, 91st Edition, 2010-2011, pp. 4-61

116. CRC Handbook of Chemistry and Physics, 91st Edition, 2010-2011, pp. 4-56

117. CRC Handbook of Chemistry and Physics, 91st Edition, 2010-2011, pp. 4-86

118. CRC Handbook of Chemistry and Physics, 91st Edition, 2010-2011, pp. 4-79

119. J.H. Lee, H. Moon, H.-W. Lee, J. Kim, J.-D. Kim, K.-H Yoon, Solid State Ionics, 148 (2002) 15-26

120. Q.-A. Huang, J. Oberste-Berghaus, D. Yang, S. Yick, Z. Wang, B. Wang, R. Hui, J. of Power Sources, 177 (2008) 339–347

121. J.-G. Li, T. Ikegami, T. Mori, Acta Materialia, 52 (2004) 2221–2228

122. S. Primdahl, P.V. Hendriksen, P. H. Larsen, B. Kindl, M. Mogensen In: Proceedings of the 7th International symposium on solid oxide fuel cells (SOFC-VII), Tsukuba (JP) 2001 M. Dokiya, S. C. Singhal, H. Yokokawa (eds.), (The Electrochemical Society, Pennington, NJ, 2001) (Proceedings volume 2001-16) p. 932-941

123. C. Zhang, C.-J. Li, G. Zhang, X-J. Ning, C.-X. Li, H. Liao, C. Coddet, Materials Science and Engineering B, 137 (2007) 24–30

124. K. R. Reddy, K. Karan, J. of Electroceramics, 15, 45–56, 2005

125. CRC Handbook of Chemistry and Physics, 91st Edition, 2010-2011, pp. 4-59

126. M.Palumbo, S.Curiotto, L.Battezzati, Calphad, 30 (2006) 171-178

127. T. Nishizawa, K. Ishida, Journal of Phase Equilibria, 5 (1984) 161

128. S. Kuroda, T. Fukushima, S. Kitahara, J. of Thermal Spray Technology, 1 (1992) 325-332

129. D. Simwonis, H. Thülen, F. J. Dias, A. Naoumidis, D. Stöver, J. of Materials Processing Technology, 92-93 (1999) 107-111

130. C. Lu and W. L. Worrell, Meeting Abstracts, 2004 Joint International Meeting - 206th Meeting of the Electrochemical Society/2004 Fall Meeting of the Electrochemical Society of Japan, MA 2004-02, p. 1723 (2004)

131. CRC Handbook of Chemistry and Physics, 91st Edition, 2010-2011, pp. 4-101

132. L. Holzer, B. Iwanschitz, Th. Hocker, B. Münch, M. Prestat, D. Wiedenmann,

U. Vogt, P. Holtappels, J. Sfeir , A. Mai, Th. Graule, Journal of Power Sources 196 (2011) 1279–1294

133. H. Hayashi, T. Saitou, N. Maruyama, H. Inaba, K. Kawamura, M. Mori, Solid State Ionics 176 (2005) 613 – 619

134. CRC Handbook of Chemistry and Physics, 91st Edition, 2010-2011, pp. 12-206

Appendices

Appendix A: Cell mounting and real-time temperature measurement apparatus for plasma spraying

A.1 General

In order to produce 1” button cells for electrochemical testing, a mounting device incorporating in-situ temperature measurement was designed to allow mounting of 1” or other button cell diameters during plasma spraying. The design is highly modular, allowing flexibility of cell dimensions and incorporation of changes if necessary of the size and shape of the sprayed substrates. An important feature of the mounting device is that it allows real time measurement of the substrate temperature during spraying. The temperature signal is transferred from a turntable through a slip ring mechanism. Initially, the temperature measurement system was designed to allow control of the substrate temperature by a heater, allowing preheating of the substrate and maintaining its temperature by a controller. Eventually, pre-heating of the substrate was conducted by the plasma torch, and a substrate heater was not incorporated into the system. The mounting device designed during this work was used by the SOFC group for spraying different SOFC components.

A.2 Design concepts

A.2.1 Modularity

One of the main goals of the mounting system design is to allow modularity, allowing easy change of mounting holders for substrates of different sizes and shapes.

The design took place at the beginning of experimental work, and there was no data available regarding the converged size and shape of the cells. The mounting device was designed to allow spraying of 24 samples simultaneously to allow averaging of the coating and cell characteristics for cell analysis purposes. Initially, the mounting device was designed with a spring loading mechanism to provide flexible backing for the ceramic cells while spraying, to reduce the chance of breaking. Later, when ceramic substrates were replaced by metallic substrates, the spring loading mechanism was no longer necessary, and it was eliminated from the design.

A.2.2 User friendliness

The mounting device was designed to be user friendly, with fast and easy insertion of the cells prior to spraying and easy removal of the cells after spraying.

A.2.3 Substrate temperature monitoring

The scientific literature emphasizes the important influence of the substrate temperature on the coating characteristics. Therefore, the capability to monitor substrate temperature during spraying was a substantial part of the experimental work, and therefore substrate temperature instrumentation was included in the cell mounting set-up. To measure the substrate temperature, several options were considered.

- Stationary infrared temperature measurement of the rotating substrate.
- Infrared sensor mounted externally on the cell mounting device.

- A thermocouple placed inside the cell mounting device, with the signal transferred through a slip ring mechanism to a temperature display or data acquisition card.

Stationary infrared temperature measurement of a rotating substrate needed to involve synchronization with the rotation of the turntable, to allow it to measure the substrate temperature while the drum is turning. In addition, the measurement might be affected by emissivity of the metallic substrate holder when it heats up during spraying.

An infrared sensor mounted on the rotating substrate holder might be exposed to excessive heat from the plasma, and this may result in malfunction of the sensor. The cheapest and most reliable set up is a thermocouple mounted inside the substrate holder, and therefore protected from the plasma combined with a slip ring that transfers the signal to a temperature display. Later, the temperature display was replaced by a data acquisition card to allow recording of the substrate temperature.

A.3 Schematics

Figure A.1 shows a mechanical drawing of the turntable as received from the manufacturer.

Figure A.1: Manufacturer's turntable system

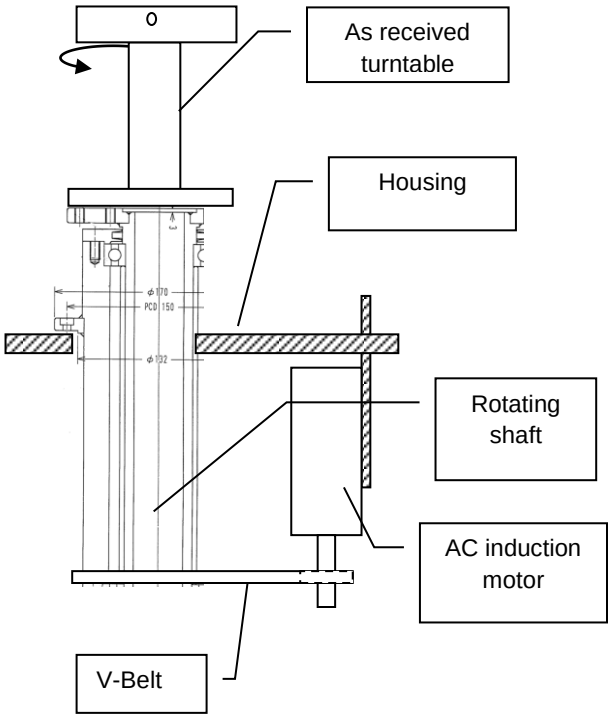

Figure A.2 shows a schematic of the temperature measurement set-up, using a thermocouple. The thermocouple is wired through a commercially available amplifier/signal conditioner mounted inside the mounting system, to reduce error and noise that might be introduced when the thermocouple signal is transferred through a slip ring before amplification and conditioning. The amplifier conditions the signal, and transforms linearly the millivoltic scale of the thermocouple signal to a current signal in the range of 4mA-20mA. Then, the signal is converted to a temperature reading by a display.

Figure A.2: Schematics of the temperature measurement apparatus in the mounting system. Electrical connections are dotted.

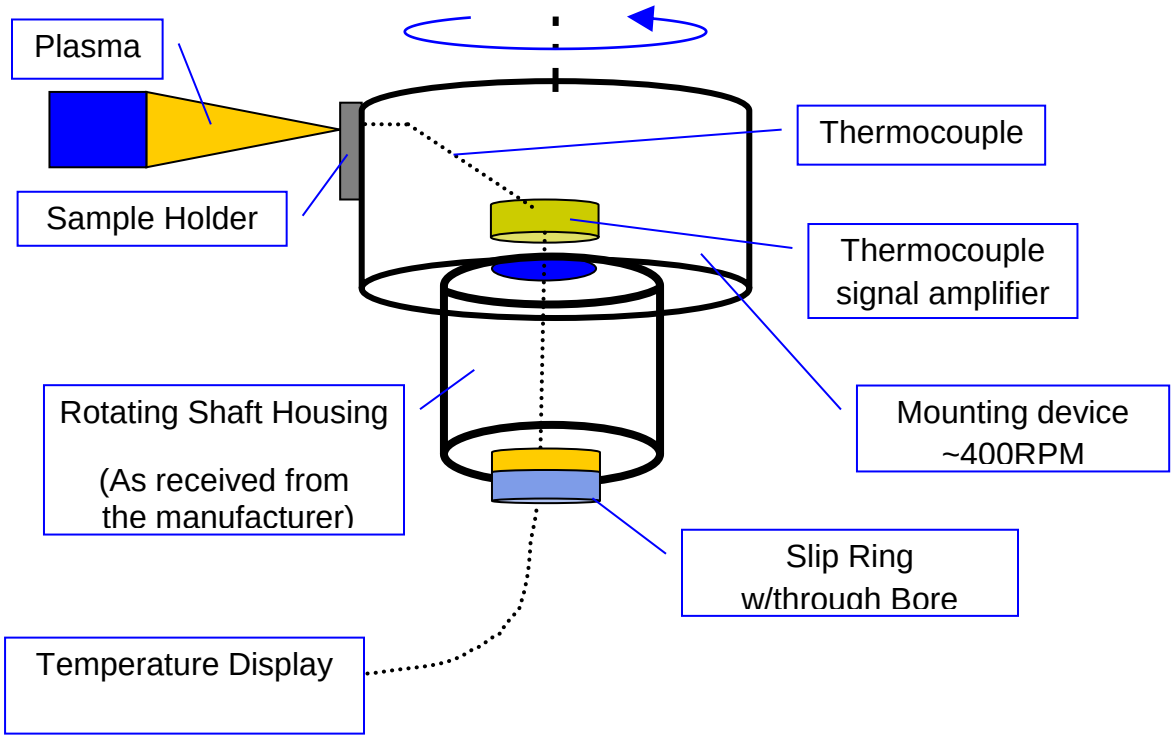

A.4 Part list

Table A.1 shows the parts that were purchased for the temperature measurement system.

Table A.1: Part list of the temperature measurement equipment

Description	Part Number	Supplier	Quantity
Slip Ring	CAY-1030	Airflyte	1
Temperature Display + Controller	CNi3253	Omega	1
Power Supply	PSU-93	Omega	1
Signal conditioner / Transmitter	TX251	Omega	1
Type K thermocouple simulator / Calibrator	CL601K	Omega	1
Solid Probe Bayonet Style Thermocouple	BTH-090-K-3-60-2	Omega	1
Adaptor for Bayonet-Type Thermocouples	BTA-2	Omega	1

A.5 Temperature measurement component description

A.5.1 Thermocouple

A low-cost type K solid probe bayonet style thermocouple was utilized. Spring loading allows continuous contact between the substrate and the thermocouple to be maintained.

A.5.2 Slip ring

A slip ring allows the maintenance of electrical connection from a rotating device to a stationary device. It is constructed from a rotating part and a stationary part with brushes maintaining electrical contact. Connecting a thermocouple to a slip ring introduces an additional junction to the temperature measurement circuit, and therefore, the thermocouple signal has to be conditioned by a signal conditioner before it is transmitted electrically through a slip ring. The signal conditioner has to be calibrated to provide an accurate reading.

A.5.3 Signal conditioner / Transmitter

A signal conditioner/transmitter is used to convert the millivolt signal of the thermocouple to a 4mA-20mA current signal, linearly correlated with the thermocouple signal corresponding to the temperature measurement. Placing the signal conditioner as close as possible to the thermocouple may reduce noise and thus lead to a more accurate temperature measurement. This is particularly important in the case of a slip ring, since the slip ring contacts introduce additional junctions to the circuit. The signal conditioner/transmitter is mounted inside the mounting device and it conditions the signal electronically before it passes through the slip ring.

A.5.4 Temperature display

A temperature display converts the output signal of the signal conditioner/transmitter into a temperature reading. It has outputs for relays, and it can also be used as a PID controller. This temperature display has been design to allow for future incorporation of a substrate heater and temperature control.

A.5.5 Thermocouple simulator

A thermocouple simulator is used to simulate a thermocouple signal for the entire temperature range, eliminating the need for an ice bath.

A.6 Electrical drawing

Figure A.3 shows the electrical drawing of the substrate temperature measurement system. The type “K” thermocouple is connected to inputs 2 and 4 of the signal

conditioner TX251, where the negative lead of the thermocouple is connected to input 2, and the positive lead of the thermocouple is connected to input 4. Outputs 1 and 5 of the TX251 signal conditioner pass through the slip ring, where output 5 is connected to the positive lead of a PSU-93 unregulated power supply, and output 1 is connected to process input 6 of the temperature display CNi3253. The negative lead of the PSU-93 power supply is connected to process input 1 of the CNi3253. The CNi3253 has an AC power source connected to power inputs 7 and 8. The AC power passes through a fuse to protect the CNi3253.

Figure A.3: Electrical diagram of the substrate temperature measurement system

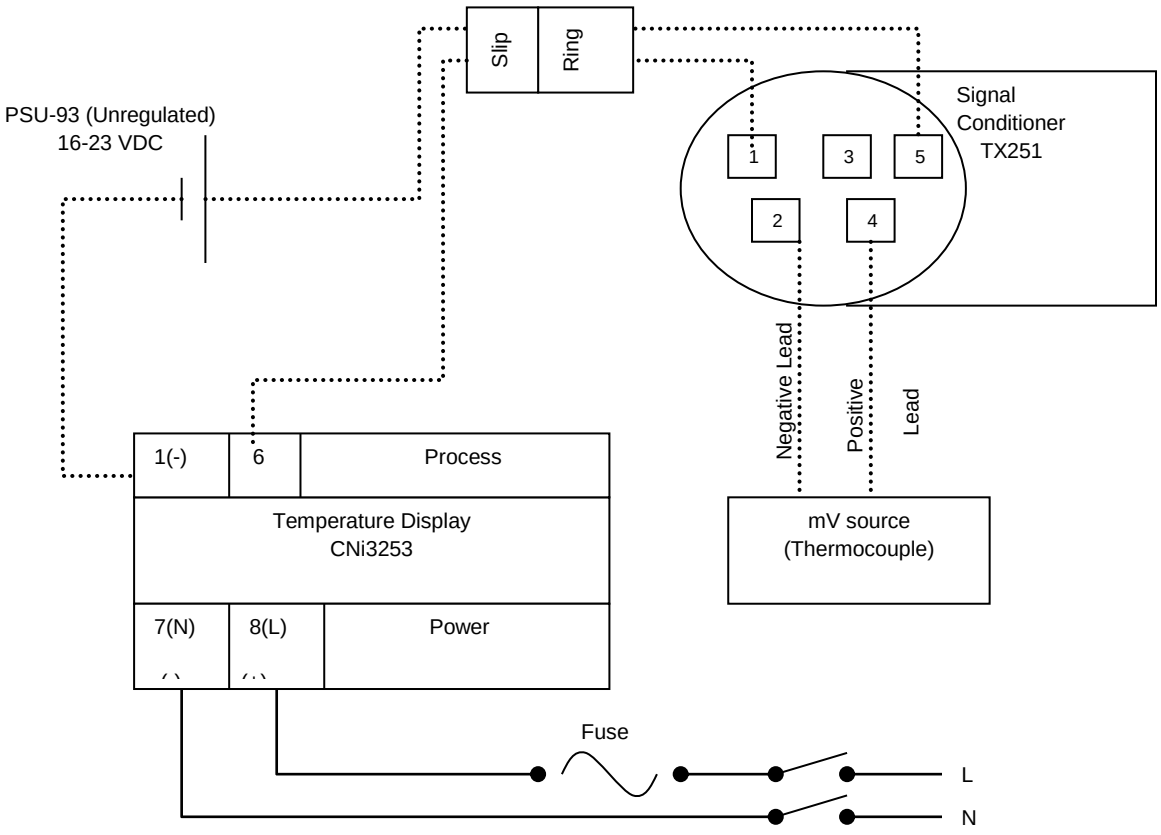

A.7 Calibration procedure of the temperature measurement circuit

Calibration of the temperature measurement system was conducted by replacing the thermocouple connection with the thermocouple simulator and setting it to 0°C followed by setting the ‘zero’ set screw of the TX251 signal conditioner so that 4mA current is produced. Next, the thermocouple simulator is set to 1000°C followed by setting of the ‘span’ set screw of the TX251 signal conditioner so that 20mA current is produced. The temperature display is set to correspond to a 4mA-20mA signal, where 4mA displays 0ºC, and 20mA displays 1000ºC.

A.8 Mechanical design

A.8.1 Assembly drawing

Figure A.4 shows an assembly drawing of the mounting device. Figure A.5 shows an assembly drawing of the mounting plate.

Figure A.4: Assembly drawing of the mounting device

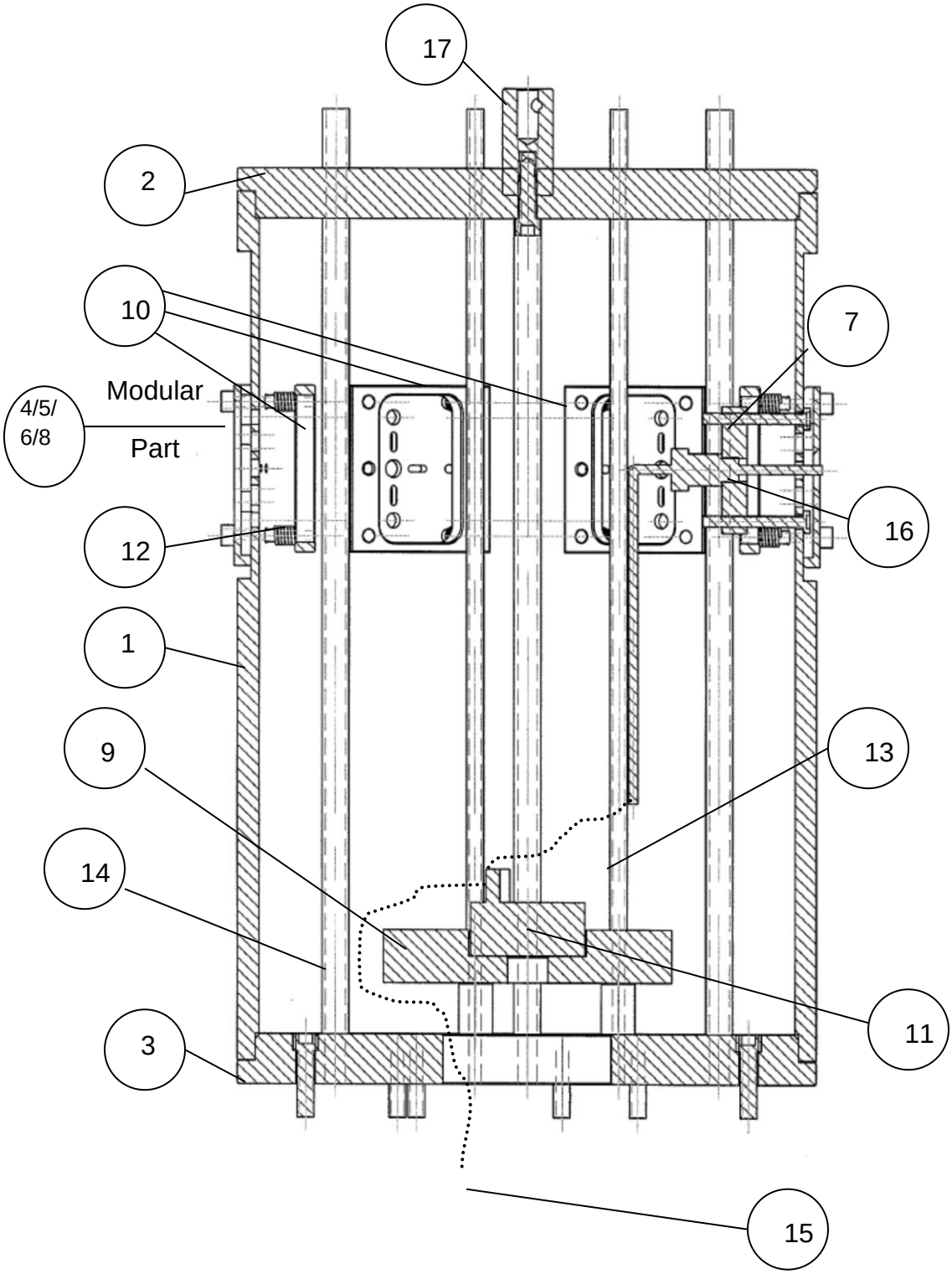

Figure A.5: Assembly drawing of the mounting plate[1]

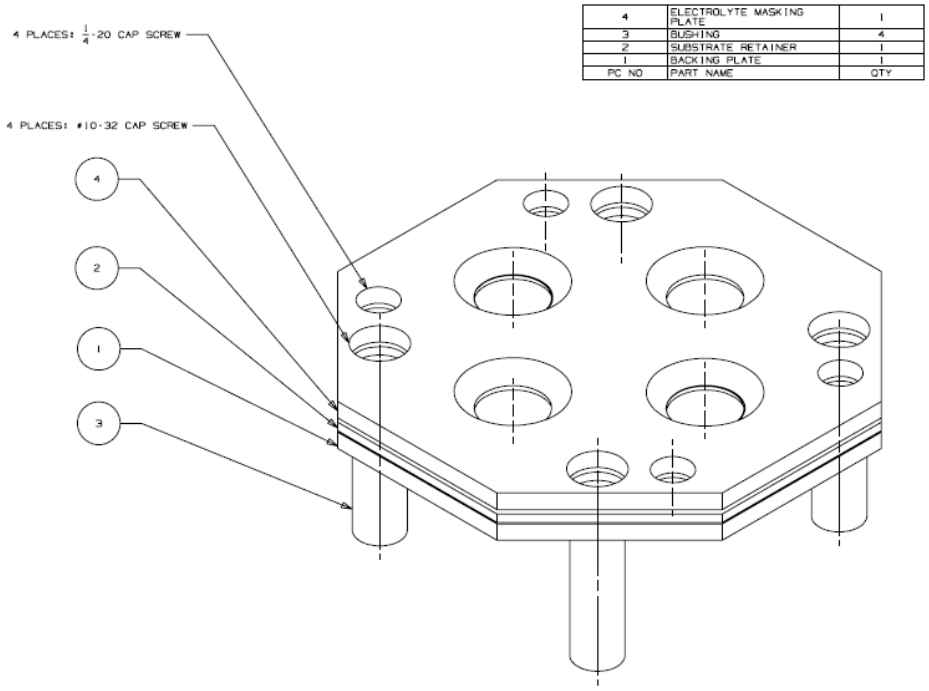

A.8.2 Parts description

Table A.2 show the parts for the assembly of the custom made mounting device.

Table A.2: Part list for mounting device assembly

Part No.	Supplier	Description	Material	Qnt.
1	Custom made	Pipe	Carbon Steel	1
2	Custom made	Upper plate	Carbon Steel	1
3	Custom made	Lower plate	Carbon Steel	1
4	Custom made	Backing plate[1]	Carbon Steel	6
5	Custom made	Substrate retainer[1]	Carbon Steel	6
6	Custom made	Electrolyte masking[1] plate	Carbon Steel	6
7	Custom made	Thermocouple mounting plate	Carbon Steel	1

[1] This part was modified from the original design by Craig Metcalfe at a later stage of the research to allow exposure of the entire substrate surface and complete coverage for spraying electrolytes in full cell configuration

Part No.	Supplier	Description	Material	Qnt.
8	Custom made	Cover plate[1]	Carbon Steel	1
9	Custom made	Signal conditioner/transmitter holder	Carbon Steel	1
10	Custom made	Opposite plate	Carbon Steel	6
11	Omega TX251	Signal conditioner / Transmitter	---------	1
12		Compression spring	Carbon Steel	24
13	Mcmaster	#1/4-20 Threaded Rod	Carbon Steel	4
14	Mcmaster	#3/8-24 Threaded Rod	Carbon Steel	6
15	---------	Electrical wire (to temperature display)	----------	-----
16	Omega BTH-090-K-3-60-2	Solid Probe Bayonet Style Thermocouple	---------	1
17	Custom made	Cylindiral specimen holder	Carbon steel	1

A.8.3 Mechanical drawings of mounting device

A.8.3.1 Pipe

Figure A.6 shows mechanical drawing of the pipe; part number 1. This part was machined of a standard 8" carbon steel pipe. The holes in detail A in the drawing are used to mount modular mounting plates for the different substrate sizes and shapes.

Figure A.6: Detailed view of the mounting holes for the modular substrate mounting plates on pipe (part 1)

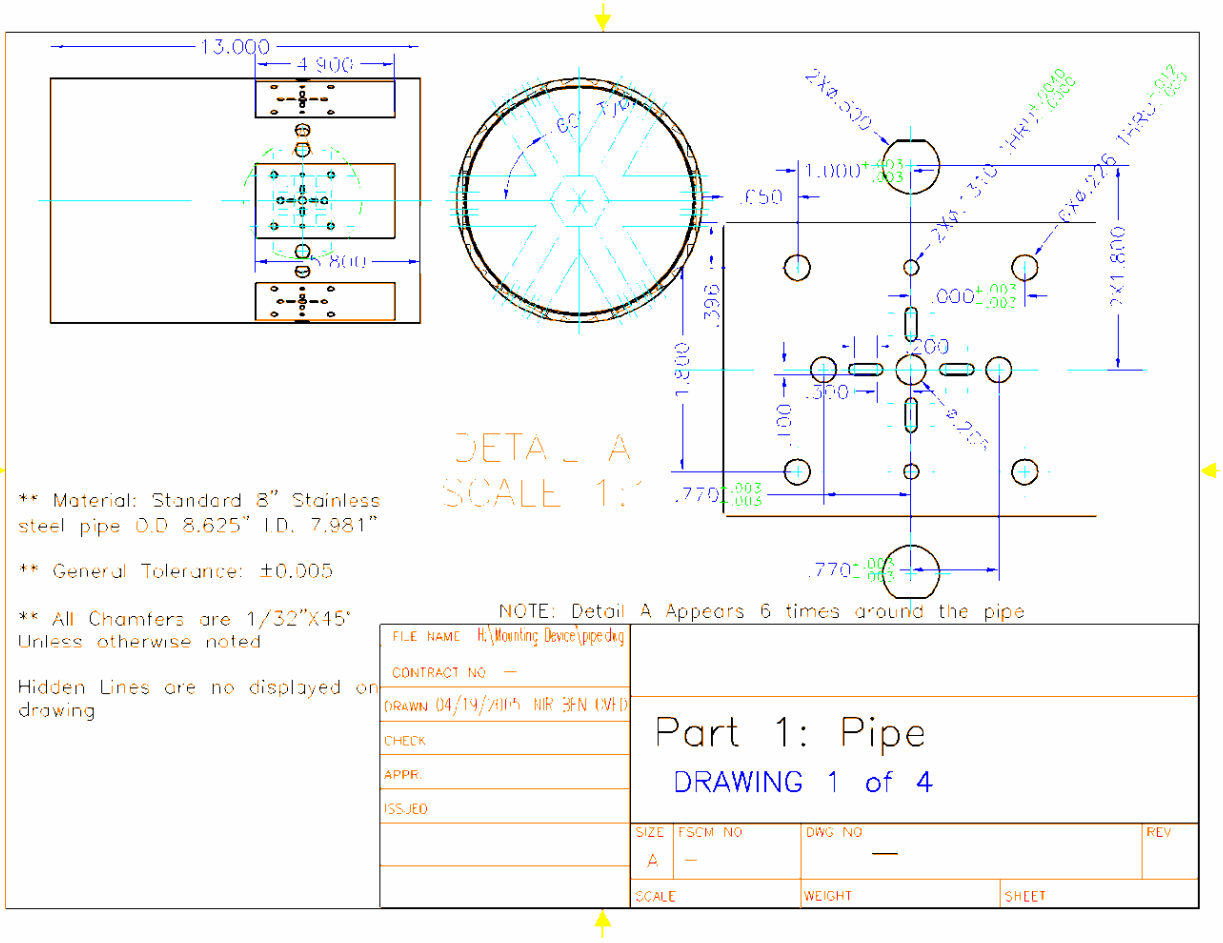

Figure A.7 shows an isometric view of the pipe. Detail C shows the area where the modular substrate plates are fitted.

Figure A.7: Isometric view of pipe (part 1)

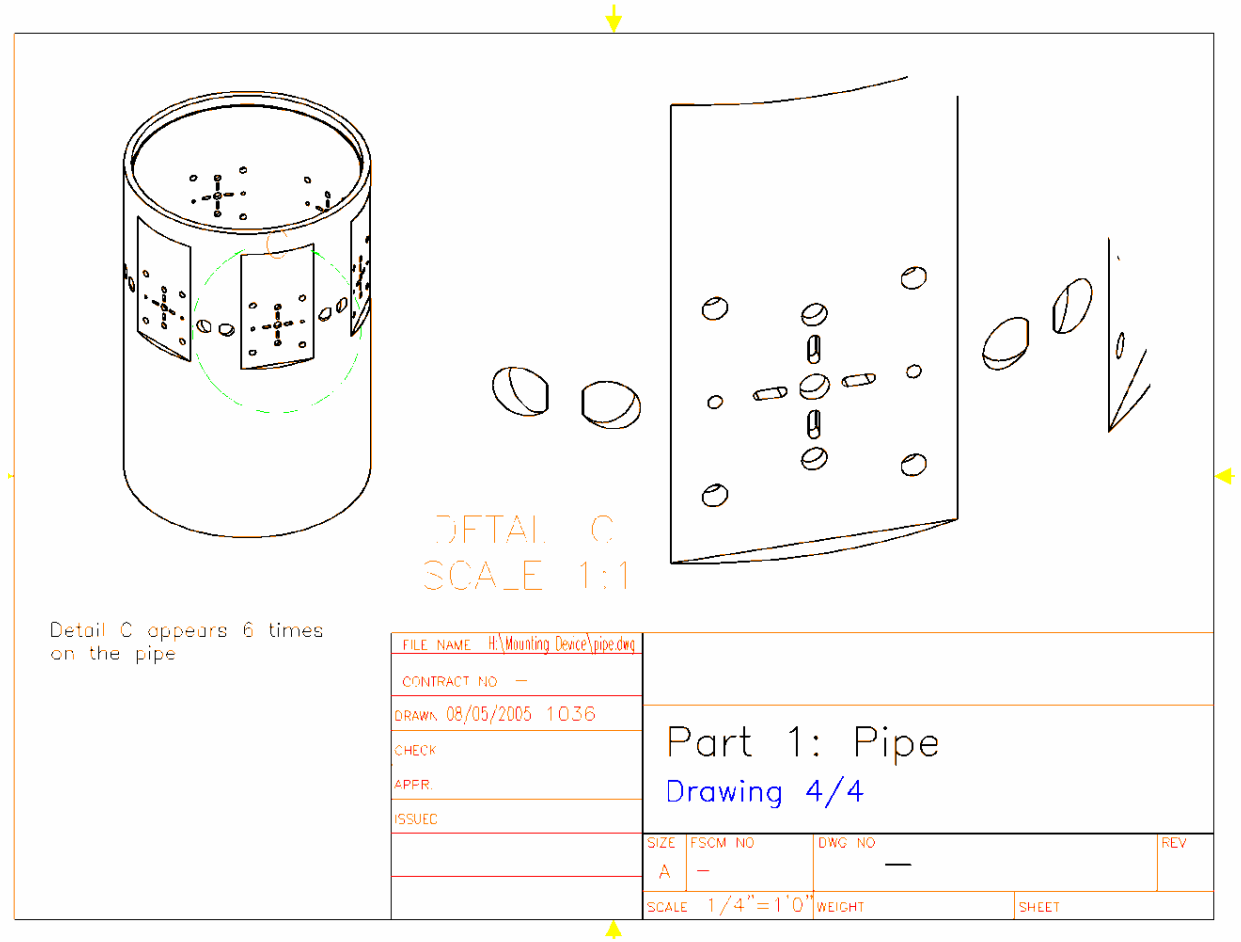

A.8.3.2 Upper plate

Figure A.8 shows the upper plate; part number 2. This part is fitted into the pipe as shown in figure A.4.

Figure A.8: Mechanical drawing of Upper Plate (part 2)

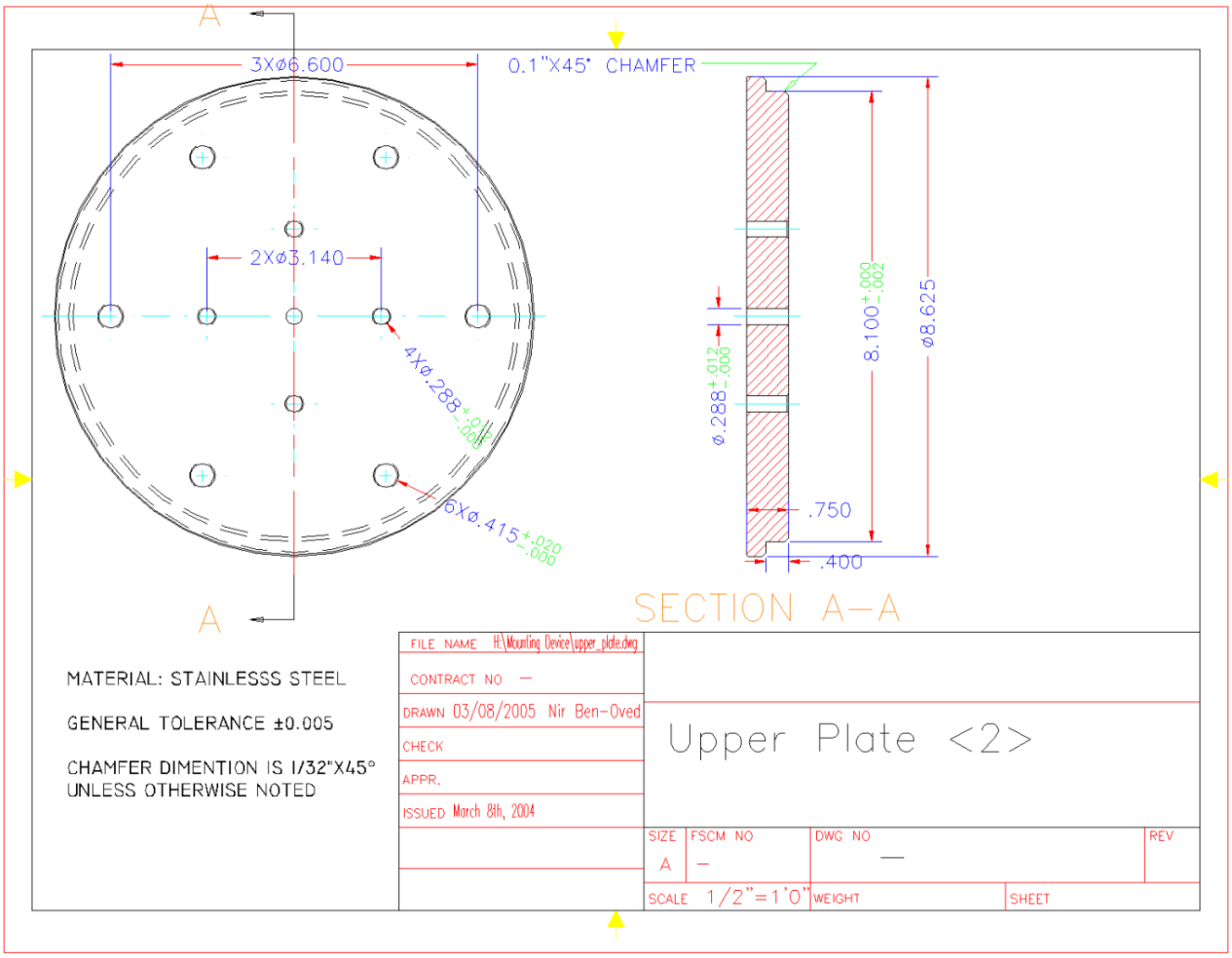

A.8.3.3 Lower plate

Figure A.9 shows the lower plate; part number 3. This part is connected to the plasma spray turntable with ¼" bolts and is fitted into the pipe as shown in figure A.4. It has a round hole that is constructed as an opening for slip ring electrical wires that pass through the plasma spray turntable hollow shaft.

Figure A.9: Mechanical drawing of Lower Plate (part 3)

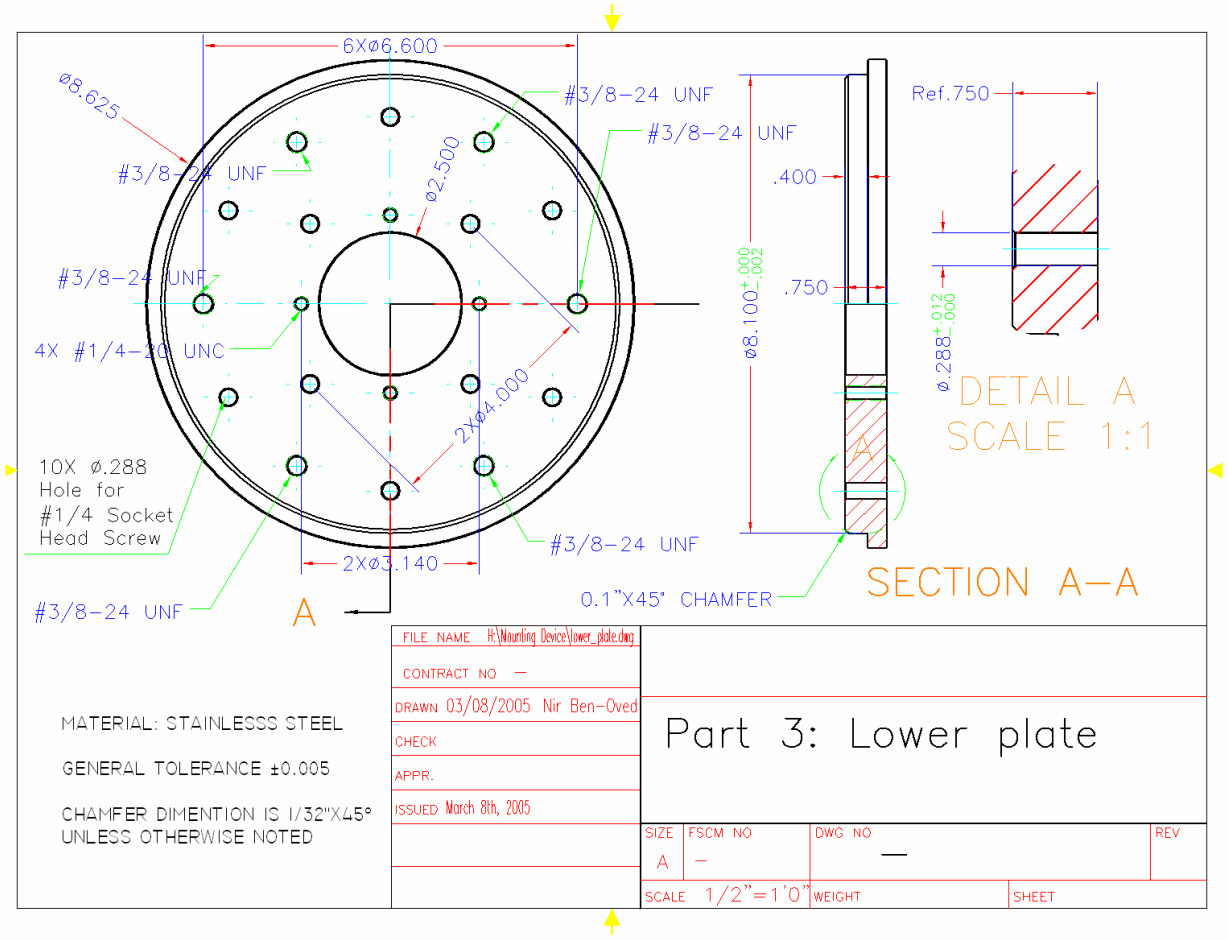

A.8.3.4 Backing plate

Figure A.10 shows a backing plate for substrate mounting; part number 4. This part is used as backing for mounted cells.

Figure A.10: Backing plate (part 4)

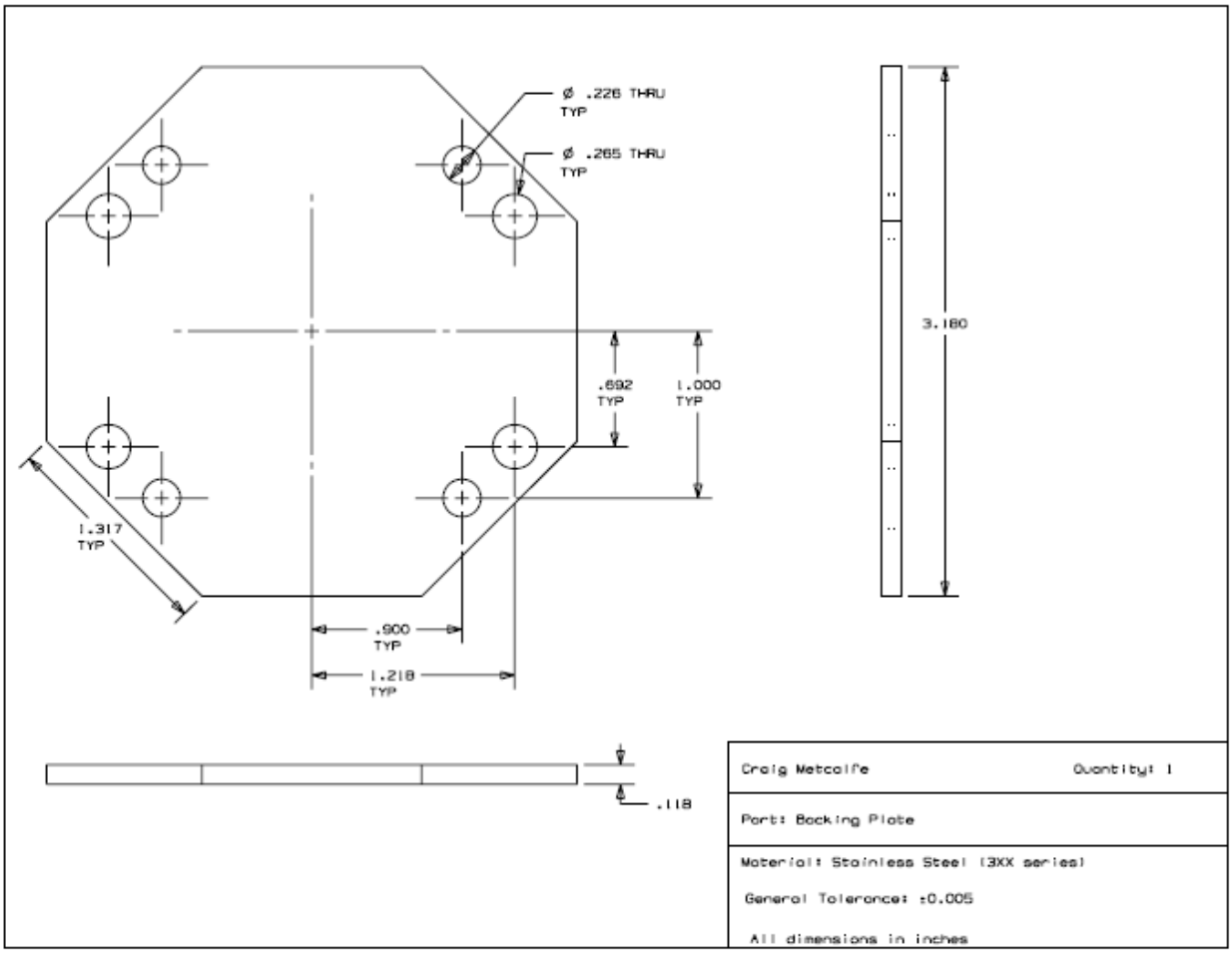

A.8.3.5 Substrate retainer

Figure A.11 shows a backing plate for substrate mounting; part number 5. This part is used to mount electrolyte supported cells utlizing 2 concentric holes with different diameters. It allows covering of the entire surface by plasma sprayed electolyte**.**

Figure A.11: Substrate retainer (part 5)

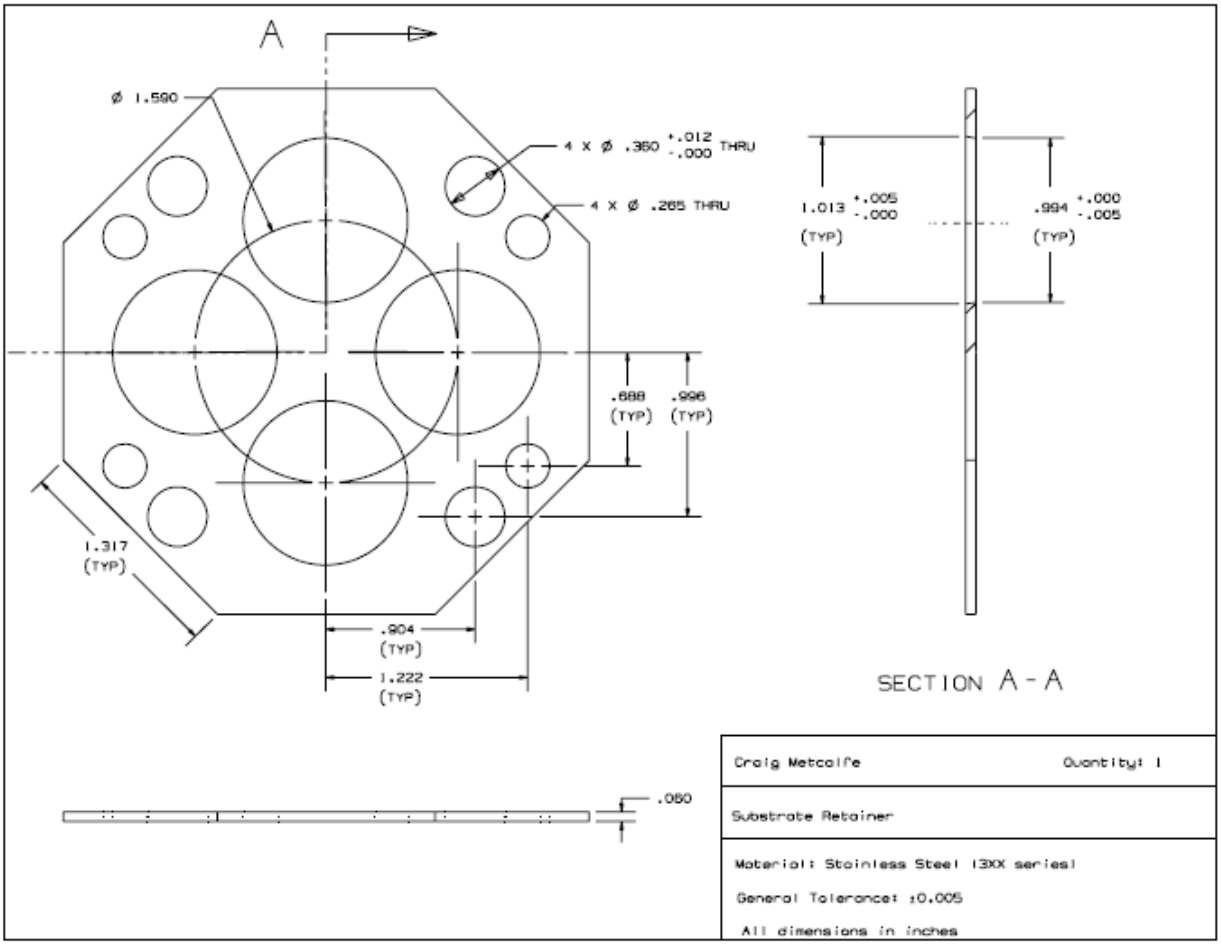

A.8.3.6 Masking plate

Figure A.12 shows a masking plate for substrate mounting; part number 6. This part is used as a mask when anodes are sprayed onto an electrolyte.

Figure A.12: Masking plate (part 6)

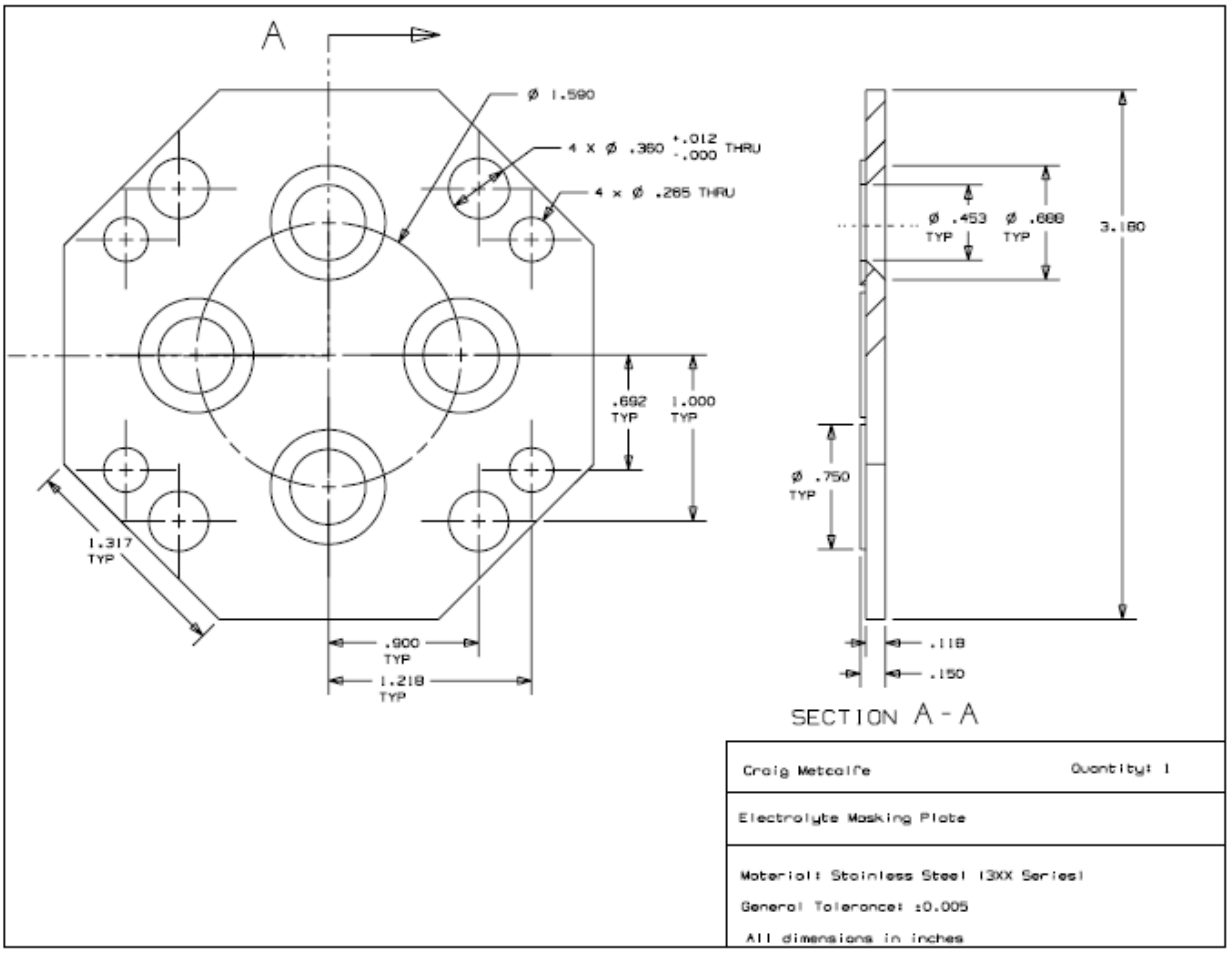

A.8.3.8 Thermocouple mounting plate

Figure A.14 shows the thermocuple mounting plate; part number 7. This part is placed inside the pipe and it has a threaded hole on which the spring loaded thermocouple (part 16 in table 3.2) is mounted.

Figure A.13: Thermocouple mounting plate (part 7)

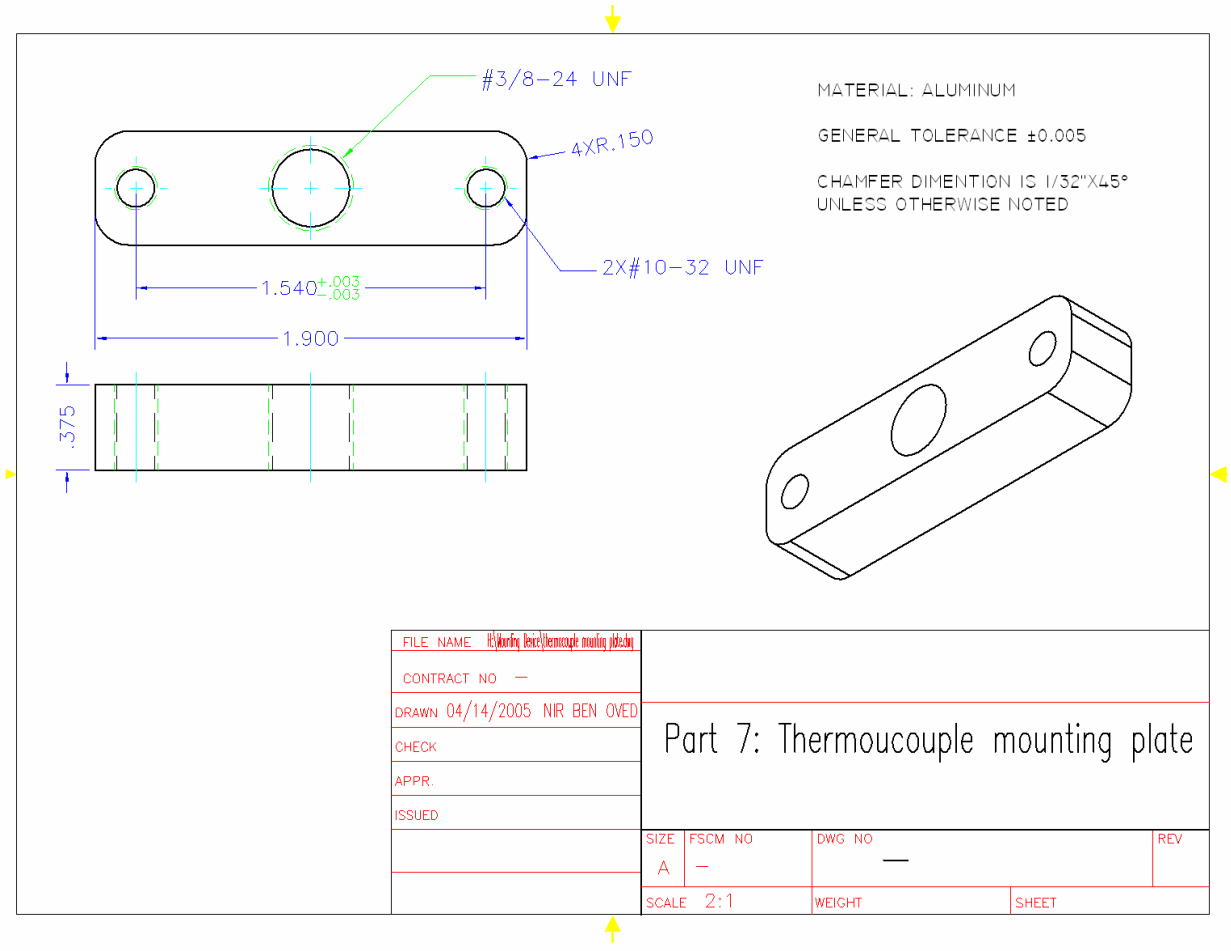

A.8.3.7 Cover plate

Figure A.13 shows a cover plate for substrate mounting; part number 8. This part is used to cover unused holders during plasma spraying.

Figure A.14: Cover plate (part 8)

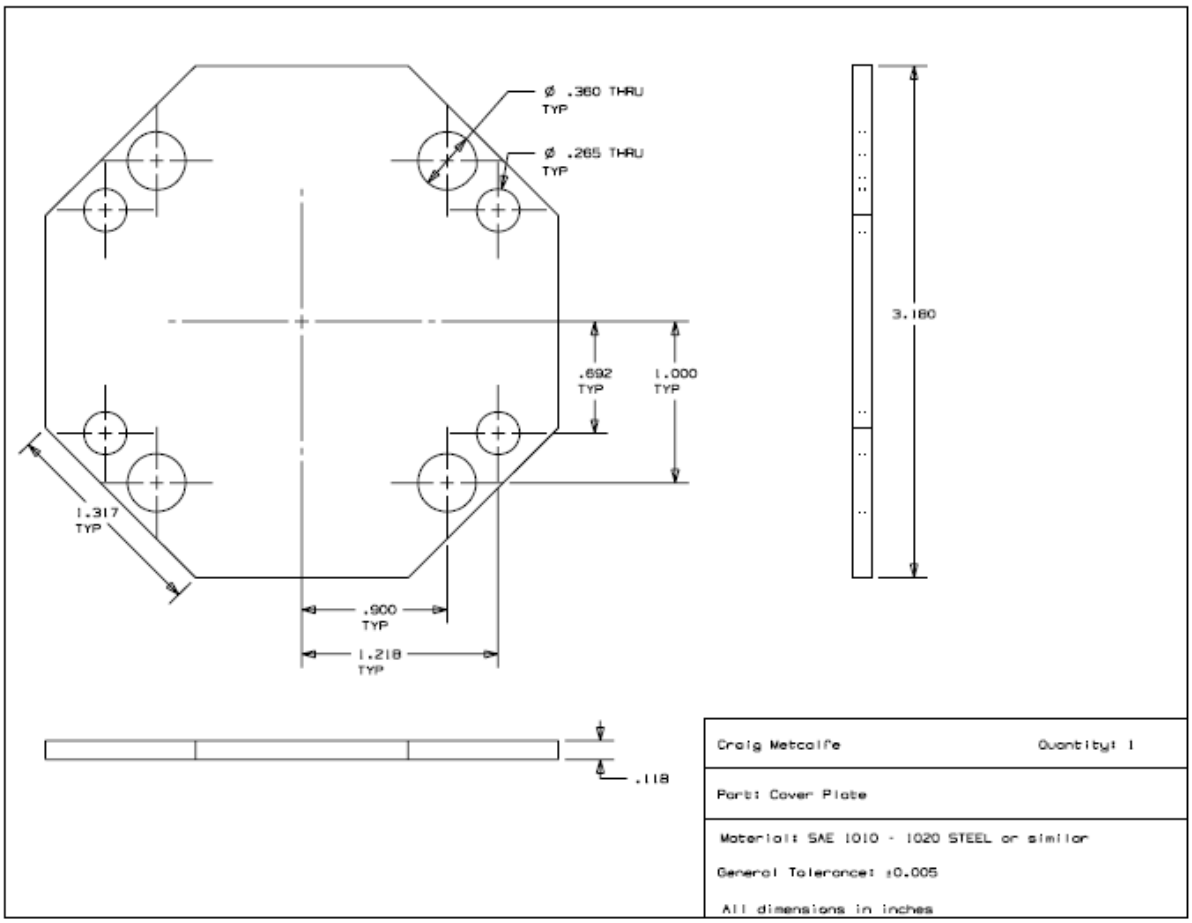

A.8.3.9 Transmitter holder

Figure A.15 shows the transmitter holder; part number 9. This part is used to mount the signal conditioner/transmitter TX251 (part 11 in Table 3.2) inside the pipe

Figure A.15: Transmitter holder (part 9)

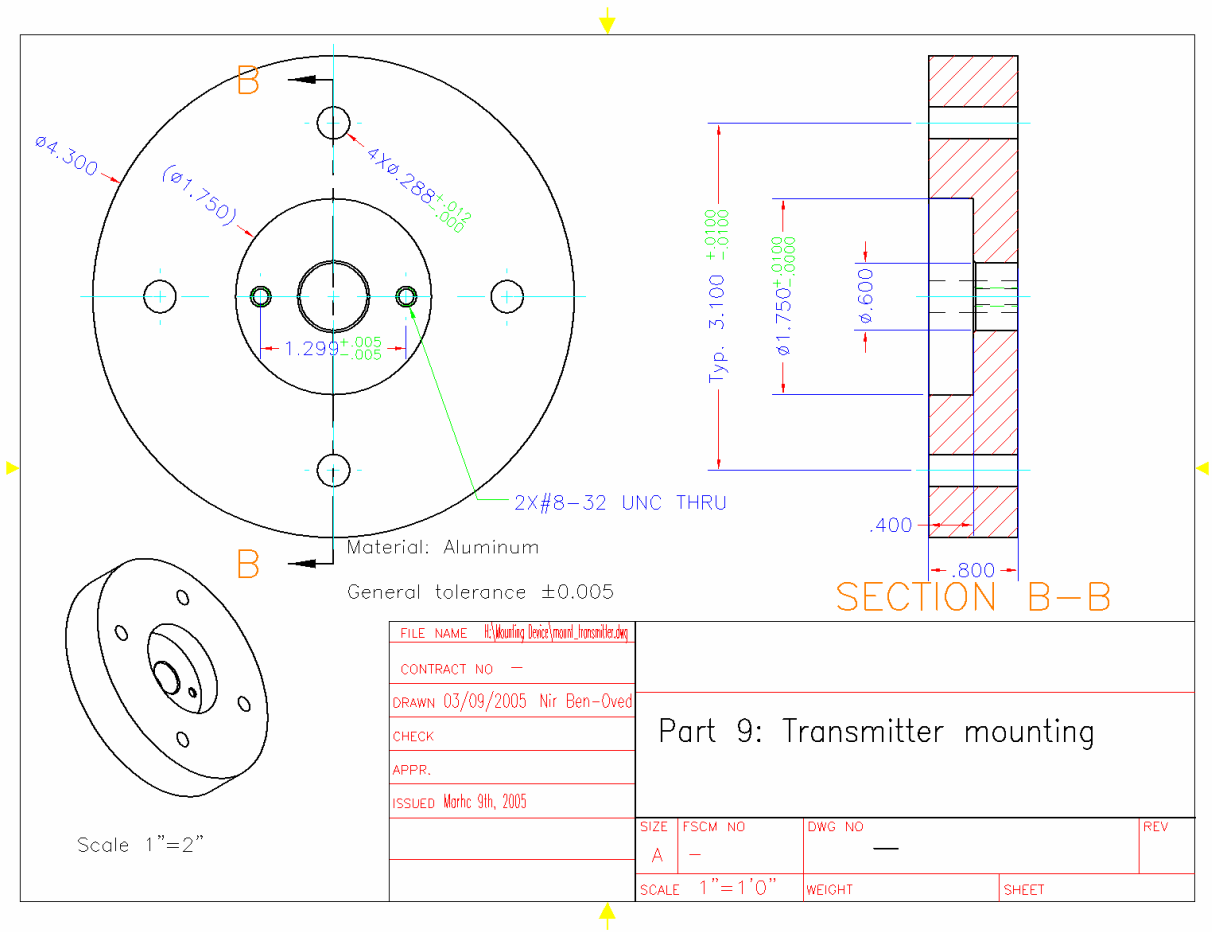

Appendix B: Button cell test station for 1” button cells in full cell configuration

B.1 General

A test station for high temperature testing of SOFCs is required for the electrochemical charactarization of the cells. Test stations for button cells are commericaly available, but they are expensive and unreliable, particularly with regard to sealing and gas transport. Sealing problems cause leakage that may lead to full or partical combustion of the anode fuel with the cathode air. This introduces errors in cell performance data, and reduces the reliabilty of the testing results. A test station for 1” button cell testing in full cell configuration was therefore custom designed and made for reduced cost and improved sealing.

B.2 1” test station for full cell testing

In full cell testing configuration, the fuel side has to be sealed to eliminate combustion. The air side can be open to the enviroment. The custom designed station for a full cell testing configuration consists of concentric ceramic tubes for suppling fuel on the anode side and air on the cathode side, for supporting electrical wires on each side, and for safely exhausting unspent fuel from the anode side. The cell is sealed on the fuel side tube using a high temperature ceramic adhesive (Cermabond 552, Aremco Inc, Valley Cottage NY, USA). A porous ceramic cap used to evenly distribute the gases to the electrode surface is mounted on the end of each ceramic tube. On the cathode side, a platinum mesh is used as a current collector. Platinum is used at the cathode side due to its excellent non-oxidizing characteristics at cell testing

temperatures, its high melting temperature, and its good electrical conductivity. Commonly, platinum is used at the anode side as a current collector. However, in a methane gas enviroment, platinum, due to its high catalytic activity, causes carbon formation. The carbon is deposited on the platinum mesh, and it may stick to the anode surface. In this case, it will be impossible to analyze the anode in regard to carbon deposition caused by the anode materials. Therefore, in the case of direct oxidation anodes, silver or gold can be utlized as an alternative to platinum due to their inert activity towards carbon deposition. Silver is more cost effective than gold and it is possible to use it within the temperature range of testing for Cu based anodes, which is not typically significantly higher than 700°C. Therefore, silver was chosen to replace platinum as a current collector at the anode side.

Behind the ceramic cap, a thermocouple is placed to allow temperature measurements close to the cell. A bubbler is used to humidify the fuel. The fuel is bubbled through a porous ceramic disk submerged in water, generating small-diameterbubbles, allowing a high contact surface area with the water and better humidification efficiency. The bubbler has no heating element, and the fuel is humidified at room temparature. The fuel and air flow are controlled by mass flow controllers prior to fuel humidification. Exhaust water is collected using a bottle with an inserted tube at the fuel exhaust. Swagelok tube fittings are used for all tube connections to allow proper sealing. The ceramic tubes are mounted to a tube furnace. Testing of a 1” cell is conducted by sealing the fuel cell onto the ceramic tube on the anode side by applying a ceramic adhesive seal (Ceramabond 552, Aremco Inc, Valley

Cottage NY, USA) and heating the cell according to the sintering temperature of the ceramic adhesive, at which it hardens and forms a seal.

B.2.1 Ceramic cap design

The ceramic cap is an essential part of the test station because it supplies mechanical support to the current collector mesh, and therefore it allows good contact with the cell and low ohmic losses due to contact resistance. In addition, it functions as gas distrubutor, distributing the gases evenly to the electrode.

Several configurations were examined for the ceramic cap. Initially, a machinable ceramic was applied to form a cap with holes to distribute the gases, as shown in Figure B.1

Figure B.1: Ceramic cap made of machinable ceramic

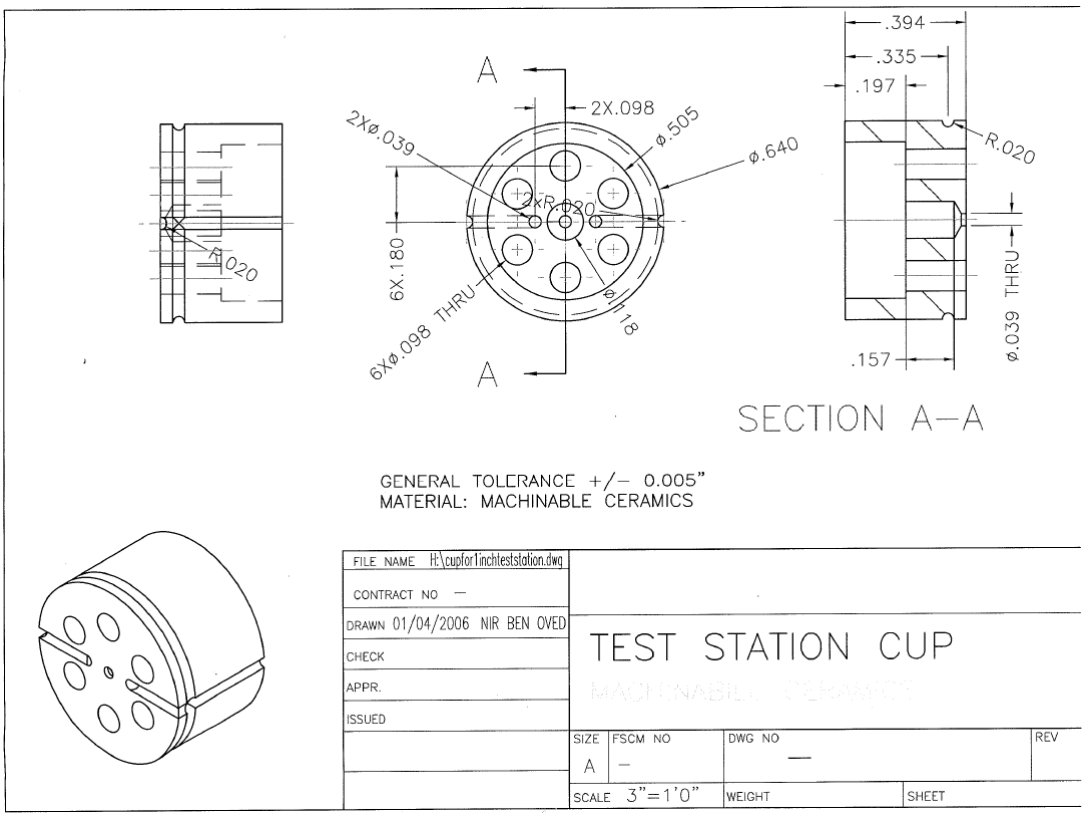

After applying the machinable ceramic cap at the test station, we found out that the gases were not evenly distrubted to the anode. Therefore, the CuO at the anode was not homogeneously reduced to Cu. Some areas at the anode were much darker than others, demostrating that the CuO was reduced homogoenously.

Due to this limitation, the cap design was changed to applying porous ceramics instead of machinable ceramics. Commercially available porous ceramic disks (Coorstek, Golden, CO, USA) with average pore diameter of 100µm and apparent porosity of 40.2% were cut with a water jet cutter to produce a porous ceramic cap. This cap demonstrated homogenous distribution of the gases to the electrode.

B.2.2 Cell sealing

After several tests, an improvement was made to the test station to allow better sealing. Ceramic adhesive works better under compression than under tensile stress. However, the thermal expansion coefficient of SS430 substrates, 11.4 μm $m^{-1}°C^{-1}$, is greater than that of the ceramic adhesive seal, which has a thermal expansion coefficient of 7.7 μm $m^{-1}°C^{-1}$. This difference results in tensile stress in the ceramic adhesive seal when the cell is heated to 700°C from room temperature. Therefore, a ceramic ring was attached to the ceramic tube to putthe ceramic adhesive seal under compression during heating. This improvement makes gas leakage through the ceramic adhesive seal less likely to occur. Figure B.2 shows (a) the original set up without the ceramic ring, and (b) the improved set up with the ceramic ring.

Figure B.2 (a) the original set up without ceramic ring, and (b) the improved set up with ceramic ring.

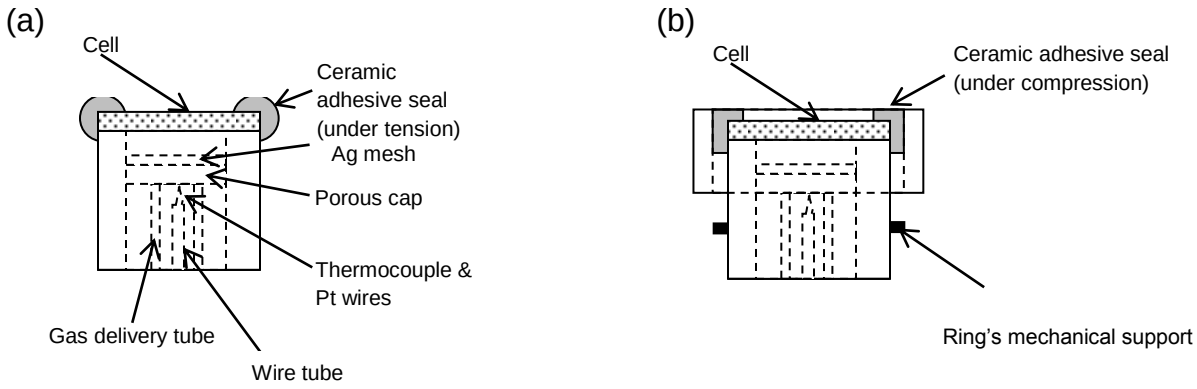

B.3 Part list for 1” Test station for full cell configuration

Table B.1 shows a part list for the custom made 1” test station of full cell configuration.

Table B.1: Part list for the custom made 1” test station of full cell configuration.

Item	Catalogue No.	Company	Description	Quantity
1	SS-1610-3-16-8	Swagelok	Reducing Union Tee, 1" Swagelok X 1" Swagelok X 1/2" Swagelok	1
2	SS-810-R-16	Swagelok	Reducer, 1/2" Swagelok X 1" Tube Stub	1
3	SS-810-3-8-6	Swagelok	Reducing Union Tee, 1/2" Swagelok X 1/2" Swagelok X 3/8" Swagelok	2
4	SS-400-R-8	Swagelok	Reducer, 1/4" Swagelok X 1/2" Tube Stub	2
5	66455	Coorstek	Alumina Tube 1”	1
6	65664	Coorstek	Alumina Tube ½”	2
7	65686	Coorstek	Alumina Solid tube w/4 bore holes O.D 0.219” Tube O.D 0.22”	2
8	60013	Coorstek	Ceramic cup (made of porous disk with avg. pore diameter of 100µm and apparent porosity of 40.2%)	
9	N/A	Heraeus Vectra, Brazil	Platinum gauze 4” X 8” 45 meshXin^{-1}	1
10	7166-26	Ace Glass Inc	Bottle Gas Washing	1
11	8762-14	Ace Glass Inc	Bubbler	1
12	N/A	Heraeus Vectra, Brazil	Platinum wire 0.4mm	5m
13	5TC-GG-K-24-36	Omega	Thermocouple Type “K”	2
14	SS-600-3	Swagelok	Union Tee, 3/8" Swagelok X 3/8" Swagelok X 3/8" Swagelok	9
15	SS-44S6	Swagelok	40 Series Ball Valve, 3/8" Swagelok X 3/8" Swagelok	5

Item	Catalogue No.	Company	Description	Quantity
16	SS-600-1-2	Swagelok	Male Connector, 3/8" Swagelok X 1/8" MNPT (for mass flow controllers)	5
17	PFA-T6-062	Swagelok	PFA Tubing, 3/8"OD x 0.062"wall thickness	
18	--------	----------	PC with Flow-Vision software. Multiply unit tracking, scripting, and data capturing software	1
19	MC-1SLPM-D/5M 5IN GAS: NITROGEN	Alicat Scientific, Inc	ALICAT Scientific MC Series Mass Flow Controller with 1SLPM full scale flow control range, local display, 0-5Vdc analog I/O, RS-232 I/O, and 1/8” NPT female process connections	1
20	MC-1SLPM-D/5M 5IN GAS: HYDROGEN	Alicat Scientific, Inc	ALICAT Scientific MC Series Mass Flow Controller with 1SLPM full scale flow control range, local display, 0-5Vdc analog I/O, RS-232 I/O, and 1/8” NPT female process connections	1
21	MC-500SCCM-D/5M 5IN GAS: METHANE	Alicat Scientific, Inc	ALICAT Scientific MC Series Mass Flow Controller with 500 SCCM full scale flow control range, local display, 0-5Vdc analog I/O, RS-232 I/O, and 1/8” NPT female process connections	1
22	MC-2 SLPM-D/5M 5IN GAS: AIR	Alicat Scientific, Inc	ALICAT Scientific MC Series Mass Flow Controller with 2 SLM full scale flow control range, local display, 0-5Vdc analog I/O, RS-232 I/O, and 1/8” NPT female process connections	1
23	DC-61	Alicat Scientific, Inc	6ft single ended cable with 8 pin mini-DIN connector.	4

B.4 Schematics of 1” Test station for full cell configuration

Figure B.3 shows schematic drawings of the 1” test station for full cell configuration. Part numbers correspond to part numbers in Table B.1. The external ceramic ring shown in Figure B.1b is not shown in this drawing.

Figure B.3: Schematic drawing of 1" Test station for full cell configuration

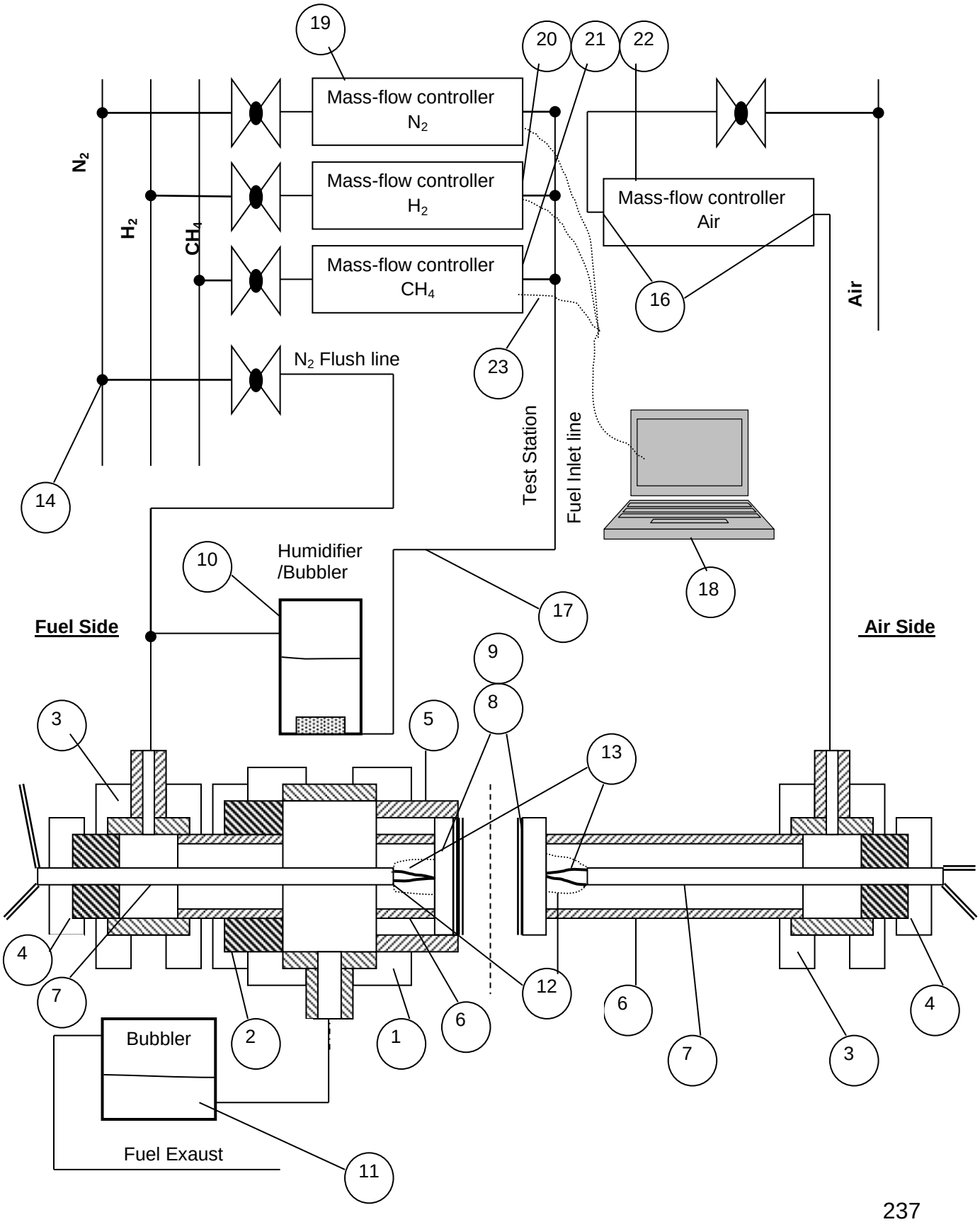

B.5 Mass flow controller calculations

The test station design incorporates mass flow controllers that can be controlled by a PC through a serial port. We chose Alicat mass flow controllers. They are factory calibrated for a wide range of different gases, and can function as a multi-unit assembly controlled by a PC and software. The Alicat mass flow controllers can handle from 0% up to 100% humidity of the gas, and pressures up to 125 psi (~8 atm).

B.5.1 Calculation of mass flow controller range

The range of volumetric flows of reactant gases can be calculated by assuming the maximum current that will be drawn from the cell, temperature and pressure conditions, and electrode area. Using the stochiometries of the half cell reactions, the maximum volumetric flow rate of each of the reactant gases is calculated.

The fuel side half cell reactions for H_2 andCH_4 are shown in Equations B.1 and B.2, respectively. Equation B.3 shows the air side half cell reaction.

$$H_2 + O^{=} \rightarrow H_2O + 2e^{-} \quad \text{(B.1)}$$

$$CH_4 + 4O^{=} \rightarrow CO_2 + 2H_2O + 8e^{-} \quad \text{(B.2)}$$

$$O_2 + 2e^{-} \rightarrow 2O^{=} \quad \text{(B.3)}$$

In order to obtain the range of the mass flow controller for each of the reactant gases, cell constants are estimated. Table B.2 shows the cell contants estimated for mass flow controller range calculations.

Table B.2: Estimated cell constants

Electrode Diameter	D=0.44" (The electrode diameter after plasma spraying with a mask)
Electrode area	A=1.02cm^2 (calculated from the electrode diameter)
Current drawn from the cell	i=0.5 Acm-^{2} (high performance cell) i=50 mAcm^{-2} (low performance cell)
Cell temperature	T=700°C
Fuel utilization	10%
Air utilization	10%
Fuel side N_2-H_2 and N_2-CH_4 mixtures	Dilution of 20% of fuel in N_2-H_2 and N_2-CH_4 mixtures

The gas mass flow rate is dependent on cell current, corresponding to the reactant gas usage equation which correlates the reactant gas molar flow rates and the resulting current, as can be seen in Equation B.4.

$$\dot{N} = \frac{iA}{nF} \tag{B.4}$$

Here, F is Faraday's constant (charge of one mole of electrons, 96485 C/mole), and n is the number of moles of electrons per 1 mole of reactant. Using equation B.2, the molar flow rate is calculated (mol s^{-1}) for high performance and low performance cells for each of the gases, shown in Table B.3.

Table B.3: Gas molar flow rates for high performance and low performance cells

Reactant Gas	Gas molar flow rate [mol s^{-1}]	
	High performance cell (i=0.5 A cm^{-2})	Low performance cell (i=0.05 A cm^{-2})
H_2	2.64e-06	2.64E-07
CH_4	6.62e-07	6.61E-08
O_2	2.64e-06	2.64E-07

The molar flow rates is converted to volumetric flow rates using equation B.4, the ideal gas equation.

$$\dot{V} = \frac{nRT}{P} \tag{B.4}$$

Here, R is the universal gas constant (R = 8.3145 $Jmol^{-1}K^{-1}$). Pressure losses due to piping resistance are assumed to be negligible, so the gases are at atmospheric pressure (P = 101.3 kPa). In addition, gases are assumed to be at cell temperature (T=700°C) when reaching the electrode.

Volumetric flow rate is converted from $m^{3b}s^{-1}$ to cm^3min^{-1} (sccm). Using Equation B.4, volumetric flow rates of the reactant gases are shown in Table B.4.

Table B.4: Volumetric flow rates of the reactant gases

Reactant Gas	**Volumetric flow rate [sccm]**	
	High performance cell (i=0.5 A cm^{-2})	**Low performance cell (i=0.05 A cm^{-2})**
H_2	12.6	1.26
CH_4	3.16	0.31
O_2	12.6	1.26

The total volumetric flow rate for the reactant gases is calculated using equation B.5.

$$\dot{V}(total) = \frac{\dot{V}}{fuel\ utilization} \quad \text{(B.5)}$$

Assuming a fuel utilization of 10%, the total reactant gas flow is shown in Table B.5

Table B.5: Volumetric flow rates of the reactant gases with fuel utilization of 10%

Reactant Gas	Volumetric flow rate [sccm]	
	High performance cell (i=0.5 A cm^{-2})	Low performance cell (i=0.05 A cm^{-2})
H_2	126	12.6
CH_4	31.6	3.16
O_2	126	12.6

The total air flow at the cathode side is calculated by the known concentration of O_2 in air. The total N_2 flow at the anode side is calculated by the estimated maximum dilution of the gas mixture of to 20% that would be used in studies of mass transport limitations at the cathode. The resultant volumetric flow rates are shown in Table B.6

Table B.6: Volumetric flow rates of Air and N_2

Reactant Gas	Volumetric flow rate [sccm]	
	High performance cell (i=0.5 A cm^{-2})	Low performance cell (i=0.05 A cm^{-2})
Air	604	60.4
N_2	633	63.3

B.6 Choice of mass flow controllers based on the range calculations

Based on the range calculations of the reactant gases, the Alicat Scientific mass flow controllers shown in Table B.7 were chosen.

Table B.7: Chosen Alicat Scientific mass flow controllers

Gas	Item	Description
H_2	Gas: Hydrogen MC-100SCCM-D/5M 5IN	ALICAT Scientific MC Series Mass Flow Controller with 100 SCCM full scale flow control range, local display, 0-5Vdc analog I/O, RS-232 I/O, and 1/8" NPT female process connections
CH_4	Gas: Methane MC-20SCCM-D/5M 5IN	ALICAT Scientific MC Series Mass Flow Controller with 20 SCCM full scale flow control range, local display, 0-5Vdc analog I/O, RS-232 I/O, and 1/8" NPT female process connections
N_2	Gas: Nitrogen MC-500SCCM-D/5M 5IN	ALICAT Scientific MC Series Mass Flow Controller with 500 SCCM full scale flow control range, local display, 0-5Vdc analog I/O, RS-232 I/O, and 1/8" NPT female process connections
Air	Gas: Air MC-500SCCM-D/5M 5IN	ALICAT Scientific MC Series Mass Flow Controller with 500 SCCM full scale flow control range, local display, 0-5Vdc analog I/O, RS-232 I/O, and 1/8" NPT female process connections

Appendix C: Equivalent circuit fitting

C.1 Equivalent circuit fitting of cathode symmetrical cells

Figure C.1 shows equivalent circuit fitting parameters of a symmetrical cathode cell at (a) 700°C (b) 650°C (c) 600°C and (d) 550°C.

Figure C.1: Equivalent circuit fitting parameters of symmetrical cathode cell at (a) 700°C (b) 650°C (c) 600°C and (d) 550°C

(a)

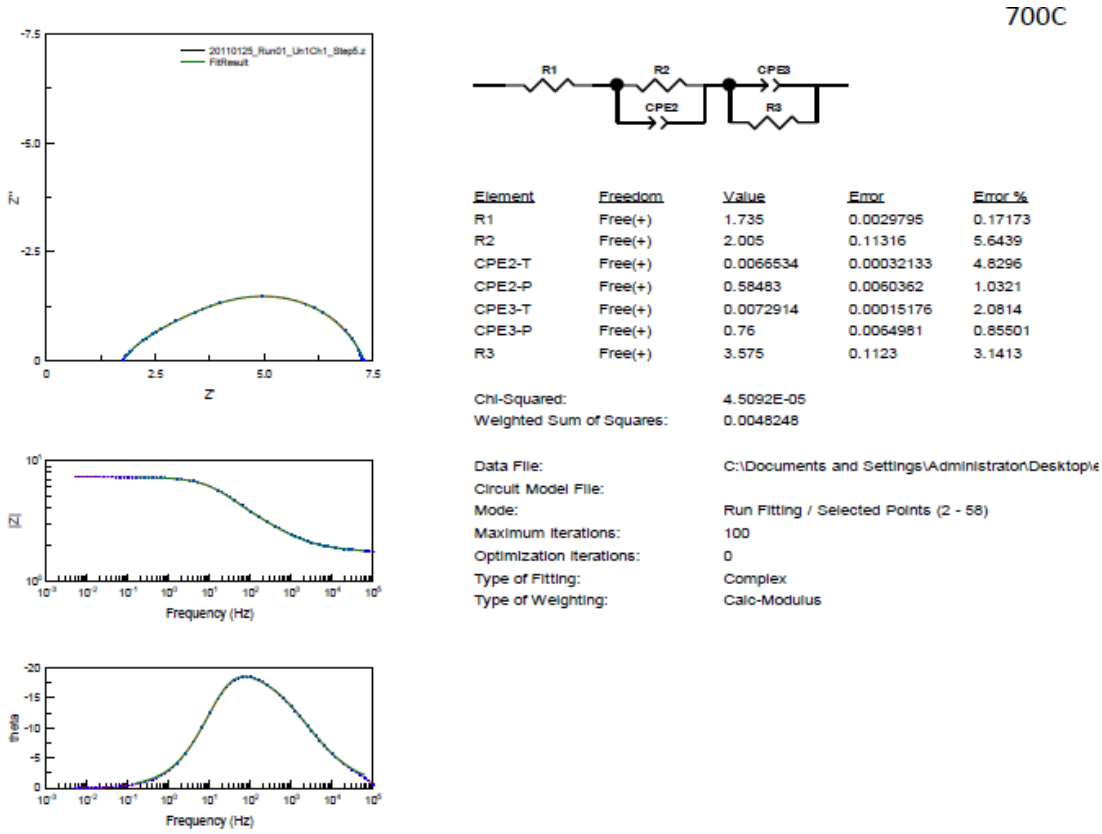

(b)

650C

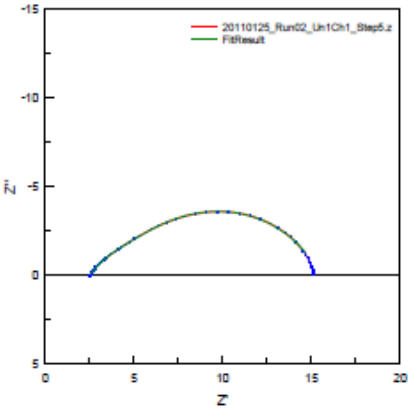

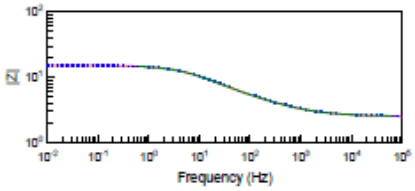

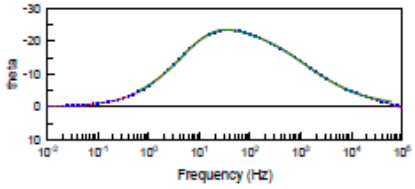

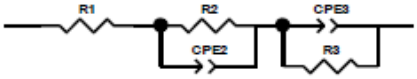

Element	Freedom	Value	Error	Error %
R1	Free(+)	2.517	0.0037709	0.14982
R2	Free(+)	2.75	0.15805	5.7473
CPE2-T	Free(+)	0.0048131	0.0002156	4.4794
CPE2-P	Free(+)	0.61945	0.0062531	1.0095
CPE3-T	Free(+)	0.0052626	6.6066E-05	1.2554
CPE3-P	Free(+)	0.73034	0.0054902	0.75173
R3	Free(+)	10.18	0.17639	1.7327

Chi-Squared:	4.3942E-05
Weighted Sum of Squares:	0.0041745
Data File:	C:\Documents and Settings\Administrator\Desktop\e
Circuit Model File:	
Mode:	Run Fitting / Selected Points (2 - 52)
Maximum Iterations:	100
Optimization Iterations:	0
Type of Fitting:	Complex
Type of Weighting:	Calc-Modulus

(c)

600C

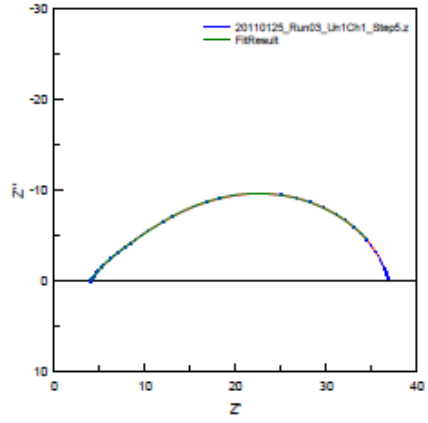

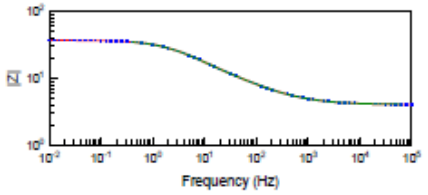

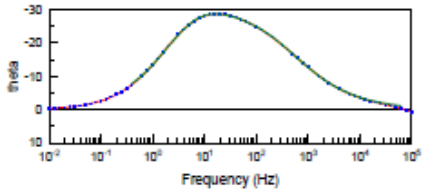

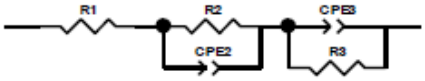

Element	Freedom	Value	Error	Error %
R1	Free(+)	4.006	0.0049882	0.12452
R2	Free(+)	5.856	0.34276	5.8531
CPE2-T	Free(+)	0.0041655	0.0001262	3.0296
CPE2-P	Free(+)	0.62238	0.0048876	0.78531
CPE3-T	Free(+)	0.0039765	4.2582E-05	1.0708
CPE3-P	Free(+)	0.73144	0.0052326	0.71538
R3	Free(+)	27.8	0.41132	1.4796

Chi-Squared:	4.4588E-05
Weighted Sum of Squares:	0.0044143
Data File:	C:\Documents and Settings\Administrator\Desktop\e
Circuit Model File:	
Mode:	Run Fitting / Selected Points (2 - 54)
Maximum Iterations:	100
Optimization Iterations:	0
Type of Fitting:	Complex
Type of Weighting:	Calc-Modulus

(d)

550C

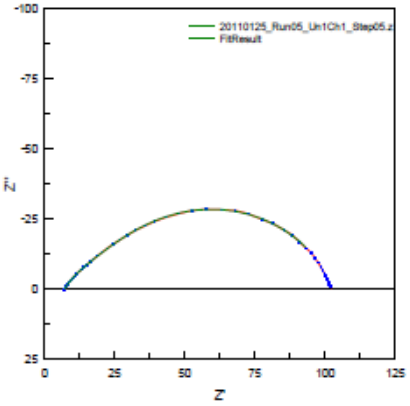

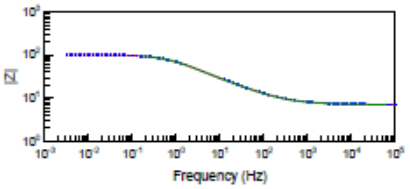

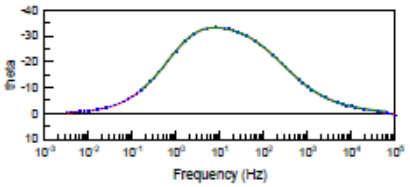

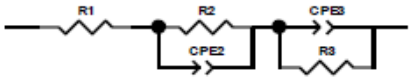

Element	Freedom	Value	Error	Error %
R1	Free(+)	6.999	0.0063288	0.090424
R2	Free(+)	16.04	0.73866	4.6051
CPE2-T	Free(+)	0.0032648	5.5931E-05	1.7132
CPE2-P	Free(+)	0.62122	0.0028685	0.46175
CPE3-T	Free(+)	0.003029	2.9741E-05	0.98188
CPE3-P	Free(+)	0.74346	0.004216	0.56708
R3	Free(+)	80.39	0.91709	1.1408

Chi-Squared:	3.4648E-05
Weighted Sum of Squares:	0.0037074
Data File:	C:\Documents and Settings\Administrator\Desktop\e
Circuit Model File:	
Mode:	Run Fitting / Selected Points (2 - 58)
Maximum Iterations:	100
Optimization Iterations:	0
Type of Fitting:	Complex
Type of Weighting:	Calc-Modulus